Detailed experimental study of mass transfer and liquid flow in a bubble column with optical measurement techniques

Dissertation

zur Erlangung des akademischen Grades

Doktoringenieur
(Dr.-Ing)

von M.Sc. Péter Miklós Kováts
geb. am 20.09.1983 in Miskolc

genehmigt durch die Fakultät für Verfahrens- und Systemtechnik
der Otto-von-Guericke-Universität Magdeburg

Promotionskommission: Prof. Dr.-Ing. habil Martin Sommerfeld (Vorsitz)
Prof. Dr.-Ing. Habil. Dominique Thévenin (Gutachter)
Prof. Dr.-Ing. Michael Schlüter (Gutachter)
Dr. Nicolas Dietrich (Gutachter)
Dr. Katharina Zähringer (Mitglied)

eingereicht am: 29.04.2021
Promotionskolloquium am: 01.11.2021

Abstract

Bubble column reactors are used for different chemical and biological processes in the industry. Dispersed gas comes into reaction with the liquid phase through gas-liquid mass transfer. Often mass transfer is the limiting factor for the reaction and its investigation and characterization becomes important for the optimization of a reactor. Non-intrusive optical mass transfer studies in two-phase flows often rely on Laser-Induced Fluorescence (LIF). To follow the gas dissolved into the liquid phase, in these cases, a tracer has to be added to the system, which reacts with the dissolved gas to form a fluorescent species.

For a better understanding of the transfer mechanisms and subsequent chemical reactions, the flow around free rising single bubbles and in a cylindrical laboratory-scale bubble column reactor with an aspect ratio of five was investigated. To this end, different non-intrusive methods have been applied around single bubbles and in the reactor. First, shadowgraphy technique is used in the bubble column for the characterisation of the bubbles (bubble diameter, velocity, shape or position) for various process conditions. The influence of water quality, filling height, pH, gas type and different glycerol-water mixtures, together with the surfactant sodium dodecyl sulphate (SDS), were analysed in this study. Thus, the present study covers a viscosity range of 0.86…9.29 mPa·s and a surface tension range of 44.8…72.24 mN·m^{-1}, accordingly, a Morton number range of 1.71x10^{-11}…7.04x10^{-7}. The shadowgraphy technique is based on particle recognition with backlight illumination and combined with Particle Tracking Velocimetry (PTV). The bubble trajectories and velocities in the column can also be obtained in this manner. The bubble sizes and velocities obtained here show a good agreement with correlations proposed in the literature. In contrast, it has been found that in the literature proposed correlations are not able to predict correctly the bubble aspect ratio in cases with higher glycerol concentration or with surfactant. Employing the several million bubble aspect ratios obtained from the present experiments, new correlations based on the Flow number have been proposed for different water-glycerol mixtures with and without surfactant. Furthermore, literature correlations for mass transfer coefficient have been verified against experimental data from the literature regarding their accuracy and applicability. The results have shown that none of the equations can predict the mass transfer coefficient adequately. For this reason, these equations have been extended with the Morton number and new correlations have been proposed. Besides these optimized correlations, a new correlation has been proposed based on the previously suggested aspect ratio calculation.

The results computed by the newly proposed correlations have revealed that with decreasing surface tension and decreasing viscosity, the bubble size is decreased but neither the addition of glycerol nor the addition of surfactant was found to be beneficial to mass transfer from the CO_2 bubbles into the liquid.

Secondly, the liquid phase flow has been analysed in the bubble column and around single bubbles by Particle Image Velocimetry (PIV) with different technical setups, changing the spatial and temporal resolutions. The combination of both measurement methods, delivering relevant information concerning disperse (bubbles) and continuous (liquid) phases, leads to a complete fluid dynamical characterization of the reactor, which is the pre-condition for the analysis of mass transfer between both phases.

Due to the bubble size and velocity change in different mixtures, the liquid flow field is

changed as well. The highest liquid velocities could be found in the high-viscosity solutions. The liquid velocity profiles are similar for different viscosities, except in the bottom section of the column where the bubble curtain is more concentrated.

Finally, the mass transfer from CO_2 and air bubbles into the liquid was investigated through two different reaction systems with LIF technique. The single bubble results have shown that behind a spherical bubble a stable stagnant cap evolves, which hinders the mixing and mass transfer. Behind ellipsoidal bubbles this stagnant cap does not exist, therefore the mass transfer is enhanced.

The PLIF (planar-LIF) experiments with a bubble chain and a curtain of CO_2 have shown that higher mass transfer from gas to liquid can be achieved with higher gas flow rates in pure water. The addition of surfactant and glycerol has a large influence on bubble size and velocity, but neither of them has advantageously affected the mass transfer. The time to reach a certain pH in the column is always prolonged in the solutions with glycerol and at lower gas flow rate. It has been found that neutralization progresses from the top of the column to the bottom. The reasons are the recirculation loops at the top, where the liquid with dissolved gas is trapped. From this loop, just a small amount of liquid is transported near the wall downwards to the column bottom, therefore the remarkable delay in the reaction at the bottom.

In a newly applied reaction system with resazurin and air bubbles, the reaction progress decreases also from the top to the bottom of the column, analogue to the CO_2 experiments. Until all oxygen is consumed by the reaction in the top section, just a small amount of free dissolved oxygen is transported to the bottom sections.

These results have also shown that the reaction of resazurin with oxygen is fast enough to visualize and quantify the mass transfer in a bubble column reactor also in a complex system with bubble curtain and it provides reliable and detailed information about the mixing and mass transfer process in a bubble column. Moreover, the sensitivity of this system at low concentrations is remarkable.

The obtained experimental data has already been used for systematic validations of numerical models describing large-scale bubble columns, thus supporting the further development of predictive simulations concerning mass transfer in bubble columns.

Zusammenfassung

Blasensäulen werden sehr häufig für verschiedene chemische und biologische Prozesse in der Industrie eingesetzt. Über gas-flüssig Stofftransport geht dispergiertes Gas in Reaktion mit der Flüssigphase. Häufig ist dabei der Stofftransport der limitierende Faktor für die Reaktion und seine Charakterisierung und Untersuchung ist darum sehr wichtig für die Optimierung eines Reaktors. In zweiphasigen Strömungen werden Studien zum Stofftransport oft mit der berührungslosen optischen Messmethode, Laser-Induzierte Fluoreszenz (LIF) durchgeführt. In die Flüssigphase eingelöstes Gas wird dabei in dem System mittels eines Tracerstoffs verfolgt, welcher mit dem eingelösten Gas fluoreszierende Spezies bildet.

Zum besseren Verständnis solcher gas-flüssig Transportmechanismen mit nachfolgenden chemischen Reaktionen wurde in dieser Arbeit die Strömung um frei aufsteigende Einzelblasen und in einem zylindrischen Blasensäulenreaktor im Labormaßstab mit einem Seitenverhältnis von fünf untersucht. Die Messungen wurden mit verschiedenen berührungsfreien optischen Messmethoden um einzelne Blasen und im gesamten Reaktor durchgeführt. Zunächst wurde das Schattenverfahren Verfahren zur Charakterisierung der Blasenparameter (Blasendurchmesser, -geschwindigkeit, -form oder -position) für verschiedene Prozessbedingungen in der Blasensäule verwendet. In dieser Studie wurde der Einfluss von Wasserqualität, Füllhöhe, pH-Wert, Gasart, Viskosität und Oberflächenspannung, auch durch die Verwendung verschiedener Glycerin-Wasser-Mischungen zusammen mit dem Tensid Natriumdodecylsulfat (SDS) analysiert. Somit deckt die aktuelle Studie einen Viskositätsbereich von 0.86…9.29 mPa·s und einen Oberflächenspannungsbereich von 44.8…72.24 $\mathrm{mN \cdot m^{-1}}$ ab, entsprechend einen Morton-Zahl von 1.71×10^{-11}…7.04×10^{-7}. Das Schattenverfahren basiert auf der Partikelerkennung mit Hintergrundbeleuchtung und wird hier mit der Particle Tracking Velocimetry (PTV) kombiniert. Mit der Hilfe der PTV, können auch die Blasentrajektorien und -geschwindigkeiten in der Säule gemessen werden. Die so erhaltenen Blasengrößen und -geschwindigkeiten zeigen eine gute Übereinstimmung mit den in der Literatur vorgeschlagenen Korrelationen. Im Gegensatz dazu wurde aber festgestellt, dass die Korrelationen für das Achsenverhältnis von Blasen aus der Literatur bei höheren Glycerinkonzentrationen oder mit Tensid dieses nicht korrekt vorhersagen können. Mittels der experimentell bestimmten, mehrere Millionen Einzelblasen betreffenden Seitenverhältnisse von Blasen werden darum neue, auf der Flow-Zahl basierende Korrelationen für verschiedene Wasser-Glycerin-Mischungen mit und ohne Tensid vorgeschlagen. Auch die Korrelationen für den Stoffübergangskoeffizienten aus der Literatur wurden auf ihre Genauigkeit und Anwendbarkeit mit Hilfe von experimentellen Daten aus der Literatur überprüft. Die Ergebnisse zeigten, dass keine der Gleichungen den Stoffübergangskoeffizienten ausreichend gut vorhersagen kann. Aus diesem Grund wurden diese Korrelationen mit der Morton-Zahl erweitert und neue Korrelationen vorgeschlagen. Neben diesen optimierten Korrelationen wurde auch eine komplett neue Korrelation vorgeschlagen, die auf der zuvor vorgeschlagenen Berechnung der Achsenverhältnisses der Blasen basiert. Die durch die neu vorgeschlagenen Korrelationen berechneten Ergebnisse aus den eigenen Messungen zeigen, dass mit abnehmender Oberflächenspannung und abnehmender Viskosität die Blasengröße sinkt, aber weder die Zugabe von Glycerin noch die Zugabe von Tensid hatten eine positive Auswirkung

auf den Stoffübergang von CO_2-Blasen in die Flüssigkeit.

Die Flüssigkeitsströmung um einzelne Blasen und in der Blasensäule wurde mittels Particle Image Velocimetry (PIV) bei verschiedenen technischen Einstellungen analysiert, wobei die räumliche und zeitliche Auflösung der Messungen verändert wurde. Die Kombination beider Messmethoden, Schattenverfahren und PIV, liefern relevante Informationen zur dispersen (Blasen) und kontinuierlichen (flüssig) Phase und erlauben so eine vollständige fluiddynamische Charakterisierung des Reaktors, die die Voraussetzung für die Analyse des Stofftransportes zwischen beiden Phasen ist.

Aufgrund der Änderungen der Blasengröße und -geschwindigkeit in verschiedenen Wasser-Glycerin Mischungen, ändert sich auch das Strömungsfeld der Flüssig-Phase. Die höchsten Flüssigkeitsgeschwindigkeiten konnten in den hochviskosen Lösungen gemessen werden. Die Profile der Geschwindigkeit sind für die verschiedenen Viskositäten ähnlich, außer im unteren Bereich der Säule, wo der Blasenvorhang noch stark konzentriert ist.

Schließlich wurde der Stoffübergang von CO_2 und Sauerstoff aus Luftblasen in die Flüssigkeit durch zwei verschiedene Reaktionssysteme mit der LIF-Technik untersucht. Die Einzelblasenergebnisse zeigten, dass sich hinter einer sphärischen Blase eine stabile stagnierende Kappe entwickelt, die das Mischen und den Stoffübergang behindert. Hinter elliptischen Blasen existiert diese stagnierende Kappe nicht, daher wird der Stoffübergang verbessert.

Die PLIF (planare-LIF) Experimente in einer Blasenkette und einem Blasenvorhang aus CO_2-Blasen zeigten, dass mit höheren Gasdurchflussmengen ein höherer Stoffübergang von Gas zu Flüssigkeit in reinem Wasser erreicht werden kann. Die Zugabe von Tensid und Glycerin hat einen erheblichen Einfluss auf die Blasengröße und -geschwindigkeit, aber keiner von beiden beeinflusst den Stoffübergang vorteilhaft. Die Zeit bis zum Erreichen eines bestimmten pH-Werts in der Säule wird in den Lösungen mit Glycerin ebenso wie bei niedrigerem Gasdurchsatz immer verlängert. Es wurde auch festgestellt, dass die Neutralisation in der Blasensäule von oben nach unten fortschreitet. Die Gründe sind die Wirbel an der Flüssigkeitsoberfläche, in denen die Flüssigkeit mit gelöstem Gas eingeschlossen ist. Aus diesen Wirbeln wird nur eine kleine Menge Flüssigkeit in Wandnähe nach unten zum Säulenboden transportiert. Deswegen ergibt sich eine bemerkbare Verzögerung bei der Gaskonzentration in den unteren Abschnitten.

Mit dem neu angewendeten Reaktionssystem mit Resazurin und Luftblasen zeigt sich ein Verhalten, analog zu den CO_2-Experimenten: die Gassättigung schreitet von oben nach unten in der Blasensäule fort. Dies zeigt sich auch daran, dass solange nicht der gesamte Sauerstoff durch die Reaktion im oberen Bereich der Säule verbraucht ist, nur geringe Mengen gelöster Sauerstoff zu den unteren Abschnitten transportiert werden.

Diese Ergebnisse haben auch gezeigt, dass die Reaktion von Resazurin mit Sauerstoff schnell genug ist, um den Stoffübergang in einem Blasensäulenreaktor zu visualisieren und zu quantifizieren. Dieses System bietet zuverlässige und detaillierte Informationen über den Misch- und Stofftransportprozess in eine Blasensäule. Darüber hinaus ist die Empfindlichkeit dieses Reaktion-Systems bei niedrigen Konzentrationen bemerkenswert. Die experimentellen Daten wurden bereits zur systematischen Validierung numerischer Modelle verwendet, die Blasensäulen im großen Maßstab beschreiben, und unterstützen so die Weiterentwicklung der Simulationswerkzeuge zum Stofftransport in Blasensäulen.

Contents

CONTENTS V

NOMENCLATURE VII

INTRODUCTION 1

CHAPTER 1 5

STATE OF THE ART 5

1.1. Gas-liquid flow in bubble columns 6
1.1.1. Research on single bubbles 6
1.1.2. Research on bubble swarms 11

CHAPTER 2 17

EMPLOYED EXPERIMENTAL SETUP AND MEASUREMENT TECHNIQUES 17

2.1. Laboratory-size bubble column reactor 18
2.2. Applied non-intrusive optical measurement techniques 20
2.2.1. Particle Image Velocimetry (PIV) 20
2.2.2. Laser Induced Fluorescence (LIF) 21
2.2.3. Shadowgraphy with Particle Tracking Velocimetry (PTV) 22
2.3. Reaction systems 23
2.3.1. CO_2*-water system with uranin and pyridine 2* 23
2.3.2. Air-water system with resorufin 25
2.4. Measurement conditions and image post-processing 28
2.4.1. Image post-processing for PIV recordings 30
2.4.2. Image post-processing for LIF recordings 31
2.5. Technical equipment 32

CHAPTER 3 35

DETERMINATION OF BUBBLE CHARACTERISTICS IN THE BUBBLE COLUMN 35

3.1. Introduction 36
3.2. Experimental setups and flow conditions 36
3.3. Influence of gas flow rate, water quality, pH and filling height on bubble characteristics 37
3.3.1. Parameters and post-processing 37
3.3.2. Results of parameter study 39
3.4. Influence of viscosity and surface tension on bubble characteristics 41
3.4.1. Post-processing of images 41
3.4.2. Bubble trajectories, diameters and velocities 42
3.4.3. Comparison with known correlations 50
3.4.4. Dimensionless correlations 52
3.5. Bubble shape in bubble swarms 56
3.5.1. Bubble shape in bubble swarms 56
3.5.2. Mass transfer determination 64
3.6. Conclusions 74

CHAPTER 4 77

SINGLE BUBBLE EXPERIMENTS 77

4.1. Introduction 78
4.2. Experimental setups and flow conditions for the measurements with air bubbles 78
4.3. Liquid flow and concentration fields around single air bubbles 79
4.4. Conclusions 85

CHAPTER 5 87

MEASUREMENT RESULTS OF THE CO_2 -WATER SYSTEM 87

5.1. Introduction 88
5.2. Experiments with bubble chain 88
  5.2.1. Experimental setup and flow conditions for the combined LIF-PIV measurements 88
  5.2.2. Flow fields in the bubble column with bubble chain 89
  5.2.3. Concentration fields (pH) in the bubble column with bubble chain 92
  5.2.4. Conclusions 93
5.3. Experiments with bubble curtain 94
  5.3.1. Experimental setups and flow conditions 94
    5.3.1.1. Experimental setups for liquid velocity measurements with PIV 94
    5.3.1.2. Experimental setups for pH measurements with 2T-LIF 96
  5.3.2. Flow fields in the bubble column with bubble curtain 97
  5.3.3. Concentration fields (pH) in the bubble column, obtained with 2T-LIF 102
  5.3.4. Conclusions 106

CHAPTER 6 109

MEASUREMENT RESULTS OF THE AIR–WATER SYSTEM 109

6.1. Introduction 110
6.2. Experiments with an air bubble chain 110
  6.2.1. Experimental setup and flow conditions for the simultaneous LIF–PIV measurements 110
  6.2.2. Liquid velocity in the bubble column with the air bubble chain 111
  6.2.3. O_2 *concentration fields in the bubble column with bubble chain* 114
6.3. Experiments with an air bubble curtain 117
  6.3.1. Experimental setup and flow conditions for the simultaneous LIF-PIV measurements 117
  6.3.2. Liquid velocity in the bubble column with an air bubble curtain 118
  6.3.3. O_2 *concentration fields in the bubble column with an air bubble curtain* 121
6.4. Conclusions 123

CHAPTER 7 125

UNCERTAINTY CONSIDERATIONS 125

7.1. Introduction 126
7.2. General error sources 127
7.3. Uncertainty of the shadowgraphy results 129
7.4. Uncertainty of the velocity field results 130
7.5. Uncertainty of the concentration field results 131
7.6. Summary 132

CHAPTER 8 134

VALIDATION OF NUMERICAL SIMULATIONS WITH THE MEASUREMENT DATA 134

8.1. Scientific database 135
8.2. Simulations with pure water as the liquid medium 135
  8.2.1. Validation of simulations with Euler-Euler two-fluid model for gas fraction and liquid velocity 135
  8.2.2. Validation of simulations with Euler-Euler model in water for bubble parameters, liquid velocity and mass transfer 140
8.3. Simulations in mixtures with different viscosities and surface tensions 144
  8.3.1. Validation of simulations with Euler-Lagrange model in low to high viscous liquids 145
  8.3.2. Validation of simulations with an Euler-Lagrange model in water and 50% water-glycerol mixture 148
8.4. Summary 150

CHAPTER 9 152

CONCLUSIONS AND OUTLOOK 152

9.1. Conclusions 153
9.2. Outlook 156

REFERENCES 158

OWN PUBLICATIONS 168

Nomenclature

Latin letters

A	[-]	constant
AR	[-]	bubble column aspect ratio; h/d_c
a	[m^{-1}]	specific interfacial area
ac	[-]	coefficient
b	[mm]	semi-major axis
Bc	[-]	coefficient
c	[mm]	semi-minor axis
cc	[-]	coefficient
C	[$g \cdot l^{-1}$, $mol \cdot l^{-1}$]	concentration
C_D	[-]	drag coefficient
D	[$m^2 \cdot s^{-1}$]	diffusion coefficient
d_B	[mm]	mean bubble diameter
d_C	[m]	bubble column inner diameter
e	[-]	numerical eccentricity
E	[-]	bubble aspect ratio
ESD	[mm, m]	equivalent sphere diameter
f	[s^{-1}]	formation frequency
fc	[-]	correction factor
g	[$m \cdot s^{-2}$]	acceleration of gravity
h	[m]	column height
hw	[-]	half-width between upper and lower limits
I_0	[J]	intensity of excitation
I_F	[a.u.]	fluorescence intensity
I_T	[$W \cdot m^{-2}$]	transmitted intensity
k	[-]	coverage factor
k_L	[$m \cdot s^{-1}$]	mass transfer coefficient
k_La	[s^{-1}]	volumetric mass transfer coefficient
l	[m]	length of the optical path
M	[$g \cdot mol^{-1}$]	molar mass
$m\%$	[-]	mass percent
n	[mol]	molar amount of substance
N	[-]	number of measurements
p	[Pa]	pressure
Q_G	[$l \cdot h^{-1}$]	volumetric gas flow rate
r	[-]	relative random error
R_{sf}	[$m^2 \cdot s^{-1}$]	rate of surface formation
s	[-]	relative systematic error

S	[-]	standard deviation
S_b	[m^2]	bubble surface area
t	[s]	time
tc	[s]	gas-liquid contact time
T	[K, °C]	temperature
U	[-]	Expanded uncertainty
u_a	[-]	Standard uncertainty (from statistical source)
u_b	[-]	Standard uncertainty (from not statistical source)
u_B	[$m\cdot s^{-1}$]	vertical bubble velocity
u_C	[-]	relative uncertainty
u_L	[$m\cdot s^{-1}$]	liquid velocity
u_S	[$m\cdot s^{-1}$]	slip velocity; $u_B - \overline{v_y}$
V_B	[mm^3]	mean spheroid bubble volume
V_C	[m^3]	liquid volume in the column
V_G	[mm^3]	gas volume
V_L	[mm^3]	liquid volume
V_{TOT}	[m^3]	total volume in the column
v_x	[$m\cdot s^{-1}$]	horizontal liquid velocity component
v_y	[$m\cdot s^{-1}$]	vertical liquid velocity component
$\overline{v_y}$	[$m\cdot s^{-1}$]	average vertical liquid velocity
Y	[-]	mass fraction of chemical species

Greek letters

α	[-]	phase fraction
β	[°]	bubble inclination
γ	[°]	bubble motion direction
ε_G	[-]	gas holdup
ε_m	[$m^2\cdot mol^{-1}$]	molar extinction coefficient
μ	[$kg\cdot m^{-1}\ s^{-1}$]	dynamic viscosity
ν	[$m^2\cdot s^{-1}$]	kinematic viscosity
ρ	[$kg\cdot m^{-3}$]	density
σ	[$N\cdot m^{-1}$]	surface tension
ϕ	[-]	quantum efficiency
χ	[-]	bubble eccentricity

Dimensionless numbers

$Eö = \frac{g(\rho_l - \rho_g)ESD^2}{\sigma}$	[-]	Eötvös number
$F = g \cdot \Delta\rho \cdot \left(\frac{ESD^8 \rho_l^2}{\sigma \mu^4}\right)^{\frac{1}{3}}$	[-]	Flow number
$Ga = \frac{gESD^3}{\nu^2}$	[-]	Galilei number
$Mo = \frac{g\mu_l^4(\rho_l - \rho_g)}{\rho_l^2 \sigma^3}$	[-]	Morton number
$Re = \frac{u_s ESD}{\nu}$	[-]	Reynolds number
$Sc = \frac{\nu}{D}$	[-]	Schmidt number
$Sh = \frac{k_L ESD}{D}$	[-]	Sherwood number
$Ta = ReMo^{0.23}$	[-]	Tadaki number
$V = u_s \left(\frac{ESD^2 \rho^2}{\sigma \mu}\right)^{\frac{1}{3}}$	[-]	Velocity number
$We = \frac{ESD \cdot u_s^2 \cdot \rho_l}{\sigma}$	[-]	Weber number

Introduction

Multiphase reactors (or contactors) are widely used all over the world in the industry in diverse fields, such as chemistry, biotechnology, pharmacy, petrochemistry etc. The reactor, where the chemical, biological or mixing process takes place, is the heart of the plant, therefore its design and optimization is crucial from the point of view of productivity and the overall economics. Generally, these reactors are operated with two- or three-phases, in diverse combinations of the gas, liquid and solid phases. These contacting devices can be divided by reactor type into two main groups: tank/vessel or pipe reactors. These groups can be divided into subgroups by operating principle [1] (Figure 1). Each of the here listed reactor types offers numerous additional configurations, specific to the exact industrial process. Some of them can be operated in batch or continuous mode; or the liquid phase can be applied in co-current or counter-current to the other phases. Each reactor design has, of course, its specific attributes, benefits and drawbacks and has to be chosen carefully for the specific task and expectations.

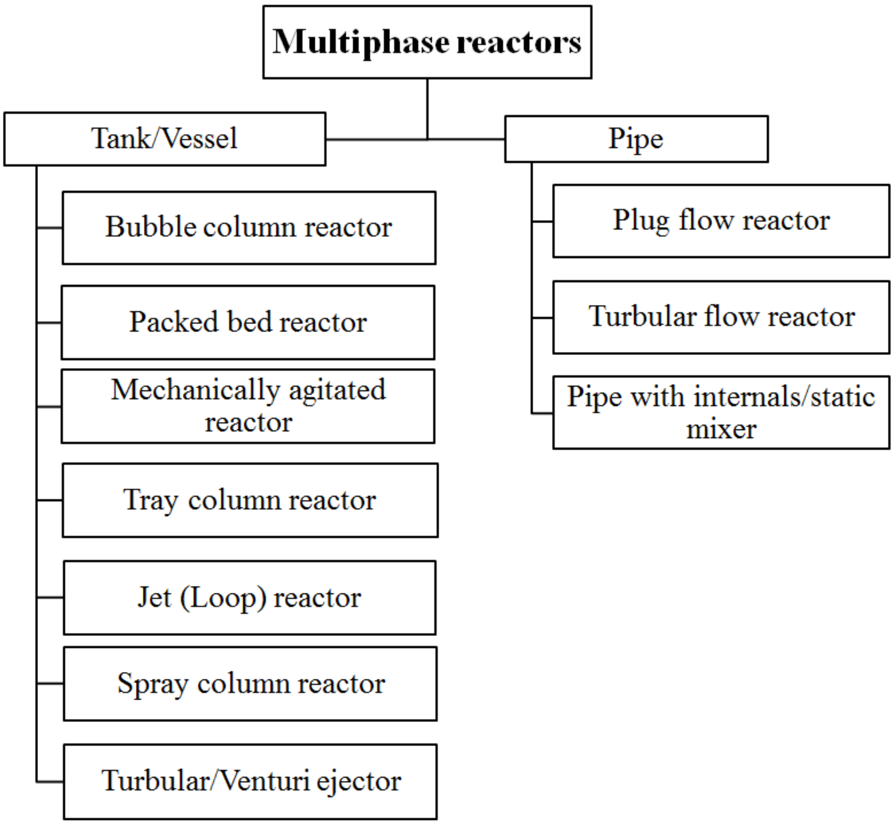

Figure 1: General multiphase reactor types from [1].

With a wisely chosen and designed contacting device not only the operational and maintenance costs can be reduced, but the amount of unreacted materials (selectivity) as well.

Within the general reactor types the bubble column reactors were widely investigated in the last few decades, because of their numerous advantages in operation and design compared to other reactor types. Despite the scale-up difficulties and significant phase back-mixing the bubble column reactors offer more advantages: good heat and mass transfer, simple construction and operation, no moving parts, low maintenance costs, low energy consumption, uniform temperature distribution, high selectivity, low shear forces. For this reason, bubble columns are widely applied in the industry (Table 1).

Table 1: Exemplary industrial scale applications of bubble column reactors from [2-5].

Biochemical processes	
Production of	Thienamycin
	Glucoamylase
	Acetic acid
	Monoclonal antibody
	Plant secondary metabolites
	Taxol
	Organic acids (acetic, butyric)
Ethanol fermentation	
Industrial processes	
Oxidation of	ethylene (partial), cumene, butane, toluene, xylene
Oxychlorination of ethylene	
Chlorination of	aliphatic and aromatic hydrocarbons
Alkylation of	methanol, benzene
Isobutene hydration	
Oxysulphonation of paraffins	
Conversation of natural gas into liquid fuels via syngas	
Methanol synthesis	
Fischer-Tropsch synthesis	
Hydroformylation (Oxo) processes	
Waste water treatment	
Wet oxidation of sludge	

In view of construction and operation, bubble columns are very simple. They consist of a cylindrical vessel and a gas sparger at the bottom. Through the sparger, gas is introduced as bubbles into the liquid or liquid-solid phase filled vessel. The vessel size depends on the process and varies in a wide range. The volumes of bubble column reactors in the industry are usually some thousands of cubic meters, but in rare cases (e.g. cell growth) they operate just with a few litres. This liquid phase can be stagnant, in case of batch operation, or counter- or co-current to the gas phase if the reactor operates in semi-batch or continuous mode. The bubble flow regimes are defined mainly by the sparger type and by the gas volume flow rate. From these regimes, the homogenous (bubbly), transition and heterogeneous (churn turbulent) flows are beneficial for the industrial processes. In contrast to the simple construction and operation, the evolving flow inside the column is quite complex and depends on many parameters. While some parameters are directly adjusted as operating parameters, many non-adjustable parameters exist, which have significant influence on the reaction and for this reason, the simulation of the flow and reaction inside bubble columns is a challenging task.

Figure 2 shows the dependency of the reactor performance on reactor design, process properties and operating parameters. It clearly shows the complexity of such a system. Almost everything depends on each other and for this reason, it becomes also very difficult to scale-up or scale-down one specific reactor design.

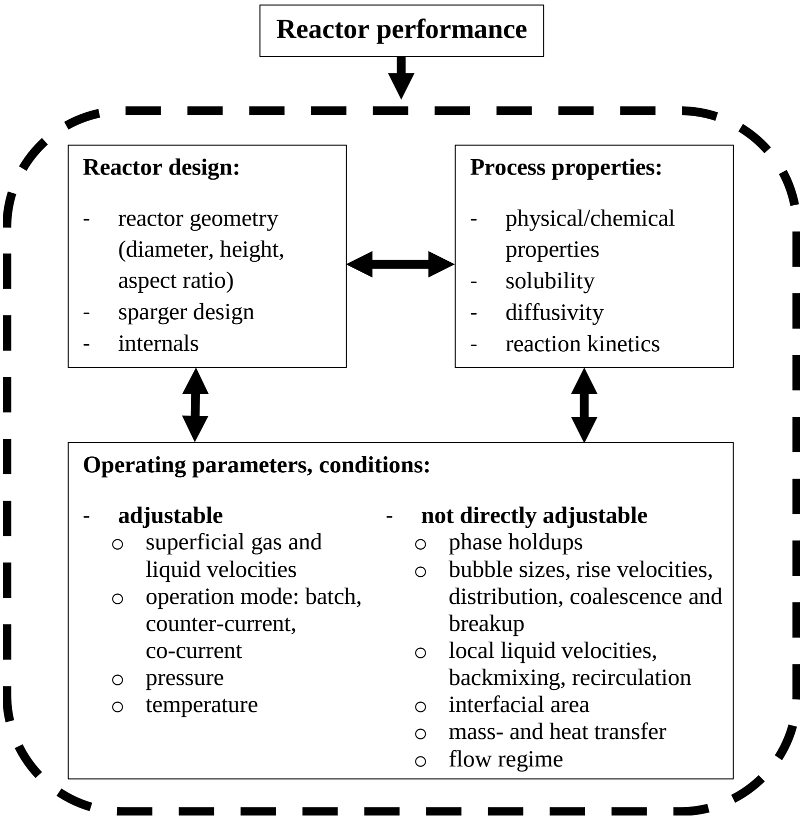

Figure 2: Reactor performance dependency on the reactor design and operation.

For instance, a change in the sparger design leads to different bubble properties (size, velocity, distribution etc.), thereby it introduces changes in the gas holdup, liquid velocities, interfacial area etc. and in consequence, the reactor performance changes [6, 7]. But the same effects occur, when a change in certain adjustable parameters happens. It is enough to modify the superficial gas velocity, to provoke changes in the bubble properties [8], and therefore changes in the whole reaction system.

During reactor planning, the operation and process has to be optimized for various criteria, e.g. performance, productivity, profitability, waste minimization etc. To this end, the adjustable parameters are directly applied and the non-adjustable parameters are derived from experiments, empirical and semi-theoretical correlations. In the literature, plenty of different correlations can be found for each non-adjustable parameter and most of these are completely empirical. Therefore, the reliability of those is usually limited to a specific experimental condition. For a general applicability further experimental validation is needed. However, the scale-up from laboratory-scale reactors to industrial scale is expensive, time consuming and in most cases very complicated. In the recent decades, with the significant development of computational fluid dynamics (CFD) and computational power, a new and cheaper way has appeared in the field of reactor design and optimization. But as before, or maybe even more, there is a high demand for experimental data for validation of these numerical simulations and the models used therein. CFD simulations then present a better, faster, flexible, reliable and cheaper tool for reactor design and optimization as numerous and point-wise experiments would be.

Because of the above mentioned reasons, the main aim of this thesis is to develop measurement tools that allow for the acquisition of a bunch of detailed and coupled experimental data without perturbation of the hydrodynamics in the column. Thus, this data, obtained in a well-defined two-phase laboratory-scale bubble column reactor with the help of non-intrusive optical measurement techniques, can also be provided to the scientific community for validation purposes. The experimental results obtained in this way include the fluiddynamical characterization of the bubbles and liquid in the column at various gas flow and liquid conditions as well as the mass transfer from bubbles to the liquid. To achieve these aims, seven objectives have been defined:

- design and construct an optically accessible laboratory-scale bubble column with flexible gas inlets;
- investigate the bubble characteristics at various flow and liquid conditions, e.g. filling height, gas flow rate and water quality;
- characterize the liquid flow field at different flow conditions, namely single bubbles, bubble chain and bubble curtain;
- find employable chemical detection reactions for CO_2 and O_2 to observe the mass transfer with optical measurement techniques in the two-phase reactor;
- study the influence of surface tension and viscosity on the fluid dynamics and mass transfer in the bubble column;
- select reliable literature correlations for the investigated parameters and verify them against the obtained experimental data; where it is possible, optimize the selected literature correlations or propose new ones based on the experimental results;
- provide an experimental database from the processed data for CFD validations.

These objectives are arranged in chapters as follows:

- Chapter 1 gives a brief theoretical and experimental background on bubble column reactors and the flow in these; moreover it gives insight concerning recent research in this field.
- Chapter 2 discusses the experimental setups, which includes the laboratory-scale bubble column and the different technical equipment for the various measurement techniques used. Furthermore, the applied optical measurement techniques and reaction systems are described.
- Chapter 3 summarizes the experimental results of the shadowgraphy experiments, where bubble characteristics have been measured and evaluated extensively. New correlations for bubble aspect ratio and Sherwood number are derived, presented and applied.
- In Chapter 4 the experiments with single air bubbles with the O_2 reaction system will be discussed.
- Chapter 5 presents the experiments in the bubble column with the CO_2 reaction system and carried out with a bubble chain and a bubble curtain.
- Chapter 6 discusses the experiments in the bubble column with the O_2 reaction system and also with bubble chain and bubble curtain.
- Chapter 7 deals with the uncertainty of the experimental data.
- Chapter 8 presents the data base generated from the experimental data. The use of the experimental data for the validation of different numerical simulation cases is presented.
- Chapter 9 gives a short conclusion to the thesis and an outlook for further studies.

Chapter 1

State of the art

Contents

1.1. GAS-LIQUID FLOW IN BUBBLE COLUMNS 6

  1.1.1. Research on single bubbles 6

  1.1.2. Research on bubble swarms 11

1.1. Gas-liquid flow in bubble columns

Bubble column reactors have been widely investigated in the recent decades, because of their importance in the industry in various fields. As it was mentioned in the introduction, a bubble column reactor in itself is a simple reactor, easy to build, but the flow and mass transfer in these is more complex because of the dependency on a number of different variables, e.g. gas holdup, size, velocity and aspect ratio of bubbles, or the flow regime. Therefore, numerous publications deal with the design of bubble column reactors or describe the fluiddynamics and transport processes in different bubbly flows at different conditions. To comprehend this complex behaviour in bubble columns it has to be investigated from two aspects. First of all, the single bubble behaviour has to be described and after, the bubbly flow in the bubble column, including swarm effects, has to be studied. In the following section studies of these two aspects of interest are reviewed.

1.1.1. Research on single bubbles

Single, in stagnant liquid rising bubbles were investigated systematically in the recent century to gain overall information about the bubble properties e.g. velocity, motion or shape. With the help of earlier experimental results in liquids with various properties, among others e.g. in different water-glycerol mixtures [9] or in various oils and syrups [10], in the extensive work of Clift et al. [11], a greatly useful diagram for the terminal velocity of air bubbles rising in water is presented (Figure 1.1). It includes experimental results accessible at that time and it can give a first guess on the terminal velocity of a single bubble rising in stagnant pure or contaminated water.

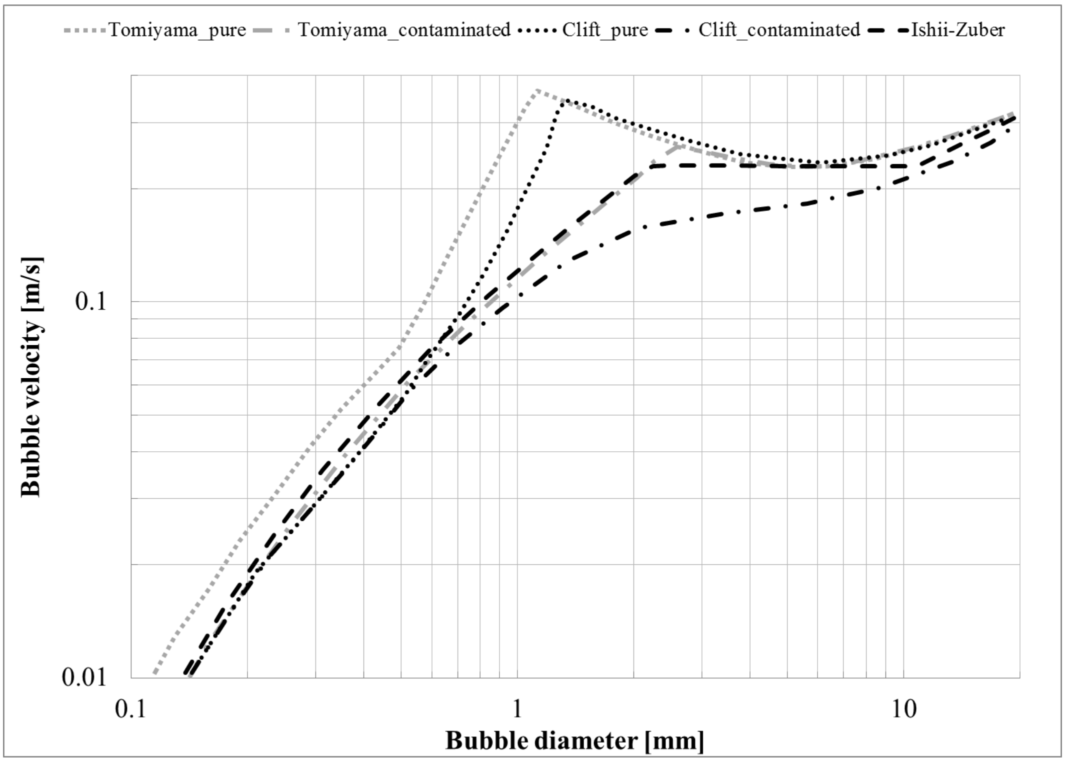

Figure 1.1: Terminal velocity of a bubble rising in pure and contaminated water from [11-13].

This diagram and approximation were refined later first by Ishii [13] for contaminated water and by Tomiyama et al. [12] for both, contaminated and pure water. These refinements, also represented in Figure 1.1, show, that the rising velocity in contaminated water was underestimated by Clift et al. [11] and the maximum bubble velocity in pure water is shifted slightly to a smaller bubble diameter. One other and frequently referred diagram from the work of Clift et al. [11] is the so-called "Grace diagram" after Grace [14] (Figure 1.2).

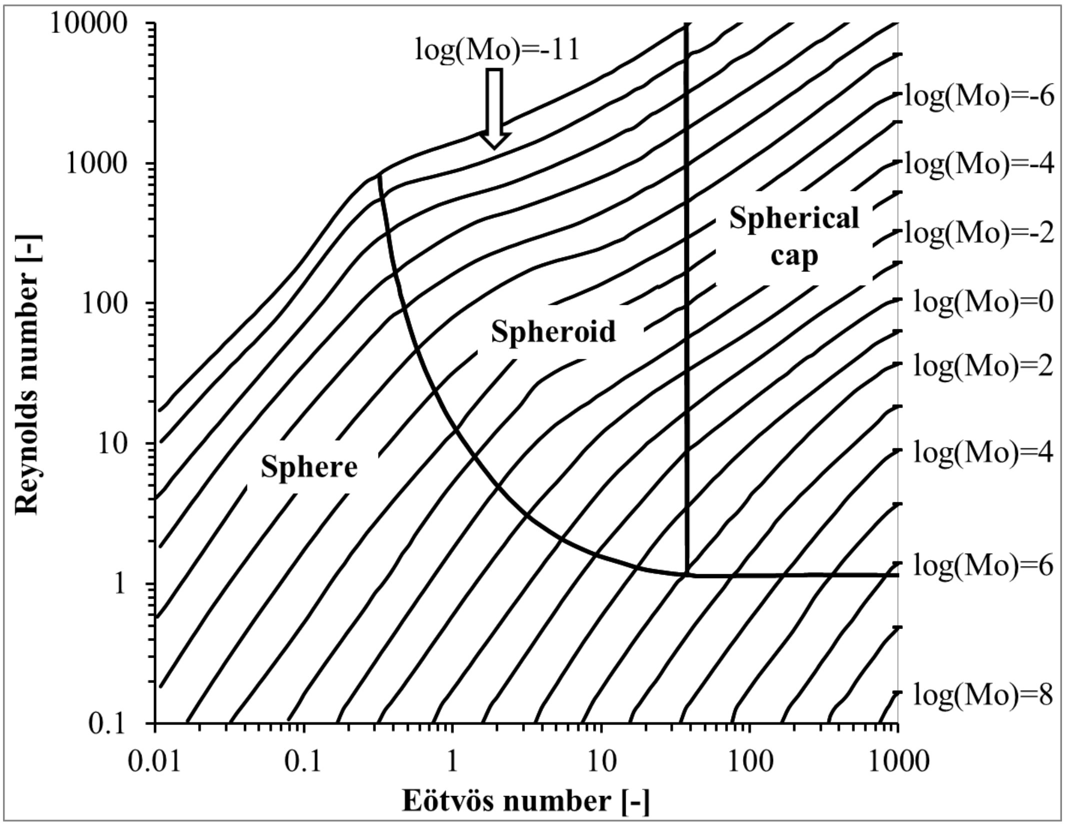

Figure 1.2: Grace diagram (bubble shape regime map).

This shape regime map depicts the bubble shapes and Reynolds number dependencies on the liquid properties, described by the Morton number, and the dependencies on the liquid-gas surface tensions, characterized by the Eötvös number. This map can be used again to estimate bubble velocities and the corresponding bubble shapes for a specific surface tension. The subdivisions of this diagram are somewhat arbitrary, therefore newer researches were carried out to define more precisely the different shape regimes. One of the most comprehensive studies is the work of Tripathi et al. [15]. In the frame of this 3D bubble simulation study, a wide range of *Eö* and *Ga* were analysed. They were able to simulate not just the bubble shape, but bubble breakage as well. The so-obtained bubble shape map differs significantly from the one of Grace and has the main advantage, that it is independent from the bubble velocity (Figure 1.3). The experimental results from Kováts et al. [16], where the investigated bubbles were spheres and wobbling spheroids without bubble breakup, added to this map as symbols, make it obvious, that the simulations were not able to predict exactly the shapes for different experimental conditions. The proposed bubble breakup regime was overestimated, because in our experiments no breakup was identified. Additionally, the stable sphere, spheroid regime was underestimated, since in our experiments with 50% and 60% water-glycerol stable, almost spherically-shaped (aspect ratio > 0.9) bubbles were observed. In the light of this comparison, it is obvious, how important detailed experimental studies are for the validation of simulations, even relying on advanced numerical models.

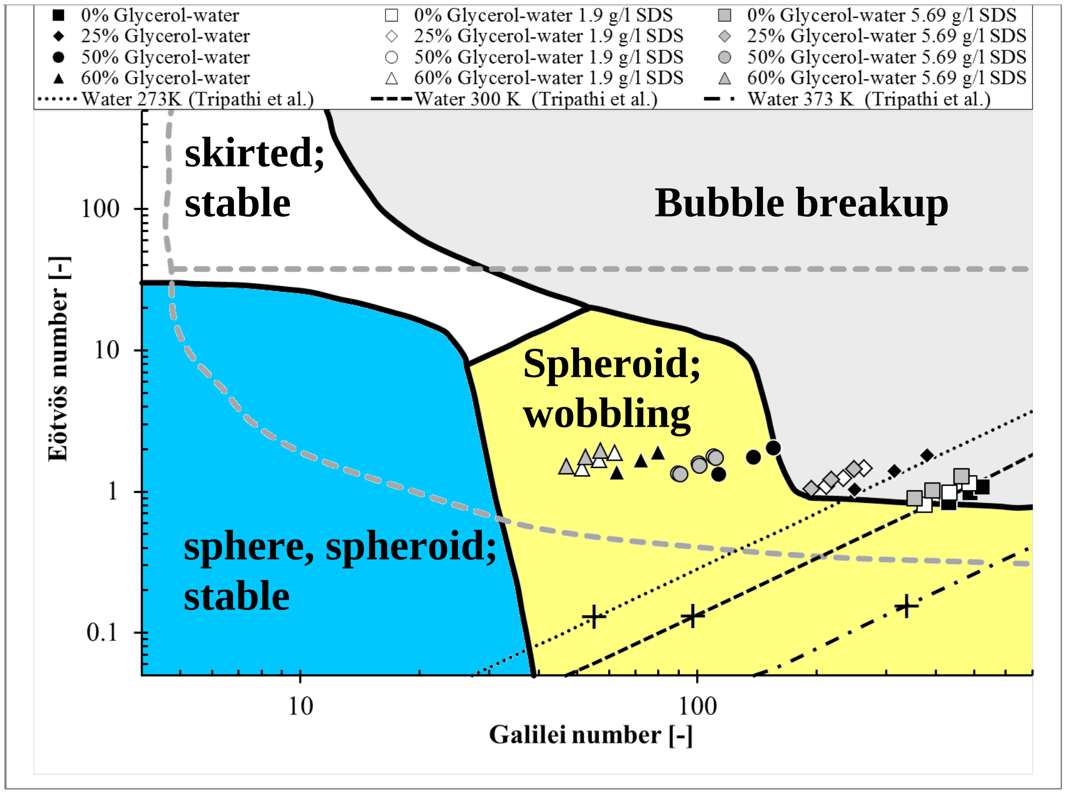

Figure 1.3: Modified bubble shape regime map from [15, 16].

As it was summarized by Joshi et al. [17], most of the experimental studies concerning bubble flows in the last few years deal with the above mentioned bubble properties, motion and turbulence behind bubbles.

Besides these bubble property investigations, most existing experimental studies concerning bubble motion coupled with mass transfer, considered the behaviour of a single bubble, e.g. [18-22]. For this, mostly gas probes have been used, but with the progress of optical measurement techniques Laser Induced Fluorescence (LIF) became the most common technique for the determination of locally transferred concentrations. During these measurements, a fluorescent dye is added to the liquid phase and reacts with the dissolved gas to form a fluorescent species, which is excited by laser light. The concentration of the dissolved gas can then be calculated from the recorded light intensity emitted by the fluorescent dye. Well-known fluorescent dyes for such studies are fluorescein [8, 23, 24], HTPS (8-Hydroxypyrene-1,3,6-Trisulfonic Acid) [21, 25, 26] and C-SNARF-4F (1,4(and 5)-benzenedicarboxylic acid, 2-[10-(dimethylamino)-4-fluoro-3-oxo-3H-benzo[c]xanthen-7-yl]) [27] for the CO_2 chemisorption and ruthenium complexes [28-35] for O_2 concentration sensing.

The absorption of oxygen is studied by the quenching of laser-induced fluorescence of ruthenium complexes in the group of Cockx, Guiraud and Hébrard in Toulouse [30-32, 36, 37] and in the group of Schlüter in Hamburg [28, 29, 33-35]. Dani et al. [30] describes in detail the method used for a single rising bubble in a quadratic column. Due to the difficulties encountered e.g. from reflections on the bubble surface, Francois et al. [31] changed the observation direction from a vertical laser light sheet to a horizontal one, with an observation of fluorescence from the bottom of the quadratic column. Thus, they can reconstruct the complete oxygen wake of a rising bubble. The mass transfer is quantified as fluxes from the bubble to the liquid for different bubble sizes (0.7-1.9mm) and ethanol-water-glycerol mixtures. Simultaneously, the bubble size and trajectory is monitored by shadowgraphy, using a high-speed camera. Jimenez et al. [32] then used this set-up for the analysis of mass transfer from ellipsoidal, zigzagging bubbles and different surface tension and viscosity liquids, also with simultaneous high-speed imaging of the bubbles. Moreover, the effect of surfactants on the mass transfer was also investigated [36].

The groups of Räbiger and Schlüter in Bremen and Hamburg also used oxygen quenching of the fluorescence of ruthenium complexes for the determination of mass transfer from single free rising bubbles [34] or under counter-current conditions [28, 29, 38]. In [29] they combine their LIF-system with simultaneous PIV measurements of the flow field around bubbles with 1-2.5mm diameter. Provided that the bubbles have strictly vertical trajectories and thus axisymmetric concentration and velocity fields, the authors derive from these measurements the convective mass transfer from the bubble to the fluid. Superimposed chemical reaction of oxygen, transferred from freely rising bubbles in a sulphite solution is analysed by the same groups in [28, 39]. In [39] they also acquire the simultaneous velocity field around the bubbles and compare with numerical simulations.

The mass transfer from CO_2 Taylor bubbles in microchannels is determined in [40]. Here the bubble shrinkage is visualised directly and used for the determination of $k_L a$-values. Mass transfer from single CO_2-bubbles has been also examined in the group of Saito [21, 41]. They developed a photoelectric optical fibre probe for the simultaneous determination of bubble cord length, velocity, void fraction and local CO_2-concentration in the liquid [41]. Mass transfer in the wake of free rising CO_2 bubbles with the help of fluorescein dye was also investigated by Valiorgue et al. [24]. Zigzagging bubbles are used in LIF experiments based on the fluorescent pH-tracer HPTS in a square column [21, 42]. Bubble shapes and trajectories, as well as mass transfer are investigated in these measurements. Recently, dual emission LIF technique with C-SNARF-4F was presented by Kong et al. [27]. They used the dual-emission ability of the C-SNARF-4F fluorescent dye to visualize and quantify the pH change behind single CO_2 bubbles.

Separately or simultaneously with mass transfer, the bubble-generated flow structure around a single bubble and the flow in the wake can be determined with the help of Particle Image Velocimetry (PIV). During these measurements, tracer particles are added to the liquid phase, which are illuminated by a light sheet in the case of 2D PIV or with a volume illumination in the case of tomographic PIV (3D). The velocity field can then be calculated with cross correlation from the recorded particle image pairs. Before the PIV technique became a common optical measurement technique, the flow structure behind single bubbles was investigated with simple photographic techniques. Komasawa et al. [43] examined the wake structure behind spherical cap shaped bubbles at different flow conditions in a counter-current channel. Some years later, Tokuhiro et al. [44-46] performed experiments behind elliptical bubbles and bubble pairs in counter-current flows with the help of PIV, combined with shadow imaging. Thus, they were able to record the flow field and the bubble shape and motion simultaneously. Brücker [47] investigated the bubble wake structure and dynamics of bubbles with zigzagging motion. In the counter-current flow channel he applied two different optical arrangements. In one, horizontal cross sections were recorded, while in the other setup vertical cross sections were realized with a scanning light sheet. In that way a quasi three-dimensional measurement was performed. Real 3D PIV and Particle tracking Velocimetry (PTV) experiments were carried out by Ortiz-Villafuerte et al. [48, 49]. With three PIV cameras, they were able to reconstruct the 3D flow field around a single rising bubble in stagnant water. In both cases a fourth camera was applied, to gain information about the bubble shape, size and trajectory with shadow imaging. Fujiwara et al. [50] extended the planar PIV measurement with two additional cameras for shadow imaging. With the help of these perpendicularly acquired bubble images it was possible to reconstruct the bubble shape, size, trajectory and position in 3D. This 3D reconstructed bubble helped then to position the calculated flow field very precisely to the bubble. Liu et al. [51, 52] performed extensive PIV measurements to gain information about the averaged liquid flow structure in a rectangular bubble column. To this end, the experiments were carried out in four different liquid viscosities with a bubble size range of 5.1-6.3 mm at different gas volume flows. They have found that the surrounding liquid flow complexity increases with decreasing liquid viscosity. Funfschilling et al. [53] have also performed experiments in viscous fluids. The bubble velocity, size and the flow around the bubbles was investigated in three viscous fluids: 99.5% glycerol – water, 2% CMC (carboxylmethylcellulose) – water and 0.5% PAAm (polyacrylamide) – water mixture. They have found that the bubble injection time has an influence on the single bubble rise velocity. In the glycerol and CMC solutions just the very fast – 0.3 s – injection period caused significant change in the bubble velocities, while in the PAAm solution all of the investigated injection periods resulted in different rising velocities. It was proved, that this behaviour occurred because of the flow structure in the bubble wake. While in the first two cases the flow in the wake was classical, with the fluid flowing upwards before and behind the bubbles, in the PAAm solution a downward motion in the wake was observed. This negative wake in non-Newtonian fluids behind bubbles was also observed by different other groups [54, 55]. The research group of Saito made remarkably extensive researches on single rising bubbles, especially focused on their zigzagging motion [56-61]. In their research they have investigated the bubble velocity, aspect ratio, surface oscillation and the vortices around the bubbles along the rising path. Moreover, the interaction between the bubble and liquid motion through a collision of a pair of bubbles was investigated [59]. Similar experiments were carried out by Fan et al. [62] in different CMC solutions. Zenit and Magnaudet [63] have investigated with high-speed PIV the vortex structures behind rising bubbles. They have found that the axisymmetric wake of a bubble becomes unstable, if the bubble aspect ratio exceeds a critical value. In the bubble wake two vortex tubes induce a horizontal force on the bubble, which leads to the path instability, and the zigzagging bubble motion. Böhm et al. [64, 65] examined single rising bubbles in narrow rectangular channels with different depths and with variations of the viscosity of the liquid. A similar thin gap cell was applied by Filella et al. [66] to investigate the oscillatory motion of the rising bubbles with a size range of 1.5-23.9 mm. The vortex structures and the lifetime of those were investigated in the wake as well. Recently Lewandowski et al. [67] have investigated the characteristics and hydrodynamics of single bubbles in presence of surfactants with PIV and Shadowgraphy. They have found, that the investigated surfactants have a significant effect on the bubble parameters e.g. diameter, centricity, rising velocity. Therefore the liquid velocity, vortex structures and gas holdup is affected as well.

1.1.2. Research on bubble swarms

Numerous articles have been published in recent years considering bubble curtains and bubble swarms.

In bubble columns different flow regimes can develop, which depend on numerous factors e.g. liquid velocity; stagnant, co-current or counter-current flow; sparger geometry; gas holdup etc. From these, the industrially relevant flow regimes are depicted in Figure 1.4. Homogeneous flow evolves generally at low superficial gas velocities, where no bubble coalescence or break up is present. For this reason, the bubble size distribution in these cases is narrow and the gas holdup distribution is uniform over the column. In heterogeneous flow, at higher superficial gas velocities, coalescence and break up occur frequently, which leads to a wide bubble size distribution and non-uniform gas holdup distribution.

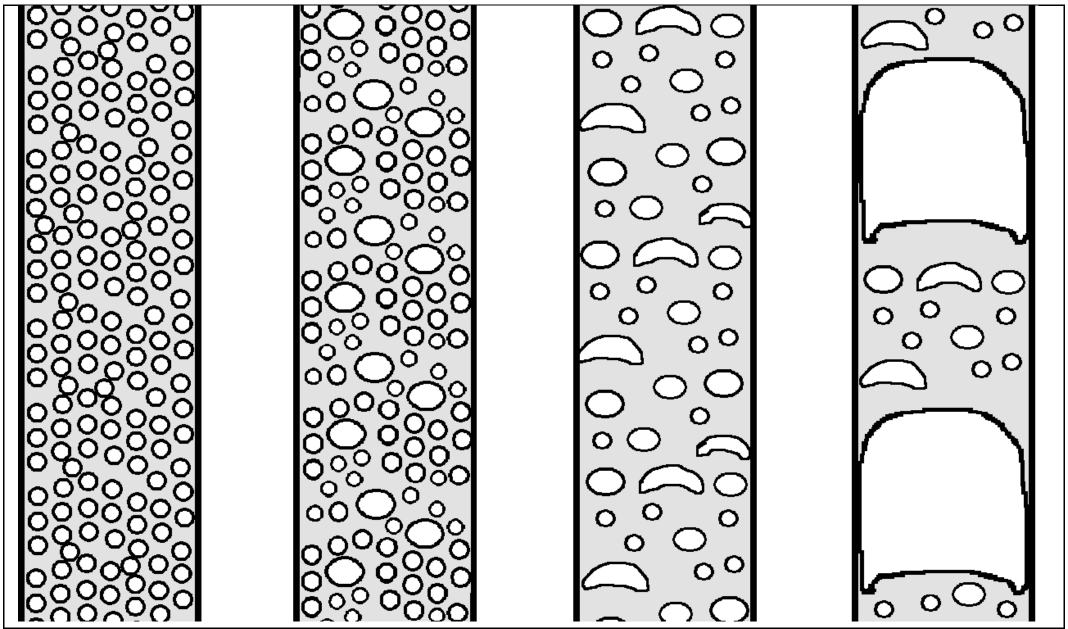

Homogeneous		Heterogeneous	
Perfect bubbly flow	Imperfect bubbly flow	Churn turbulent flow	Slug flow

Figure 1.4: Flow regimes in bubble column.

Consequently, at different flow regimes different liquid flows appear, which leads to different mixing, heat and mass transfer rates. Moreover, between the different flow regimes a transition range exists.

The measurement of the properties of the two phases is much more challenging as in the case of single bubbles. In the case of nearly industrial operating conditions – high gas holdup, therefore opaque system – non-intrusive optical measurement techniques cannot be used to determine the bubble and liquid characteristics. However, these systems can be measured locally with intrusive methods such as optical needle probes and hot-wire probes. The drawback of these techniques, besides that they are intrusive, is, that they are point measurement techniques. This means, that the probes have to be driven from point to point over the whole column cross section and over the column height to gain sufficient data about the flow for a complete characterization. It is not just time consuming, but of course, at the end it provides only average general data about the two-phase flow in the bubble column. However, the benefit of these methods is that they can provide data over the whole column almost in every system and the outcome of these measurements is evidently useful to optimize a system or to validate numerical simulations.

In optically transparent setups, like laboratory-scale acrylic bubble columns with moderate gas holdup, non-intrusive optical measurement techniques (e.g. Laser Doppler Velocimetry (LDV), Particle Image Velocimetry (PIV), Particle Tracking Velocimetry (PTV), Shadow imaging, Laser Induced Fluorescence (LIF)) come to the fore. These optical methods are non-intrusive measurement methods, like the complex tomography and radiography techniques, which were extensively described by Chaouki et al. [68].

Since optical experimental methods are used in this thesis, the tomography and radiography techniques will not be described further, even if these techniques can also provide promising results [69-75]. The main benefit of the optical experimental methods is that they do not disturb the flow and that they can deliver detailed measurement data with high spatial and temporal resolution. The main drawback of these is, that the investigated system has to be optically transparent. This is valid not only for the reactors, but for the investigated fluid as well. Most of the optical techniques (LDV, PIV, PTV, LIF) use laser beams or laser light sheets as light source for the measurements. With the help of this light the tracer particles in the liquid are illuminated or the fluorescent tracer dyes are excited. The light has to reach the investigation area undisturbed and the scattered or emitted light has to get to the sensor. In other methods (Shadow imaging, Particle Shadow Velocimetry (PSV)), the illumination takes place from the back and the shadows of the particles or bubbles are recorded by a camera. The applicability of shadow imaging is presented through a simple example on Figure 1.5. It shows images of an imperfect bubbly flow in an acrylic bubble column at different gas holdups ε_G, where the bubbles are generated with a porous glass plate. It is easy to accept, that at the lowest gas holdup almost each bubble can be recognized separately and the liquid gap in between is more or less optically accessible. With increasing gas holdup, the bubbles start to overlap and the number of recognizable single bubbles drastically decreases. At $\varepsilon_G = 4\%$ the liquid gap between the bubbles becomes almost invisible.

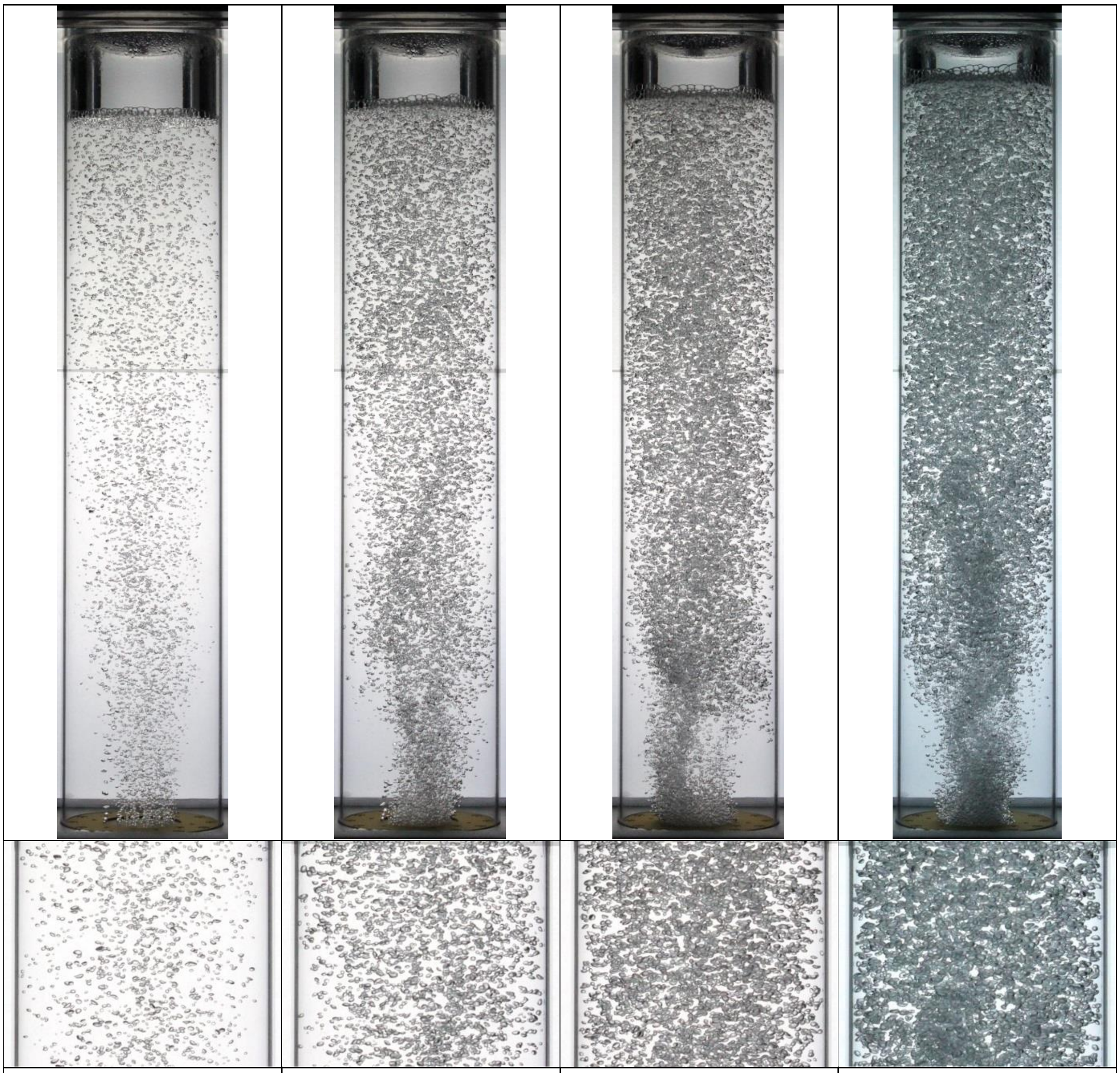

ε_G=0.5% **ε_G=1.5%** **ε_G=2.5%** **ε_G=4%**

Figure 1.5: Bubbly flow images at different gas holdups (top row: the whole column; bottom row: zoom onto the centre of the column).

For this reason, shadow imaging and PSV are employable just at low gas holdups, up to ~ $\varepsilon_G = 1.5\%$. In the case of laser measurement techniques, where the liquid motion is the target of the investigations, the maximal gas holdup can be just around 0.5%. Measurements with lasers can of course be carried out at higher gas holdups. However, in that case, just the near wall flow can be measured. For this reason, these methods cannot be used with industrial conditions, where the gas holdup is much higher. But these techniques have their benefits: they provide much detailed information about the liquid flow at low gas holdup and more data about the bubble characteristics. While with the probes just bubble sizes, velocities and their distributions can be obtained, with the optical methods detailed bubble characteristics, bubble motions (wobbling, trajectories), bubble coalescence, break-up and bubble shrinkage can be acquired additionally. All of these data are crucial for a proper development and validation of numerical simulations of bubble columns.

As summarized extensively by Joshi et al. [17], most of the experimental studies concerning bubble flows in the last few years deal with bubble motion and turbulence in bubble column reactors. Most of these measurements in bubble columns were carried out fully or partly with probes (optical, needle, hot wire, electrical conductivity, oxygen probes), combined with other techniques like shadow imaging, LDV or PIV. The reason for this, are the simple and cost-effective technique and the fact that it can be applied in opaque systems. If the subject of interest is the gas phase (gas holdup, bubble size and velocity), usually optical or needle probes are applied [6, 76-80]. These setups can be extended e.g. with oxygen or pH probes, which record the dissolved gas concentration changes at one point during the experiment [77, 81-83]. If the employed reactor is transparent, in many cases researchers have used digital cameras for shadow imaging to record the bubble properties [84-93], patterns of the flow in the reactor [94, 95], or to reconstruct the 3D bubble swarm motion inside the column [96-98]. The experimental setups could be extended with hot-wire probes [99] in the case of opaque systems, or optical measurement techniques like LDV [96, 100, 101] or PIV [8, 16, 23, 102-114] if the system is transparent, to gain information about the liquid flow as well. However, the mixing behaviour, concentration changes or mass transfer in bubble columns were barely investigated with optical measurement techniques [8, 16, 23, 102, 115-118]. To characterize the hydrodynamics, most of the experiments were carried out in pseudo-2D [84, 86, 119-124] or rectangular [87, 88, 104-106, 109, 113, 125-128] bubble columns, which are far from practical configurations. Two-phase flows in cylindrical bubble columns were investigated only in few cases in the past [82, 83, 85, 96, 107, 108]. They now receive more attention [6-8, 16, 23, 76-79, 81, 92, 94, 102, 110, 111, 114, 129-132].

Here it is important to mention, that most of the studies were carried out in aqueous systems. However, gas-liquid mass transfer in bubble columns is very strongly influenced by the hydrodynamics in the column. Furthermore, in the majority of industrial processes the liquid phase is not a simple aqueous system. Therefore, it is important to examine how the dispersed gas interacts with the liquid phase, especially for liquids with viscosities and surface tensions different from water. In the following, studies related to the influence of viscosity and surfactants in the bubble columns will be reviewed.

The influence of viscosity on the hydrodynamics of bubble columns has already been examined by several authors in the past. Since optical experimental methods are used in a bubble column in Newtonian liquid solutions in this thesis, the following literature review only considers such papers. Numerical studies and non-Newtonian liquids are not presented hereafter. The variation of viscosity significantly changes the rising behaviour of bubbles. With increasing viscosity, the zigzag path of big bubbles becomes tighter until they remain in a vertical line [51, 64]. The last authors also examined the drawbacks on the liquid velocities in a bubble column, and concluded that turbulence intensities become more inhomogeneous for liquids with higher viscosity. Zhang et al. [133] determined the terminal bubble velocities in different glycerol and sucrose solutions and found a decreasing velocity with increasing viscosity. The influence of viscosity on the hydrodynamic regimes in a bubble column filled with different Newtonian solutions has also been examined by Olivieri et al. [134]. They found that the homogeneous regime is stabilized by an increasing viscosity for viscosities smaller than 4.25 mPa.s. For higher viscosities, the onset velocity of the vertical-spiral flow regime decreases with viscosity. These effects have been recently confirmed in a study from

Gemello [6], who used distilled water, tap water, and additions of ethanol. They found a decrease in bubble size, an increase of gas hold-up, and a delay of the transition from the homogeneous to the heterogeneous regime when adding ethanol. Additionally, the group of Besagni, e.g. [135-137], has worked intensely on these subjects during the last few years. They also confirm this "dual effect of viscosity", that leads to a stabilization of the homogeneous flow regime by a large number of small bubbles in the case of low viscosities, and a destabilization with decreasing gas holdup and larger bubbles in the case of moderate and high viscosities. These effects are attributed to the bubble interfacial properties that reduce or promote coalescence phenomena. Also this group recently demonstrated, that reducing the gas sparger openings and increasing the liquid viscosity leads to an increased gas holdup [7]. Bubble plume oscillations have been analysed for different viscosities and surface tensions by Laupsien et al. [138]. They also found different behaviours for smaller and higher viscosities, where time scales of the oscillation decrease and increase, respectively.

The volumetric mass transfer coefficient has been determined by Buchholz et al. [139], as well as gas holdup and bubble size distributions. They find that an increasing viscosity leads to decreasing oxygen transfer rates in their bubble column. This has been confirmed by Ferreira et al. [127], who developed an optical method for the determination of bubble size distributions and determined the volumetric mass transfer coefficient by an oxygen electrode. Probe measurements of CO_2 concentrations at different viscosities and superficial gas velocities led Bajón Fernández et al. [140] to the conclusion that the impact of viscosity on the mass transfer coefficient was higher with higher superficial gas velocity, but nevertheless higher gas velocity increased the mass transfer in all examined cases. Similar conclusions have been found by Thobie et al. [124] for oxygen bubbles.

The effect of surfactants on the hydrodynamics of bubble columns has also been examined by several authors in the past. According to Saito et al. [58], an addition of surfactant, which causes a drop of surface tension, leads to a decreasing bubble diameter and bubble velocity. It confirms the observations in ethanol-water mixture [82], where the same behaviour of bubbles was reported. Recently, Lewandowski [67] showed the same trends for haxadecylamine and methyl isobutyl carbinol. They also examined the surrounding liquid velocity by PIV and found an increase of velocity and kinetic energy with increasing surfactant concentration. Similar results were found by Jimenez et al. [36], who also investigated mass transfer from oxygen bubbles and concluded that also the liquid side mass transfer is decreased with an increasing surfactant concentration, by congregation of surfactant at the bubble surface. In [42, 141], similar conclusions have been found and attributed to the Marangoni effect. The influence of Marangoni effect on bubble motion and bubbly flows was also investigated by Takagi et al. [142]. They have found that small amounts of surfactant can drastically influence the bubble behaviour because of the Marangoni effect and it leads to a change in the whole bubbly flow structure. Asgharpour et al.[143] have investigated the effect of surface contaminants on oxygen transfer in bubble columns at different alkane concentrations. As contaminant, immiscible hydrocarbons were utilized. Moreover, an anionic surfactant (SDS) was added to the system to investigate its effect on organic-aqueous systems. They have found similar results as the authors previous. With decreasing surface tension the bubble size and velocity decrease, which is more obvious in presence of surfactant. However, the surface contaminants decrease the mass transfer coefficient by increasing the liquid-side mass transfer resistance. Different types of surfactants have been examined by Sardeing et al. [144]. They observed that the bubble diameter decreases from water, to anionic, to cationic, and then to non-ionic surfactants. In a similar manner, both, the bubble formation frequency and the specific interfacial area increase. For the volumetric mass transfer coefficient $k_L a$, the trend is different; it decreases from water to anionic, to non-ionic, and finally to cationic surfactants. This fact has also been stated by Bischof et al. [145], who measured a stronger influence for bigger bubbles than for small ones. The same group also describes the influence of surfactants on the bubble trajectories that become more straight with increasing surfactant concentration and decreasing bubble velocity [146]. Mouza [147] performed experiments in a bubble column with changing the physical properties of the liquid phase (density, viscosity, surface tension) to gain sufficient information for its correlation formulation. With the new correlations he was able to predict the gas holdup and bubble Sauter mean diameter (d_{32}) with reasonable accuracy.

Most of the studies mentioned above used optical methods for the determination of bubble parameters and hydrodynamics in the column, but concentrations and mass transfer coefficient calculations are based on local probe measurements. The only publication using an optical measurement technique (LIF) for the determination of concentrations is the one from Jimenez et al. [36].

From this literature review it is clearly evident, that bubbles, bubbly flows and two-phase flows in bubble columns were widely investigated in the past and are still examined intensively in the present days as well, because of the importance of bubble columns in the industrial sector. These experiments form a good basis for validation of numerical simulations, but the demand from the numerical side of high-quality experimental data in well-defined environments is still high. Therefore, the aim of the present thesis is not just to develop and confirm the applicability of non-intrusive optical measurement techniques for mass transfer studies in bubble columns, but the author provides at the end detailed spatially and temporally resolved fluiddynamical and mass transfer data in a laboratory-scale bubble column.

Chapter 2

Employed experimental setup and measurement techniques

Contents

2.1. Laboratory-size bubble column reactor 18
2.2. Applied non-intrusive optical measurement techniques 20
  2.2.1. Particle Image Velocimetry (PIV) 20
  2.2.2. Laser Induced Fluorescence (LIF) 21
  2.2.3. Shadowgraphy with Particle Tracking Velocimetry (PTV) 22
2.3. Reaction systems 23
  2.3.1. CO_2-water system with uranin and pyridine 2 23
  2.3.2. Air-water system with resorufin 25
2.4. Measurement conditions and image post-processing 28
  2.4.1. Image post-processing for PIV recordings 30
  2.4.2. Image post-processing for LIF recordings 31
2.5. Technical equipment 32

2.1. Laboratory-size bubble column reactor

A laboratory-scale bubble column reactor was designed specifically for the optical measurements in two-phase flows. This reactor consists of three main parts. The core of the reactor is a pipe, made of poly-methyl methacrylate (Plexiglas XT, Evonik) with an outer diameter of 150 mm (±1.5 mm), 4 mm (±0.45 mm) wall thickness and an aspect ratio AR=5 (h=0.7 m, d_c≈0.14 m). The visible light transmittance of this material is 92%, which is proper for the planned optical measurements. Because of the curved column surface, refraction has to be reduced. To this end, the column was surrounded by a rectangular acrylic tank, which was filled always with the same liquid, as the working liquid inside the column (Figure 2.1, a). Preliminary experiments have shown that this gives better results, than to match the refractive index of the acrylic glass. This setup allows for an optical access for the cameras and light sources from all four sides. The importance of the refractive index correction can be seen on Figure 2.1 (b), where the column is completely filled with water, but the surrounding tank is just filled up to the half. In the bottom section, where light refraction is negligible due to the surrounding liquid, no optical distortion is visible. In the top section, where the surrounding tank contains air, noticeable refraction appears.

The third main part of the bubble column is the exchangeable sparger at the bottom. The gas line is connected to the bottom of the sparger element. Here, the gas enters into a buffer cavity, which serves to distribute equally the gas between the outlet nozzles (Figure 2.2, a). The cover plate of the sparger can be changed from a single nozzle gas outlet to a four nozzle in-line outlet, where the nozzles are spaced by 2.2 cm (Figure 2.2, b and c). These nozzles are stainless steel capillaries with an inner diameter of 0.25 mm or 0.13 mm, depending on the performed experiment. Finally, because of the considerable weight of the filled column, the entire setup is mounted on a rigid frame made of X95 aluminium profiles (Qioptiq) (Figure 2.2, d).

This bubble column was filled with ~11 l liquid in every experiment, except the experiments with single bubbles and some experiments, where the effect of filling height on the bubble properties was investigated.

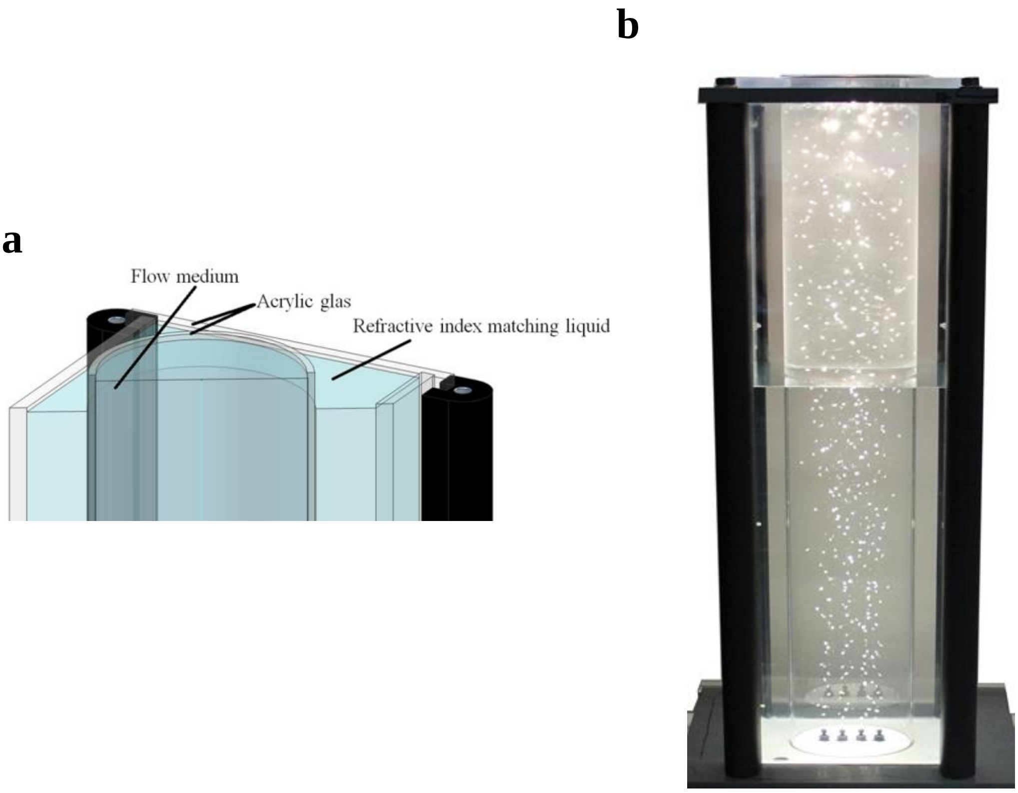

Figure 2.1: Reactor structure (a) and light refraction differences in the bubble column, if outer tank is only filled half (b).

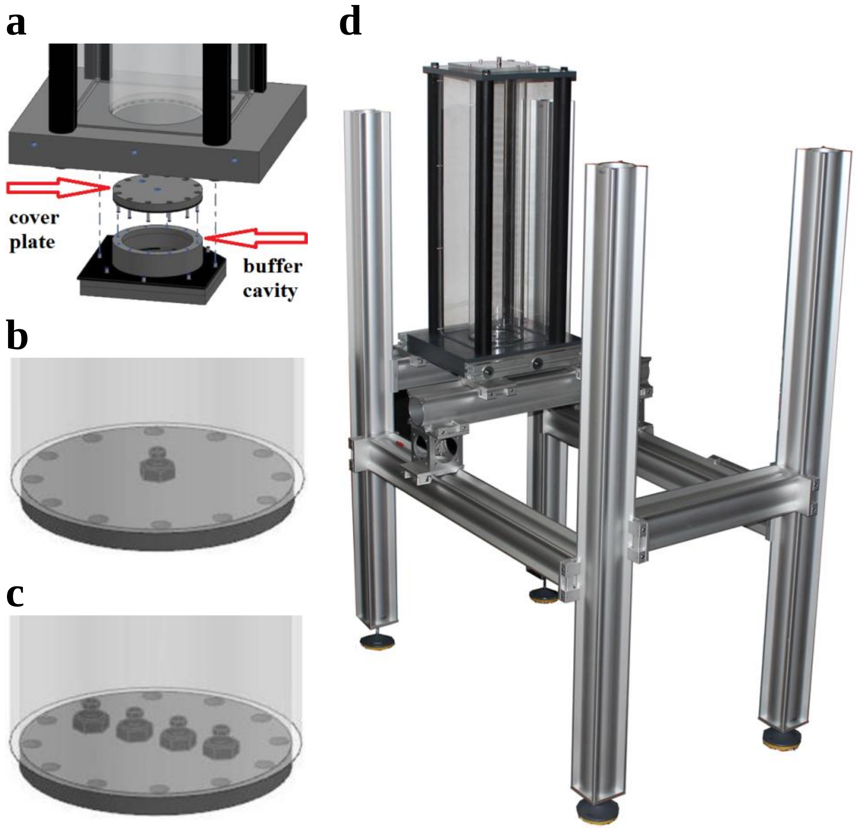

Figure 2.2: Complete bubble column setup: sparger part (a); single and four nozzles cover plate (b and c) and the column with frame (d).

2.2. Applied non-intrusive optical measurement techniques

The aim of the performed experiments was to gain spatially and temporally resolved information about the bubble properties and behaviour and to investigate the flow field and mass transfer in the bubble column reactor. It was particularly important, to avoid interfering effects from the measurements, which can affect the bubble motion or the whole hydrodynamics of the column. To this end, non-intrusive optical measurement methods were chosen for the investigations. Moreover, these techniques are planar measurement methods, with which a large 2D-field of view can be investigated. These methods will be described in detail in the following subsections.

2.2.1. Particle Image Velocimetry (PIV)

Information about the liquid flow around single bubbles and in the bubble column reactor was obtained with the help of Particle Image Velocimetry (PIV). This non-intrusive planar measurement method is based on recorded tracer particle images [148]. Seeding particles are introduced to the liquid, which are moving together with it. The investigated area is illuminated with a laser light sheet and, depending on the employed particles, the scattered light from the particle surfaces or the emitted fluorescence light is recorded by a camera. The recorded images are separated by a time delay (Δt). The velocity calculation is based on the displacement of the seeding particles between two recorded images. The big advantage of this method is, that it is non-intrusive and, contrary to Laser Doppler Velocimetry (LDV), makes it possible to acquire instantaneous flow fields over a large area.

For the velocity calculation, the recorded images are divided into smaller interrogation windows. In these windows not the displacement of single particles, but the average displacement of the particle pattern is calculated by cross-correlation (Figure 2.3). This method is described in details by Adrian and Atkins [149, 150].

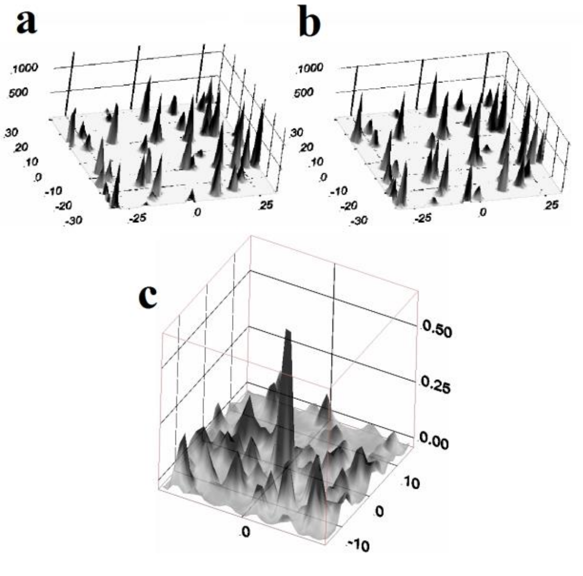

Figure 2.3: Particle displacement calculation. First image (a) and second image (b), peaks indicate particle patterns; result of cross-correlation of the first and second image, highest peak indicates the probable displacement.

The calculated displacement results in a displacement vector for each interrogation window. After an appropriate geometrical calibration, this displacement vector, which represents in fact a pixel shift, can be converted into a velocity vector.

2.2.2. Laser Induced Fluorescence (LIF)

The second non-intrusive optical measurement technique, which was employed in the experiments, is the Laser Induced Fluorescence (LIF).

Nowadays in most experiments with LIF, a laser light sheet illuminates the flow and the fluorescent species, therefore this method is also often called Planar Laser Induced Fluorescence (PLIF). This technique is applied to measure instantaneous concentration or temperature fields. It is based on species, which are capable to emit fluorescent light. The ground-state molecules in the flow are illuminated by a light source and they absorb the incident light, thus they are excited to a higher electronic energy state.

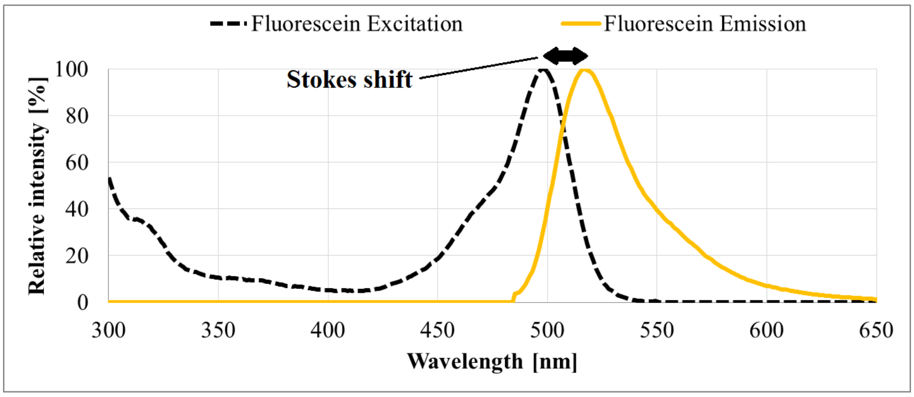

Figure 2.4: Typical excitation and emission spectra of fluorescein. Source [151].

This excited state is instable. The excited molecules fall back to the ground state, usually in a few nano- or microseconds, meanwhile they emit light. The emitted light is called fluorescence, which wavelength is larger than the excitation wavelength (Figure 2.4). This difference between the two – excitation and emission – maxima is called Stokes shift (Figure 2.4).

During the experiments this emitted light is recorded on a digital camera. It is proportional to the amount of absorbed light,

$$I_F = \phi(I_0 - I_T) \tag{2.1}$$

where I_0 is the intensity of the excitation light, I_T is the intensity of the transmitted light and ϕ is the quantum efficiency, the ratio of emitted and absorbed photons. The amount of transmitted light can be expressed from the Beer-Lambert law,

$$\frac{I_T}{I_0} = 10^{-\varepsilon_m l C}. \tag{2.2}$$

By combining Eqs.(2.1) and (2.2) the amount of emitted fluorescent light can be written as,

$$I_F = \phi I_0 (1 - 10^{-\varepsilon_m l C}), \tag{2.3}$$

where ε_m is the molar extinction coefficient, l is the length of the optical path, and C is the concentration of the fluorescing species.

When in LIF measurements the amount of excitation light, the light sheet thickness, and the extinction coefficient are constant, the measured fluorescence energy depends just on the concentration and the quantum efficiency. In most cases the quantum efficiency of a fluorescent species changes only with temperature or pH. This feature was applied for the 2T-LIF experiments for CO_2 mass transfer, where one pH sensitive and one pH passive fluorescent dye were applied simultaneously (see subsection 2.3.1).

If in the measurements just the concentration of the measured quantity changes, the measured fluorescence intensity depends on it, while the other parameters are kept constant. In fact, one prefers a linear relationship between the recorded fluorescence intensity and the concentration. This can be achieved at low fluorescent species concentration. High concentrations can cause non-linearities in fluorescence due to absorption related local changes. This concept was employed in the present measurements, where the oxygen mass transfer was investigated with planar LIF in the bubble column (see subsection 2.3.2).

2.2.3. Shadowgraphy with Particle Tracking Velocimetry (PTV)

The bubble properties at different flow conditions were determined with the help of shadow imaging (shadowgraphy) combined with Particle Tracking Velocimetry (PTV). In a typical shadow imaging setup, the investigated area is illuminated by a homogenous background light and this light is recorded by a camera. When an object passes through this area, it covers the light and a shadow is generated. This object shadow is then recorded by the camera. After a proper geometrical calibration, the shadow size on the recorded image can be defined exactly. With this simple technique, the object size, form and its coordinates can be determined. Furthermore, if in a recorded image sequence, the object displacement is not too large between two following images, the displacement can be calculated with a simple PTV method. To this end, the centre of the object has to be defined on both images and from the shift of that point, the displacement vector, which after geometrical calibration becomes the velocity vector, can be calculated. An exemplary image processing is shown on Figure 2.5. Here, for bubble size detection, from the raw images (Figure 2.5, a) a previously recorded background was first removed (Figure 2.5, b) to enhance contrast. Then, the high intensity areas are recognized for each bubble (Figure 2.5, c) and their equivalent diameters are calculated (Figure 2.5, d), as well as coordinates and centricity parameters. For the bubble velocity detection, two subsequent images are evaluated. Using an additional PTV algorithm [152], it was possible to follow in the second frame the movement of the bubbles that have been recognised in the first frame. The produced vectors show the movement of each bubble and according to this, the bubble velocity (Figure 2.5, d).

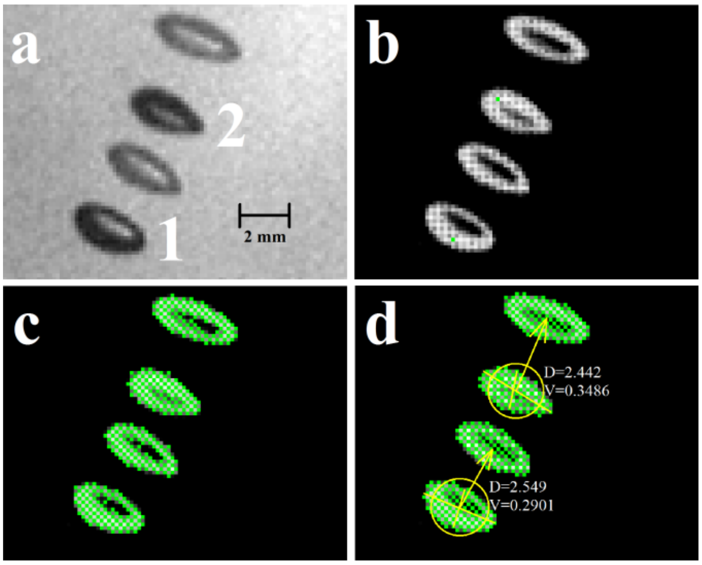

Figure 2.5: Shadowgraphy processing with two exemplary bubbles (1 and 2). For a better visibility the double frame recording was overlapped in one image. (a) – raw images, (b) – images after subtraction of the background, (c) – bubble recognition, (d) – bubble diameter and calculated trajectories. From [8].

2.3. Reaction systems

As presented in Chapter 1, plenty of possibilities exist to trace optically the mass transfer from gasses to liquids. In this study, two reaction systems were used. Firstly was the widely used CO_2 – NaOH/water reaction system employed, where during absorption of CO_2, a neutralization reaction takes place in the liquid and the pH of the solution changes. This change can be traced with a suitable LIF tracer. This system is often used to validate numerical simulations, because its chemistry is well-known and simple. Further, the necessary chemicals are easy to handle and affordable also for bigger installations, as in our case. The other reaction system used here is based on the redox reaction of resorufin with oxygen. The application of this dye was limited in the literature to colorimetric measurements. In this study, the fluorescence of resorufin was foremost used in the bubble column reactor to quantify the oxygen mass transfer from air bubbles to water. Also this system can be used in bigger installations of several litres of volume and environmental and health concerns are weak and easy to handle.

2.3.1. CO_2-water system with uranin and pyridine 2

For the characterization of mass transfer from CO_2-bubbles to the liquid, 2T-LIF was used, measuring the pH in the bubble column reactor, that changes due to the absorption reaction of CO_2 [153].

The chemisorption of CO_2 starts in the first step with the mass transfer of gaseous CO_2 into the liquid

$$\mathrm{CO}_{2,(g)} \rightarrow \mathrm{CO}_{2,(l)} \tag{2.4}$$

There, as first major reaction step and for pH>10, the dissolved $\mathrm{CO}_{2,(l)}$ reacts with hydroxide ions (OH^-) and forms hydrogen carbonate ions (HCO_3^-).

$$\mathrm{CO}_{2,(l)} + \mathrm{OH}^- \rightleftharpoons \mathrm{HCO}_3^- \tag{2.5}$$

As second major reaction step, HCO_3^- ions react with OH^- ions to carbonate ions (CO_3^{2-}).

$$\mathrm{HCO}_3^- + \mathrm{OH}^- \rightleftharpoons \mathrm{CO}_3^{2-} + 2\mathrm{H}^+ \tag{2.6}$$

In addition, for pH<8, the reaction of dissolved CO_2 to carbonic acid ($\mathrm{H}_2\mathrm{CO}_3^-$) takes place.

$$\mathrm{CO}_{2,(l)} + \mathrm{H}_2\mathrm{O} \rightleftharpoons \mathrm{H}_2\mathrm{CO}_3^- + \mathrm{H}^+ \tag{2.7}$$

This last reaction will be the most relevant in the experiments presented hereafter, since the pH-range is, due to the stability of the pH-tracer used, limited to pH<9.

The investigated quantity is the mass transfer from CO_2 bubbles into an initially basic water-NaOH liquid phase. During this process, the pH value in the liquid is decreasing and can be tracked by a fluorescent pH-tracer. From different suitable dyes, fluorescein sodium salt (uranine, CAS No.: 518-47-8) was chosen, because of its strong fluorescence intensity, accessibility, eco-acceptability and cost-effectiveness. Fluorescein is fluorescing strongly when excited by laser light at 532 nm. A monotonic relationship between fluorescence intensity and pH can be established in a pH range of 4.5 to 9 [154].

Unfortunately, the shadows created behind the bubbles when a laser light-sheet is passed, would not allow the investigation of pH in these shadow regions. Therefore, a second inert tracer should be used as active background tracer for the correction of the light field. This technique called Two-Tracer-LIF (2T-LIF) relies on the use of two fluorescing tracer molecules, which are imaged simultaneously, but separately, by two cameras and appropriate optical filters. One of these tracers is sensitive to the measured quantity; the other is inert and serves as a live background for the compensation of illumination inhomogeneity. A detailed description of this method can be found in [154].

Fluorescein fluoresces in a wavelength range up to about 650 nm (Figure 2.6), thus the second inert tracer should fluoresce at higher wavelengths. Pyridine 2 (CAS No.: 89846-21-9), which has proven to be a good combination with uranine in previous studies [154, 155] is chosen for this purpose. Its fluorescence maximum lies at about 710 nm (Figure 2.6).

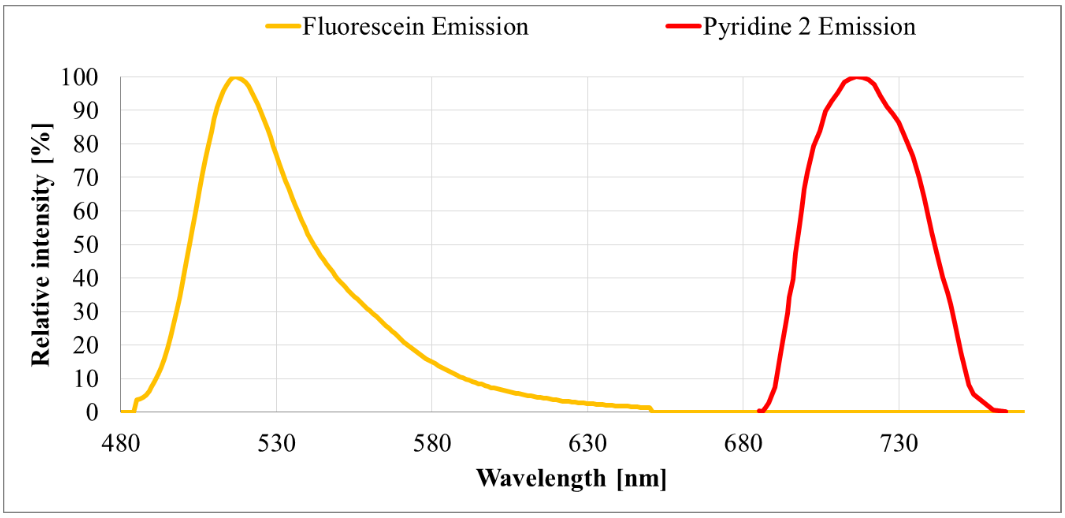

Figure 2.6: Fluorescence emission curves of fluorescein and pyridine 2 dyes. Source [151].

Its recorded fluorescence light serves as live background image to show the actual illumination intensity at each point in the measurement zone. Thus, dividing the uranine image (Figure 2.7, a) by the pyridine 2 image (Figure 2.7, b) gives, after calibration, the correct pH-image (Figure 2.7, c), where optical distortions, induced by the bubbles are drastically reduced.

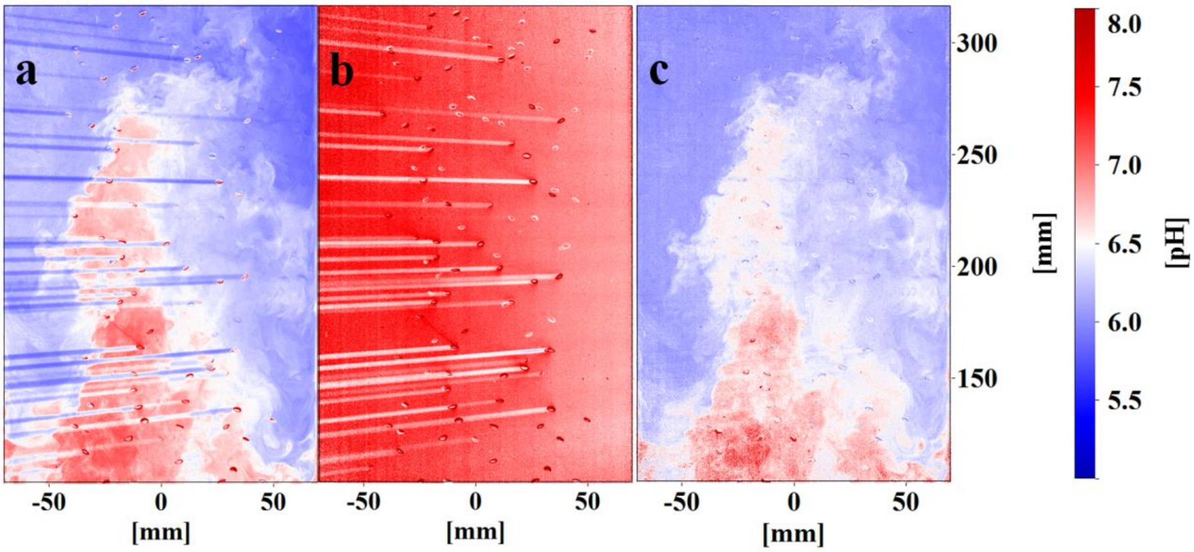

Figure 2.7: (a) raw image from 1st camera imaging the pH-tracer uranine; (b) raw image from 2nd camera imaging the inert tracer pyridine 2; (c) treated image after calibration showing the pH. All three images show a region from 100-320mm from the bottom of the column. From [8].

In order to transform the measured fluorescence intensities into pH-values, a calibration curve has to be established. For this, fluorescence image sets are recorded with different pH values of the liquid in the column without bubbles, to identify the typical fluorescence intensity for each pH value. NaOH is added in appropriate amounts and the pH is controlled by a WTW Profiline 3320 Multi pH-meter to get the desired pH in the solution. Afterwards, these images have to be treated in the same way as the experimental images. The obtained intensity values can then be associated to a particular pH value and a calibration curve can be fitted (Figure 2.8). Thus, every pixel intensity on the bubble 2T-LIF images can now be associated to a specific pH value. This calibration has to be done for each change of experimental conditions like tracer concentration, change of field of view, change of camera, laser intensity, etc.

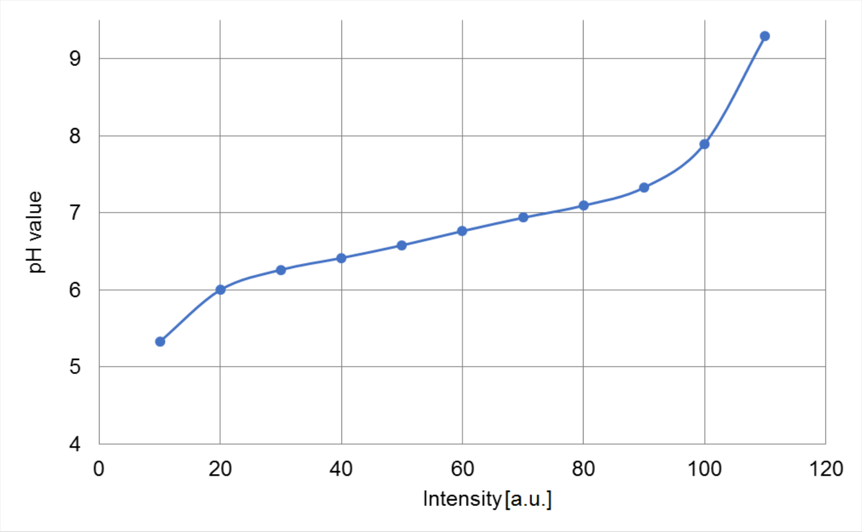

Figure 2.8: Example of calibration curve for 25 m% glycerol and 0 g/l surfactant in the upper part of the column. From [16].

Before every measurement start, the solution in the column had to be prepared for the measurements. To this end, the pH of the deionized water was set to pH>8 with a 10% NaOH solution. This initial pH will then be decreased during the neutralization reaction. Meanwhile, to degas the liquid and get a homogenous dye and PIV-particle distribution, argon gas was introduced into the column for half an hour.

2.3.2. Air-water system with resorufin

Resazurin was successfully applied as an oxygen-sensing dye using a colorimetric technique in other studies [156-159]. Resazurin (Figure 2.9, left) is reduced to resorufin in the presence of glucose and sodium hydroxide. The pink coloured resorufin solution (Figure 2.9, centre) is highly fluorescent and reduces further to dihydroresorufin, which is colourless and has no fluorescence (Figure 2.9, right). This redox-reaction is reversible and in the presence of oxygen, dihydroresorufin oxidizes back to resorufin. Resorufin has an emission maximum at 590 nm with an excitation at 532 nm. Because of its high fluorescence intensity, this dye was employed in the LIF measurements to track the dissolved oxygen concentration from air bubbles in the bubble column reactor. This reversible oxidation-reduction process is quasi-instantaneous concerning the oxidation, but the reduction takes a few minutes or even hours, depending on the recipe used for the solution.

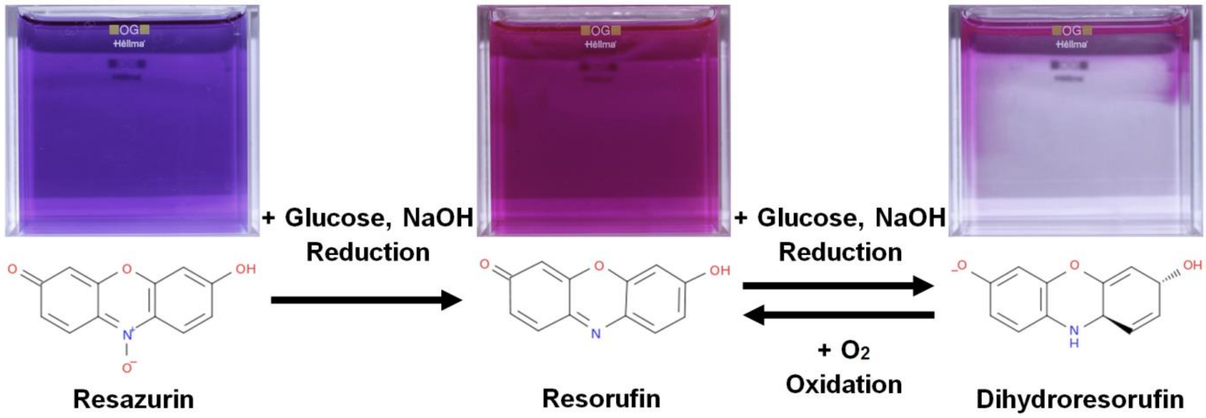

Figure 2.9: Reaction scheme for the redox-reaction starting with resazurin (purple, left), going to resorufin (pink, centre) and then dihydroresorufin (transparent, right). From [102].

The emitted fluorescent light is recorded by a digital camera. From the recorded intensities the dissolved oxygen concentration can be calculated. In fact, the calculated concentration is only an equivalent concentration, since, due to the fast reaction, no oxygen remains dissolved in reality. A linear relationship exists between the recorded intensity and the dissolved oxygen for resorufin concentrations up to 10 mg/l (Figure 2.10, left). Therefore, it is sufficient in these cases for the concentration calibration to know the intensity of the initial nearly clear dihydroresorufin-image and the intensity of the oxygen-saturated resorufin solution at the end of the reaction. Then, a linear curve can be established to calculate the equivalent oxygen concentrations in-between (Figure 2.10, right).

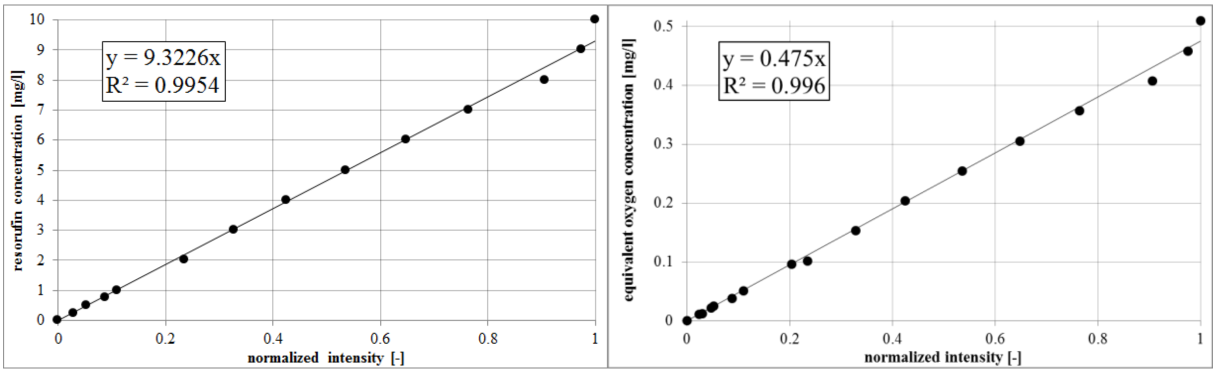

Figure 2.10: Exemplary calibration curve up to 10 mg/l resorufin (left) and for equivalent oxygen concentration (right) obtained for resorufin concentration of 10 mg/l.

For that calculation the exact amount of dissolved resazurin has to be determined. The reaction equation of the redox reaction is:

$$2\ \text{Dihydroresorufin} + \text{O}_2 \rightarrow 2\ \text{Resorufin}\ +\ 2\ \text{H}_2\text{O}\ , \tag{2.8}$$

which means, that the number of reacted moles of oxygen is half the number of reacting colorant moles.

During the reaction, the entire dissolved resazurin reacts to resorufin and this relation can be written as:

$$n_{O_2,transported} = \frac{n_{resazurin}}{2} = \frac{n_{resorufin}}{2}, \tag{2.9}$$

$$n = \frac{C}{M}. \tag{2.10}$$

Here, n is the molar amount of substance, C is the concentration and M is the molar mass.

For the experiment, resazurin sodium salt (CAS No.:62758-13-8) from Sigma Aldrich was used. Its dye content is around 80%, therefore the real dye content of the salt, which comes into reaction, can be calculated:

$$\frac{M_{resazurin}}{M_{resazurin\ sodium\ salt}} = \frac{229{,}17\ {}^{g}/_{mol}}{251{,}17\ {}^{g}/_{mol}} = 0.9124. \tag{2.11}$$

Therefore, the amount of resazurin in 1 g resazurin sodium salt is:

$$1\ \text{g resazurin sodium salt} \cong 0{,}7299\ \text{g resazurin}. \tag{2.12}$$

Thereby the saturated equivalent oxygen concentration, necessary for the two-point calibration, can be calculated as:

$$C_{O_2,saturated} = \frac{C_{resazurin\ sodium\ salt}}{2} \cdot \frac{M_{O_2}}{M_{resazurin}} \cdot 0.7299 \tag{2.13}$$

The amount of applied salt is known for every measurement. Therefore, the saturated equivalent oxygen concentration can be calculated and can be used to establish the calibration curve (Figure 2.10, right).

Table 2.1: Specification of the resazurin solutions for the different experiments.

	De-ionized water [l]	Resazurin sodium salt [mg/l]	Sodium hydroxide [g/l]	Glucose [g/l]	Saturated equiv. oxygen conc. [mg/l]
Single bubble (Table 2.2-2.4, No.11)	2	1.9	10	16.9	0.0968
Bubble chain and curtain (Table 2.2-2.4, No.12)	11.3	0.45	3.1	16.9	0.0229
Bubble curtain (Table 2.2-2.4, No.13)	11.3	0.225	3.1	16.9	0.0114

For the experiments, three different resazurin concentrations were used. In the single bubble case, the light absorption of the fluorescent dye is negligible, because in these experiments the reaction occurs just around a single bubble and the intensity change occurs only in this small region. Here the limiting factor is the camera dynamic range. For that reason, in these experiments it was possible to use a quite high dye concentration (Table 2.1), thus wider intensity range and better signal to noise ratio.

In the cases of bubble chain and curtain, where the reaction occurs in the whole bubble column, the applied dye concentration has to be reduced to minimize the light absorption (Table 2.1). These dye concentrations were than used to calculate the saturated equivalent oxygen concentrations for the calibration with Eq.(2.13). It is important to mention that with these amounts of dye the oxygen saturation concentration (9 mg/l) cannot be visualised in the liquid. After the reactant is fully consumed (Table 2.1, saturated equivalent oxygen concentration), oxygen still dissolves into the liquid, but from this point the amount of dissolved oxygen cannot be calculated.

Before every measurement start, the solution in the column had to be prepared for the measurements. To degas the liquid and get a homogenous dye and PIV-particle distribution, argon gas was introduced into the column for half an hour. Meanwhile part of the resazurin is reduced to resorufin and dihydroresorufin. The applied argon gas with a purity of 99.996% contains also a small amount of oxygen. Therefore, after the argon gas was stopped, the final reduction process is relatively slow; it takes around an hour in 11 l liquid. After the solution became, due to the reduction, completely transparent and colourless, the background images have been generated and then the measurement could be started. At the end of one measurement, the air feeding was stopped and images were recorded without air bubbles for the calibration image of the saturated solution.

2.4. Measurement conditions and image post-processing

For this thesis, the above mentioned measurement techniques were applied in thirteen different experimental setups. These setups mostly differ in the employed reaction system, the applied measurement technique, in spatial and temporal resolution and in their inlet conditions. All these different set-ups are summarized in Table 2.2. The measurements were always carried out at atmospheric pressure and room temperature.

Table 2.2: Measurement conditions of the performed experiments.

No.	Reaction system	Inlet	Measurement technique	Applied gas	Liquid bulk	Gas flow rates	Investigated position
	CO_2-water						
	Single bubbles						
1		one nozzle *d* =0.25 mm	High-speed LIF	CO_2 - 99.5%	de-ionized water + NaOH	single bubbles	right after the nozzle
2			High-speed PIV	CO_2 - 99.5%	de-ionized water + NaOH	single bubbles	33-48 mm
3			Simultaneous 2T-LIF–PIV	CO_2 - 99.5%	de-ionized water + NaOH	single bubbles	33-48 mm
	Bubble chain						
4		one nozzle *d* =0.25 mm	Simultaneous LIF–PIV	CO_2 - 99.5%	de-ionized water + NaOH	1.62 and 3.24 l/h	0-705 mm, in two sections
	Bubble curtain						
5		4 nozzles in-line *d* =0.25 mm	PIV	CO_2 - 99.5%	de-ionized water + NaOH	6 l/h	0-704 mm, in four sections
6			High-speed PIV	CO_2 - 99.5%	de-ionized water + NaOH	6 l/h	0-730 mm, in six sections
7			2T-LIF	CO_2 - 99.5%	de-ionized water + NaOH	6 l/h	0-704 mm, in four sections
8			Simultaneous 2T-LIF–PIV	CO_2 - 99.5%	de-ionized water + NaOH	6 l/h	0-704 mm, in two sections
9			Shadowgraphy 1.	CO_2 - 99.5%	de-ionized water + NaOH/HCl; tap water; distilled water	3.5-10 l/h	0-300 mm
10			Shadowgraphy 2.	CO_2 - 99.5%	de-ionized water + glycerol/SDS/NaOH	4, 6 and 8 l/h	0-590 mm, in two sections
	Air-water						
	Single bubbles						
11		one nozzle *d* =0.25 mm one nozzle *d* =0.13 mm	Simultaneous LIF-PIV	Air	de-ionized water + glucose + NaOH	single bubbles	18-35 mm
	Bubble chain						
12		one nozzle *d* =0.25 mm	Simultaneous LIF-PIV	Air	de-ionized water + glucose + NaOH	2 and 4 l/h	0-705 mm, in two sections
	Bubble curtain						
13		4 nozzles in-line d=0.25 mm	Simultaneous LIF-PIV	Air	de-ionized water + glucose + NaOH	6 and 8 l/h	0-700 mm, in three sections

During the experiments acquired images are in RAW format, which contains just the intensity information of each pixel. In order to convert this information into concentration fields or to calculate velocity fields from these images, the acquired experimental images have to be treated and calibrated. The fundamental way of the image post-processing is similar for the images made with the same measurement technique, but because of the different spatial and temporal resolutions (PIV), or the different chemical reaction systems (LIF), some changes in the post-processing pipeline have been necessary. For the image post-processing, velocity and concentration field calculations the software DaVis (LaVision GmbH) has been used.

The image post-processing steps are summarized in Table 2.3 for the PIV and in Table 2.4 for the LIF experiments. They will be described in details in the following.

Table 2.3: Image post-processing steps of the PIV recordings.

No.	Reaction system	Inlet	Measurement technique		PIV processing steps						
					Bubble masking	Gaussian smoothing	Single-pass cross-correlation	Multi-pass cross-correlation, decreasing size	Interrogation window [pixels]	Overlap [%]	Vector refinement with median filter
	CO_2-water										
	Single bubbles										
2		one nozzle *d* =0.25 mm	High-speed PIV		x			x	64x64 to 32x32	50	x
3			Simultaneous 2T-LIF–PIV	PIV	x			x	64x64 to 32x32	50	x
	Bubble chain										
4		one nozzle *d* =0.25 mm	Simultaneous LIF–PIV	PIV	x			x	32x32 to 24x24	50	x
	Bubble curtain										
5		4x nozzle in-line *d* =0.25 mm	PIV					x	64x64 to 32x32	50	x
6			High-speed PIV				x		16x16	50	x
8			Simultaneous 2T-LIF–PIV	PIV	x			x	32x32 to 16x16	50	x
	Air-water										
	Single bubbles										
11		one nozzle *d* =0.25 mm one nozzle *d* =0.13 mm	Simultaneous LIF-PIV	PIV	x	x		x	64x64 to 32x32	50	x
	Bubble chain										
12		one nozzle *d* =0.25 mm	Simultaneous LIF-PIV	PIV	x			x	64x64 to 48x48	50	x
	Bubble curtain										
13		4x nozzle in-line d=0.25 mm	Simultaneous LIF-PIV	PIV	x			x	64x64 to 32x32	50	x

Table 2.4: Image post-processing steps of the LIF recordings.

No.	Reaction system	Inlet	Measurement technique		Image processing steps					
					Dark image subtraction	Laser sheet correction	Geometrical calibration	2T-LIF	pH calibration	Oxygen concentration calibration
	CO_2-water									
	Single bubbles									
1		one nozzle *d* =0.25 mm	High-speed LIF		x	x	x			
3			Simultaneous 2T-LIF–PIV	2T-LIF	x	x	x	x	x	
	Bubble chain									
4		one nozzle *d* =0.25 mm	Simultaneous LIF–PIV	LIF	x	x	x		x	
	Bubble curtain									
7		4x nozzle in-line *d* =0.25 mm	2T-LIF		x	x	x	x	x	
8			Simultaneous 2T-LIF–PIV	2T-LIF	x	x	x	x	x	
	Air-water									
	Single bubbles									
11		one nozzle *d* =0.25 mm one nozzle *d* =0.13 mm	Simultaneous LIF-PIV	LIF	x		x			x
	Bubble chain									
12		one nozzle *d* =0.25 mm	Simultaneous LIF-PIV	LIF	x	x	x			x
	Bubble curtain									
13		4x nozzle in-line d=0.25 mm	Simultaneous LIF-PIV	LIF	x	x	x			x

2.4.1. Image post-processing for PIV recordings

In the first post-processing step for PIV recordings, the image coordinates were calibrated. For this step geometrical calibration images were acquired with the help of a calibration plate, which is usually three-dimensional for a better precision, and a distortion correction field was generated for each camera, which was later applied on the measurement images.

The PIV recordings for evaluation of the liquid velocity also contain images of the bubbles and their shadows. Thus, as a next post-processing step, and if it was technically possible, the bubbles and their shadows were masked out on the original recordings by the help of an algorithmic mask function, to avoid the calculation of vectors in that region (Figure 2.11). This step was crucial in the case of single bubbles. However, the experience has shown, that in certain cases e.g. in the measurements with bubble curtains, the spurious vectors in the shadows can be filtered out with a median filter, which will be described later.

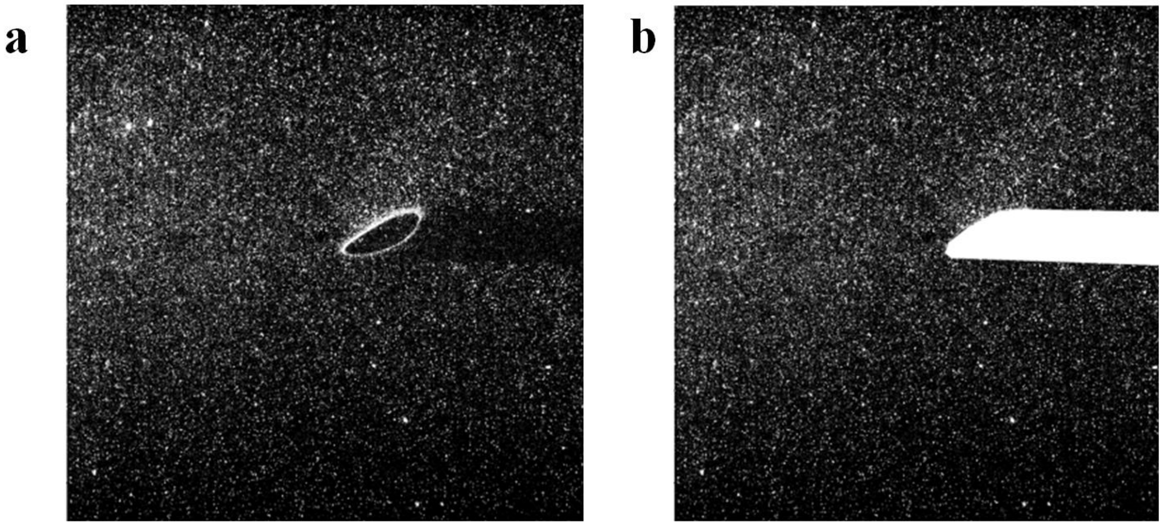

Figure 2.11: Exemplary PIV image from the experiments: raw image (a) and the masked image, where the bubble and its shadow are masked (b).

In the single-bubble experiments with air bubbles, a Gaussian smoothing filter had to be applied to reduce the noise of the images and enhance the particle signal, because of the low particle signal to noise ratio.

In the next step, the velocity fields from the images were calculated with a common PIV cross-correlation algorithm. Because of the different spatial resolutions, the settings of the cross-correlations are different for the different setups. They are listed in Table 2.3.

To remove false vectors and refine the vector field, especially in the vicinity and shadows of the bubbles if no masking was possible, vector postprocessing was necessary. The efficiency of the applied vector filter will be presented by an example, where the bubbles and their shadows were not masked out. After the cross-correlation step, the bubbles and their shadows are clearly visible in this case, due to a wealth of spurious vectors (Figure 2.12, a, deep red and blue regions). Superimposing the raw image with the visible bubbles on the PIV velocity field, it is clear that the false vectors come from the bubbles: the laser sheet coming from the right in these pictures, there are no tracer particles at all within the bubbles, or the illumination is too weak (in the shadows of the bubbles). Thus, these regions cannot be processed appropriately using a standard cross-correlation. To get rid of these imperfections, it is necessary to use further, dedicated post processing steps.

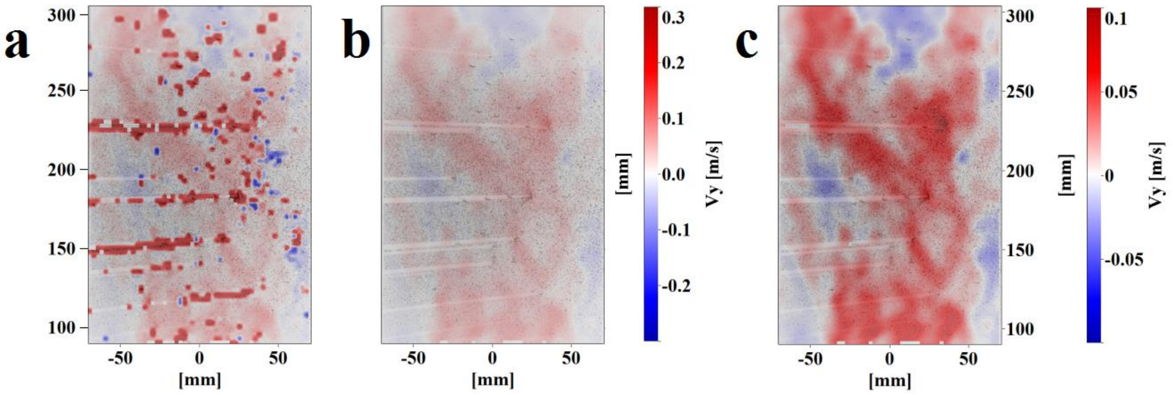

Figure 2.12: Vertical velocity component (m/s) for one snapshot without any vector postprocessing (a) and after postprocessing (b). The image "b" is reprinted on the right with an adapted colour scale showing only physically meaningful values (c). The raw particle image is used as background for the location of the bubbles and of the shadows. From [8].

For this purpose, an allowable vector range filter was first employed according to the generated v_x/v_y velocity scatter plot. Then, with the help of a median filter, which computes the median vector from the 8 neighbouring interrogation areas and then compares the vector in the centre with this median vector and its deviation from the neighbouring vectors, the highest (but in some cases wrong) correlation peak was replaced by the second, third or fourth highest correlation peak, until a sufficient agreement is obtained within the neighbourhood. The current vector position was disabled if none of the four peaks were in the allowed range of the median vector. These few disabled areas were afterwards replaced with an interpolated value from the 8 neighbours. With these steps, the complete velocity field can be determined, also in the shadow regions behind the bubbles, if these shadows are not too dense.

The result obtained in this manner can be seen exemplarily in Figure 2.12(b), once more with the superimposed raw image to locate the bubbles and their shadows. For a better readability, the same velocity field is presented again with a different colour scale (now adapted to the real maximum and minimum values) on Figure 2.12(c).

As a final step of post-processing, except in the single-bubble experiments, the individual instantaneous PIV velocity fields were averaged.

2.4.2. Image post-processing for LIF recordings

For the LIF experiments two different reaction systems were used (see previous subsection 2.3), to quantify the pH change or dissolved oxygen concentration in the bubble column. Despite of the differences in the used systems, the main image processing pipeline is similar for both reactions, also for measurement and concentration calibration images.

During image post-processing, first the image properties will be improved, then, in the case of 2T-LIF, the image will be treated with the live background, and finally the intensity values will be converted to pH values or equivalent oxygen concentrations. Since digital cameras were used, all images contain digital noise. During the image properties refinement in the first step, this noise has to be subtracted from the images. To this end, 50 images have been taken with closed lenses, which were then averaged to obtain the dark image. This dark image was then subtracted from the calibration and measurement images. Another interfering effect, which has to be taken into account, is the laser sheet inhomogeneity. Due to the Gaussian shape of the beam, the light sheet has higher power in the centre of the illuminated area and less power on the top and at the bottom of the image. To correct this inhomogeneity, for each camera in every LIF setup an image set with 50 images was recorded with the fluorescent dyes, but without bubbles. Preliminary tests have been shown that 50 images are enough to cover also the laser energy fluctuations and gain a homogenous laser sheet profile. The mean of these images is then used to normalize the experimental and calibration images, except in the case of single air bubbles (Table 2.4, No. 11), where the light absorption of the fluorescent dye was negligible. In these experiments, the reaction occurs just around a single bubble and the intensity change occurs only in this small region.

In the last refining step, the image coordinates were calibrated. For this step geometrical calibration images were acquired with the help of a calibration plate and a distortion correction field was generated for each camera, which was applied on the concentration calibration and measurement images.

In the case of 2T-LIF, where two cameras were used for LIF (Table 2.4, No. 3, 7 and 8), applying this distortion field on the images ensures also, that both camera images will have the same coordinate system. Therefore, the images can be overlapped for the following 2T-LIF and pH calibration steps. From this step, the image processing differs for the two reaction systems.

During the 2T-LIF image evaluation process an active background is used to reduce light inhomogeneities due to the bubbles (reflections, shadows). Therefore, the camera image with fluorescein (uranine) dye is divided with the live background image (got from pyridine 2 image) and the obtained values are multiplied with a value 100, thus enlarging the intensity range for a better visibility (see also subsection 2.3.1).

In the last step, to convert the intensity values into pH values, a calibration polynomial (Figure 2.8) is applied. Thus, every pixel-intensity on the experimental 2T-LIF images can now be associated to a specific pH value.

To quantify O_2 mass transfer (Table 2.4, No. 11-13), the intensities were converted into equivalent concentration values. In fact, a linear relationship exists between the recorded intensity and the dissolved oxygen concentration. This oxygen is immediately consumed by the reaction, and represents thus an “equivalent concentration”, as explained in subsection 2.3.2. Therefore, for the concentration calibration it is sufficient to know the intensity of the initial nearly clear dihydroresorufin-image and the intensity of the oxygen-saturated resorufin solution at the end of the reaction. Then a linear curve can be established to calculate the equivalent oxygen concentrations for a specific intensity value in-between.

2.5. Technical equipment

A typical measurement setup used for the determination of liquid velocity fields and mass transfer in the column can be seen on Figure 2.13. To excite the fluorescent dyes for the LIF measurements and/or the particles for the PIV experiments, two types of double pulsed lasers were used. While for the low-speed measurements a Nd:YAG laser (Spectra Physics PIV-400) with 532 nm wavelength and a nominal power of 200 mJ/pulse@10 Hz was employed, for the high-speed recordings a Nd:YLF laser (Litron LDY-304 PIV) with 527 nm wavelength and a nominal power of 30 mJ/pulse@1kHz was applied (Figure 2.13, 1). The generated laser light beam was directed to the light sheet optics (Figure 2.13, 3) through special adjustable mirrors (Figure 2.13, 2). With this light sheet optics, the incident light beam is converted to a thin, less than 0.5 mm thick light sheet. This achieved laser light sheet is used to illuminate the investigated area in the bubble column (Figure 2.13, 6). After excitation of some nanoseconds, the emitted or scattered light was recorded with scientific-grade digital cameras (Figure 2.13, 4). In the case of shadow imaging, instead of the laser, halogen and LED lights were employed with diffusers from the column back to generate a homogeneous background illumination for the measurements. For 2T-LIF, two cameras were coupled with an image doubler (Figure 2.13, 5), to gain better image overlapping between the two camera recordings. The working principle of the image doubler is shown on (Figure 2.13, 7)

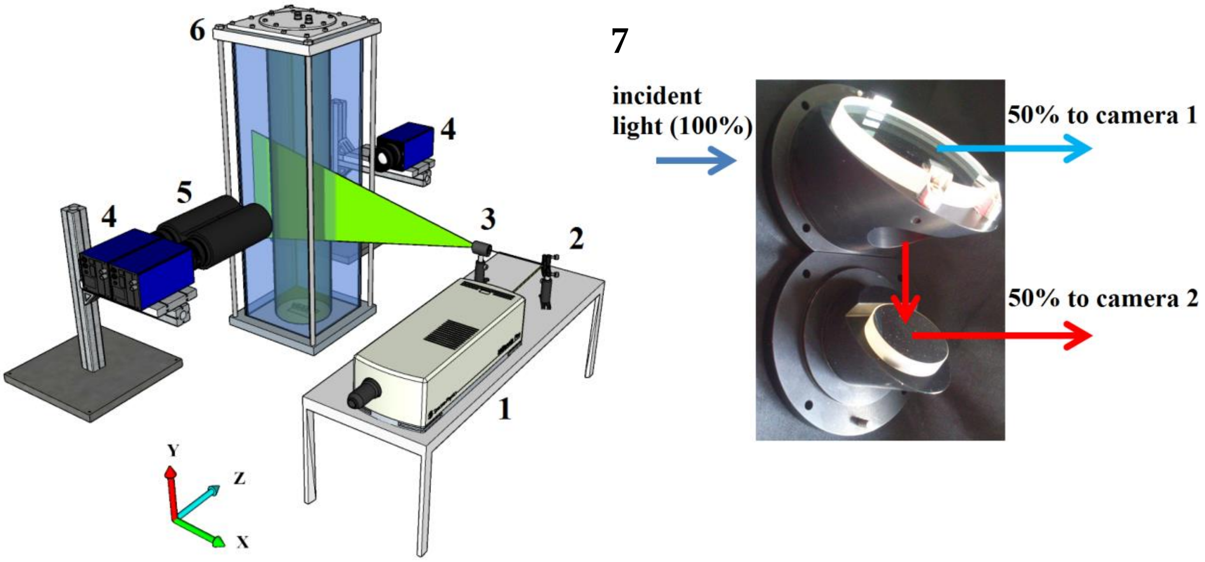

Figure 2.13: Typical experimental setup.

Due to the different spatial and temporal resolutions in the experiments and due to the continually developing technical equipment park at the department, the different measurements were carried out not always with the same cameras and same experimental setup. The main properties of all applied cameras (all from LaVision GmbH) are summarized in Table 2.5.

Table 2.5: Properties of the applied cameras.

	Sensor type	**Pixel size** [µm]	**Resolution (horizontal x vertical)** [pixel]	**Dynamic range** [bit]	**Readout frequency** [Hz]
Imager Intense	CCD	6.45	1376 x 1040	12	10
Imager LX 8M	CCD	5.5	3312 x 2488	12	8.5
Imager pro HS 4M	CMOS	11	2016 x 2016	12	1279
Imager sCMOS	sCMOS	6.5	2560 x 2160	16	50

To avoid repetitions in the technical description of each experiment, an overview table was created for all of the utilized equipment in each experimental setup (Table 2.6). For this reason, in the later descriptions of the experiments, reference will be given to this table for the technical details. The experimental images were recorded and, in most cases, processed with the software DaVis (LaVision GmbH).

Table 2.6: Technical overview of the performed experiments.

No.	Reaction system	Inlet	Measurement technique		Camera(s)	Lens(s)	Filter(s)	Fluorescent dye(s)	Tracer particles	Light source	Recording rate [Hz]
	CO$_2$-water										
	Single bubbles										
1		one nozzle *d* =0.25 mm	high-speed LIF		Imager pro HS 4M CCD	Nikon AF Micro-Nikkor 105 mm f/2.8D + image intensifier	555 nm LP	uranine	-	Litron LDY300 PIV Nd:YLF laser; 527 nm	450
2			high-speed PIV		Imager pro HS 4M CCD	Nikon AF Micro-Nikkor 105 mm f/2.8D	537 nm LP	-	polymethyl methacrylate (PMMA) Rhodamin B doped particles; 10µm	Litron LDY300 PIV Nd:YLF laser; 527 nm	1000
3			Simultaneous 2T-LIF–PIV	2T-LIF	Imager LX 8M CCD	Nikon AF Micro-Nikkor 105 mm f/2.8D	550 nm BP(10 nm)	uranine + pyridine 2	-	Spectra Physics PIV-400 Nd:YAG laser; 532 nm	3.3
				PIV	Imager Intense CCD	Nikon AF Micro-Nikkor 105 mm f/2.8D	555 nm LP	-	ethidium bromide doped melamine resin particles, 6.72 µm		
	Bubble chain										
4		one nozzle *d* =0.25 mm	Simultaneous 2T-LIF–PIV	LIF	Imager Intense CCD	Nikon AF Nikkor 50mm f/1.4D	550 nm BP(10 nm)	uranine	-	Spectra Physics PIV-400 Nd:YAG laser; 532 nm	2.5
				PIV	Imager LX 8M CCD	Nikon AF Nikkor 35mm f/2D	580 nm LP	-	polymethyl methacrylate (PMMA) Rhodamin B doped particles; 10µm		
	Bubble curtain										
5		4x nozzle in-line *d* =0.25 mm	PIV		Imager Intense CCD	Nikon AF Micro-Nikkor 60mm f/2.8D	537 nm LP	-	polymethyl methacrylate (PMMA) Rhodamin B doped particles; 10µm	Spectra Physics PIV-400 Nd:YAG laser; 532 nm	6.6
6			high-speed PIV		Imager pro HS 4M CCD	Nikon AF Micro-Nikkor 60mm f/2.8D	537 nm LP	-	polymethyl methacrylate (PMMA) Rhodamin B doped particles; 10µm	Litron LDY300 PIV Nd:YLF laser; 527 nm	1000
7			2T-LIF		2x Imager Intense CCD	Nikon AF Micro-Nikkor 60mm f/2.8D	550 nm BP(10 nm) 705 nm BP(25 nm)	uranine + pyridine 2	-	Spectra Physics PIV-400 Nd:YAG laser; 532 nm	3.3
8			Simultaneous 2T-LIF–PIV	2T-LIF	2x Imager Intense CCD	Nikon AF Nikkor 50mm f/1.4D	550 nm BP(10 nm) 705 nm BP(25 nm)	uranine + pyridine 2	-	Spectra Physics PIV-400 Nd:YAG laser; 532 nm	3.3
				PIV	Imager LX 8M CCD	Nikon AF Nikkor 35mm f/2D	polarization filter + 580 nm LP	-	polymethyl methacrylate (PMMA) Rhodamin B doped particles; 10µm		
9			Shadowgraphy 1.		Imager pro HS 4M CCD	Carl-Zeiss Makro Planar T*2/50mm ZF-I	-	-	-	Dedocool CoolH halogen lights	100
10			Shadowgraphy 2.		2x Imager pro HS 4M CCD	Nikon AF Nikkor 50mm f/1.4D	-	-	-	Dedocool CoolH halogen lights + LED	100
	Air-water										
	Single bubbles										
11		one nozzle *d* =0.25 mm	Simultaneous LIF-PIV	LIF	Imager sCMOS	Tokina ATX-Pro D Macro 100mm f/2.8	600 nm BP(40 nm)	resazurin (resorufin)	-	Spectra Physics PIV-400 Nd:YAG laser; 532 nm	10
		one nozzle *d* =0.13 mm		PIV	Imager sCMOS	Tokina ATX-Pro D Macro 100mm f/2.8	532 nm BP(10 nm) + ND2	-	polyamide particles; 17-25 µm polymethyl methacrylate (PMMA) Rhodamin B doped particles; 10µm		
	Bubble chain										
12		one nozzle *d* =0.25 mm	Simultaneous LIF-PIV	LIF	Imager Intense CCD	Nikon AF Nikkor 50mm f/1.4D	550 nm BP(10 nm)	resazurin (resorufin)	-	Spectra Physics PIV-400 Nd:YAG laser; 532 nm	2.5
				PIV	Imager LX 8M CCD	Nikon AF Nikkor 35mm f/2D	580 nm LP	-	FluoGreen polystyrene particles; 60 µm		
	Bubble curtain										
13		4x nozzle in-line d=0.25 mm	Simultaneous LIF-PIV	LIF	Imager sCMOS	Tokina ATX-Pro D Macro 100mm f/2.8	600 nm BP(40 nm)	resazurin (resorufin)	-	Spectra Physics PIV-400 Nd:YAG laser; 532 nm	10
				PIV	Imager sCMOS	Tokina ATX-Pro D Macro 100mm f/2.8	532 nm BP(10 nm)	-	polyamide particles; 55 µm		

Chapter 3

Determination of bubble characteristics in the bubble column

Parts of the results and subsections presented in this chapter have been published in Heat and Mass Transfer (Kováts et al. [8]) and in the International Journal of Multiphase Flow (Kováts et al. [16]).

Contents

3.1. INTRODUCTION 36
3.2. EXPERIMENTAL SETUPS AND FLOW CONDITIONS 36
3.3. INFLUENCE OF GAS FLOW RATE, WATER QUALITY, PH AND FILLING HEIGHT ON BUBBLE CHARACTERISTICS 37
  3.3.1. Parameters and post-processing 37
  3.3.2. Results of parameter study 39
3.4. INFLUENCE OF VISCOSITY AND SURFACE TENSION ON BUBBLE CHARACTERISTICS 41
  3.4.1. Post-processing of images 41
  3.4.2. Bubble trajectories, diameters and velocities 42
  3.4.3. Comparison with known correlations 50
  3.4.4. Dimensionless correlations 52
3.5. BUBBLE SHAPE IN BUBBLE SWARMS 56
  3.5.1. Bubble shape in bubble swarms 56
  3.5.2. Mass transfer determination 64
3.6. CONCLUSIONS 74

3.1. Introduction

Gas-liquid reactions in a bubble column are highly depending on the characteristics of the generated bubbles and on the properties of the liquid medium. For this reason, optical measurements were first carried out in the bubble column with Shadowgraphy technique to determine the typical bubble properties for a variety of flow conditions, like different gas flow rates, different liquid viscosities or surface tensions. Moreover, the influence of the water quality, filling height, pH and gas type was investigated. To this end, two measurement series were carried out separately. The first experimental series was achieved in the bottom part of the bubble column to investigate the influence of gas flow rate, water quality, pH, and filling height on the bubble properties. The purpose of the second shadowgraphy experiments was to gain information about the influence of surface tension and viscosity on bubble size, form, motion, and rising velocity at different gas flow rates.

From the results of these measurement series a new correlation for bubble eccentricity, based on the Flow number, is developed and compared with literature correlations. This equation was then used to propose a new correlation for mass transfer coefficient determination, based on the well-known correlation of Higbie.

3.2. Experimental setups and flow conditions

Due to the various spatial and temporal resolutions and to avoid unnecessary repetitions, the applied experimental setups will be described only briefly with referring to the detailed technical description in Chapter 2.

For all experiments the bubble column described in Chapter 2 with a diameter of 0.14 m and a height of 0.7 m was employed. The refractive index matching liquid filled in the surrounding box was always the same as the actual working liquid. In the bottom sparger plate 4 in-line nozzles were placed, which are spaced by 2.2 cm. The nozzles are stainless steel capillaries with an inner diameter of 0.25 mm. In all cases – except for filling height and water quality measurements – the column was filled up with 11.5 l de-ionised water or de-ionised water–glycerol–surfactant mixtures.

The following Table 3.1 shows the physical properties for the different mixtures of water/glycerol/SDS used for the second measurement series in this study. The viscosity was measured with a Malvern Kinexus pro+ rotational rheometer, and the surface tension was obtained using the pendant drop method.

In both measurement series high-speed CCD cameras were applied to record the shadow images of the bubbles. To this end, the bubble column was illuminated from the back with a diffused homogenous light. Experimental images were taken with a frame rate of 100 Hz for each flow condition in the lower 0.3 m of the bubble column during the first and over the whole column height in the second measurement campaign. More detailed technical information about the measurement setups can be found in Chapter 2, Table 2.2 and Table 2.6, No. 9 and 10.

Table 3.1: Physical properties of the mixtures.

Glycerol conc. [m%]	Surfactant [g/l]	ρ [kg/m^3]	μ [mPa·s]	σ [mN/m]	log$_{10}$(Mo) [-]
0	0	996.89	0.9	72.24	-10.7673
0	1.9	996.89	0.86	58.19	-10.5645
0	5.69	996.89	0.89	51.34	-10.3417
25	0	1057.7	1.78	69.45	-9.5569
25	1.9	1057.7	1.79	52.7	-9.1876
25	5.69	1057.7	1.82	50.79	-9.1106
50	0	1123.6	4.76	67.81	-7.8433
50	1.9	1123.6	4.78	49.29	-7.4204
50	5.69	1123.6	4.538	47.52	-7.4630
60	0	1150.7	8.752	66.51	-6.7704
60	1.9	1150.7	8.875	48.86	-6.3443
60	5.69	1150.7	9.286	44.8	-6.1527

3.3. Influence of gas flow rate, water quality, pH and filling height on bubble characteristics

3.3.1. Parameters and post-processing

In this first experimental series just the lower part of the bubble column was investigated at different flow conditions (gas flow rate, water quality, pH, and filling height). These results have been published in Kováts et al. [8]. Here, during one measurement, four series of 250 images were taken for each parameter, which are listed in Table 3.2. Preliminary experiments showed that this number of images is sufficient to get statistical convergence (Figure 3.1).

Table 3.2: Investigated parameters in the first measurement series.

Filling volume [l], (Q_g= 4 l/h)	11.5	9	7	5	3
Water quality, (Q_g= 4 l/h)	1x distilled	2x distilled	de-ionized	tap water	
pH, (Q_g= 4 l/h)	12.48, raised with NaOH	6. 4, decreased with CO_2	3.8, decreased with HCl		
Gas flow rate, Q_g (l/h)	10	7.5	5	3.5	

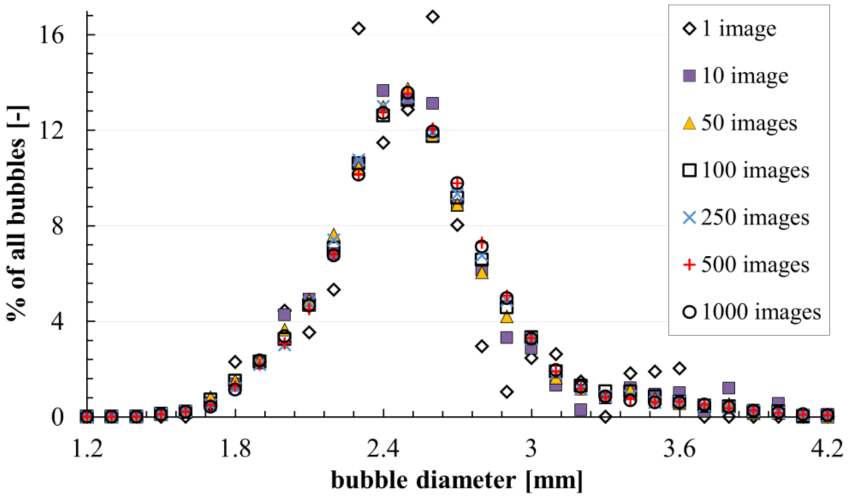

Figure 3.1: Bubble size distribution as function of averaged image numbers.

For bubble size detection, a common shadowgraphy image processing combined with PTV was applied. The detailed description of this technique can be found in subsection 2.2.3.

After the PTV processing, the produced vectors show the movement of each bubble and according to this, the bubble velocity. With the help of these vectors, a trajectory can then be reconstructed for each bubble (Figure 3.2). Here, four bubbles are tracked and coloured with the corresponding vertical velocity component.

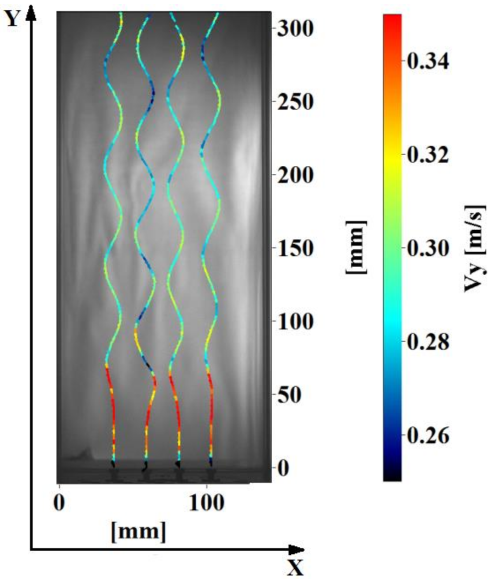

Figure 3.2: Exemplary bubble trajectories, coloured with the instantaneous vertical velocity component. From [8].

As it can be seen in Figure 3.3, showing a long-time acquisition (2.5 s), the bubbles follow a three-dimensional helical path, as expected for the generated bubble diameter. The considered bubbles present an average diameter of 2.3-3.1 mm (see Table 3.3 later). In this size range the bubbles are no longer spherical and follow a helical path.

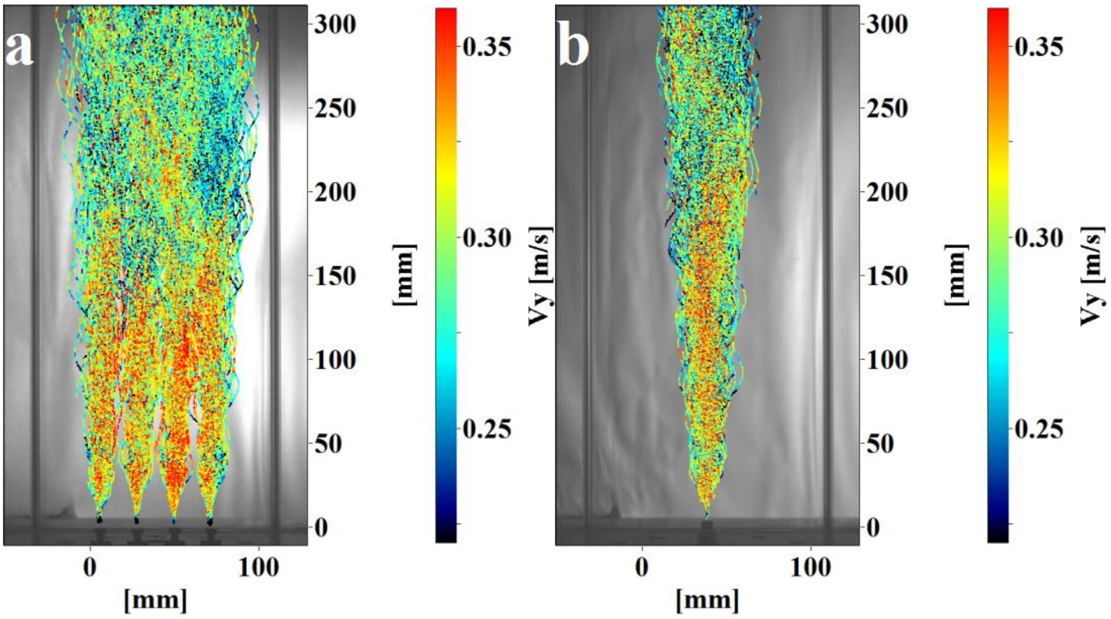

Figure 3.3: Bubble trajectories in front view (a) and side view (b), coloured with the instantaneous vertical velocity component. From [8].

3.3.2. Results of parameter study

In order to identify possible modifications in bubble behaviour when varying process conditions, those have been modified systematically, once at a time. First, the influence of filling height on bubble diameter and velocity was determined. The images were taken for five different filling volumes of 3, 5, 7, 9 and 11.5 l (maximum filling volume). No distinct differences could be observed between the five cases at the same gas flow rate (Table 3.3). The average bubble diameter remained at 2.3-2.4 mm and the average velocity was around 0.33 m/s.

Then, the influence of water quality was investigated. The applied water was always clear, not contaminated, but in different qualities: 1) tap water, 2) de-ionised water, 3) distilled water and 4) bi-distilled water. The results showed that the water quality did not influence significantly the bubble behaviour in our case (Table 3.3). The average diameter and velocity were nearly the same as measured previously for the different filling heights. Apparently the effect of different ionic content of the water is smaller than the measurement accuracy (see later in Chapter 7).

The next investigated parameter was the pH, since CO_2 mass transfer determination leads to a change in pH. An acidic, a nearly neutral and a basic water solution were tested. As expected, the CO_2 dissolved best in the basic and nearly neutral liquid, so that at pH 12.5 and pH 6 the measured average bubble diameter was only 2.3 mm, compared to the two acidic cases with 2.4 and 2.5 mm (see Table 3.3). In contrast to the diameter, the average velocity showed no measurable differences.

This result is confirmed by the diagram shown for instance in [11] and also later in Figure 3.15, where the difference in the average velocity for bubble sizes between 2.3 and 2.5 mm is extremely small.

Table 3.3: Measurement results showing mean bubble diameters (mm) and mean bubble vertical velocities (m/s).

		Mean bubble diameter [mm]	Mean bubble vertical velocity [m/s]
Filling volume (l)	11.5	2.42	0.33
	9	2.32	0.33
	7	2.38	0.33
	5	2.38	0.34
	3	2.27	0.34
Water quality	1x distilled	2.39	0.31
	2x distilled	2.33	0.33
	de-ionized	2.33	0.33
	tap water	2.28	0.33
pH	12.48, raised with NaOH	2.33	0.33
	6	2.30	0.33
	3.8, decreased with HCl	2.41	0.33
	4, decreased with CO_2	2.54	0.33
Gas flow rate (l/h)	3.5	2.25	0.33
	5	2.45	0.33
	7.5	2.86	0.31
	10	3.06	0.31

The last parameter varied was the gas flow rate. Different values were set by a variable-area flow-meter (Yokogawa). The lowest investigated flow rate was 3.5 l/h, because this is the lowest flow rate, where the four nozzles still produced regular bubbles. Table 3.3 and even more Figure 3.4 and Figure 3.5 show that the flow rate has a large impact on bubble size and velocity. The higher the flow rate, the larger is the bubble diameter, but also the broader is the bubble size distribution (BSD).

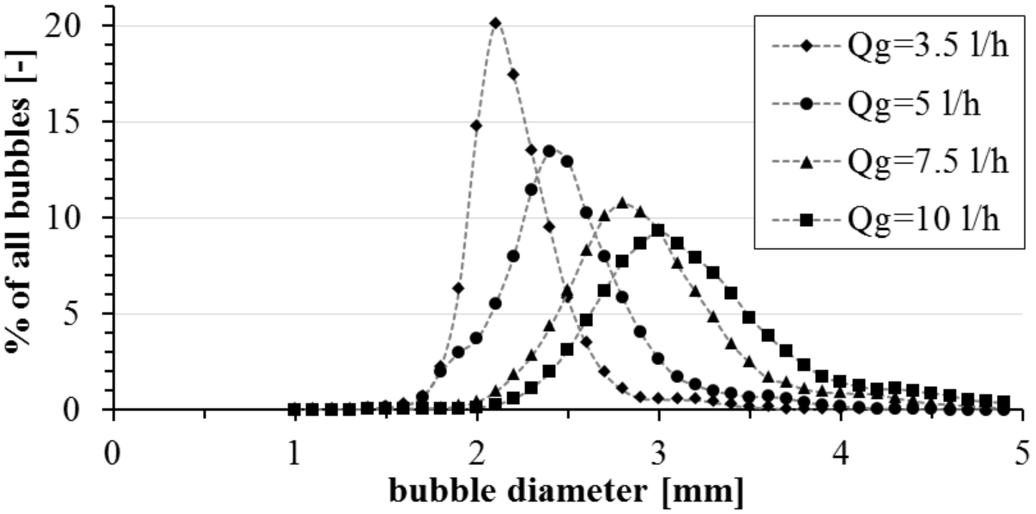

Figure 3.4: Bubble size distribution (BSD) as function of gas flow rate. From [8].

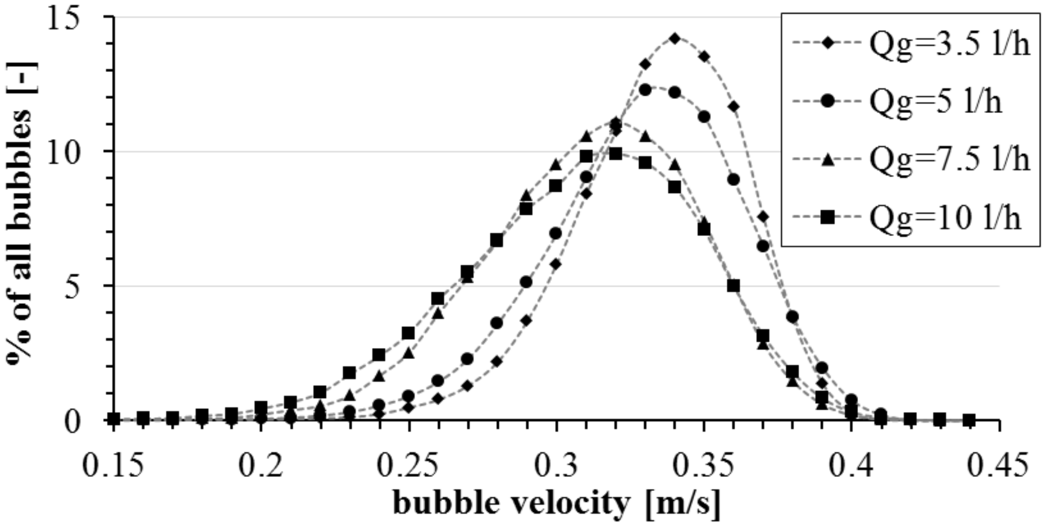

Figure 3.5: Bubble velocity distribution as function of gas flow rate. From [8].

Concerning the velocity distribution, the effect is naturally inversed: the smaller bubbles induced by a low flow rate show higher velocities with a narrower velocity distribution (Figure 3.5). The higher the flow rate, the broader the velocity distribution.

Summarizing these results, it appears that only the gas flow rate has a pronounced influence on the velocity and size distributions of the bubbles in the investigated bubble column. The value of the pH influences bubble size, but only in a very slight manner (less than 10% relative difference) and has thus no noticeable impact on bubble velocity. All other operating parameters do not influence the bubble sizes and velocities at all (Table 3.3).

3.4. Influence of viscosity and surface tension on bubble characteristics

As it was proved during the previous measurement campaign, from the investigated various flow conditions just the change of the gas flow rate showed noticeable impact on the bubble characteristics. For this reason, in the next step the influence of surface tension and viscosity on bubble size, form, motion, and rising velocity at different gas flow rates was investigated extensively. This section is mainly based on a paper published in the International Journal of Multiphase Flow in 2020 [16].

3.4.1. Post-processing of images

During these Shadowgraphy experiments, images were recorded with two cameras almost over the whole height of the bubble column.

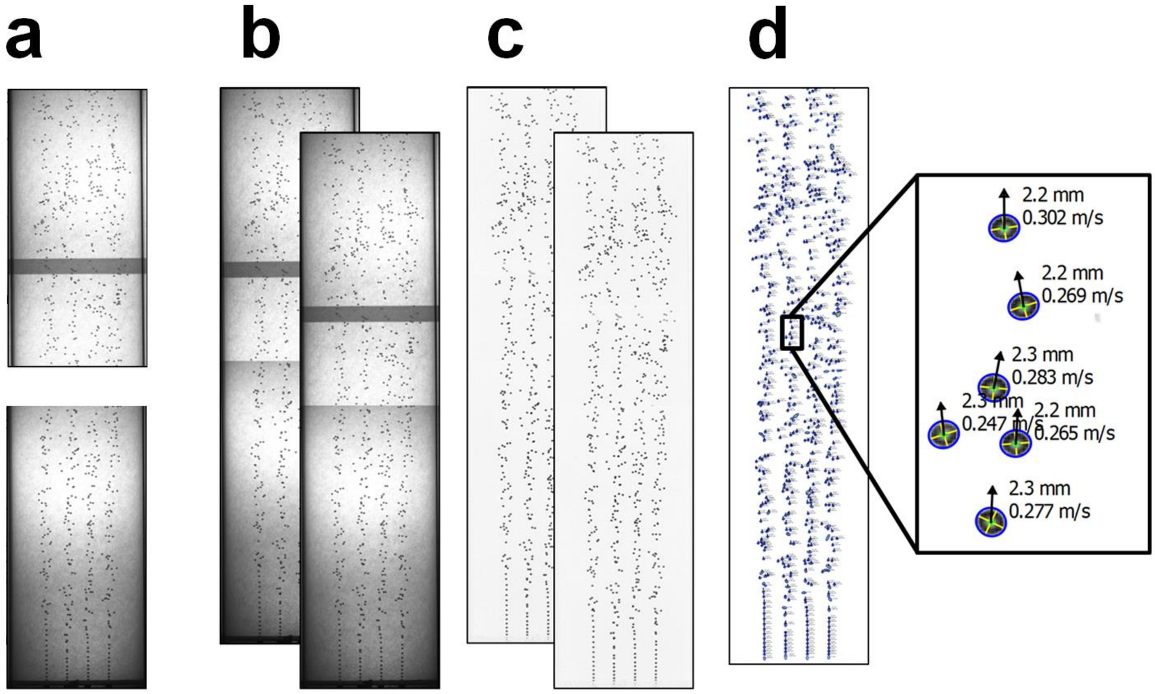

Figure 3.6: Shadowgraphy image processing: a) raw images for the two column sections, b) stitched and subsequent images for velocity determination, c) images after background correction, and d) bubble recognition on the two images (grey and blue) with zoom on six bubbles. From [16].

The main steps of post-processing are shown in Figure 3.6. The acquired raw images from the upper and lower section (Figure 3.6, a) were stitched together and double-frame images were created with the subsequent image, in order to be able to calculate the bubble displacement between the two images (Figure 3.6, b). From the calculated displacement in pixels, the bubble velocity was obtained in m/s through a geometric calibration. For the purpose of better bubble recognition and to supress background lightening inhomogeneities (dark band in Figure 3.6 a and b), these images were divided by a pre-recorded background image without bubbles (Figure 3.6, c). The resulting bubble recognitions for the two subsequent images are then shown on Figure 3.6, d in blue and grey.

In a further post-processing step, overlapping bubbles and bubble groups were filtered from the raw bubble recognition images by two filters (Figure 3.7, a, raw recognition and Figure 3.7, b, filtered recognition). These filters were obtained from the initially recognized bubble diameters by plotting the histograms and density functions, as can be seen in Figure 3.7 c and d, respectively. The histogram (Figure 3.7, c) shows the occurrence of a second, much smaller peak which is due to the overlapping bubbles, and thus would falsify the calculation of mean bubble sizes. Figure 3.7, shows that these overlapping bubbles appear in all images at relatively small numbers and are distinctly separated from the diameters obtained from single bubbles. Thus, a correct diameter range could be defined for each experimental run that is indicated in Figure 3.7, d by red vertical lines. The lower bound was defined to exclude the rarely occurring recognition of dust particles or other impurities in the image. These bounds had to be determined manually in a case by case manner by visual inspection of the raw bubble recognition images. For the case of elliptical bubbles, a second filter was necessary that took into account the major bubble axis. It was defined in the same manner as the first filter from plots of the major axis. This filter eliminates elliptical bubbles that are superimposed in the vertical direction, and thus are recognized erroneously as spherical bubbles.

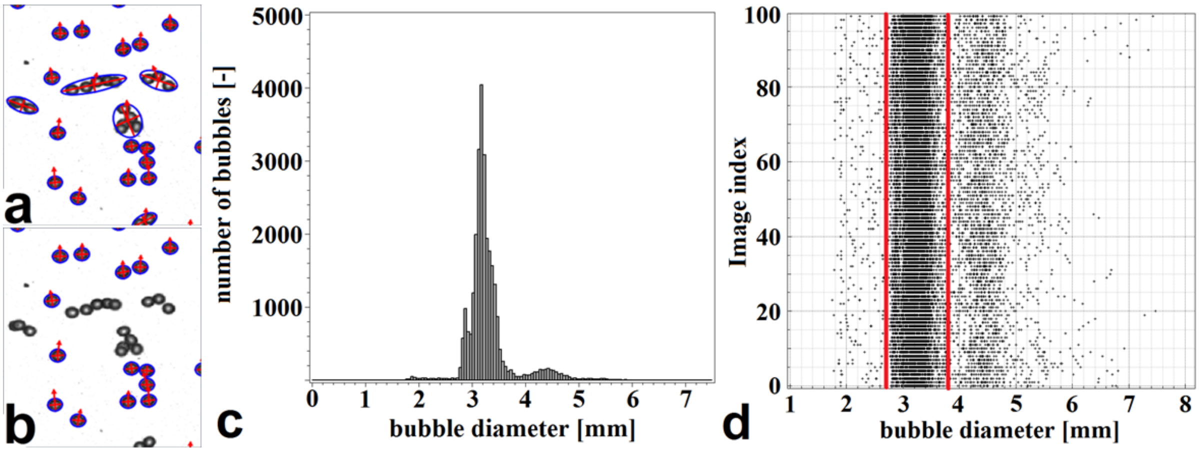

Figure 3.7: Shadowgraphy post-processing: (a) raw bubble recognition, (b) bubble recognition after filtering, (c) bubble diameter histogram for all recognized bubbles in 100 images, and (d) bubble diameter for individual images of the same 100 images. From [16].

3.4.2. Bubble trajectories, diameters and velocities

During the shadowgraphy processing, 4000 images were investigated at each water–glycerol–surfactant–gas flow rate combination, which leads to approximately 2 million recognized bubbles in each setup. Due to the relatively high image resolution, the uncertainty in the recognized bubble sizes and calculated bubble velocities is below 5%. A first impression of the influence of viscosity and surface tension on the bubble aspect and trajectories can be obtained from Figure 3.8, which shows a matrix of instantaneous shadowgraphy images for each of the examined compositions at a flow rate of 6 l/h CO_2. With increasing viscosity and decreasing surface tension, the bubbles become rounder and their paths become straighter and more regular in the lower, developing part of the column. In the upper, equilibrium conditions part, the bubbles become more elliptical and their trajectories change to zig-zagging and helical aspects. Thus, two different regions can be observed in the column and the flow regime becomes pseudo-homogeneous.

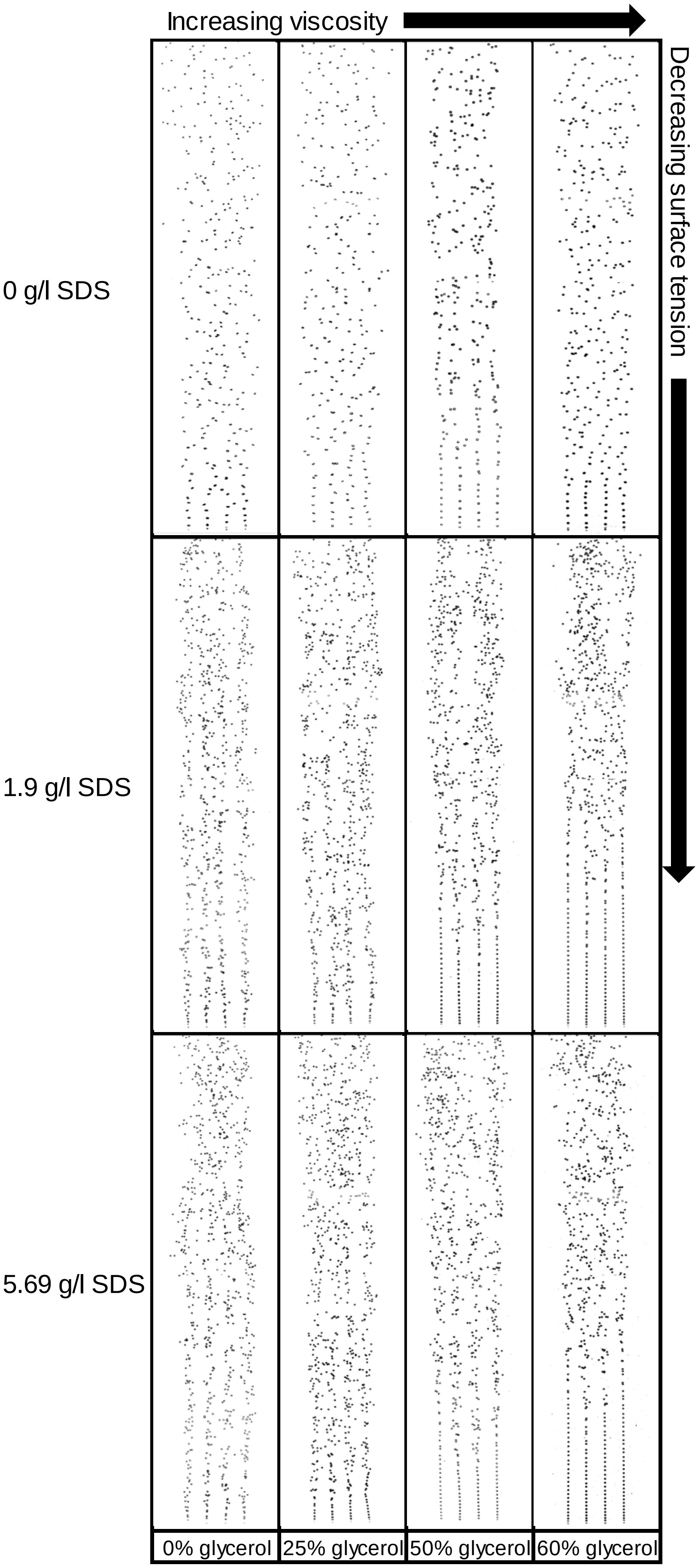

Figure 3.8: Instantaneous shadowgraphy images of the raising bubbles for each viscosity and surface tension condition at 6 l/h gas flow rate. From [16].

When calculating the mean bubble diameters and velocities from these images for each composition, the mean values of Table 3.4 are obtained.

Table 3.4: Mean equivalent sphere diameters and mean velocities for all investigated cases.

	Mean equivalent sphere diameter [mm] / mean bubble velocity [m/s]						
		Surfactant [g/l]					
Gas flow rate [l/h]	Glycerol concentration [m%]	0		1.9		5.69	
4							
	0	2.49	0.31	2.20	0.23	2.17	0.23
	25	2.63	0.31	2.36	0.23	2.27	0.23
	50	2.86	0.25	2.46	0.26	2.39	0.26
	60	2.86	0.24	2.52	0.28	2.45	0.28
6							
	0	2.70	0.31	2.42	0.24	2.32	0.23
	25	3.06	0.30	2.52	0.24	2.43	0.23
	50	3.28	0.26	2.67	0.24	2.58	0.24
	60	3.14	0.27	2.70	0.25	2.64	0.25
8							
	0	2.83	0.30	2.61	0.25	2.60	0.24
	25	3.47	0.30	2.73	0.25	2.66	0.24
	50	3.54	0.27	2.82	0.25	2.74	0.25
	60	3.36	0.28	2.86	0.25	2.79	0.25

The bubble diameter is presented here as the equivalent sphere diameter (ESD) and was calculated from the minor and major axis of the spheroid:

$$ESD = \sqrt[3]{\frac{3V_B}{4\pi}} \cdot 2\,, \tag{3.1}$$

$$V_B = \frac{4}{3}\pi b^2 c, \tag{3.2}$$

where V_B is the volume of the spheroid, b is the major semi-axis, and c is the minor semi-axis.

The results show that with increasing gas volume flow, the bubble size is increasing (Figure 3.9, a), as well as with an increasing viscosity (Figure 3.9, b) and surface tension (Figure 3.9, a and c). Only a slight decrease of the diameter can be recognized at 60% glycerol in the case where no surfactant was added to the mixture (Figure 3.9, b and d). Additionally, the bubble size does not change significantly between 50% and 60% glycerol (Figure 3.9, c). A significant change is noticeable for the bubble size between the measurements with and without surfactant, but the increase of surfactant concentration only has small influence on the bubble size (Figure 3.9, d).

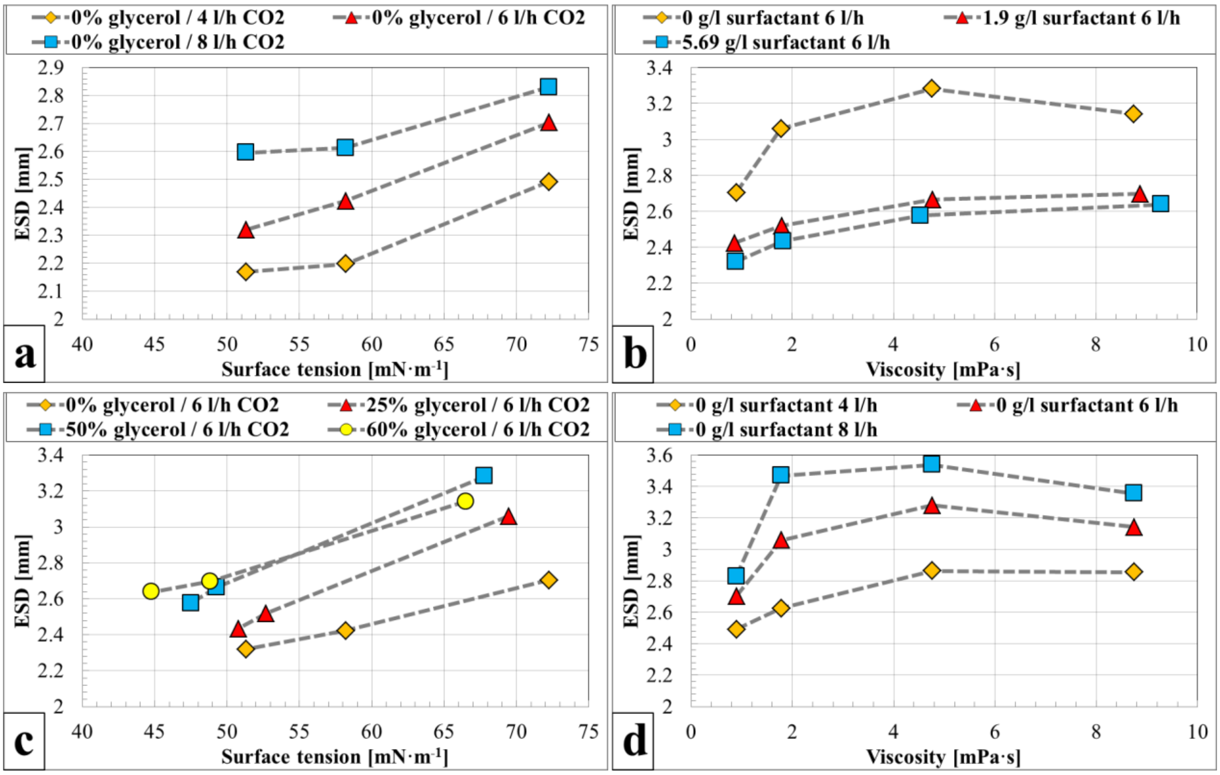

Figure 3.9: Equivalent sphere diameter (ESD): (a) as a function of surface tension for different flow rates without glycerol, (b) as a function of viscosity for different flow rates without surfactant, (c) as a function of surface tension for different glycerol concentrations at 6l/h, and (d) as a function of viscosity for different SDS concentrations at 6 l/h.

When investigating the bubble size distributions (Figure 3.10 and Figure 3.11), important differences can also be recognized depending on the viscosity and surface tension. While the bubble diameter distribution in compositions without glycerol and surfactant shows a distribution with large standard deviation (squares on Figure 3.10, a), an increase of viscosity (Figure 3.10, a) or decrease of surface tension (Figure 3.10, b) leads to a narrowing of the bubble size distributions. These results also show that with decreasing surface tension, the mean bubble diameter and distribution width is considerably reduced, while increasing the viscosity results in the distribution of the bubbles becoming narrower but the average bubble size growing.

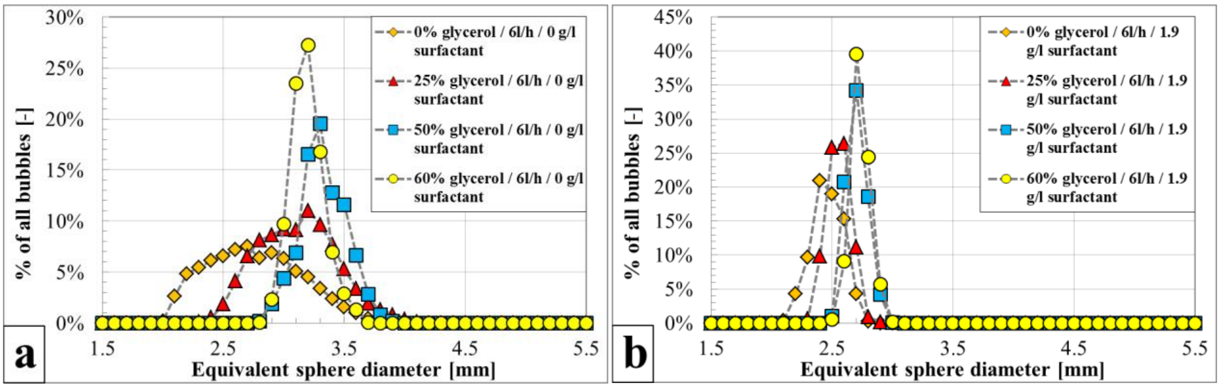

Figure 3.10: Bubble ESD distributions at different glycerol concentrations without (a) or with (b) surfactant at 6 l/h gas volume flow rate.

Although no coalescence was observed in the investigated cases, another effect, namely bubble shrinkage due to the dissolution of CO_2 in the liquid, has an influence on the above presented mean bubble diameters and bubble size distributions. To demonstrate this effect, bubble diameters were averaged in an 11mm high slice along the diameter x and at different heights of the bubble column (the origin of the coordinate system is the top of the nozzles) (Figure 3.11).

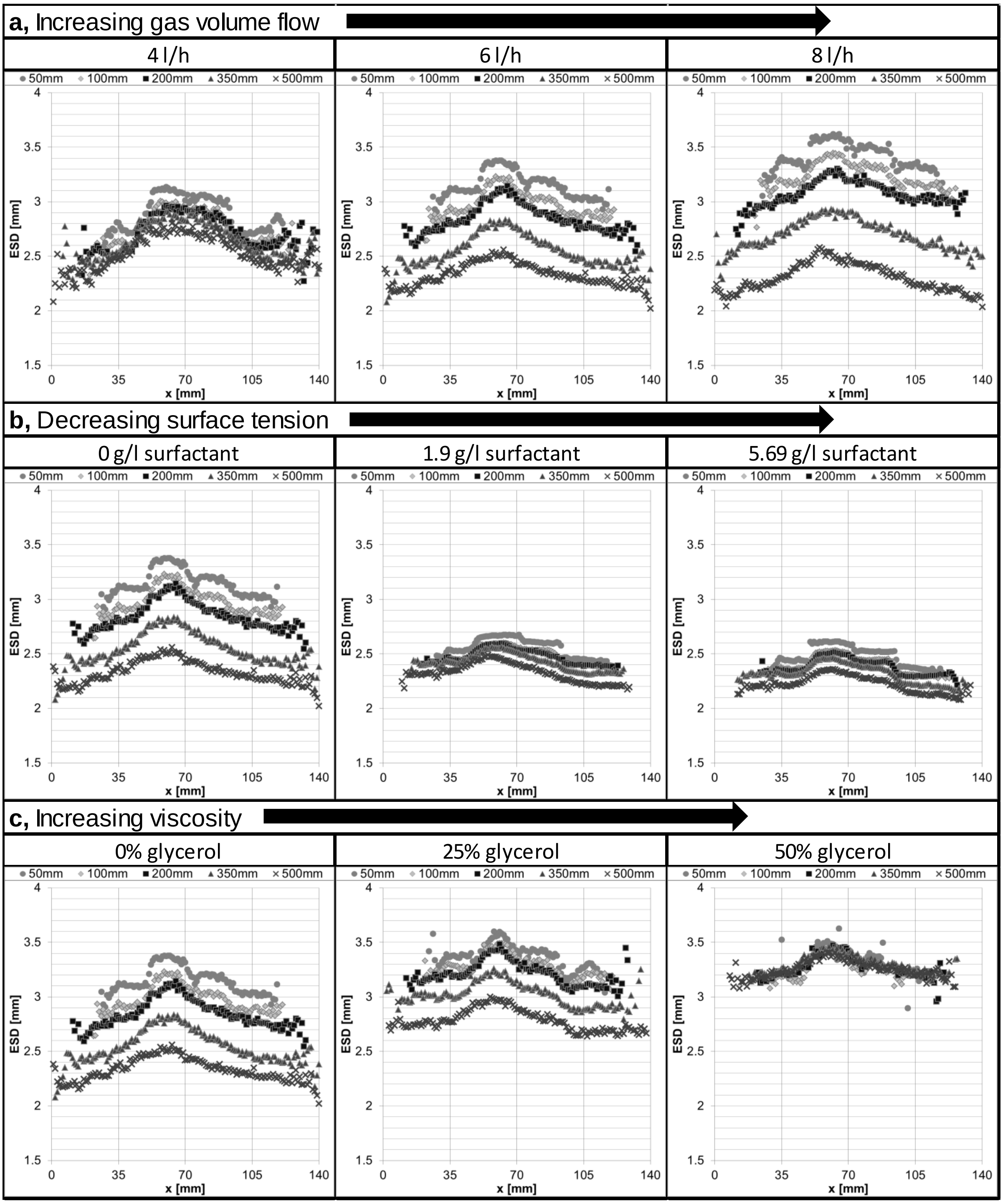

Figure 3.11: Bubble diameter profiles at different heights for different gas volume flows (a), with 0.9 mPa·s viscosity and 72.24 mN/m surface tension (0% glycerol), (b) different surfactant concentrations with 0% glycerol at 6 l/h flow rate, and (c) different glycerol concentrations at 6 l/h flow rate with 72.24 mN/m; 69.45 mN/m; 67.81 mN/m surface tensions. From [16].

With increasing gas volume flow rate, the bubbles shrink in a stronger fashion (Figure 3.11, a). While the difference in the mean bubble size between the top and the bottom investigated areas is just 12.5% at 4 l/h gas volume flow, this difference is growing to 26.1% at 6 l/h gas volume flow and reaches 32.6% at 8 l/h. When varying surface tension at a 6 l/h gas flow rate, the initial 26.1% mean diameter difference without surfactant is decreasing with an addition of 1.9 g/l and 5.69 g/l surfactants to 9.2% and 10.5%, respectively (Figure 3.11, b). In the third analysed case, with increasing viscosity, bubble shrinkage is decreased from the initial 26.1% to 17.3% and 4.8% for the 25% and 50% glycerol solutions, respectively (Figure 3.11, c). It was also observed that at higher glycerol concentrations (50% and 60%), bubble shrinkage remains below 5% at different gas flow rates, as well as at different surface tensions. These findings are a first indication of reduced mass transfer rates from the bubble to the liquid at higher viscosities and lower surface tensions.

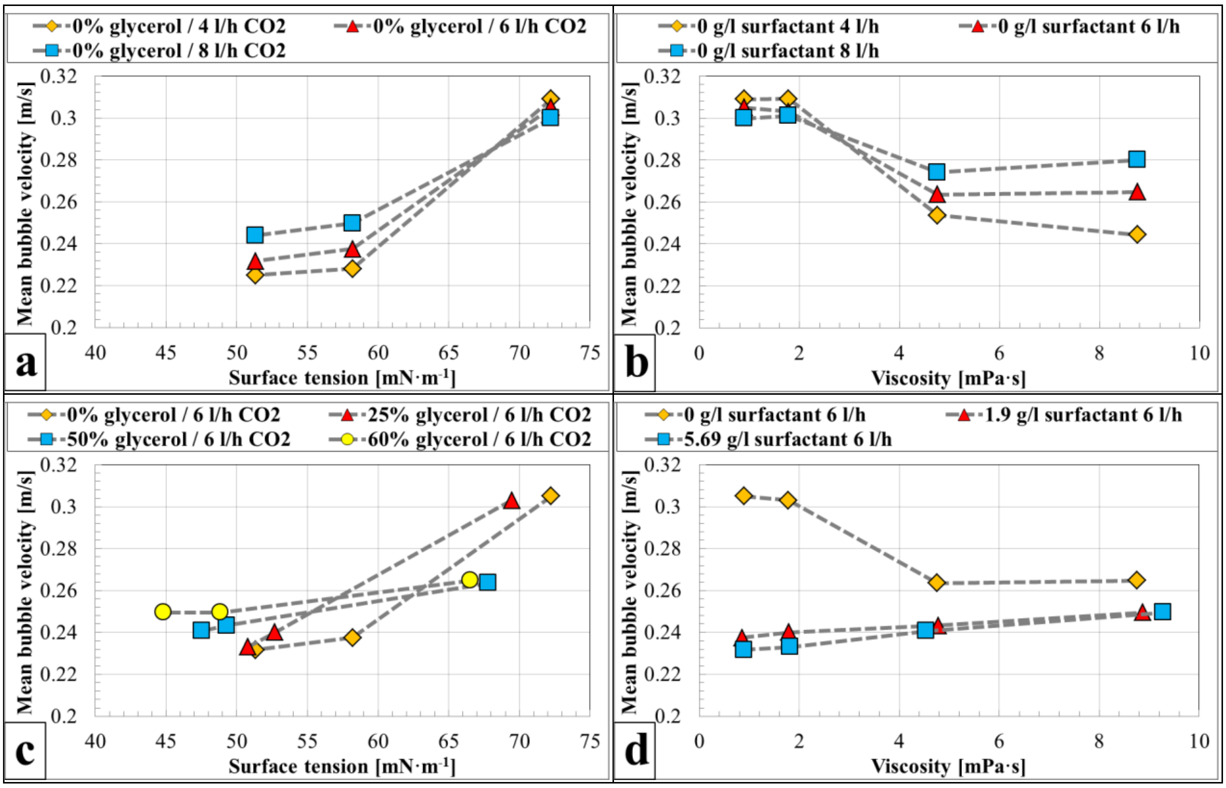

Figure 3.12: Mean bubble velocity as a function of surface tension (a) for different flow rates without glycerol, (b) as a function of viscosity for different flow rates without surfactant, (c) as a function of surface tension for different glycerol concentrations at 6l/h, and (d) as a function of viscosity for different SDS concentrations at 6 l/h.

The bubble velocities corresponding to the investigated cases and obtained from two subsequent images of the different experimental series are shown in Figure 3.12 to Figure 3.14. With an increasing gas volume flow rate, the mean bubble velocity is increasing, as well as with an increasing surface tension (Figure 3.12, a). However, at the highest surface tension in pure water the effect of the flow rate (although not very strong) on bubble size is reversed. Growing viscosity leads to a decrease of the mean velocity (Figure 3.12, b), although this effect is not strong between 0%-25% glycerol and 50%-60% glycerol concentrations. These findings support the results of [134], who also found different behaviour for solutions with viscosity lower or higher than 4.25 mPa·s. It is also observable that the effect of the surfactant is decreasing with increasing viscosity (Figure 3.12, c). Higher surfactant concentration always leads to lower bubble velocity for all examined viscosities (Figure 3.12, d), but with only minor changes at high surfactant concentrations.

The considerable mean velocity change of the bubbles at different surface tensions and viscosities can also be analysed from the velocity distributions in Figure 3.13. With increasing viscosity, the velocity distributions show similar aspects, but the peak of the distribution is shifted at 50% and 60% glycerol concentrations from 0.31 m/s to 0.26 m/s, respectively (Figure 3.13, a). Additionally, with an addition of surfactant (1.9 g/l SDS, Figure 3.13, b) the peak is progressively shifted to smaller velocities. At 50 % and 60% glycerol content, the monodisperse distribution turns into a polydisperse distribution with two separate peaks. This distribution exactly describes the phenomena which can be seen in Figure 3.8, namely that two different bubble behaviours exist at these surface tensions and viscosities: the straight upward rising bubbles in the bottom section of the bubble column with higher velocity, and the wobbling bubbles in the centre and top section with lower velocity.

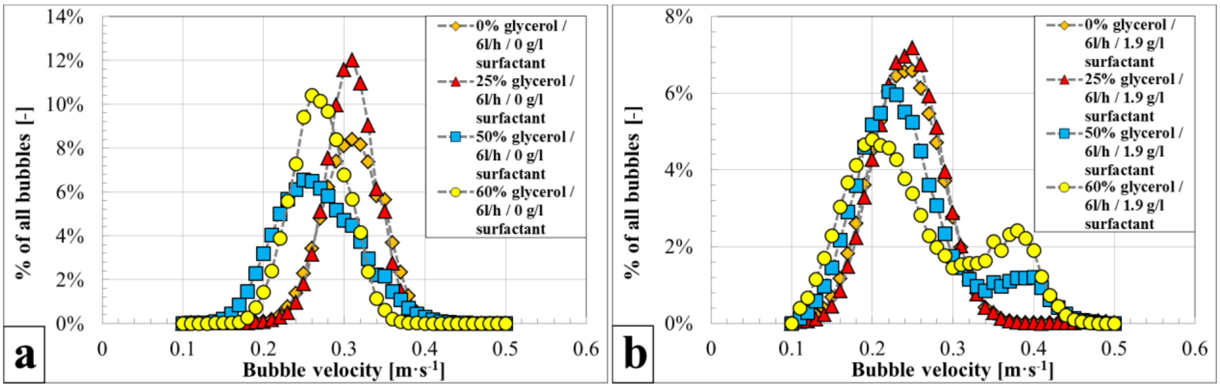

Figure 3.13: Bubble velocity distributions for different glycerol concentrations (a) without surfactant, and (b) with 1.9 g/l surfactant at 6 l/h gas volume flow rate.

In addition to the bubble diameters, velocities were averaged in 11 mm high slices along the diameter of the bubble column at five different heights (Figure 3.14). With an increasing gas flow rate, the bubble velocities are almost the same at different heights in the column. It is only at 350 mm and 500 mm that a slight decrease can be observed with a rising gas flow rate (Figure 3.14, a). With addition of the surfactant, a noticeable drop of the velocity can be seen throughout the column, but almost no difference exists for the two different surfactant concentrations (Figure 3.14, b). With increasing viscosity, the velocity becomes slightly lower, and at 25 % glycerol the differences between the different heights become smaller. At 50 % glycerol concentration, four velocity peaks are visible up to 100 mm. These correspond to the position of the inlet nozzles in the bubble column. From 200 mm these peaks disappear, the bubble velocity profile smoothens out, and velocities become smaller due to the wobbling motion of the bubbles (Figure 3.14, c).

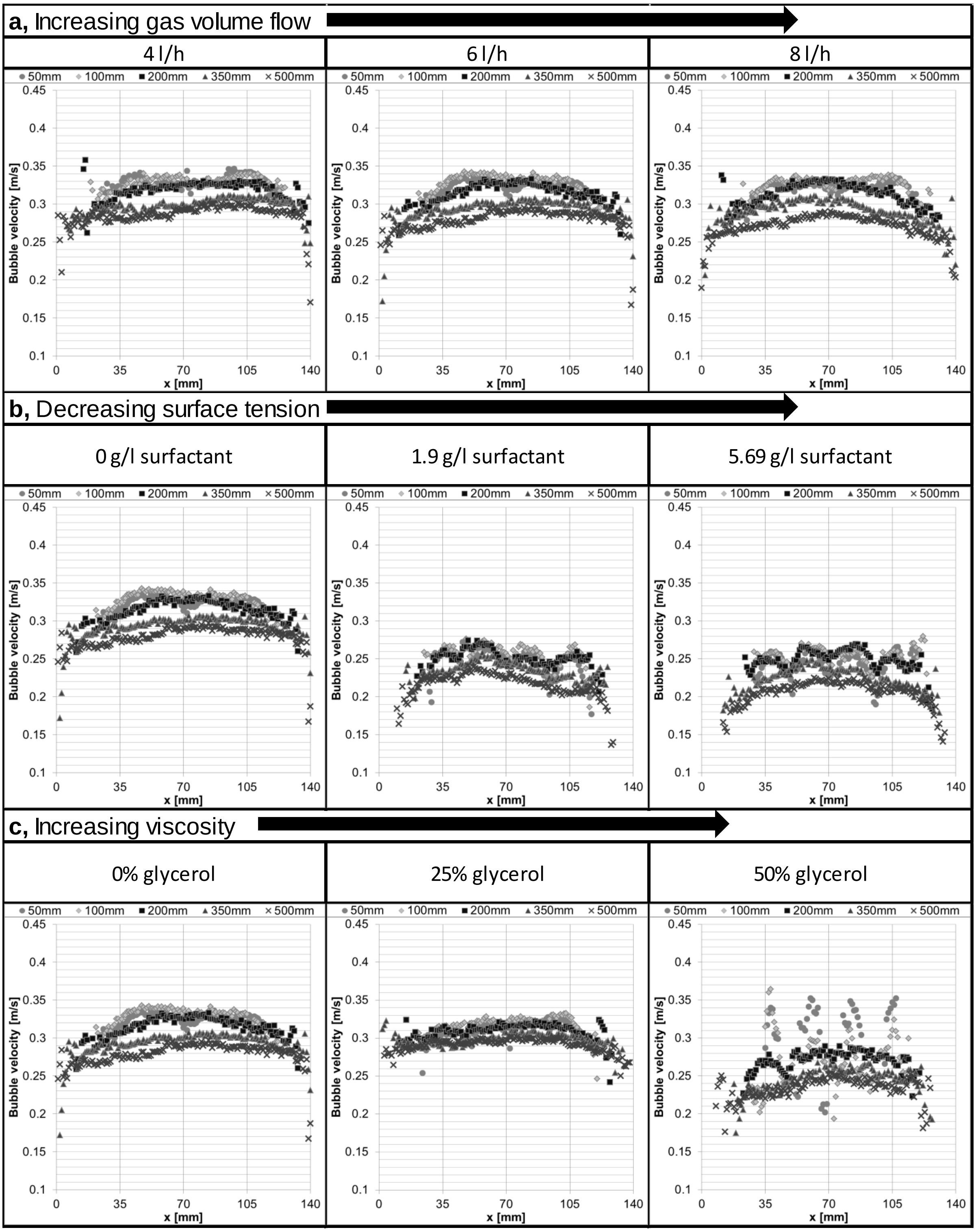

Figure 3.14: Bubble velocity profiles in the bubble column at different gas volume flow rates (a), with 0.9 mPa·s viscosity and 72.24 mN/m surface tension (0% glycerol), (b) different surfactant concentrations with 0% glycerol at 6 l/h flow rate, and (c) different glycerol concentrations at 6 l/h flow rate with 72.24 mN/m; 69.45 mN/m; 67.81 mN/m surface tensions. From [16].

3.4.3. Comparison with known correlations

The bubble velocities described above are measured in a bubble curtain of CO_2, and not from single air bubbles in a quiescent liquid. Therefore, these velocities include both, the effect of the bubble interaction in the curtain, and the bubble-induced liquid motion. For comparison with the well-known correlations from Clift et al. [11], Tomiyama et al. [12], and Ishii and Zuber [13], for the terminal velocity of single air bubbles in a stagnant liquid and for comparison with experimental data from Bryn [9], Haberman et al. [10], and Maxworthy et al. [160], the bubble velocities measured here have to be corrected. The slip or relative bubble velocity can be derived from the equation:

$$u_S = u_B - \overline{v_y}, \tag{3.3}$$

where the slip velocity u_S is the difference of the measured bubble velocity, u_B, from the shadowgraphy experiments and the mean vertical liquid velocity, $\overline{v_y}$, from the PIV measurements at the same position (x,y) in the bubble column. The slip velocity was obtained from six different mixtures with 6 l/h gas flow rate, where PIV data was available, at five different heights. The mean slip velocities for each height are presented in Table 3.5.

Table 3.5: Mean measured and slip velocity of bubbles at different heights.

6 l/h flow rate	**50 mm**			**100 mm**			**200 mm**			**350 mm**			**500 mm**		
	u_b [m/s]	**u_s [m/s]**	diff. [%]	u_b [m/s]	**u_s [m/s]**	diff. [%]	u_b [m/s]	**u_s [m/s]**	diff. [%]	u_b [m/s]	**u_s [m/s]**	diff. [%]	u_b [m/s]	**u_s [m/s]**	diff. [%]
0% Glycerol-water	0.325	**0.295**	9.2	0.328	**0.29**	11.6	0.313	**0.284**	9.3	0.291	**0.266**	8.6	0.278	**0.254**	8.6
0% Glycerol-water 1.9 g/l SDS	0.247	**0.224**	9.3	0.255	**0.223**	12.5	0.25	**0.215**	14	0.233	**0.199**	14.6	0.215	**0.182**	15.3
25% Glycerol-water	0.311	**0.288**	7.4	0.316	**0.284**	10.1	0.309	**0.275**	11	0.297	**0.27**	9.1	0.29	**0.266**	8.3
25% Glycerol-water 1.9 g/l SDS	0.223	**0.197**	11.7	0.248	**0.215**	13.3	0.247	**0.212**	14.2	0.237	**0.202**	14.8	0.223	**0.19**	14.8
50% Glycerol-water	0.31	**0.298**	3.9	0.271	**0.239**	11.8	0.27	**0.231**	14.4	0.244	**0.212**	13.1	0.234	**0.202**	13.7
50% Glycerol-water 1.9 g/l SDS	0.366	**0.355**	3	0.266	**0.246**	7.5	0.234	**0.194**	17.1	0.221	**0.184**	16.7	0.2	**0.168**	16

The result shows, that the slip velocity is decreasing with increasing height in the column and with decreasing surface tension. Further, the average deviation of the slip velocity from the measured bubble velocities is ~11.5% with a standard deviation of 15%. Since for the 4 and 8 l/h gas flow rate no liquid phase velocities were available, this correction factor was applied as well in those cases to estimate the bubble slip velocity. This means, $u_S = u_B * 0.885$ has been used for the cases with 4 and 8 l/h for further comparison in Figure 3.15. This concept should be verified through more detailed investigations in the future.

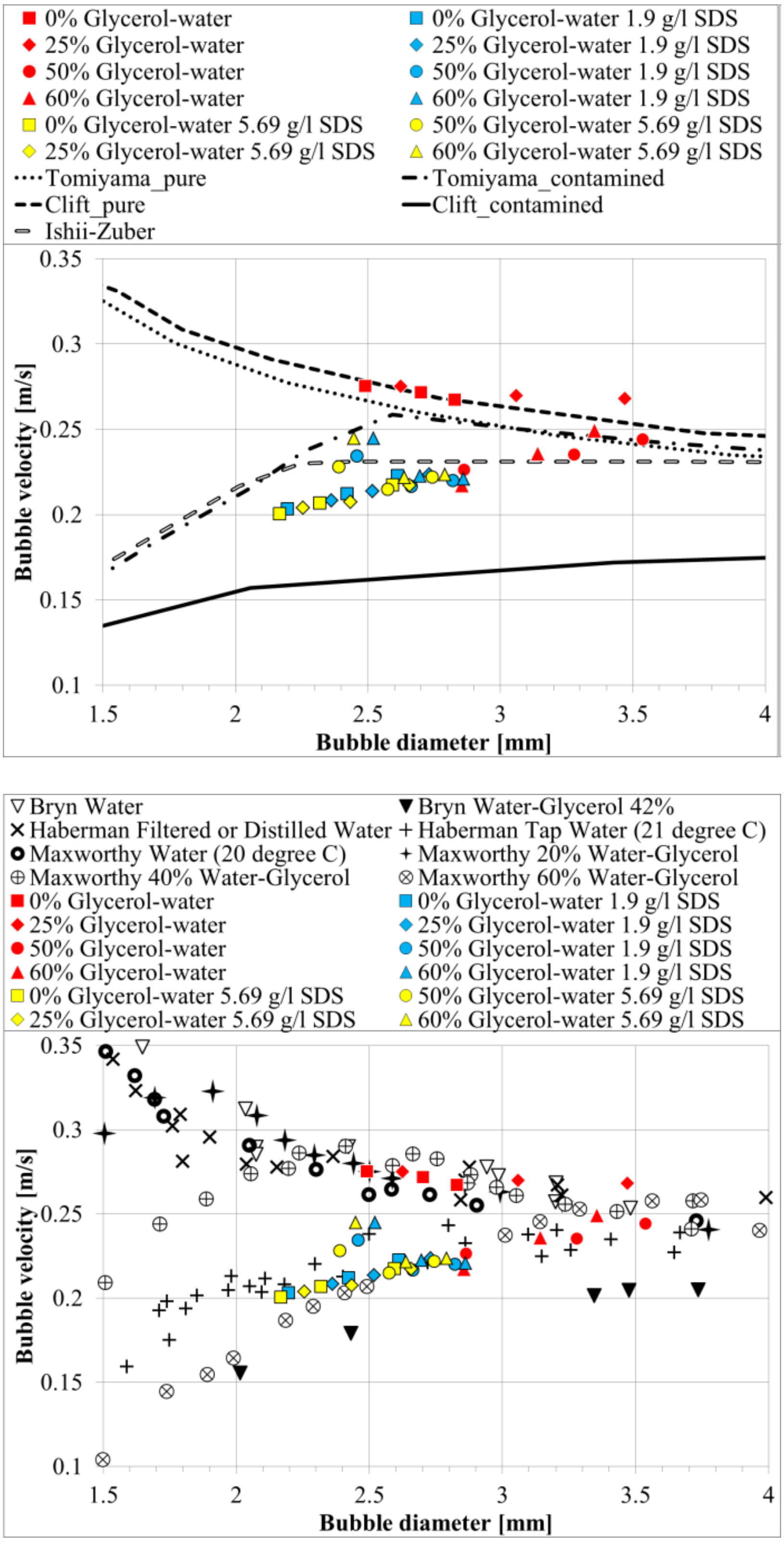

Figure 3.15: Bubble velocity versus bubble diameter: present experimental results (in colour) compared to the correlations of Clift, Tomiyama, and Ishii on the top; compared to experiments from Bryn, Haberman, and Maxworthy at the bottom. From [16].

The comparison with the known correlations (Figure 3.15, left) shows the expected results. The experimentally obtained bubble velocities for pure water fit very well to Clift's correlation for pure water. The results for the glycerol-water mixtures without surfactant show higher velocities than those with SDS and correspond more to the correlations for pure water.

The results for the highest surfactant concentration (lowest surface tension, yellow symbols in Figure 3.15, left) are below the correlations of Ishii-Zuber and Tomiyama for contaminated water, but above Clift's correlation for contaminated water. Although the experimental results from the literature (Figure 3.15, right) are quite dispersed, the bubble velocities obtained here fit very well in this point cloud. The velocities for the mixtures without and with 25% glycerol, but without surfactants, lie in the range of the data reported by Bryn, Habermann, and Maxworthy for clear water. The 50% and 60% water-glycerol mixture results, as well as all mixtures with surfactant, show a good agreement with the data from Maxworthy for a 60% water-glycerol mixture.

3.4.4. Dimensionless correlations

From the aforementioned bubble variables, Eötvös, Reynolds and Morton numbers can be derived. The results are plotted in a diagram originally proposed by Grace [14] (Figure 3.16).

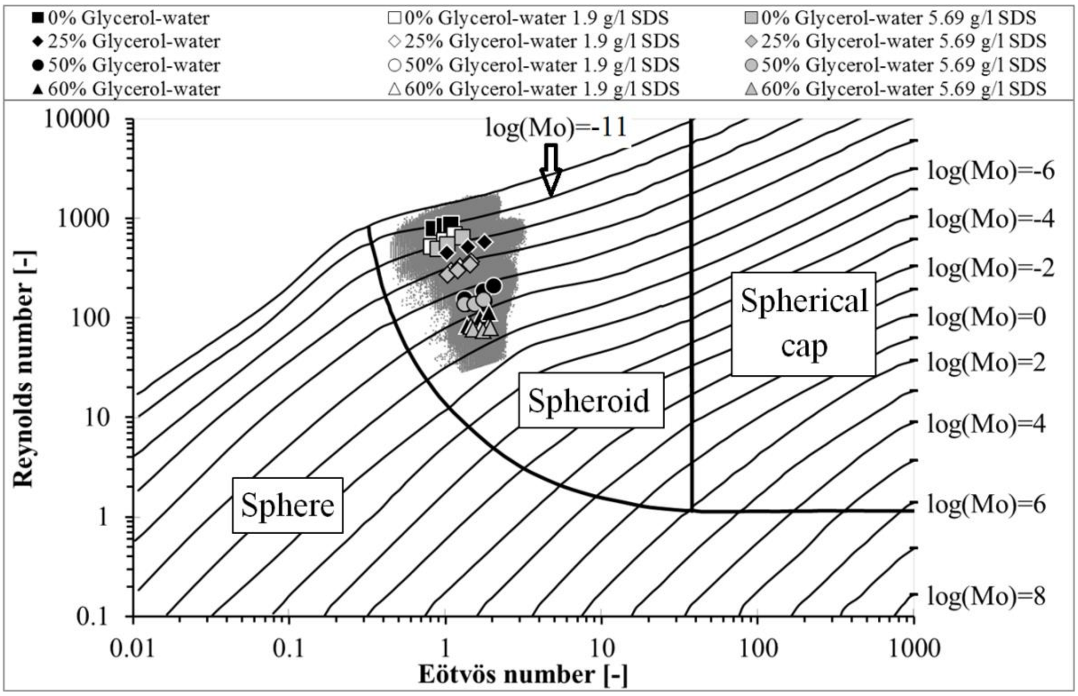

Figure 3.16: Mean experimental results (symbols) and complete investigated region (grey cloud) on bubble shape regime map from Grace. From [16].

As expected and found by other researchers before, e.g. Ziegenhein et al. [93], the present experimental results of the 0% Glycerol-water mixtures lay on the log(Mo)=-11 isoline. With an addition of surfactant or increasing viscosity, the Morton number increases, while the Reynolds number decreases with increasing viscosity and the measured points are shifted downwards. It can be observed, that the influence of the surface tension is rather weak. Between the mean experimental results with 1.9 and 5.69 g/l SDS this difference is so small that the used symbols are overlapping. The change of liquid viscosity leads to a much stronger change of Reynolds, Morton and Eötvös numbers. All investigated cases are situated in the Spheroid region of the diagram, even for the high viscosity and low surface tension cases. In fact, a detailed analysis of the aspect ratio of the "spherical" bubbles in the lower part of the column shows a smaller vertical, than horizontal axis for these cases and thus "spheroid" behaviour. Also, the frontier between "Sphere" and "Spheroid" appears too sharply in the diagram.

Finally, unambiguous influence of the bubble size and velocities on the gas holdup can be found, when investigating the gas holdup in the bubble column at different conditions (Figure 3.17 and Figure 3.18). To this end, from the calculated spheroid volumes, V_B, the gas holdup, ε_G, can be expressed as follows:

$$\varepsilon_G = \frac{V_G}{V_L + V_G}\,, \tag{3.4}$$

$$V_G = \overline{\sum V_B}\,, \tag{3.5}$$

where $\sum V_B$ is the total volume of all recognized bubbles on one simultaneously recorded image pair (top and bottom part of the column) and $\overline{\sum V_B}$ is the mean total volume of bubbles calculated from the 4000 instantaneous recordings.

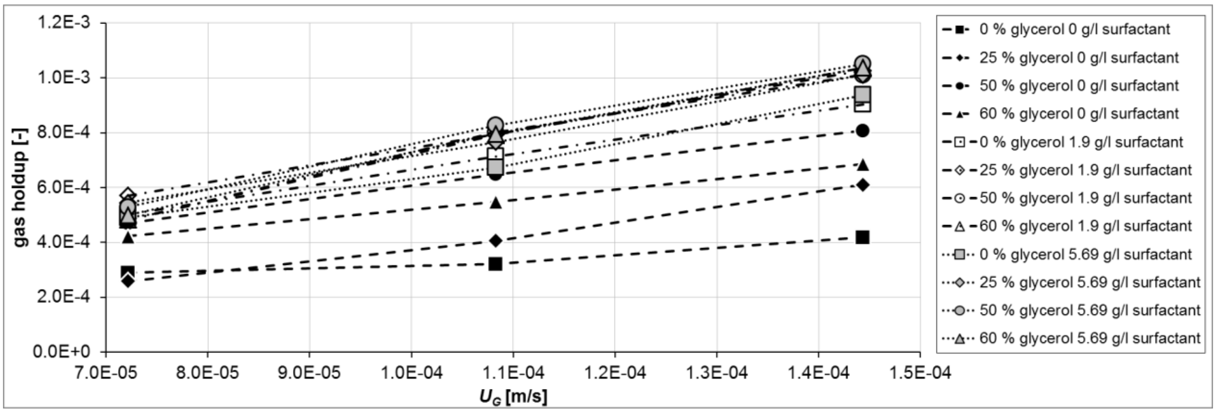

Figure 3.17: Gas holdup in function of superficial gas velocity for all investigated cases. From [16].

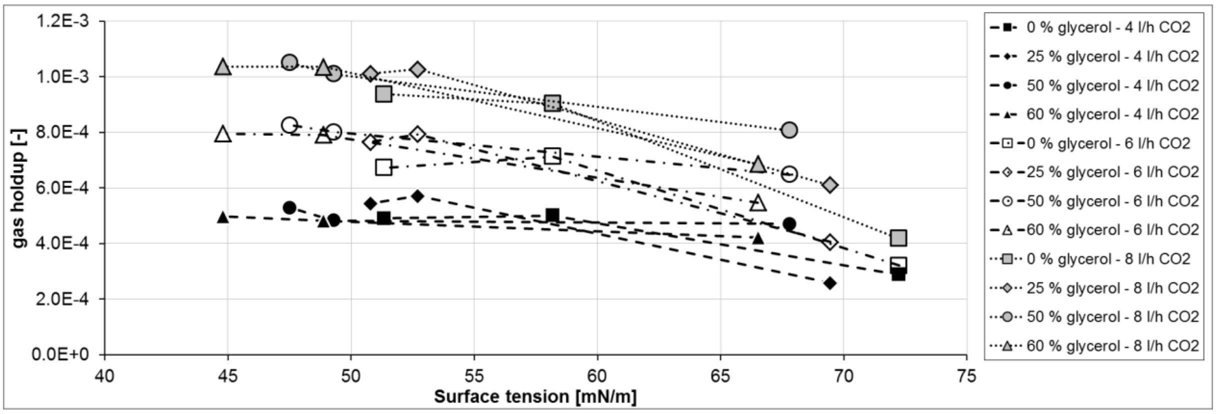

Figure 3.18: Gas holdup in function of surface tension for all investigated cases. From [16].

As expected, the gas holdup increases with increasing gas flow rate/superficial velocity (Figure 3.17). In the presence of surfactant, the bubble size and velocity decreases. For this reason, the residence time of the bubbles in the bubble column increases and the overall gas holdup becomes higher (Figure 3.17). This can also be seen more explicitly in Figure 3.18, where with increasing surface tension, the gas holdup drops. The influence of viscosity is much less pronounced, especially at low surface tension. For the case without surfactant, a tendency to higher gas hold up with higher viscosity is visible, but inverses between 50 and 60% glycerol content.

In conclusion, it can be said that the bubble sizes decrease with decreasing viscosity and decreasing surface tension. The addition of surfactant or glycerol (which constitutes a contamination), causes decreasing bubble velocities. The decreased bubble velocity further leads to a higher gas holdup and a longer contact time, which could enhance mass transfer in the bubble column. But on the other hand, with additives the bubble shrinkage drastically decreases, which indicates a reduced mass transfer from the CO_2 bubbles into the liquid.

From the above presented experiments the essential properties of the bubbly flow can be gathered and used to describe the effect of bubble size and velocity on the liquid flow through the Flow number *F*. This dimensionless number was first introduced by Abou-El-Hassan in 1983 [161]. It is a combination of the well-known Reynolds-, Weber- and Eötvös-numbers, and can be obtained from the variables associated with bubble motion through the pi-theorem. All these parameters have been changed during the experiments. This section has been presented in a paper in the International Journal of Multiphase Flow in 2020 [16]

The *F*-Number is defined as:

$$F = g \cdot \Delta\rho \cdot \left(\frac{ESD^{8/3} \cdot \rho_l{}^{2/3}}{\mu^{4/3} \cdot \sigma^{1/3}}\right) = E\ddot{o} \cdot \left(\frac{Re^{4/3}}{We^{2/3}}\right), \text{ where} \tag{3.6}$$

$$Re = \frac{u_S \cdot ESD \cdot \rho_l}{\mu_l}, \tag{3.7}$$

$$E\ddot{o} = \frac{g \cdot (\rho_l - \rho_g) \cdot ESD^2}{\sigma}, \tag{3.8}$$

$$We = \frac{u_S^2 \cdot ESD \cdot \rho_l}{\sigma}, \tag{3.9}$$

with the density difference *Δρ* between liquid and gas, the equivalent bubble diameter *ESD* (m), the liquid density ϱ_l, dynamic viscosity *μ*, and surface tension *σ*.

Figure 3.19 shows the development of the Flow number with the vertical position in the bubble column. There exists an obvious difference between the curve of pure water (black squares) and the development of those of all the other mixtures.

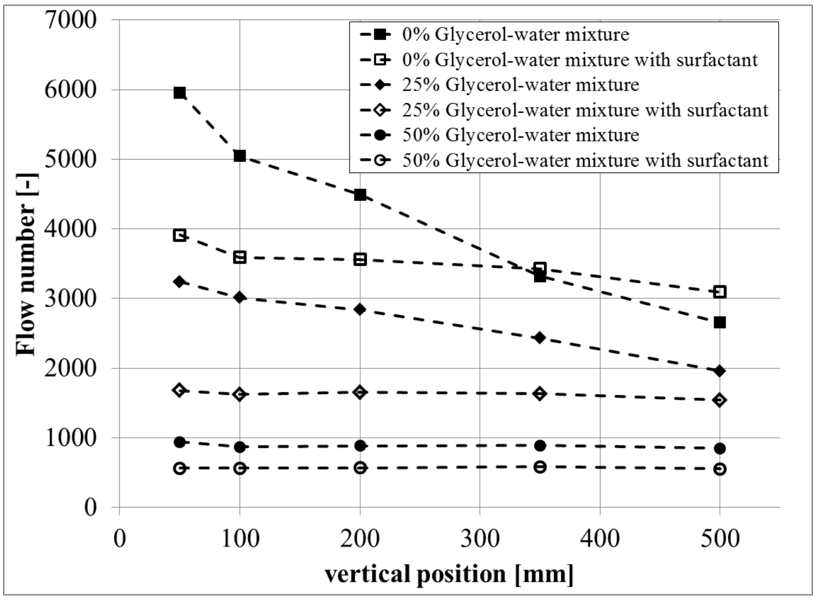

Figure 3.19: Flow number in the bubble column at different heights and in different mixtures. From [16].

It is the steepest and decreases to about half the initial value at the bottom of the column. This effect is due to the highest bubble shrinkage and bubble velocity change throughout the column compared to the other cases. Because of these changes, the vertical liquid velocity was noticeably changed as well. The mixture with 25% glycerol also shows a slope between the column bottom and surface, but less steep due to the smaller bubble shrinkage. The solutions with surfactant, as well as the highest glycerol content examined, induce a nearly constant Flow number throughout the column. It means, that in these cases bubble shrinkage was not significant. For this reason, the profiles of vertical liquid velocity at different heights (see later in subsection 5.3.2, Figure 5.10) are almost identical in these cases.

Abou-El-Hassan also proposed a generalized correlation between Flow number F and Velocity number V, which is defined as:

$$V = u_s \cdot \left(\frac{ESD^{2/3}\rho^{2/3}}{\sigma^{1/3}\mu^{1/3}}\right) = (Re \cdot We)^{1/3}. \tag{3.10}$$

This correlation reads:

$$V = 0.75 \cdot (logF)^2, \tag{3.11}$$

and has been extended by Rodrigue [162] to form:

$$V = \frac{F}{12+0.049 \cdot F^{3/4}}. \tag{3.12}$$

In Figure 3.20, the experimentally obtained Velocity and Flow numbers were compared to these two correlations. The agreement is rather good. The values for the mixtures without surfactant are close to the curve of Rodrigue, whereas the results for the solutions with surfactant show a different behaviour.

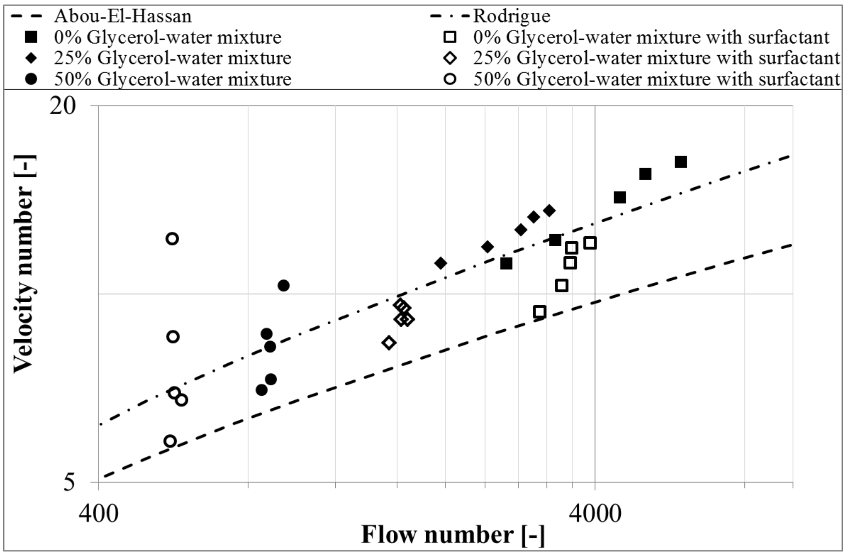

Figure 3.20: Experimentally determined Velocity numbers and Flow numbers compared to the correlations of Rodrigue and Abou-El-Hassan. From [16].

Results without surfactant are spread around the correlation and more or less follow its slope. Points measured with surfactant are arranged nearly vertically, which means that their Flow numbers do not change significantly with Velocity number. This can be explained by the bubble sizes, which do not change significantly throughout the column in the cases with surfactant. The highest Velocity numbers for each mixture were calculated with the bubble velocities and diameters from the bottom segment of the bubble column. Here, the bubbles and their velocities are the biggest. The lowest Velocity number in each mixture can be found in the top segment of the bubble column, where the bubbles are the smallest and occupy the whole column diameter, and therefore have reduced velocities. These findings indicate, that both correlations, from Abou-El-Hassan and Rodrigue, are not sufficiently taking into account the effect of bubble shrinkage and associated bubble velocity change inside the column.

3.5. Bubble shape in bubble swarms

This subsection deals with the further analysis of the bubble data, obtained from the above experiments to analyse and predict bubble shapes and behaviours in bubble swarms or to calculate the mass transfer at different flow conditions.

3.5.1. Bubble shape in bubble swarms

The shape of the bubbles is one of the most important parameters in bubbly flows, because it plays a very important role in the determination of mass transfer. In addition, the bubble shape determines the motion of the bubble, which has an effect on the wake behaviour and thus also on mass transfer. For this reason, a quantitative description of the bubble shape is essential [11, 14].

The shape of the bubble can be described quantitatively with the bubble aspect ratio, E or with the eccentricity χ:

$$E = \frac{2c}{2b} \ , \ \ 0 \leq E \leq 1 \tag{3.13}$$

$$\chi = \frac{2b}{2c} = \frac{1}{E} \ , \ \ \chi \geq 1 \tag{3.14}$$

where b is the semi-major and c the semi-minor axis of the bubble.

To describe the bubble shape quantitatively, a large number of correlations have been developed by correlating the aspect ratio E or eccentricity χ to different dimensionless numbers. In these correlations the researchers proposed to correlate the aspect ratio among others to *Eö* [163], to *We* [164] or to *Ta* [165]. Other researchers have chosen a combination of several dimensionless numbers [166-168].

Some of these studies are based on single bubble experiments in quiescent liquids. For this reason, the applicability and accuracy of the proposed correlations in bubble swarms is questionable. Therefore, new correlations are developed in the following, based on the present experimental bubble data.

To this end, the bubble data has to be processed differently and the major and minor axis of all bubbles have been determined. This shows, that for bubbles with the same equivalent diameter, the measured aspect ratio is not unique (Figure 3.21, a). This means that bubbles with the same equivalent sphere diameter can have different shapes.

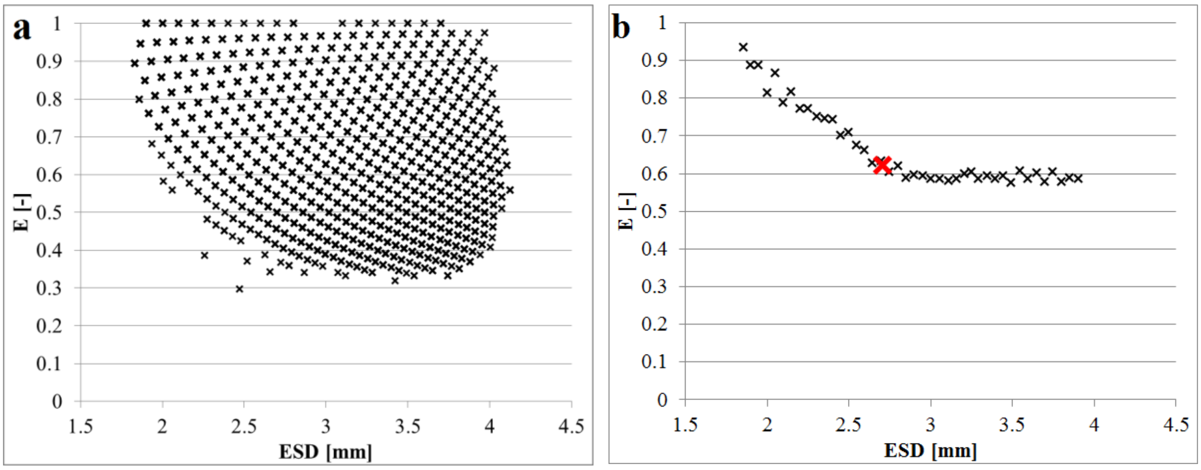

Figure 3.21: Exemplary relationship between bubble aspect ratio *E* and the equivalent sphere diameter *ESD* at 8 l/h flow rate in pure water. Raw (a) and reduced (b) data. The red cross represents the global average value.

In order to obtain an average aspect ratio for each bubble diameter, the raw bubble data has to be reduced. For this reason, the bubble data was reduced first to unique bubbles, based on the measured minor and major axes. Here, bubble sizes were taken into account, which were recognized at least 100 times in one recorded set. In the next step the bubbles were arranged by *ESD* into groups with an interval of 0.05 mm and an average major and minor axis, average velocity, average *ESD* (Figure 3.21, b) and an average aspect ratio was calculated for each group.

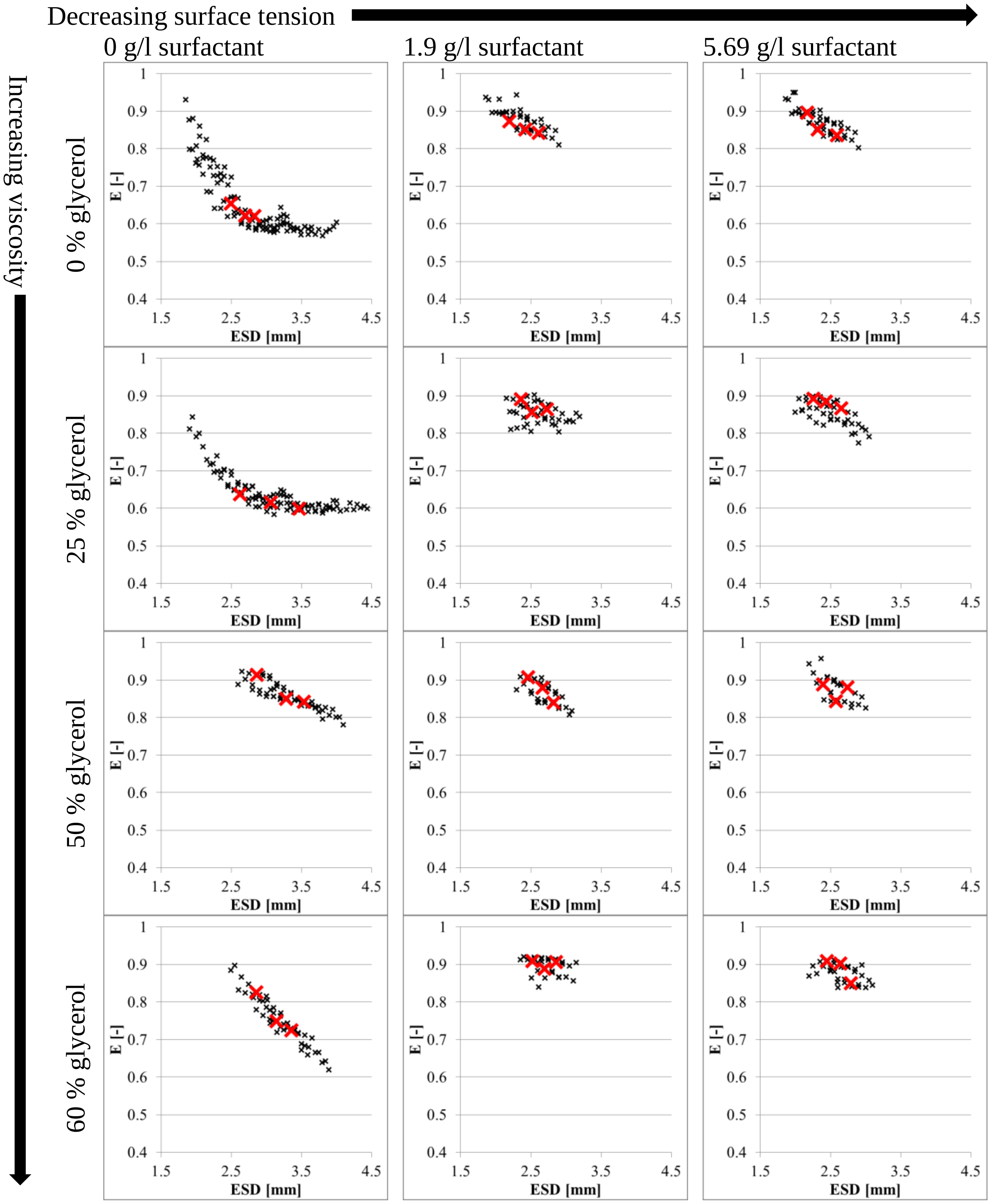

Figure 3.22: Relationship between bubble aspect ratio *E* and equivalent sphere diameter *ESD* of each investigated cases. The red crosses represent the global average value at each flow rate (4, 6 and 8 l/h).

In this way a more precise description of the bubble properties for each flow condition is possible. Figure 3.22 summarizes the results of all investigated fluid conditions. With increasing viscosity, the range of the generated equivalent sphere diameter decreases and the aspect ratio shifts towards unity corresponding to the perfect sphere shape. With decreasing surface tension, the range of the equivalent sphere diameter decreases even further and the values of *E* are always bigger than 0.8 in the presence of surfactant.

If the results from Figure 3.22 are plotted in one graph, two separate clouds of *E* can be distinguished (Figure 3.23). The bottom red one represents the data obtained with 0 and 25 % of glycerol, without surfactant. The upper blue one represents all of the cases with surfactant and the cases with 50 and 60% glycerol. In the top group the upper spike corresponds to the results in 50 % glycerol without surfactant and the bottom spike represents the result of the 60 % glycerol without surfactant.

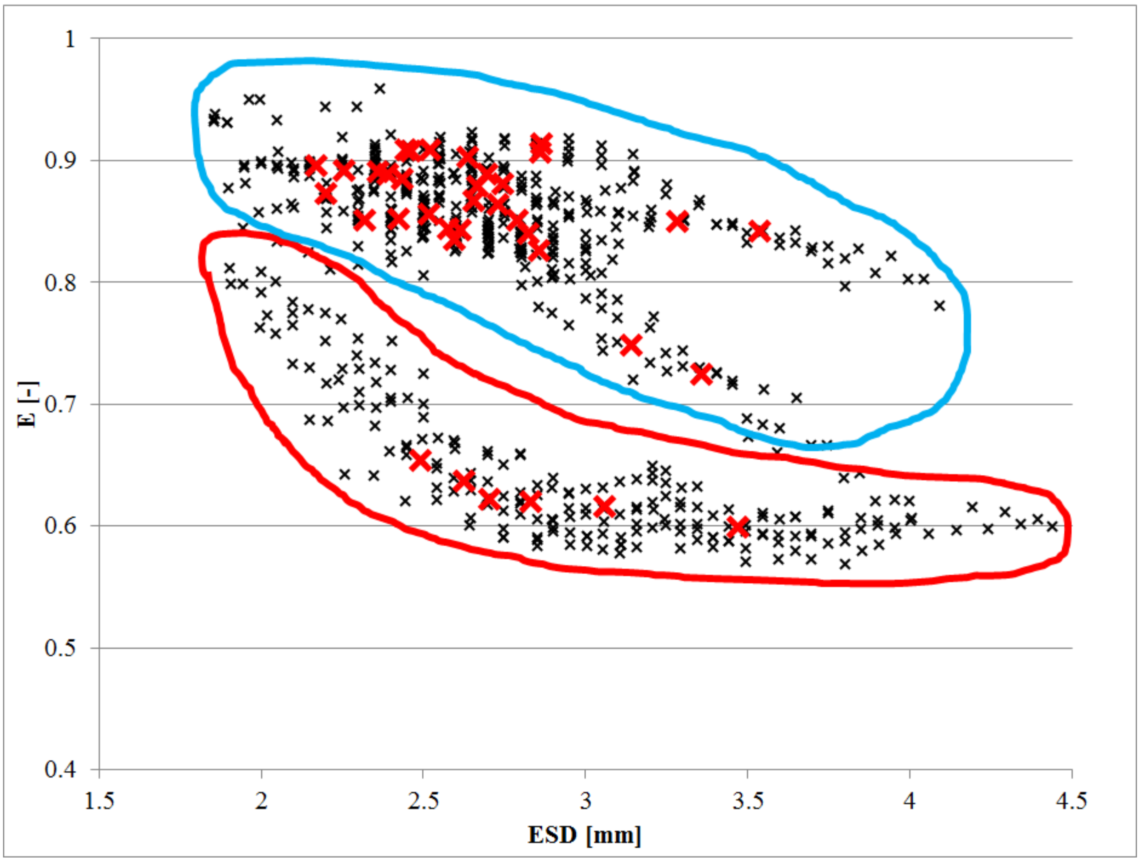

Figure 3.23: Relationship between bubble aspect ratio *E* and equivalent sphere diameter *ESD*, all cases. The red crosses represent all the global average values at each flow rate (4, 6 and 8 l/h).

From this plot it can already be seen, that the trends of the aspect ratio change of the two cases highly differ and these trends cannot be described with one equation. It is also noticeable, that in the cases with 0 and 25% glycerol concentration and without surfactant (red cloud in Figure 3.23), the aspect ratio does not decreases any more when reaching about ESD=3 mm and remains constant as the bubble diameter increases.

The reduced bubble data now can be used to compare it to the empirical correlations in the literature and to develop a new correlation, relating the aspect ratio *E* to dimensionless numbers, characterizing the flow and fluid conditions. For the comparison, two equations were used: (i) Eq. (3.15) from Besagni and Deen [168], because a large number of different experimental data with different flow conditions has been used to derive it; (ii) Eq. (3.16) proposed by Liu et al. [166]. For the latter equation they have used exclusively bubble data in swarm conditions.

$$E = \frac{1}{[1+0.45\cdot(E\ddot{o}Re)]^{0.07}} \tag{3.15}$$

$$E = \frac{1}{[1+0.0255\cdot(E\ddot{o}Re)]^{0.1572}} \tag{3.16}$$

Both equations are based on the combination of the Reynolds *Re* and Eötvös *Eö* numbers. Figure 3.24 shows both equations as red and blue lines respectively, together with the data of the present study. It is obvious from this figure, that they cannot predict the bubble aspect ratio in cases with higher glycerol concentration or with surfactant. On the other hand, they follow well the trend of aspect ratio change for the cases with 0 and 25% glycerol concentration, without surfactant (yellow and red circles in Figure 3.24).

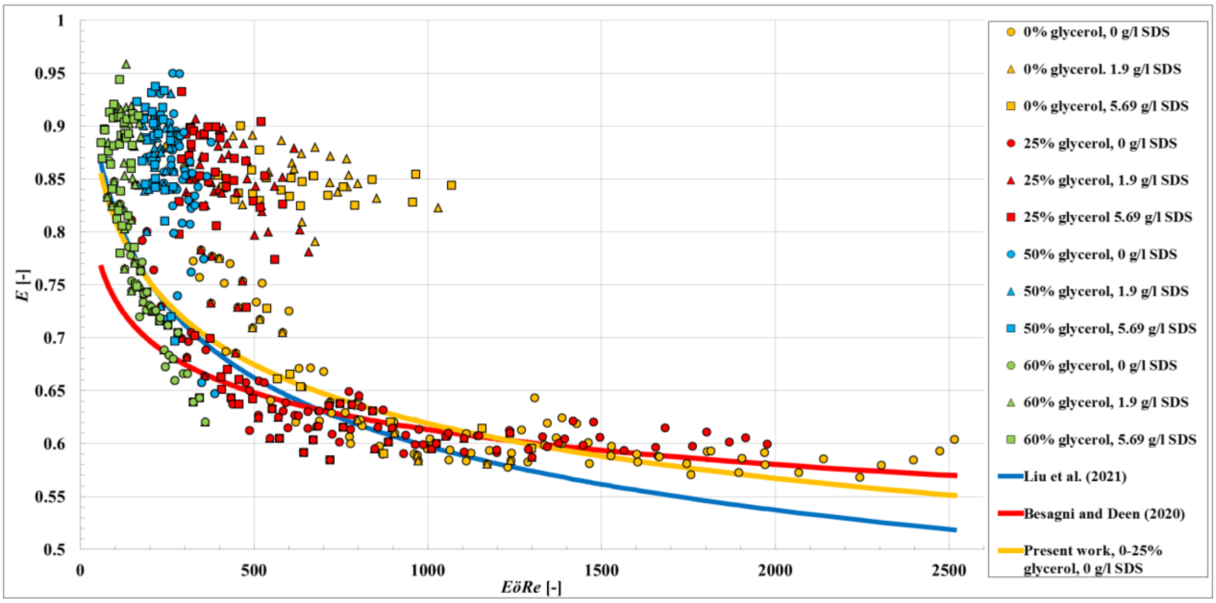

Figure 3.24: Relationship between bubble aspect ratio *E* and *EöRe*. Points from the present work and solid lines calculated with Eq.(3.15), Eq.(3.16) and Eq. (3.17).

Using the same structure of the proposed equations, new coefficients *ac* and *bc* were calculated with nonlinear least-squares fitting (NLSF) for the experimental data from the cases with 0 and 25% glycerol without surfactant. The resulting equation delivers:

$$E = \frac{1}{[1+ac\cdot(E\ddot{o}Re)]^{bc}} = \frac{1}{[1+0.041\cdot(E\ddot{o}Re)]^{0.1283}} \tag{3.17}$$

and it is represented in Figure 3.24, as a yellow line. However, this equation does not follow perfectly the trend line of the present measurements. For the other investigated cases, new coefficients were also calculated. The cases with surfactant were taken into account together, because of the very narrow distribution of the measurement points. The resulting coefficients and sum of squared residuals (SSR) are summarized in Table 3.6 and the curves are plotted on Figure 3.25.

Table 3.6: Sum of squared residuals and coefficients of the *EöRe*-based correlations.

Flow condition		Liu et al (2021)			Besagni (2020)			Present work		
Glycerol conc. [%]	Surfactant conc. [g/l]	ac	bc	SSR	ac	bc	SSR	ac	bc	SSR
0	0	0.0255	0.1572	1.485	0.45	0.08	1.6403	0.0151	0.1668	0.7399
25	0	0.0255	0.1572	0.6158	0.45	0.08	0.381	0.1454	0.0985	0.3476
0-25	0	0.0255	0.1572	2.1008	0.45	0.08	2.0213	0.041	0.1283	1.4292
50	0	0.0255	0.1572	3.9575	0.45	0.08	6.2429	0.0052	0.1528	0.0254
60	0	0.0255	0.1572	0.2018	0.45	0.08	0.5906	0.0061	0.395	0.0417
0-60	1.9-5.69	0.0255	0.1572	26.5865	0.45	0.08	37.4711	0.5313	0.0276	0.4378

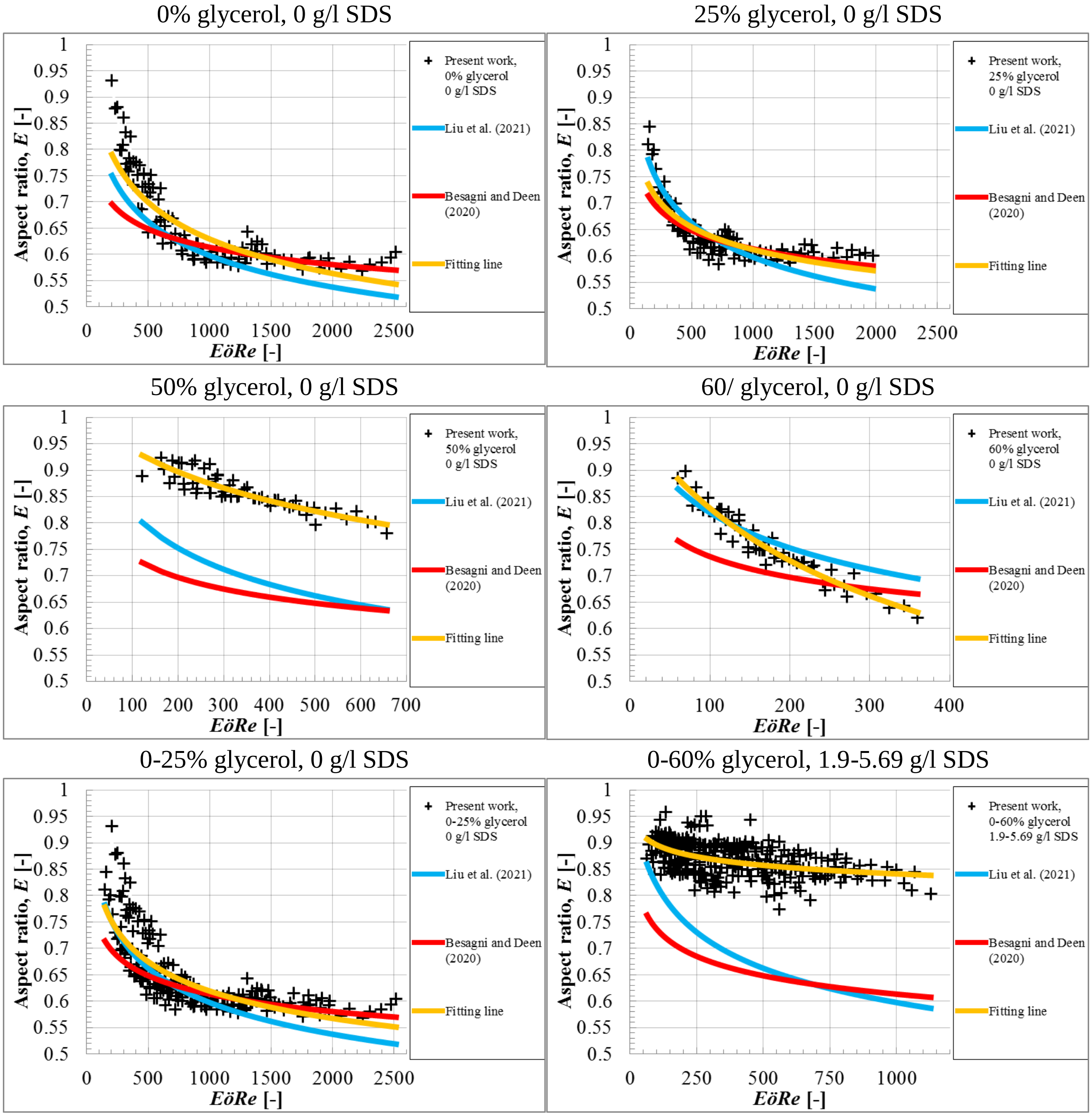

Figure 3.25: Relationship between bubble aspect ratio, *E* and *EöRe*.

It is obvious from these plots, that the aspect ratio cannot be well predicted with just one equation, at least if the equation is based only on the combination of *Eö* and *Re*. It is also remarkable, that the point distribution in the cases with higher glycerol concentration or with surfactant is nearly linear and for this reason, they could be calculated with a linear correlation. This means, that the influence of the viscosity and surface tension are not accounted for correctly with the aforementioned equations.

Considering this, NLFS was also performed using the flow number, F. As it was described before, the flow number is the combination of three dimensionless numbers ($E\ddot{o}$, Re, We), which takes into account the gravitational, viscous and surface tension forces. Therefore, it might be more suitable to predict the bubble aspect ratio.

Similar to Figure 3.24 the aspect ratio is plotted now against the flow number F on Figure 3.26. Here the separation of the different flow conditions is more obvious as on Figure 3.24. It is therefore also not possible to fit one single curve on all the points with surfactant, but a linear fit seems still possible. Moreover, there is no significant difference between the points with the two surfactant concentrations. Therefore, they can be fitted with one curve for each glycerol concentration.

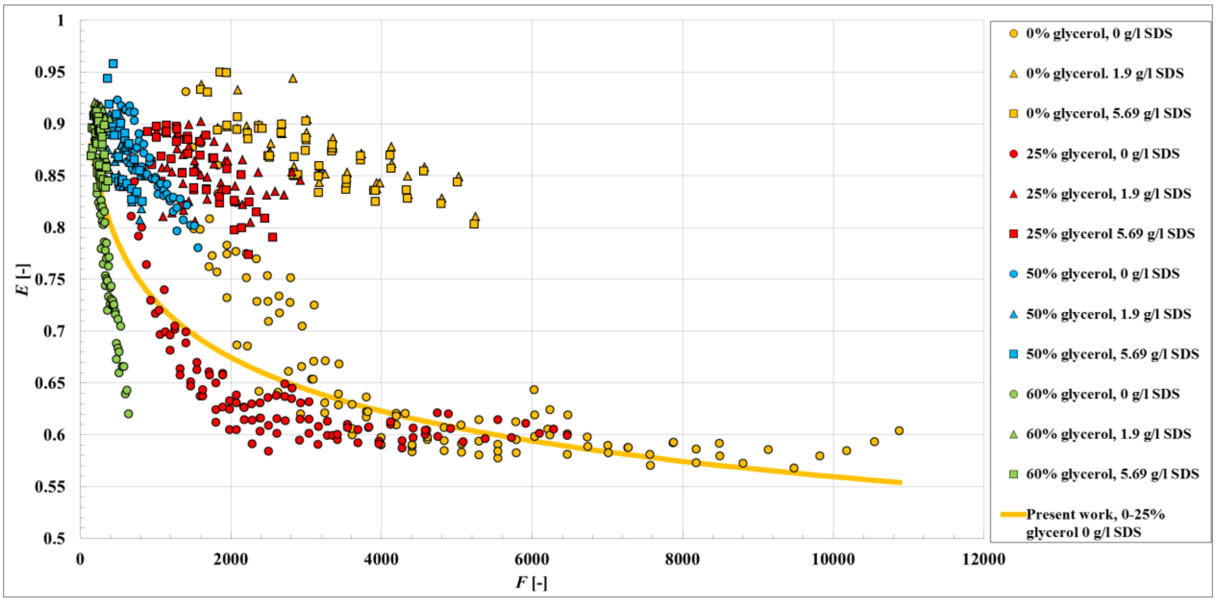

Figure 3.26: Relationship between bubble aspect ratio *E* and Flow number *F*. Points from the present work and solid line calculated with Eq.(3.17).

Taking into account all of these observations, new equations were calculated. As it was already mentioned, in the cases with 0 and 25% glycerol without surfactant and starting from a certain value of the bubble diameter, the aspect ratio does not decrease any more, but remains constant as the diameter increases (see Figure 3.21, b and Figure 3.23).

For this reason, two linear equations are proposed to cover all of the measured points:

$$E = \begin{cases} \frac{1}{(1+ac\cdot F)} & F < bc \\ \frac{1}{(1+cc)} & F \geq bc \end{cases}, \tag{3.18}$$

While for the other cases with higher glycerol concentration and with surfactant, one linear equation is proposed:

$$E = \frac{1}{1+ac\cdot F} \tag{3.19}$$

Presumably for these cases also a point could be found, from which the bubble eccentricity stays constant while the bubble diameter increases. Unfortunately, the present experimental data is not sufficient to define these points.

The resulting coefficients and sum of squared residuals (SSR) are summarized in Table 3.7 and the curves are plotted on Figure 3.27.

Table 3.7: Sum of squared residuals and coefficients of correlations based on the Flow number *F*.

Flow condition		ac	bc	cc	SSR $F < bc$ or no bc	SSR $F \geq bc$
Glycerol conc. [%]	Surfactant conc. [g/l]					
0	0	$1.562 \cdot 10^{-4}$	4500	0.7	0.318	0.088
25	0	$3.02 \cdot 10^{-4}$	2200	0.65	0.171	0.09
50	0	$1.799 \cdot 10^{-4}$	—	—	0.0253	
60	0	$8.897 \cdot 10^{-4}$	—	—	0.0573	
0	1.9-5.69	$4.604 \cdot 10^{-5}$	—	—	0.0623	
25	1.9-5.69	$9.987 \cdot 10^{-5}$	—	—	0.1864	
50	1.9-5.69	$2.662 \cdot 10^{-4}$	—	—	0.0584	
60	1.9-5.69	$4.867 \cdot 10^{-4}$	—	—	0.0849	

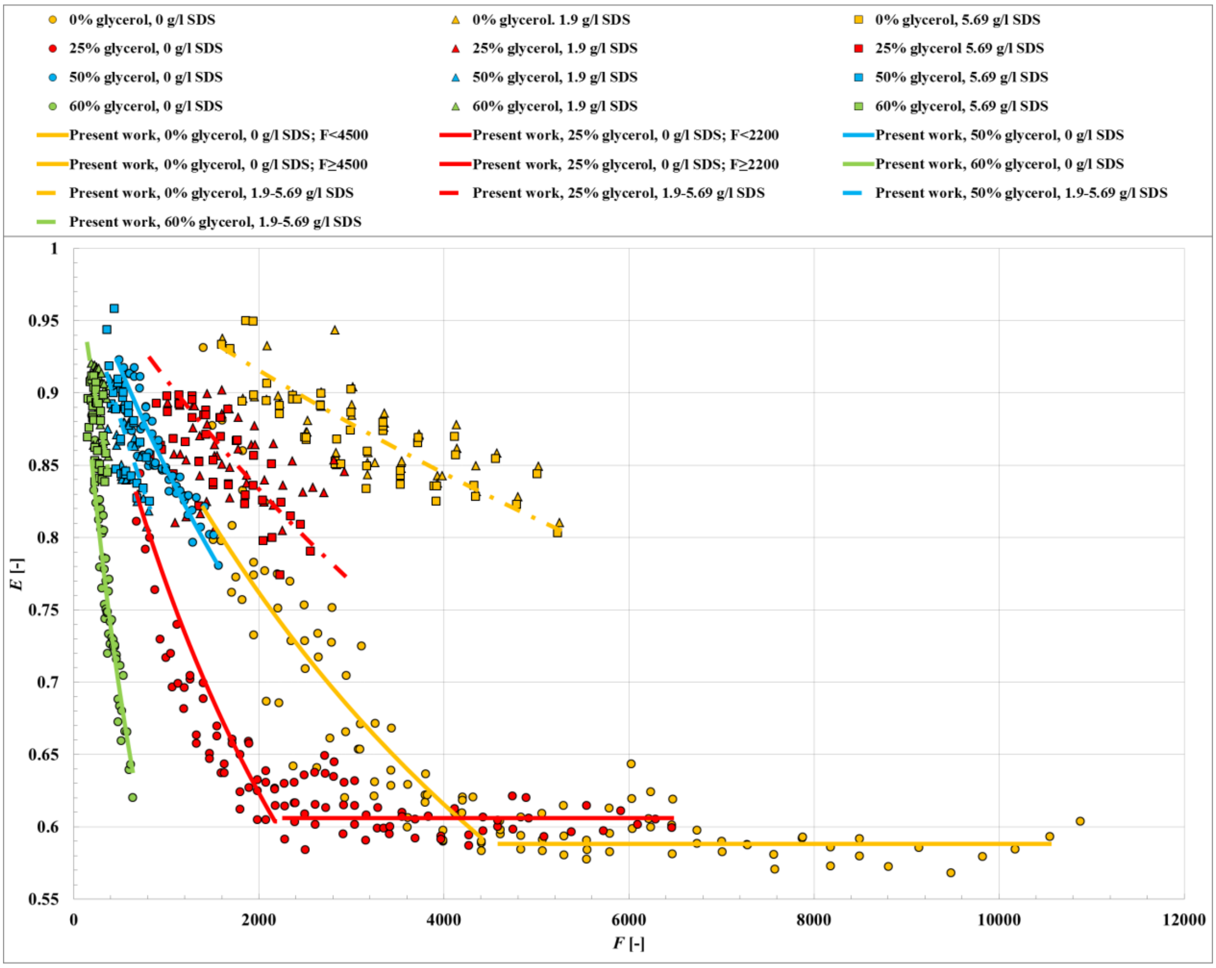

Figure 3.27: Relationship between bubble aspect ratio *E* and Flow number *F*. Points from the present work, solid and dashed lines calculated with Eq.(3.18) and Eq.(3.19).

In a further attempt to unify these correlations and to find one single equation for all cases, the product of viscosity, surface tension and density of the liquid are plotted against the regression parameter ac in Figure 3.28, a. Different trends of these points can be observed for the solutions with and without surfactant, but a nearly linear relationship can be observed in both cases. The dimensionless number, which contains all of these parameters, is the Morton number.

Considering these relationships, it was substituted into Eq. (3.19) and now the general equation for E can be written as:

$$\boldsymbol{E} = \frac{\mathbf{1}}{[\mathbf{1+0.0164}\cdot \boldsymbol{Mo}^{\mathbf{0.1854}}\cdot \boldsymbol{F}]}, \text{ for the cases without surfactant} \qquad (3.20)$$

and

$$\boldsymbol{E} = \frac{\mathbf{1}}{[\mathbf{1+0.018}\cdot \boldsymbol{Mo}^{\mathbf{0.2466}}\cdot \boldsymbol{F}]}, \text{ for the cases with surfactant} \qquad (3.21)$$

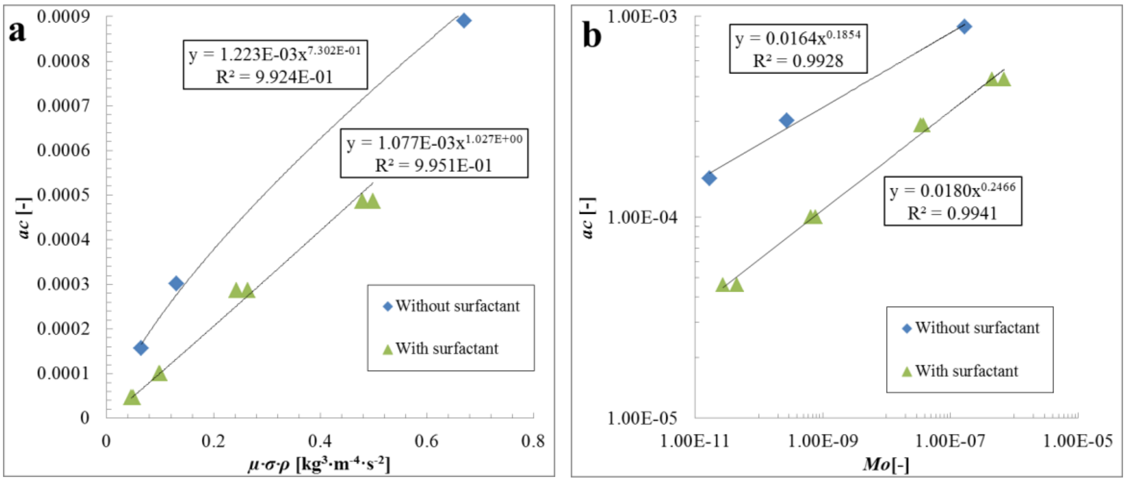

Figure 3.28: Relationship between the regression coefficient *ac* and a, the product of dynamic viscosity, surface tension and density and b, the Morton number.

On Figure 3.29 are now plotted the aspect ratio curves for each investigated cases, calculated with Eq.(3.20) and Eq.(3.21). The curves are very similar to the ones on Figure 3.27, which underlines the applicability of these new correlations. To develop these equations CO_2 bubble aspect ratio data in different water-glycerol mixtures were used. The covered Flow number range is in between 100 and 11000 for these cases. For this reason the validity of the correlations can be given in this Flow number range, but the correlations could probably predict the bubble aspect ratios beyond this range.

Only in one case, with 50 m% glycerol w/o surfactant, the aspect ratio is completely underestimated. The reason for that until now is unclear.

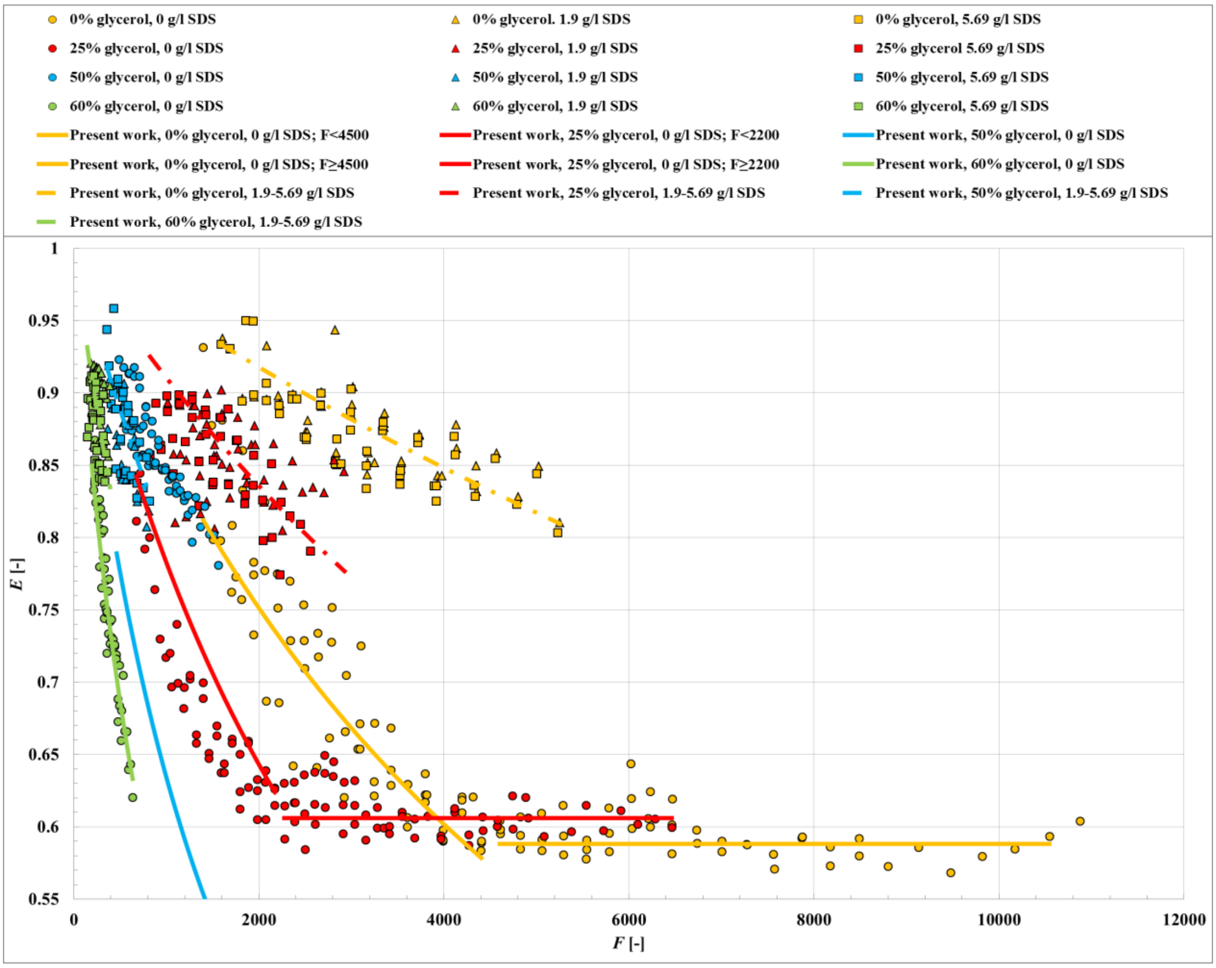

Figure 3.29: Relationship between bubble aspect ratio *E* and Flow number *F*. Points from the present work, solid and dashed lines calculated with Eq.(3.20) and Eq.(3.21).

3.5.2. Mass transfer determination

From the experimentally determined bubble properties, the Sherwood number and with this the mean volumetric mass transfer coefficient, $k_l a$, can be determined for the different water-glycerol-surfactant systems. For this calculation, the bubble size and velocity, gas holdup, the diffusion rate of CO_2 in water and the liquid flow around the bubbles play an important role.

The mass transfer in bubble columns can be calculated by the product of the mass transfer coefficient at the liquid side, k_L, and the specific interfacial area, a. In general, the range of the mass transfer coefficient in a system can be predicted from the bubbles and liquid characteristics with two equations, without measuring the mass transfer coefficients themselves.

For the upper boundary, where it is assumed that the bubbles have totally mobile surfaces, the value of k_L can be predicted with the equation proposed by Higbie [169]:

$$k_L = 2\sqrt{\frac{D}{\pi \cdot t_c}} = 2\sqrt{\frac{D \cdot u_S}{\pi \cdot ESD}} = \frac{2}{\sqrt{\pi}} \cdot \sqrt{ReSc} \cdot \frac{D}{ESD} = \frac{Sh \cdot D}{ESD}, \qquad (3.22)$$

where t_c is the contact time $\frac{ESD}{u_S}$, and

$$Sc = \frac{\mu_l}{D \cdot \rho_l}. \qquad (3.23)$$

The dimensionless form of Higbie's equation is then:

$$Sh_{Higbie} = \frac{2}{\sqrt{\pi}}\sqrt{ReSc}. \tag{3.24}$$

For the lower boundary, where the bubbles have totally rigid surface, the laminar boundary layer theory from Frössling [170] applies:

$$k_L = cf\sqrt{\frac{u_S}{ESD}} \cdot D^{\frac{2}{3}} \cdot \nu^{-\frac{1}{6}}, \tag{3.25}$$

where cf is a case-specific constant.

The dimensionless form of Frössling's equation is then

$$Sh_{Frössling} = Sh_0 + cf \cdot Re^{1/2}Sc^{1/3}, \tag{3.26}$$

where Sh_0 is a constant Sherwood number for a stationary sphere and its value is taken typically as 2.

Both equations are based on the Reynolds and Schmidt numbers, taking into account the viscous forces, but neglecting the effect of surface tension on the mass transfer. As presented before, the surface tension has a significant effect on the bubbles shape and, therefore, a key influence also on mass transfer.

To compute the Sherwood number/mass transfer coefficient for the investigated experimental cases, first of all three types of correlations were tested against experimental literature data of the k_L from Calderbank and Moo-Young [171] for CO_2 bubbles in different water-glycerol mixtures. This data was chosen, because these experiments were carried out at six different glycerol concentrations with a bubble swarm.

The first correlation for oscillating bubbles from Brauer [172] is based on the Frössling's equation.

$$Sh_{Br} = 2 + 0.015Re_B^{0.89}Sc^{0.7}. \tag{3.27}$$

The second correlation is proposed by Akita and Yoshida [173], and is based on experimental investigations in different liquid media with air as gas phase. It takes into account the viscous, gravitational and surface tension forces independently from the bubble velocity.

$$Sh_{Ak} = 0.5 \cdot Sc^{1/2} \cdot Ga^{1/4} \cdot Eö^{3/8}, \tag{3.28}$$

where

$$Ga = \frac{g \cdot ESD^3}{\nu_l^2}. \tag{3.29}$$

The third correlation is from Nedeltchev et al. [174] and is based on Higbie's equation:

$$Sh_{Ne} = \frac{\left[fc \cdot \left(\frac{4 \cdot D}{\pi \cdot t_C}\right)^{1/2}\right] \cdot ESD}{D}, \tag{3.30}$$

where

$$fc = 0.142 \cdot Eö^{1.257} = A \cdot C_D \cdot (\chi - 1) \cdot \left(\frac{T}{273.15}\right),\ A = 1.185, \tag{3.31}$$

$$tc = \frac{Bubble\ surface}{Rate\ of\ surface\ formation} = \frac{S_b}{R_{sf}} \sim \frac{ESD}{u_S}, \tag{3.32}$$

$$S_b = \pi \cdot \frac{b^2}{2}\left[1 + \left(\frac{c}{b}\right)^2 \cdot \frac{1}{2e} \cdot ln \cdot \frac{(1+e)}{(1-e)}\right], \tag{3.33}$$

$$e = \sqrt{1 - \left(\frac{c}{b}\right)^2}, \tag{3.34}$$

$$R_{sf} = \pi \cdot \sqrt{\frac{b^2+c^2}{2} - \frac{(b-c)^2}{8}}u_S. \tag{3.35}$$

All these equations are compared to the experimental literature data from Calderbank and Moo-Young [171] and the resulting plots are presented on Figure 3.30.

It is clearly visible, that none of the equations performs better than the others. In almost all cases the experimental values lie between the two theoretical boundaries of Higbie and Frössling. However, at lower glycerol concentrations the experimental values exceed the upper boundary.

At this point a strong weakness of these correlations has to be mentioned. In general, the bubble or liquid velocities are rarely measured and then only for single rising bubbles. However, for the above computations, e.g. for *Re* and *We* numbers or for the drag coefficient C_D, the bubble velocity is mandatory. For this reason, it is usually estimated from the drag coefficient C_D, which can only be calculated correctly for single rising bubbles but not for swarm conditions. Also the data from Calderbank et al. does not contain the bubble velocities, which were calculated from the drag coefficient, according to Bozzano and Dente [18].

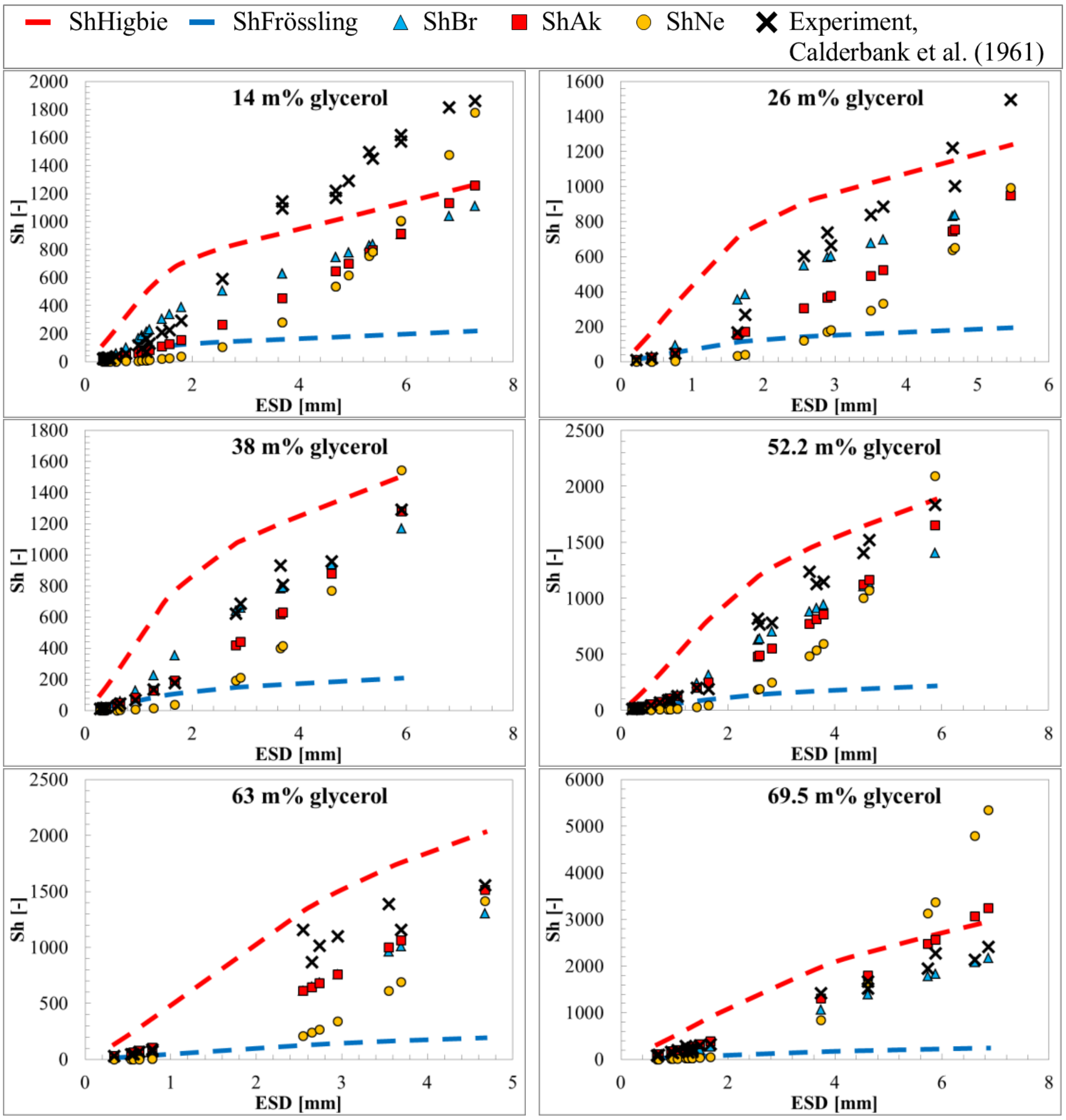

Figure 3.30: Comparison of the experimental data of Calderbank and Moo-Young [171] and the computed Sherwood numbers for six glycerol concentrations.

In order to ameliorate the prediction of Sherwood number (and thus mass transfer coefficients) the above correlations were extended. This has been done by using the Morton number as a dimensionless correction parameter and new coefficients were computed with NLSF for Eq.(3.27), Eq.(3.28) and Eq.(3.30). Also a new correlation was proposed (Eq. (3.37)), based on the structure of the correlation of Nedeltchev; but instead of the Eötvös number, the bubble eccentricity was used as correction factor.

The resulting equations are the following:

$$Sh_{Ne} = \frac{\left[0.458 \cdot Mo^{-0.017} \cdot E\ddot{o}^{0.063 \cdot Mo^{-0.092}} \cdot \left(\frac{4 \cdot D}{\pi \cdot t_c}\right)^{1/2}\right] \cdot ESD}{D}, \tag{3.36}$$

$$Sh_{Higbie,ecc} = \frac{\left[0.69 \cdot Mo^{-0.013} \cdot (\chi - 1)^{0.049 \cdot Mo^{-0.089}} \cdot \left(\frac{4 \cdot D}{\pi \cdot t_c}\right)^{1/2}\right] \cdot ESD}{D}, \tag{3.37}$$

$$Sh_{Ak,corr} = 0.21 \cdot Mo^{0.007} \cdot Sc^{0.503} \cdot E\ddot{o}^{0.016} \cdot Ga^{0.4}, \tag{3.38}$$

$$Sh_{Br,corr} = 2 + 2.89 \cdot 10^{-6} \cdot Mo^{0.391} \cdot Re_B^{0.332 \cdot Mo^{-0.06}} Sc^{1.258 \cdot Mo^{-0.036}}. \tag{3.39}$$

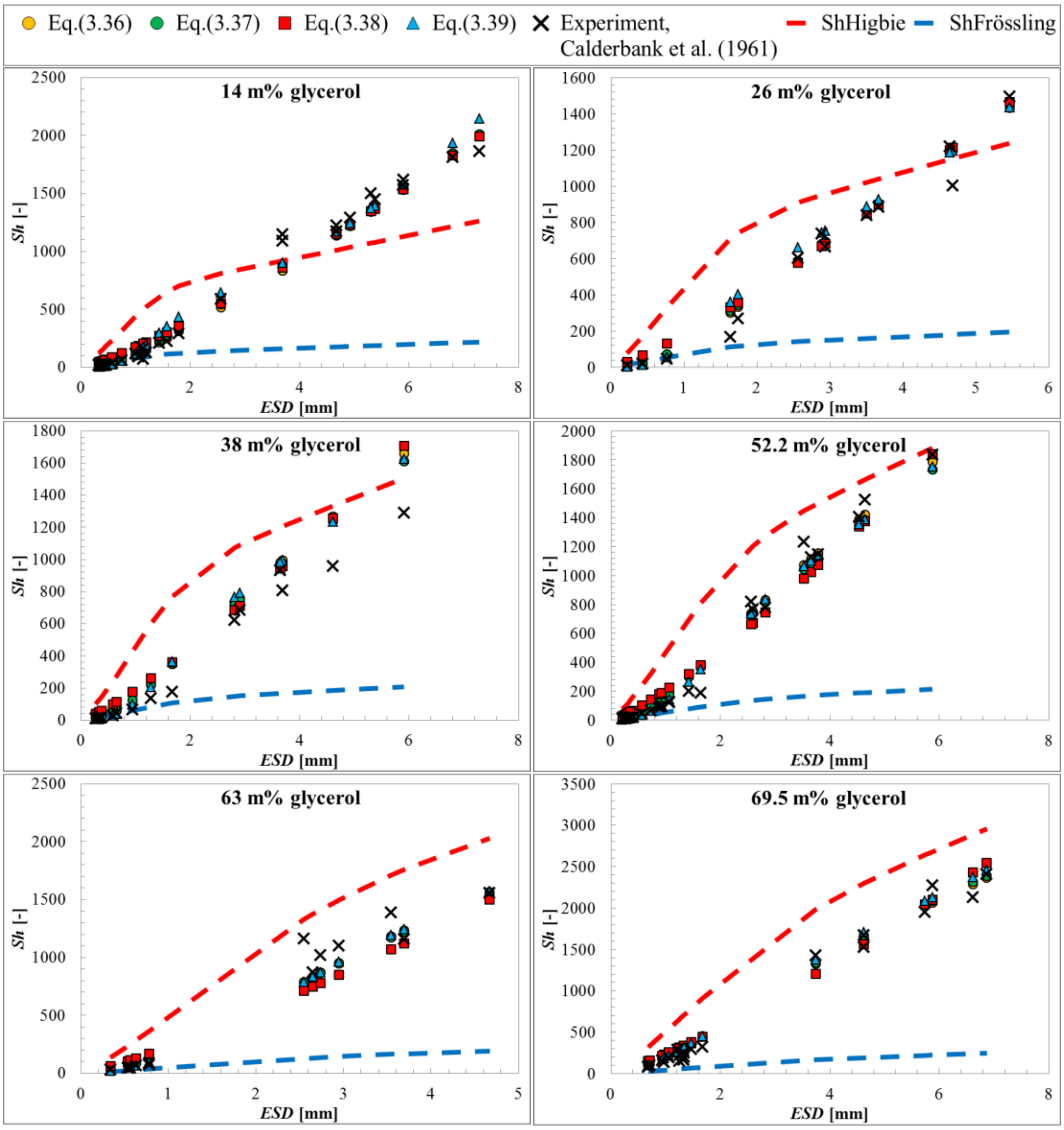

Figure 3.31: Application of the new equations: Comparison of the calculated Sherwood numbers with the experimental results from Calderbank and Moo-Young [171] in function of *ESD*.

The Sherwood numbers computed from these equations are plotted in Figure 3.31. All of the equations overestimate the case with 38% glycerol. In all other cases the agreement is quite good. All in all, if all cases are considered, a best fitting equation cannot be chosen. Considering the Sherwood number, all equations (3.36) – (3.39) perform similarly. Further investigations are necessary.

The mass transfer coefficient k_L in bubble columns can be calculated by dividing the product of the diffusion coefficient, *D*, and the Sherwood number, *Sh* with the bubble diameter *ESD* (Eq. (3.22)).

The investigated bubbles are in most cases not spherical, but spheroid and therefore they follow a zig-zag or helical path. As it has been described in [111], bubbles with this diameter have an oblate spheroid form. Therefore, the bubble volume is calculated here as an ellipsoid using Equation (3.2).

Since the bubble formation frequency f, the mean absolute bubble velocity u_b and the bubble volume V_b are known from the measurements, the total bubbly liquid volume in the bubble column can be determined as:

$$V_{TOT} = V_C + V_B f \frac{h}{u_S}, \tag{3.40}$$

where h is the column height and the liquid volume in the column is:

$$V_C = \left(\frac{d_C}{2}\right)^2 \pi h\,. \tag{3.41}$$

From these two volumes the gas holdup can be simply expressed as:

$$\varepsilon_G = \frac{V_{TOT} - V_C}{V_{TOT}}. \tag{3.42}$$

From the gas holdup the specific interfacial area of the bubbles can then be calculated with a simple equation from Akita and Yoshida [173]:

$$a = 6\frac{\varepsilon_G}{ESD}. \tag{3.43}$$

To define the diffusion rate of carbon-dioxide, which is crucial to calculate the mass transfer coefficient, usually the correlation given by Versteeg and Swaaij [175] is used, if the liquid medium is water:

$$D^{CO_2,water} = 2.35 \cdot 10^{-6} e^{-\left(\frac{2119}{T}\right)}. \tag{3.44}$$

Unfortunately, this correlation works just for pure water. Therefore, another one is needed for the water-glycerol-surfactant solutions. Calderbank and Moo-Young [176] and Brignole and Echarte [177] investigated and determined the diffusion coefficient of CO_2 in a wide range of water-glycerol mixtures at 25°C. The correlation proposed by Song et al. [178] for the diffusion coefficient of CO_2 in water-glycerol mixtures is in good agreement with these, and with other experimental data (see Fig.4. in the article by Song et al. [178]) measured at different temperature:

$$D^{CO_2,water-glycerol} = 0.3169 T(°\mathrm{C})^{0.5206} \mu(cP)^{-0.7407}. \tag{3.45}$$

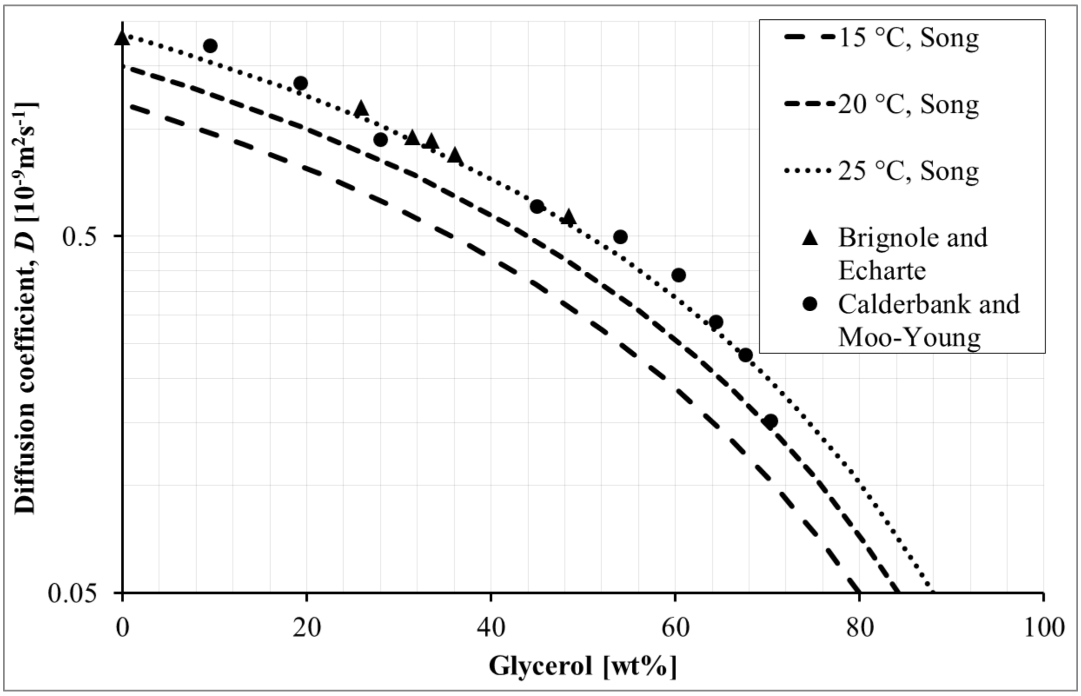

Figure 3.32: Experimentally determined diffusion coefficients for CO_2 in water-glycerol solutions compared to the correlation of Song.

Farajzadeh et al. [179] investigated experimentally the effect of SDS on the mass transfer of CO_2 into water. They have found that the addition of SDS to water has no measureable effect on the mass transfer rate in their experiments. For this reason Eq.(3.45) was applied to determine the diffusion coefficient of CO_2 for all the different solutions in the current experiments.

Since now the interfacial surface area of the bubbles is known and the mass transfer coefficient can be computed, the volumetric mass transfer coefficient can easily be calculated as

$$k_L a = k_L * a \,. \tag{3.46}$$

Also the mass transfer coefficient k_L is calculated with the new equations and the results are plotted in Figure 3.33. Now, the differences between the measured and calculated values become more visible. Eq.(3.36) and Eq.(3.37), which are based on the Higbie equation, perform similarly and the predicted k_L values are nearly the same. Eq.(3.39) delivers also similar results to Eq.(3.36) and Eq.(3.37), but it overestimates the value of k_L at lower glycerol concentrations. The one exception is Eq.(3.38), which strongly overestimates the mass transfer coefficient for *ESD* < 2 mm.

Since Eq.(3.36) and Eq.(3.37) seems to fit similarly to the complete range of viscosities tested by Calderbank, Eq.(3.37) will be chosen for the calculation of the mass transfer coefficient k_L from our data, because the sum of squared residuals (SSR) was here the less. The measured eccentricities and bubble velocities will be considered in that equation. For comparison, Eq.(3.38), is also computed, since it is independent from known eccentricity and bubble velocity values and can thus be applied with less experimental effort over 2 mm bubble size.

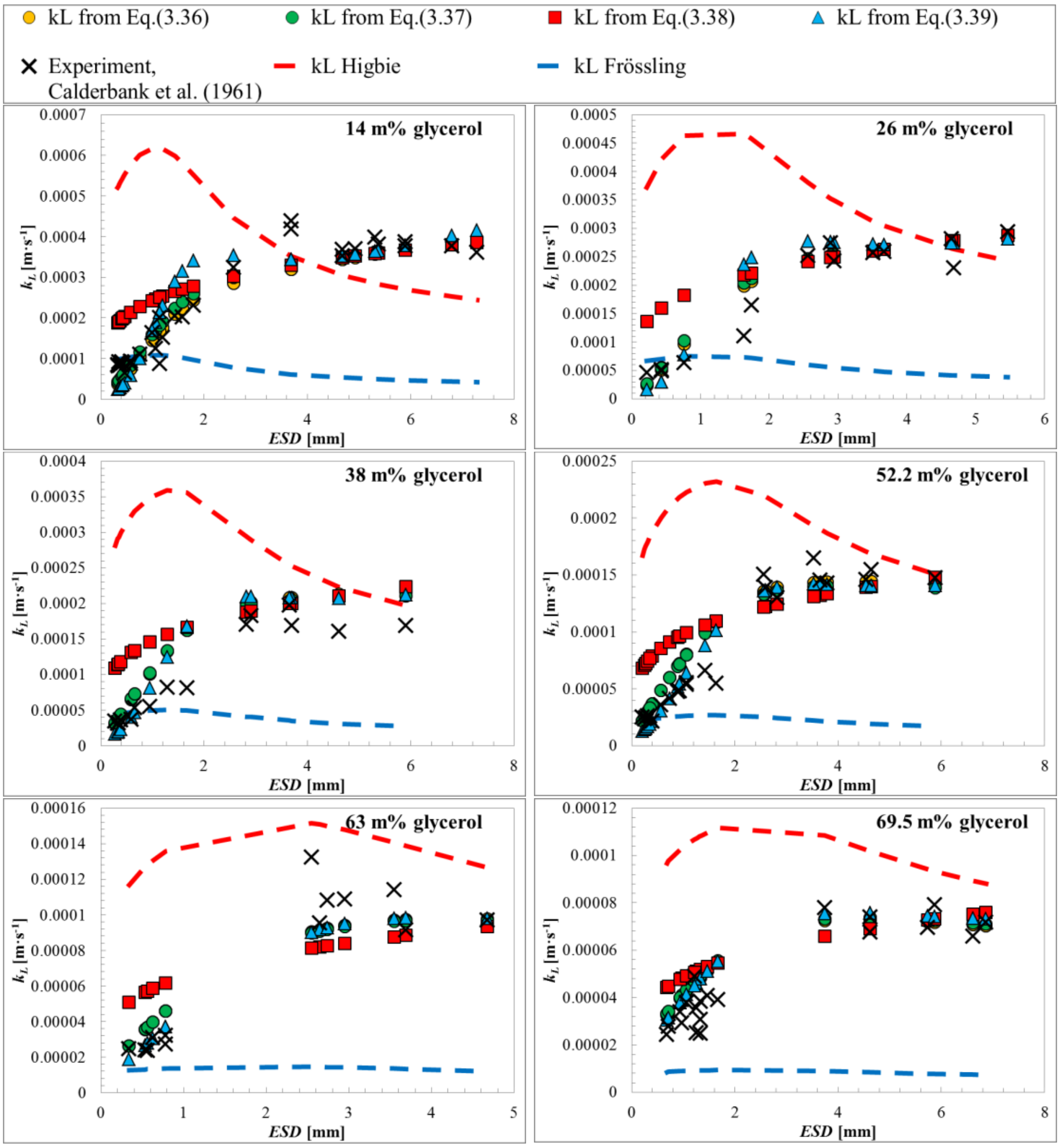

Figure 3.33: Mass transfer coefficient values against *ESD* calculated with the newly proposed equations.

The results obtained with Eq.(3.37) are presented in Figure 3.34. Here, and also on the following figures the error bars are scatter bars and represent the calculated values for bubble groups, determined for each setup (see subsection 3.5.1) and the full marks represent the results, calculated with the global average bubble diameter. With increasing gas flow rate, the value of k_L without and with 25% glycerol decreases very slightly (Figure 3.34, a), but at even higher glycerol concentrations it remains constant. With the obtained accuracy, the curves are basically flat. The origin of this behaviour is, that at lower viscosity with increasing gas flow rate, the bubble size increases and the bubble velocity decreases. But in liquids with higher viscosity, with growing bubble size, the bubble velocity increases (please, refer to Figure 1.1 and Figure 3.15). When multiplying with the interfacial surface area a, the resulting $k_L a$ shows an increasing trend with increased gas flow rate (Figure 3.34, b) for all considered viscosities. The highest value for the volumetric mass transfer coefficient is reached at 8 l/h gas flow rate in pure water. With increasing glycerol concentration as well as with decreasing flow rate the value of $k_L a$ decreases, until reaching saturation.

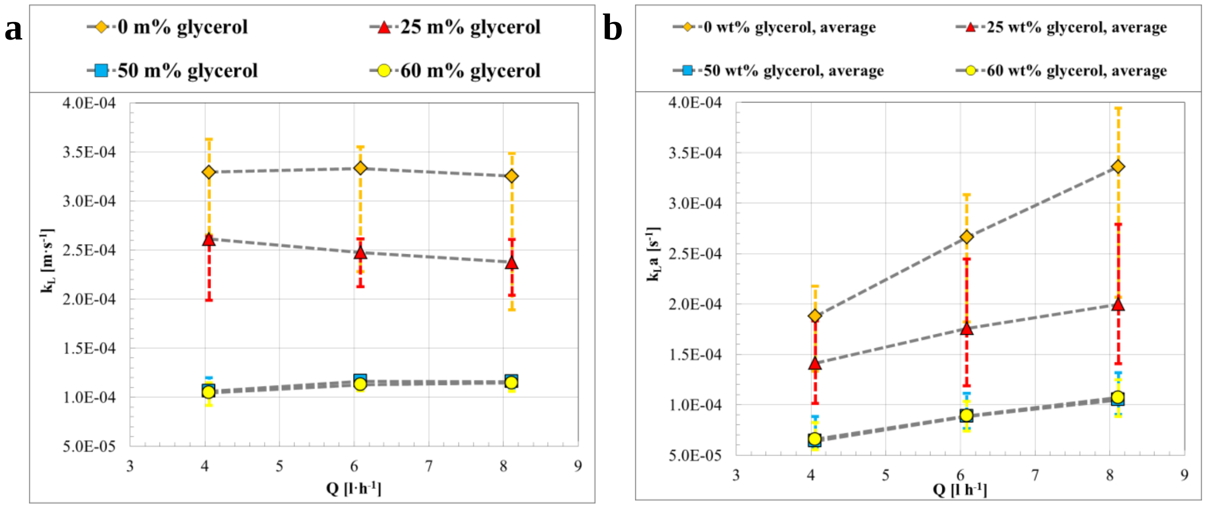

Figure 3.34: Calculated (Eq.(3.37)) k_L (a) and k_La values (b) as a function of gas flow rate for different glycerol concentrations.

Figure 3.35 shows the effect of SDS on the mass transfer and volumetric mass transfer coefficients, still calculated with Eq. (3.37). As it was previously described, the amount of SDS added to the liquid has negligible effect on the bubble properties. Therefore, the results are very similar for both SDS concentrations; however the effect of the surfactant against solutions without SDS (rightmost symbols at 72 mN·m^{-1} in Figure 3.35) is clearly visible.

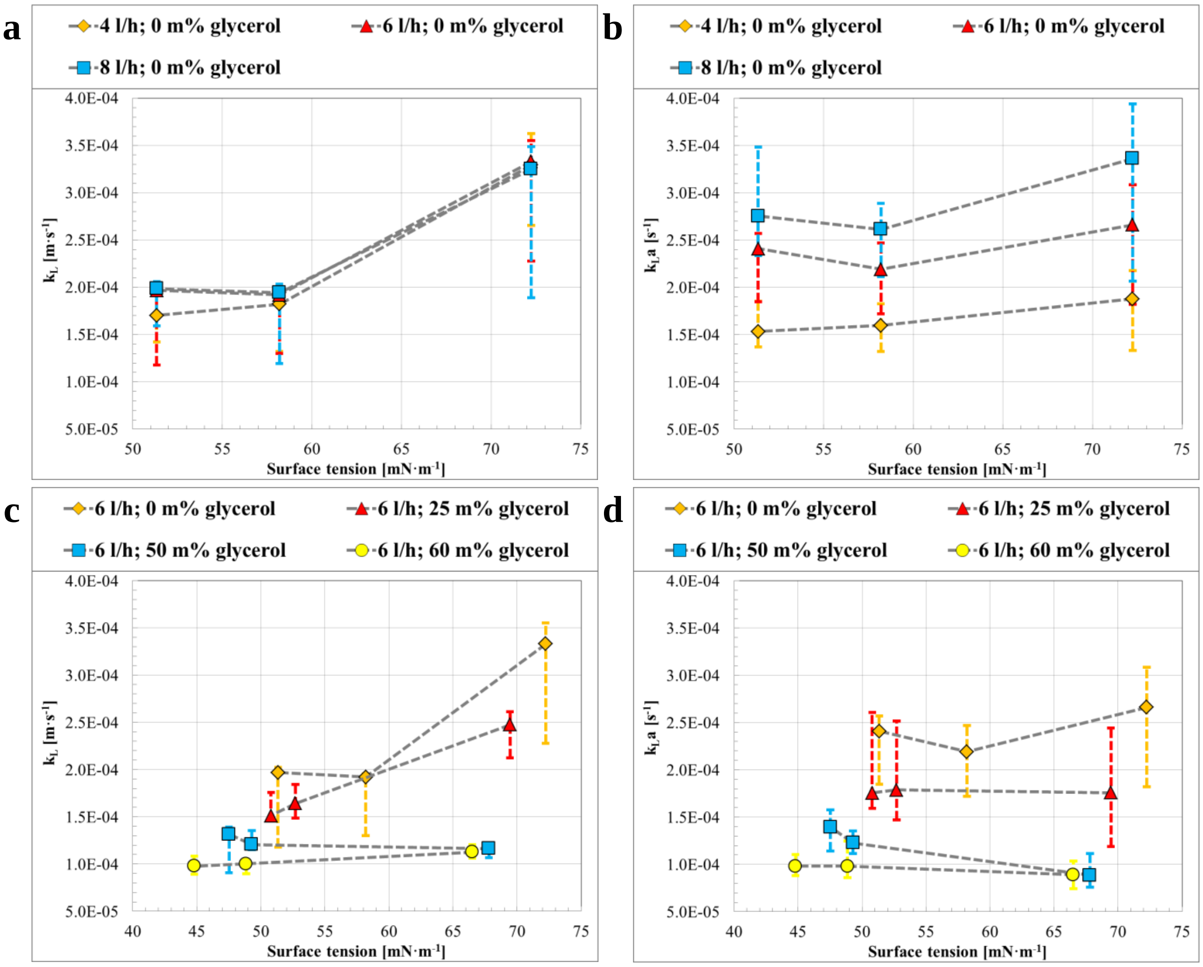

Figure 3.35: Calculated (Eq.(3.37)) k_L and k_La values as a function of surface tension for different flow rates without glycerol (a, b) and for different glycerol concentrations (c, d) at 6 l/h.

With the addition of surfactant, the mass transfer coefficient decreases (Figure 3.35, a), and the volumetric mass transfer coefficient decreases too (Figure 3.35, b). In both cases a plateau seems to be reached. Moreover, with increasing gas flow rate the $k_L a$ increases, but the values of k_L stay almost constant. Figure 3.35, c shows the effect of surfactant on k_L in different water-glycerol mixtures at 6 l/h gas flow rate. As observable, at lower viscosities the addition of SDS reduces the mass transfer coefficient, whereas in mixtures with higher viscosity, almost no effect can be noticed. Concerning $k_L a$, the effect of SDS is negligible, a clear trend cannot be identified.

The change of the k_L and $k_L a$ at different liquid viscosities are depicted on Figure 3.36. With increasing viscosity the value of k_L continuously decreases, but the effect of different gas flow rates is negligible (Figure 3.36, a). Figure 3.36, b shows the unambiguous effect of the multiplication with the interfacial surface area. The values of $k_L a$ show also a decreasing trend with increasing viscosity, but here, the effect of the gas flow rate can also be recognized.

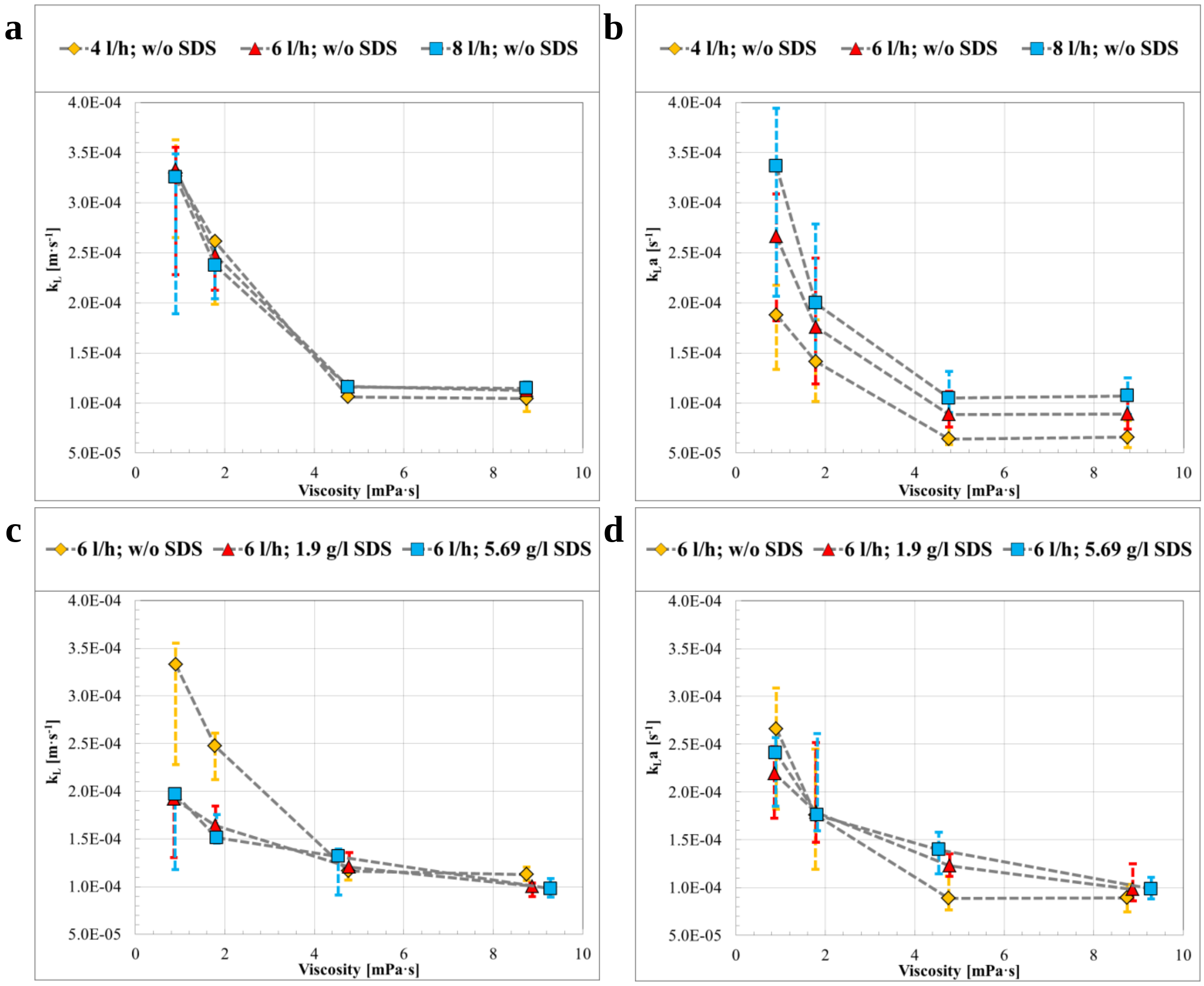

Figure 3.36: Calculated (Eq.(3.37)) k_L and $k_L a$ values as a function of viscosity for different flow rates without surfactant (a, b) and as a function of viscosity for different SDS concentrations at 6 l/h (c, d).

The higher the gas volume flow, the higher is the value of the volumetric mass transfer coefficient. Furthermore, a sudden drop can be seen between the results of pure water and the 25% water-glycerol mixture (Figure 3.36, d). The origin of this drop can be found in Table 3.4. The bubbles are bigger in the 25% water-glycerol mixture than bubbles in pure water, but they have almost the same rising velocities. Therefore, it has a significant effect on the gas holdup and on the interfacial surface area. After this drop, with increasing viscosity the values of $k_L a$ decrease more slowly before reaching a plateau. This joint effect of surface tension and viscosity is depicted on Figure 3.36, c. With increasing glycerol concentration the mass transfer coefficient decreases and as it was already shown on Figure 3.35, a, the highest k_L values were calculated for pure water. With addition of surfactant, the bubble size decreases and the gas holdup increases, which result in slightly higher $k_L a$ values for the mixtures with surfactant (Figure 3.36, d), but these values show also a decreasing trend with increasing viscosity.

The k_L values derived with Eq.(3.37) are compared in Figure 3.37 to the correlation Eq.(3.38) and to the Higbie and Frössling equations. On these figures all investigated gas flow rates (4, 6 and 8 l/h) are plotted in one diagram. It is noticeable, that the gas volume flow rate has almost no influence on the mass transfer coefficient k_L, in the range examined here. It is also obvious, that the trend of the predicted k_L values differs for all cases for Higbie, Frössling, Eq.(3.37) and Eq.(3.38). Eq.(3.38) always predicts an increasing mass transfer coefficient with increasing bubble size, while the three others show a mostly decreasing behaviour at 0 and 25 m% glycerol w/o SDS; at higher viscosities and with SDS, a slightly decreasing or stagnating trend can be observed. Overall, the predicted mass transfer coefficient ranges are similar with Eq.(3.37). and Eq.(3.38). The more scattered k_L values at 0 and 25 m% glycerol predicted with Eq.(3.37) may be attributed to the bubble shape, since this equation is the only to considering the eccentricity. With increasing bubble size the eccentricity of the bubbles decreases; therefore, also the computed k_L values decrease. At higher glycerol concentrations and in the cases with surfactant the bubble shape remains almost the same, and k_L is predicted as an almost straight line.

All in all, with increasing viscosity and also with decreasing surface tension the mass transfer coefficient decreases. This trend is well captured by both equations.

Liquid viscosity, surface tension and diffusion coefficient and also the bubble shape have a strong influence on calculated mass transfer coefficients and volumetric mass transfer coefficients. Kulkarni and Joshi [180] and Besagni et al. [137] have already described this phenomenon, attributing it to the influence of liquid viscosity on bubble size, velocity and gas holdup. A higher liquid viscosity increases the mean bubble diameter in the reactor, therefore reducing the surface-to-volume ratio, and reducing also mass transfer. Additionally, a higher liquid viscosity also decreases liquid-side diffusivity [171, 178] and liquid renewal along the bubble surface; therefore, mass transfer is again decreased.

It is also noteworthy, that Eq.(3.38) predicts the k_L values in the same range as Eq.(3.37), without necessitating bubble shape and velocity data. This equation could be a good choice to calculate the mass transfer coefficient, if only the fluid properties, bubble diameters and liquid velocity are known:

$$\boldsymbol{Sh_{Higbie,ecc}} = \frac{\left[\mathbf{0.69} \cdot \boldsymbol{Mo}^{-\mathbf{0.013}} \cdot (\chi - \mathbf{1})^{\mathbf{0.049} \cdot \boldsymbol{Mo}^{-\mathbf{0.089}}} \cdot \left(\frac{\mathbf{4} \cdot \boldsymbol{D}}{\pi \cdot \boldsymbol{t_c}}\right)^{\mathbf{1/2}}\right] \cdot \boldsymbol{ESD}}{\boldsymbol{D}}, \tag{3.37}$$

and

$$\boldsymbol{Sh_{Ak,corr}} = \mathbf{0.21} \cdot \boldsymbol{Mo}^{\mathbf{0.007}} \cdot \boldsymbol{Sc}^{\mathbf{0.503}} \cdot \boldsymbol{E}\ddot{\mathrm{o}}^{\mathbf{0.016}} \cdot \boldsymbol{Ga}^{\mathbf{0.4}}. \tag{3.38}$$

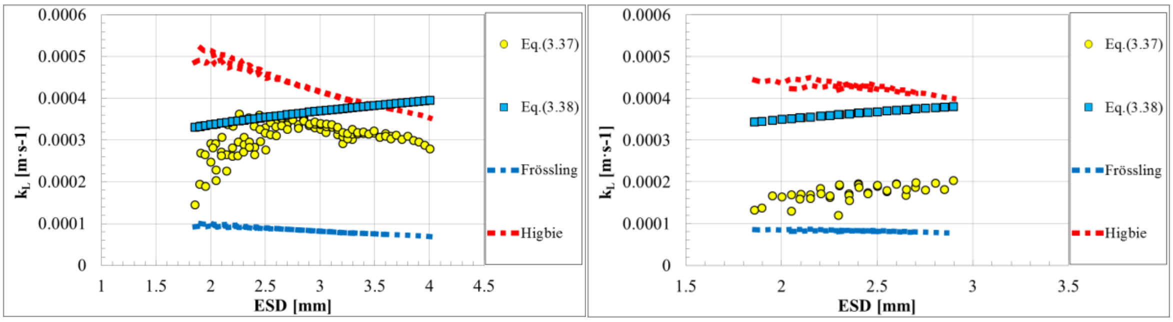
0 m% glycerol; w/o SDS

0 m% glycerol; 1.9 g/l SDS

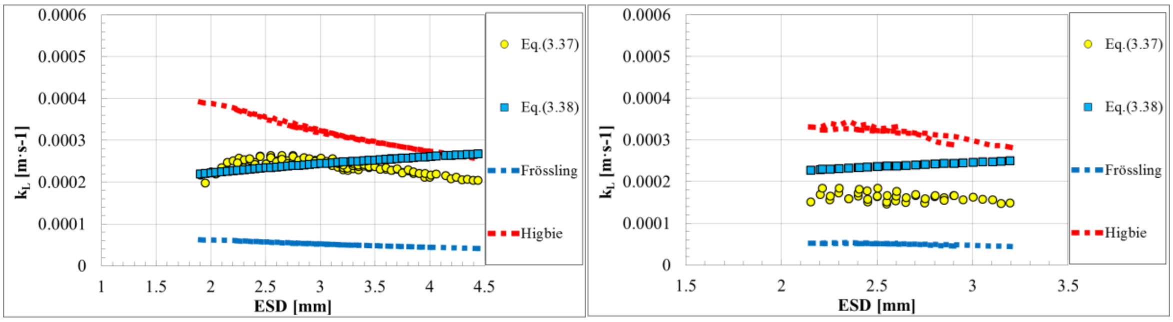
25 m% glycerol; w/o SDS

25 m% glycerol; 1.9 g/l SDS

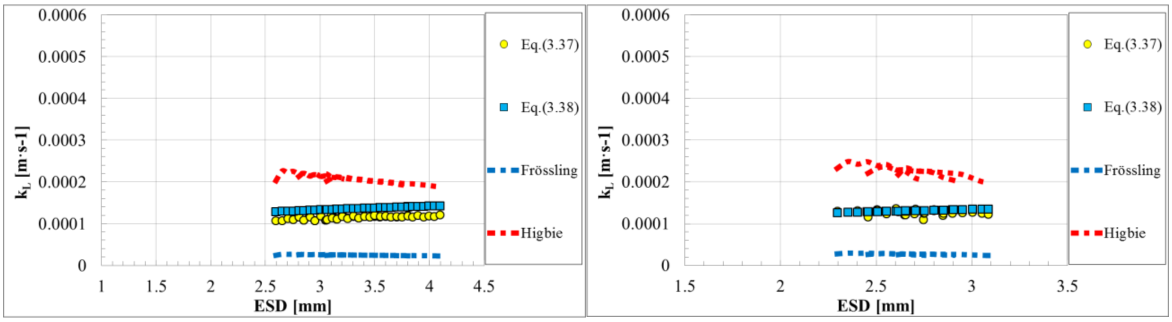
50 m% glycerol; w/o SDS

50 m% glycerol; 1.9 g/l SDS

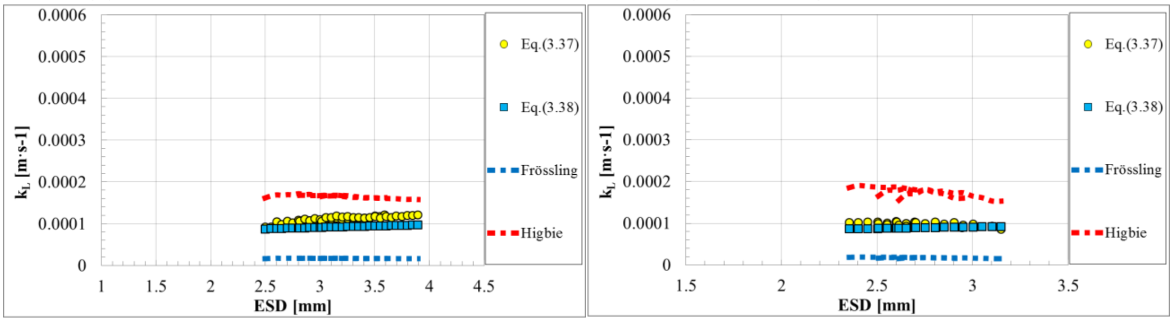
60 m% glycerol; w/o SDS

60 m% glycerol; 1.9 g/l SDS

Figure 3.37: Calculated k_L values from the experiments with Eq.(3.37), compared to the correlation Eq.(3.38) for water-glycerol mixtures with and w/o SDS in function of the bubble diameter.

3.6. Conclusions

In this chapter, bubble parameters were investigated with Shadowgraphy in a laboratory-scale bubble column reactor under different flow conditions and liquid properties. Through several experiments, bubble size and velocity were determined experimentally for different water qualities, pH levels, filling heights, viscosities, surface tensions and gas volume flows.

It has been found, that only the gas flow rate induced significant changes in bubble size and velocity in pure water. Increasing the gas flow rate, larger bubbles are generated, but travelling at lower velocities. In the whole bubble column height significant bubble shrinkage, as well as bubble velocity change from bottom to the top of the column were observed in the cases without surfactant. Bubble size is increasing with increasing viscosity and surface tension. Bubble velocity decreases with increasing viscosity and decreasing surface tension. Bubble size and velocity distributions experience not only a shift of the maximum, but also their aspect changes by broadening. Since bubble size, shape and velocity directly impact mass transfer and mixing, it is clear that the gas flow rate, surface tension, viscosity and bubble eccentricity are essential parameters to determine correctly the liquid-side mass transfer coefficient and the volumetric mass transfer coefficient in a bubble column reactor.

For this reason, a new correlation was proposed for the calculation of bubble eccentricity, based on the Flow number and thus including the fluid properties. Extending Higbie's correlation for mass transfer coefficients with this equation for eccentricity, a good prediction of mass transfer coefficients was achieved for all examined cases and in comparison with data from Calderbank [171]. New coefficients were also computed for the equation from Akita [173], Eq.(3.38), which predicts also adequately the values of mass transfer coefficient, without taking into account the bubble velocity or eccentricity.

It has been found by applying these equations, that the addition of glycerol has a large influence on the liquid-side mass transfer, the specific interfacial area and, therefore, the volumetric mass transfer decreases as well with increasing viscosity. With the addition of surfactant, the liquid side mass transfer decreases because of the decreasing Reynolds number, but contrary to this, the volumetric mass transfer increases due to the increasing specific interfacial area. The experimental results presented here have shown that the highest mass transfer from gas to liquid can be achieved with pure distilled water with and without surfactant.

The effect of surface tension is very difficult to account for, and neither the correlations using Flow and Velocity number nor the known Clift correlation for bubble size and velocity, are able to correctly represent the changes due to a decreasing surface tension.

Because of the three dimensional motion of the bubbles, planar shadowgraphy cannot resolve completely bubble movement. To avoid this problem, a stereo-shadowgraphy setup with two cameras should be used in the future.

In the frame of the DFG Priority Program SPP 1740 "Reactive Bubbly Flows", an Internet-based database has been created to share all the above mentioned data with the scientific community, supporting validation of numerical simulations (see also Chapter 8) and comparisons with results from other groups. The complete data sets containing the measured bubble parameters are available through this online database, freely accessible with a password under http://141.44.132.124/spp1740/.

Chapter 4

Single bubble experiments

Parts of the results and subsections presented in this chapter have been presented in a peer-reviewed paper and a presentation at the 18th International Symposium on the Application of Laser and Imaging Techniques to Fluid Mechanics, 2016, in Lisbon, Portugal (Kováts and Zähringer [181]) and at the 19th International Symposium on the Application of Laser and Imaging Techniques to Fluid Mechanics, 2018, in Lisbon, Portugal (Kováts and Zähringer [102]).

Contents

4.1. INTRODUCTION 78
4.2. EXPERIMENTAL SETUPS AND FLOW CONDITIONS FOR THE MEASUREMENTS WITH AIR BUBBLES 78
4.3. LIQUID FLOW AND CONCENTRATION FIELDS AROUND SINGLE AIR BUBBLES 79
4.4. CONCLUSIONS 85

4.1. Introduction

This chapter deals with single bubble measurements in the bubble column reactor with O_2 mass transfer. Similar experiments have been executed for the chemisorption of CO_2, but will not be presented here, due to the strong similarities in the findings for both gases. As explained in Chapter 2, in the case of the neutralization reaction, the pH of the liquid decreases in consequence of the amount of dissolved CO_2. This pH change can be followed by optical measurement techniques, like LIF or 2T-LIF, which were used for these experiments. The results have been presented in detail in a peer-reviewed paper and a presentation at the 18th International Symposium on the Application of Laser and Imaging Techniques to Fluid Mechanics, 2016, in Lisbon, Portugal [181].

Regarding O_2 mass transfer, through a simple redox reaction the amount of dissolved O_2 can be calculated from the fluorescence intensity of resorufin dye. This reaction can also be followed by LIF, which was used in these experiments. The liquid flow field around single bubbles was determined with PIV. These results have also been presented in a peer-reviewed paper and a presentation at the 19th International Symposium on the Application of Laser and Imaging Techniques to Fluid Mechanics, 2018, in Lisbon, Portugal [102].

The aim of these measurements was to gain information about the mass transfer and liquid flow around single spherical and ellipsoidal bubbles and to provide experimental data for validation of numerical simulations.

4.2. Experimental setups and flow conditions for the measurements with air bubbles

All these measurements were carried out in the same model bubble column, which was described in detail in Chapter 2. To avoid unnecessary repetitions, the applied experimental setups here will be described only briefly with referring to the detailed technical description in Chapter 2.

In the centre of the sparger plate, a single stainless steel nozzle with an inner diameter of 0.25 mm is mounted for the generation of elliptical gas bubbles with a diameter of 2.3-3.5 mm or a stainless steel nozzle with an inner diameter of 0.13 mm is placed to produce spherical bubbles with a diameter of 1-1.5 mm. In both cases, bubbles rise in a stagnant liquid.

For the characterization of the flow field and mass transfer around single spherical and elliptical air bubbles, PIV and LIF techniques were used simultaneously, according to the O_2 reaction system (see subsection 2.3.2. and Tables Table 2.2 and Table 2.6).

The experimental images for the simultaneous LIF-PIV measurements around the single air bubbles were recorded with two Imager sCMOS cameras – one for LIF, one for PIV – which were placed opposite to each other. Because of the close camera setup, the reflections on the bubble surface were very strong on the PIV images. For this reason, a neutral-density filter with 2.0 optical density was mounted onto the PIV camera lens. To use the maximal spatial resolution, extension tubes were mounted onto the lenses to shift the focal point. Thus, an investigation window size of around 16x14 mm^2 was reached. The detailed measurement conditions and more technical details of this setup can be found in Chapter 2 (Table 2.2 and Table 2.6, No. 11).

Bubbles were generated in this case with the help of an automatic titrator (Mettler DL21), where the burette was filled with air. The titrator pushed every 10 seconds 0.02 ml air into the pipeline and thus 1 bubble was generated in the bubble column. In all experiments 2 l of de-ionized water mixed with resazurin, glucose and sodium hydroxide was used as liquid phase in the experiments (Table 2.1). The mixture was degassed with argon after filling it into the bubble column.

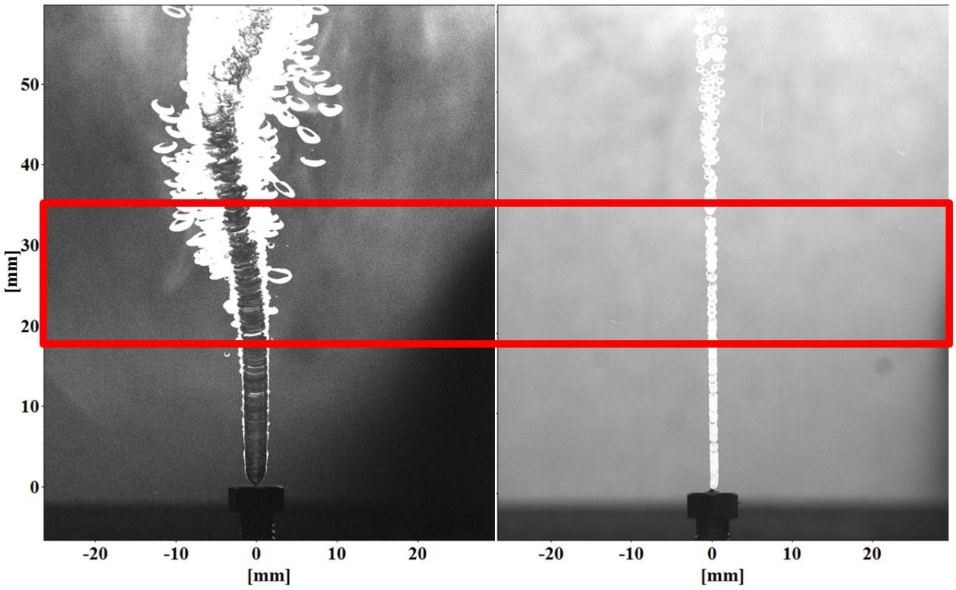

Figure 4.1: Averaged images of elliptical and spherical air bubbles; the measurement section is marked in red. From [102].

The generated bubbles were rising vertically close to the inlet nozzle, but after some centimetres started to wobble and left the measurement plane. For a planar optical measurement such a PIV or LIF the investigated target should be positioned centrically in the measurement plane. To find the appropriate investigation area, first images were taken in a larger 60x50 mm^2 window with a simple background illumination. The averaged image (Figure 4.1) showed that the ideal height for the measurements is 18 mm above the outlet. In this region the bubbles were still following the straight path upwards and they were enough far away from the nozzle.

To quantify O_2 mass transfer, the intensity counts recorded with the LIF camera were converted into equivalent concentration values as described in detail in subsection 2.3.2., 2.4.2 and in Table 2.4 (No.11).

Simultaneously with the LIF images, PIV images were recorded to gain information about the liquid flow around the bubbles. To achieve a sufficient amount of tracer particles around the bubbles, a high concentration of particles had to be introduced to the column. For the vector calculation a cross-correlation (multi-pass, decreasing size) PIV algorithm was used. More details of this processing can be found in subsection 2.4.1 and in Table 2.3, No. 11.

4.3. Liquid flow and concentration fields around single air bubbles

For the characterization of the flow field and mass transfer around single spherical and elliptical air bubbles, PIV and LIF techniques were used simultaneously.

During the single-bubble experiments with air bubbles, two main bubble forms and sizes were investigated: elliptical bubbles with a major-axis diameter of around 3 mm and spherical bubbles with a diameter of around 1 mm. Figure 4.2 shows two typical concentration fields behind these bubbles.

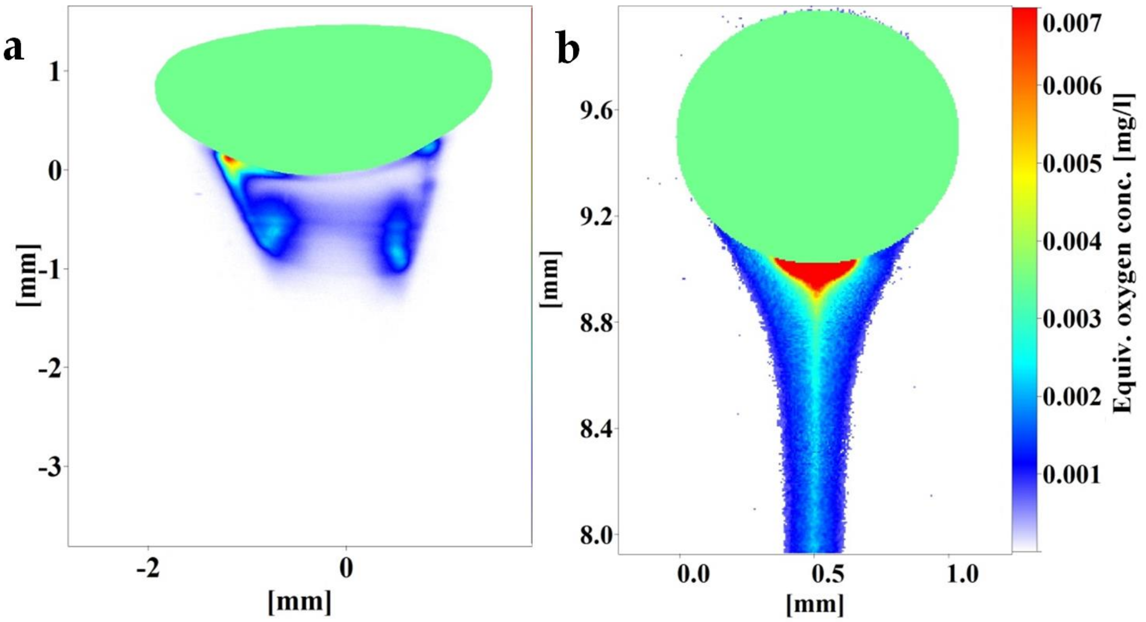

Figure 4.2: Equivalent oxygen concentrations around an elliptical air bubble (a) and around a spherical air bubble (b). From [102].

The single-bubble experiments with air bubbles show, just as the experiments with CO_2 bubbles, that due to the vertical velocity difference between the bubbles and the liquid bulk, the liquid with high dissolved oxygen concentration is transported from the bubble top surface to its bottom and a tail with higher oxygen concentration is formed. The form of the tail highly depends on the bubble shape. If the bubble is elliptical (Figure 4.2, a), vortex structures can be seen behind the bubble. If the bubble has a spherical shape (Figure 4.2, b), a single long tail forms behind the bubble with high concentration in the centre next to the bubble bottom. This tail shape is always the same if the bubble is spherical, but a variety of shapes are found for elliptical bubbles (Figure 4.3).

Here, the tail shape and the associated vortices depend on the bubble shape, motion, and the rising angle. Contrary to the spherical bubbles, where a stagnant cap forms at the bottom of the bubble, right behind the bottom of elliptical bubbles, just a small amount of dissolved gas can be measured in the centre.

Generally, a higher dissolved oxygen concentration can be found in the core of the generated vortex structures and on the sides, near the bubble bottom, where the liquid with high dissolved gas concentration tears off from the bubble surface. Similar mass transfer structures have been found in the literature in numerical simulations [182, 183] and experiments [27] behind elliptical bubbles.

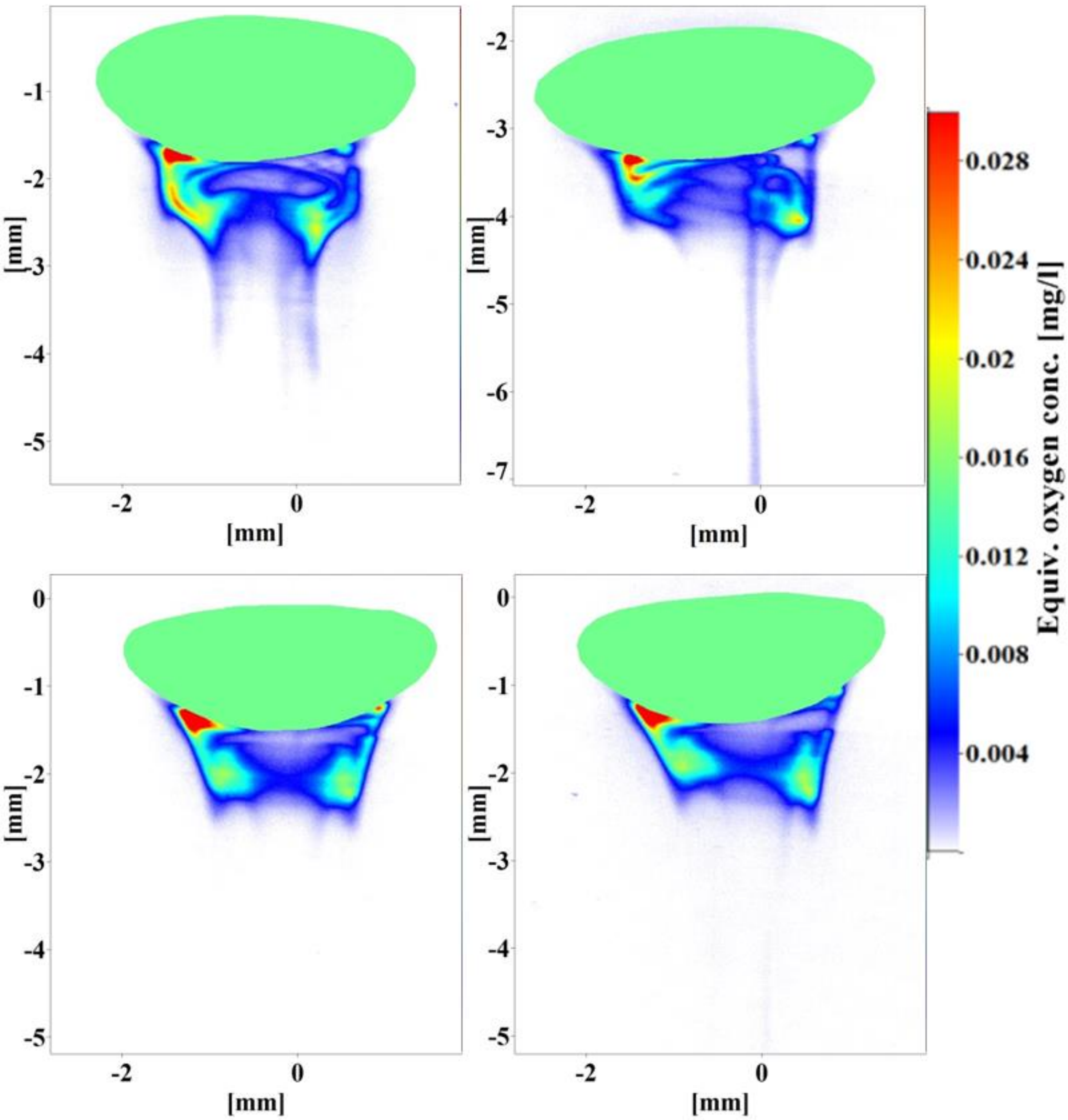

Figure 4.3: Equivalent oxygen concentrations around different elliptical air bubbles. From [102].

Figure 4.4 shows the simultaneous PIV results for a spherical bubble. As it was expected from the LIF images, the liquid flows around the bubble and leaves with a higher velocity at its bottom. This higher velocity remains in the tail and slowly weakens. The horizontal velocity component (Figure 4.4 b) shows a symmetrical velocity distribution around the bubble. On the vertical velocity component (Figure 4.4 c) it is noticeable, that the bubble pushes the liquid on its front, and on the sides recirculation zones form.

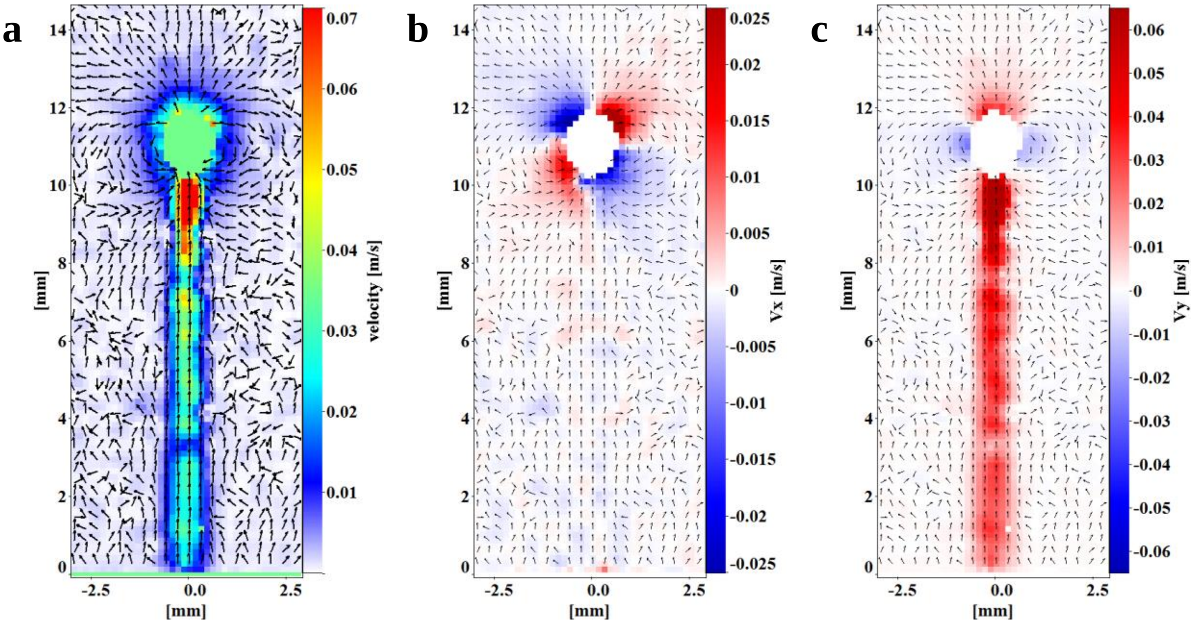

Figure 4.4: Flow field around a single spherical air bubble; velocity magnitude (a), horizontal velocity component (b), vertical velocity component (c).

The PIV results for elliptical bubbles (Figure 4.5 and Figure 4.6) show the same behaviour, but the velocity values are higher, because elliptical bubbles have a higher terminal velocity. Vortices are formed behind the bubble and the higher liquid velocity in the tail dissipates much faster.

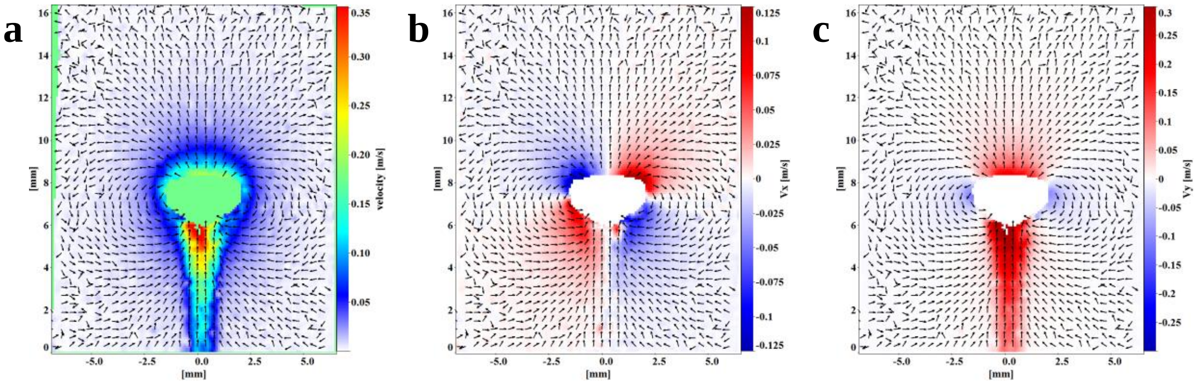

Figure 4.5: Flow field around a single elliptical air bubble, straight rising; velocity magnitude (a), horizontal velocity component (b), vertical velocity component (c).

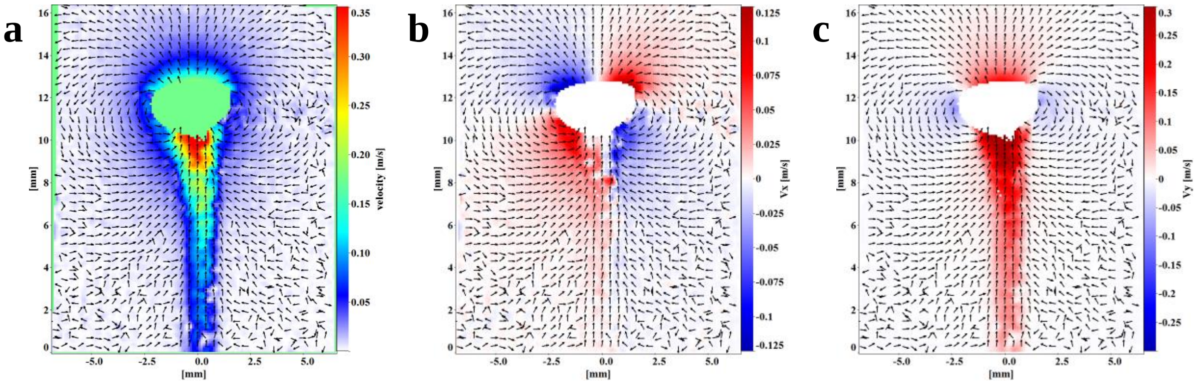

Figure 4.6: Flow field around a single elliptical air bubble, slant rising; velocity magnitude (a), horizontal velocity component (b), vertical velocity component (c).

Figure 4.7 shows horizontal and vertical velocity profiles at defined positions of the investigated bubbles. It is noticeable, that in the case of a spherical bubble (Figure 4.7 a and b) measurable horizontal velocities can be found just around the bubble, but not in the wake, where the vertical velocity is dominant. Contrarily to this, in the wake of elliptical bubbles (Figure 4.7 c-f) noticeable horizontal velocity can be measured up to 2 mm behind the bubbles. In the wake of the bubbles, the vertical velocity distribution differs as well. Behind a spherical bubble the vertical liquid velocity drops suddenly in the first 1 mm, but after this drop, the velocity decreases just slowly along the wake. In the wake of elliptical bubbles, the vertical velocity decreases gradually, not so sudden.

Moreover, these velocity profiles clearly show that around an elliptical bubble the horizontal velocity is around 8 times, the vertical velocity around 4 times higher than around a spherical bubble. Because of the higher liquid velocities, the liquid renewal on the surface of elliptical bubbles is faster and the liquid with dissolved gas is transported much faster into the wake. Therefore, it should lead to a higher mass transfer rate, than in the case of spherical bubbles.

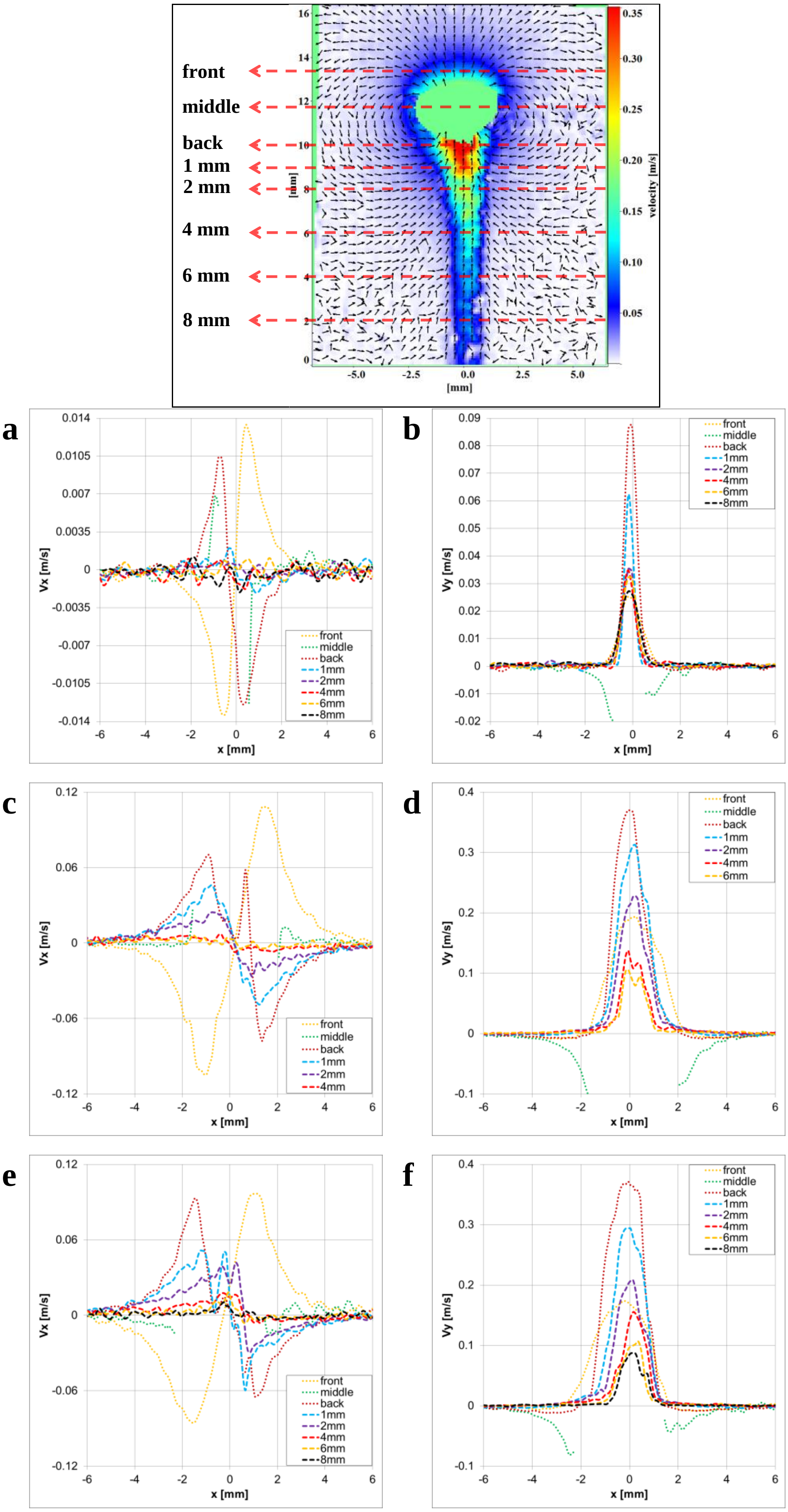

Figure 4.7: Horizontal and vertical velocity profiles: spherical air bubble (a,b); straight rising elliptical air bubble (c,d); and slant rising elliptical air bubble (e,f).

4.4. Conclusions

In this chapter the liquid flow and mass transfer around single ascending air bubbles in a stagnant fluid has been examined. The experiments were carried out in a bubble column with an inner diameter of 142mm, to avoid wall effects to the bubble motion. The final aim was to investigate the flow and the mass transfer at the same time around a single bubble.

Combined PIV-LIF experiments were carried out with air bubbles. Quantifying the amount of dissolved gas was very efficient due to the high fluorescence intensity of the applied tracer in this reaction system. The simultaneous images of PIV and LIF were taken 18mm above the nozzle, where the ascending bubbles are still following a straight path and stay in the generated laser light sheet. Therefore, it was possible to measure velocity and O_2 concentration simultaneously in the wake of the bubbles. The investigations showed: the dissolved gas is transported to the sides in the case of ellipsoidal bubbles, or to the bottom of the bubbles and forms a stagnant cap, if the bubble is spherical. It was also proved, that the liquid velocity around elliptical bubbles is much higher than around the spherical ones, which leads to a faster liquid renewal on the bubble surface and a higher mass transfer from the bubbles into the liquid bulk.

Similar measurements have been carried out in the same configuration with CO_2 bubbles. The results confirm a similar behaviour and have been presented in detail in [181]. They showed that dissolved CO_2 is transported to the sides and mainly the bottom of the bubbles, where it lowers the pH of the liquid and forms a long wake behind the bubble. In this wake, the pH is around 0.3 points less than in the bulk liquid. This small pH change can best be followed in the range of pH=6…7, where the applied fluorescent dye (uranine) fluorescence intensity changes the most dynamically. The acquired live background image with an inert second dye (2T-LIF) allowed for a much more exact calibration of the surrounding liquid pH.

In the light of these results it can also be concluded, that three dimensional measurements of the process, like e.g. tomographic PIV would allow obtaining more information about the flow around ellipsoidal, zigzagging single rising bubbles.

Chapter 5

Measurement results of the CO_2 -water system

Parts of the results and subsections presented in this chapter have been published in Heat and Mass Transfer (Kováts et al. [8]), in the International Journal of Multiphase Flow (Kováts et al. [16]) and in Chemical Engineering and Technology (Kováts et al. [23]).

Contents

5.1. INTRODUCTION 88
5.2. EXPERIMENTS WITH BUBBLE CHAIN 88
  5.2.1. Experimental setup and flow conditions for the combined LIF-PIV measurements 88
  5.2.2. Flow fields in the bubble column with bubble chain 89
  5.2.3. Concentration fields (pH) in the bubble column with bubble chain 92
  5.2.4. Conclusions 93
5.3. EXPERIMENTS WITH BUBBLE CURTAIN 94
  5.3.1. Experimental setups and flow conditions 94
    5.3.1.1. Experimental setups for liquid velocity measurements with PIV 94
    5.3.1.2. Experimental setups for pH measurements with 2T-LIF 96
  5.3.2. Flow fields in the bubble column with bubble curtain 97
  5.3.3. Concentration fields (pH) in the bubble column, obtained with 2T-LIF 102
  5.3.4. Conclusions 106

5.1. Introduction

This chapter deals with the optical measurements in the bubble column reactor with the first investigated reaction, the CO_2-chemisorption. These experiments were carried out to find out the effect of the gas flow rate, surface tension and viscosity on the mass transfer. The CO_2-chemisorption has already been explained in Chapter 2. The pH change of the liquid bulk can be followed by LIF or 2T-LIF techniques, which were used in the following experiments at different spatial and temporal resolutions. The liquid flow field in the bubble column was determined with PIV technique. All the measurements were carried out in the same model bubble column, which was also described in details in Chapter 2.

In these experiments two different cases were studied:

- Mass transfer of CO_2 and liquid flow in the bubble column with a bubble chain
- Mass transfer of CO_2 and liquid flow in the bubble column with a bubble curtain, generated by 4 nozzles.

Due to the various spatial and temporal resolutions and the continually developing technical equipment park in the department the experiments were not carried out always with the same equipment. To avoid unnecessary repetitions, the applied experimental setups will only be described briefly with referring to the detailed technical description in Chapter 2.

5.2. Experiments with bubble chain

First, the experiments with a bubble chain in the bubble column reactor will be presented. With simultaneous PIV and LIF measurements the flow field in the bubble column and the mass transfer were determined at two different gas flow rates. The aim of these experiments was to gain information about the mass transfer and liquid flow in the bubble column with a bubble chain generated with a single nozzle.

5.2.1. Experimental setup and flow conditions for the combined LIF-PIV measurements

The bubble chain of CO_2 was generated in the bubble column with one stainless steel nozzle, with an inner diameter of 0.25 mm. This nozzle was fixed in the centre of the sparger plate. The CO_2 bubbles were generated at 2 and 4 l/h air equivalent gas flow rate. The detailed measurement conditions can be found in Chapter 2 (Table 2.2, No. 4).

The experimental images were recorded with an Imager Intense CCD camera for LIF and on the opposite side with an Imager LX 8M CCD camera for PIV, simultaneously. For a better spatial resolution, the bubble column was divided into two measurement sections (Figure 5.1, F1 and F2). More technical details concerning this setup can be found in Chapter 2 (Table 2.6, No. 4).

From the pre-processed particle images, the liquid velocity was calculated with multi-pass PIV cross-correlation. More details of this processing can be found in subsection 2.4.1 and in Table 2.3, No. 4. At last, the calculated 1500 instantaneous velocity fields were averaged.

The recorded raw LIF images have to be also processed to determine the pH change due to CO_2 absorption into the liquid. The image processing is described in details in subsection 2.4.2. and the processing steps are summarized in Table 2.4., No. 3.

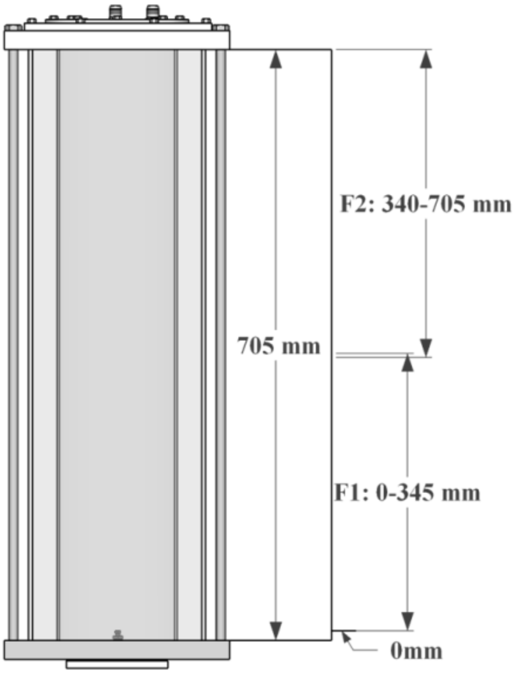

Figure 5.1: Measurement sections in the bubble column for the bubble chain measurements.

In the current processing, the 2T-LIF step was not used, because in this bubble chain experiment, the effect of bubbles and their shadows on the overall results was negligible. For this reason, this measurement was performed just with one fluorescent dye (uranin).

5.2.2. Flow fields in the bubble column with bubble chain

As expected, the structure of the velocity fields at 2 and 4 l/h air equivalent gas flow rate (Figure 5.2) are very similar. Bubbles rising in a chain occupy just the centre of the bubble column and they generate a vertical upward flow. The rising elliptical bubbles follow a helical path that is widening from bottom to top and their initial vertical velocity decreases.

Therefore, the liquid velocity decreases too. Close to the wall, where no bubble exists, a wide descending zone can be observed. Moreover, the mean horizontal velocity field (Figure 5.2, b and e) shows two large recirculation zones. The two counter-rotating zones on the top cover around 100 mm from the column height. In this area, the recirculation of the liquid is quite strong. The bottom recirculation zone is even bigger: it spreads up to 200-300 mm in the column. On the vorticity fields (Figure 5.2, c and f) these two strong recirculation zones can also be observed. Furthermore, this representation of the measured vorticity shows the very good overlap and continuity of the PIV results of the two fields of view, obtained from the two superimposed cameras.

At 2 l/h a maximum vertical liquid velocity of 0.066 m/s was measured, while at 4 l/h the maximum was 0.079 m/s. These highest velocities can be measured at 100-110 mm above the outlet (Figure 5.2 a, d and Figure 5.3, e), where the bubbles reach the terminal velocity and their 3D motion is still narrow. The vertical velocity is decreasing from this plateau to the top of the column, due to the 3D bubble motion.

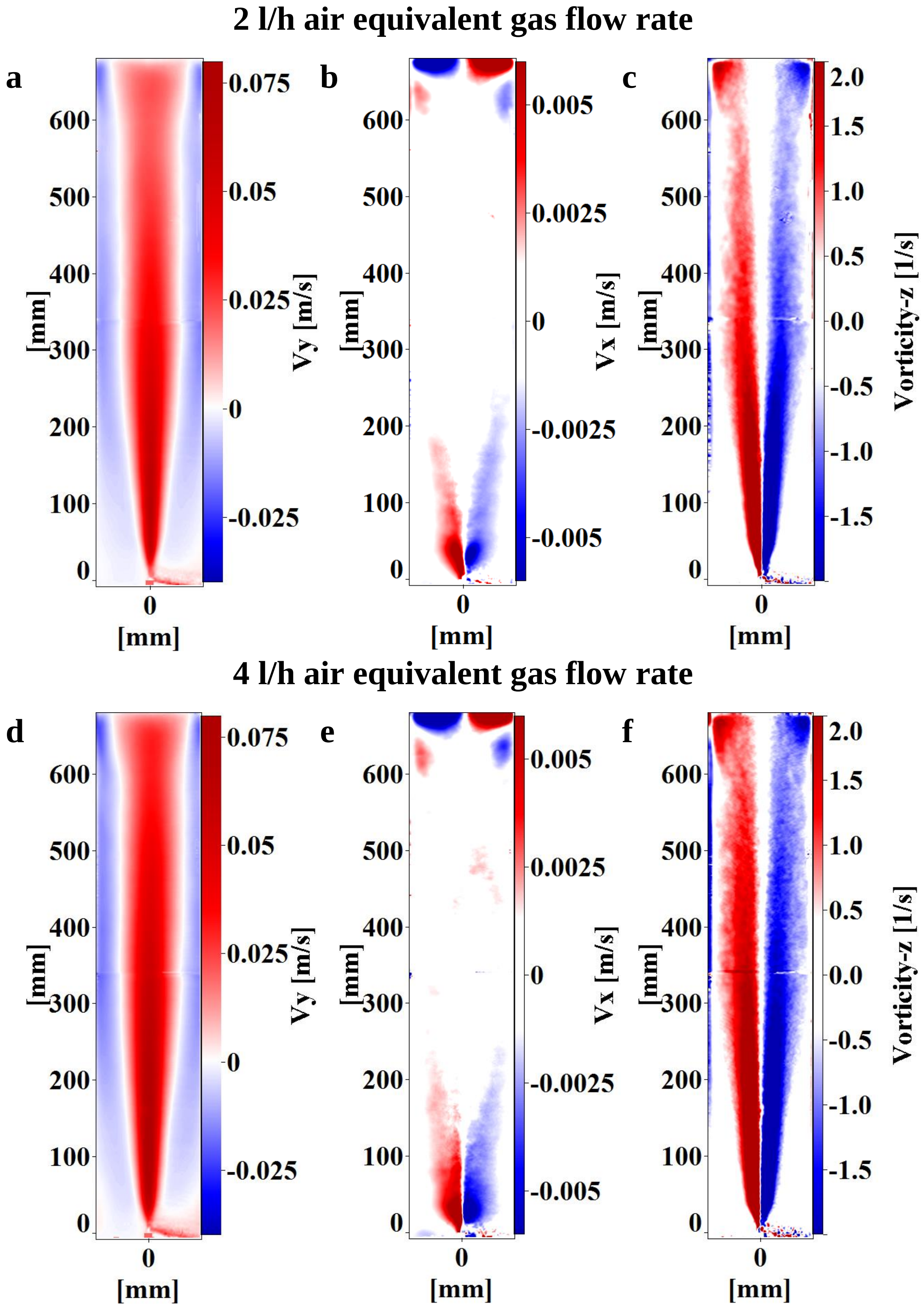

Figure 5.2: Mean vertical and horizontal liquid velocity field in a CO_2 bubble chain for 2 l/h (a and b) and 4 l/h (d and e) air equivalent gas flow rate, and the derived vorticity for both cases (c and f).

The horizontal velocity profiles of the horizontal and vertical velocity components (Figure 5.3, a-d) show these motions in details. With increasing height, the maximum of the vertical velocity decreases in both cases and the profiles are more flattened (Figure 5.3, a and b). At the same time, the backflow velocity close to the wall is increasing. In the recirculation zones, at the bottom and on the top, high horizontal velocities can be found, but heading to the middle of the column, the horizontal velocities drastically decrease (Figure 5.3, c and d). On the vertical profiles of the mean vertical velocities at 2 l/h and 4 l/h gas flow rates (Figure 5.3, e), a systematic shift can be observed in the velocity values, due to the doubled gas flow rate. This average shift in the measured vertical velocities amounts to 0.012 m/s.

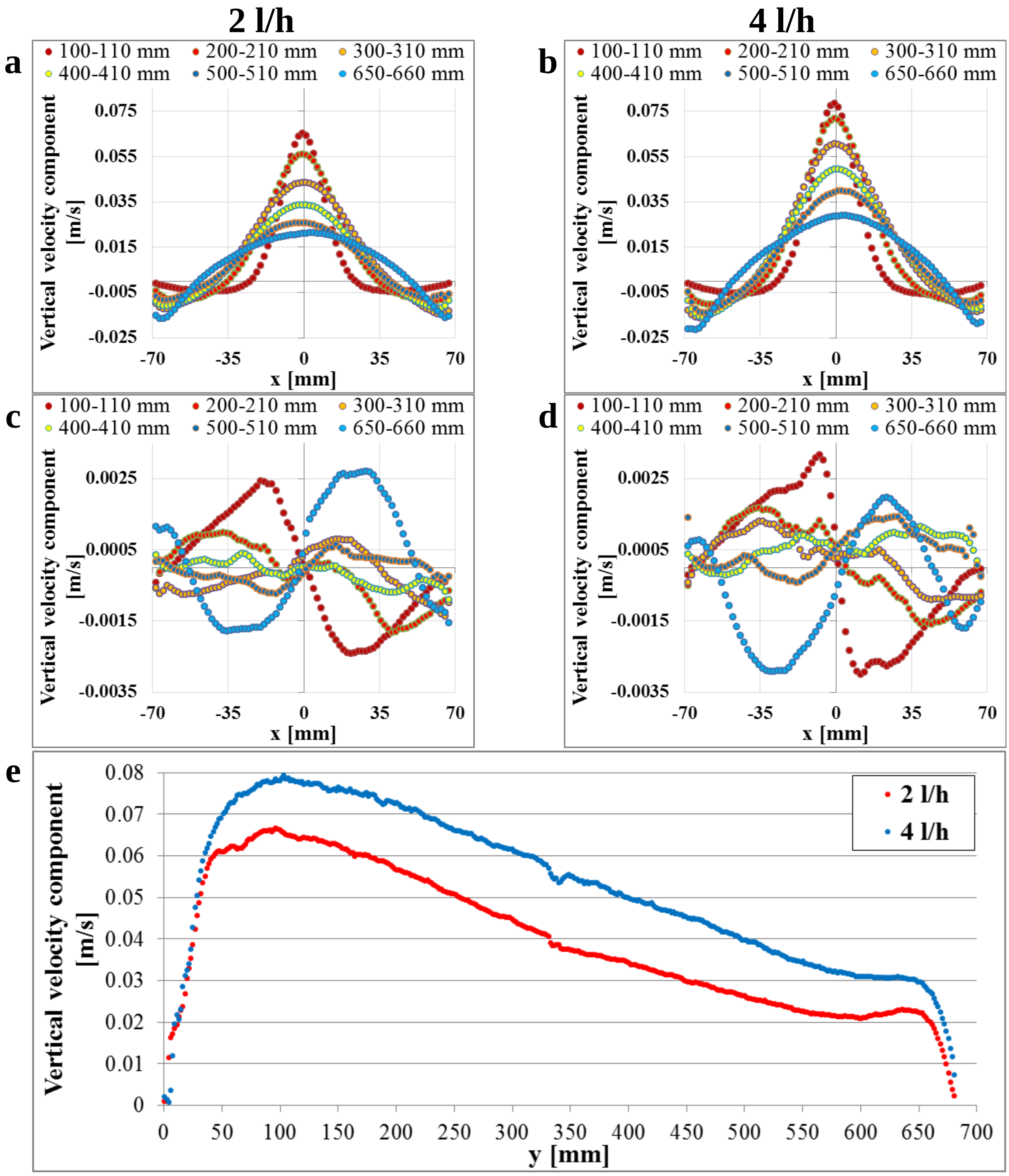

Figure 5.3: Mean liquid velocity profiles in a CO_2 bubble chain in different sections: vertical (a, b) and horizontal velocity component (c, d) at different heights; vertical profile of vertical velocity component in the centre of the bubble column (e).

5.2.3. Concentration fields (pH) in the bubble column with bubble chain

From the processed pH images, horizontal plots were extracted at seven different heights (Figure 5.4) for the first 300 seconds of an experimental run. On the results from the first investigation window (Figure 5.4, a and c), it can be seen, that with increasing height the speed of the pH change increases.

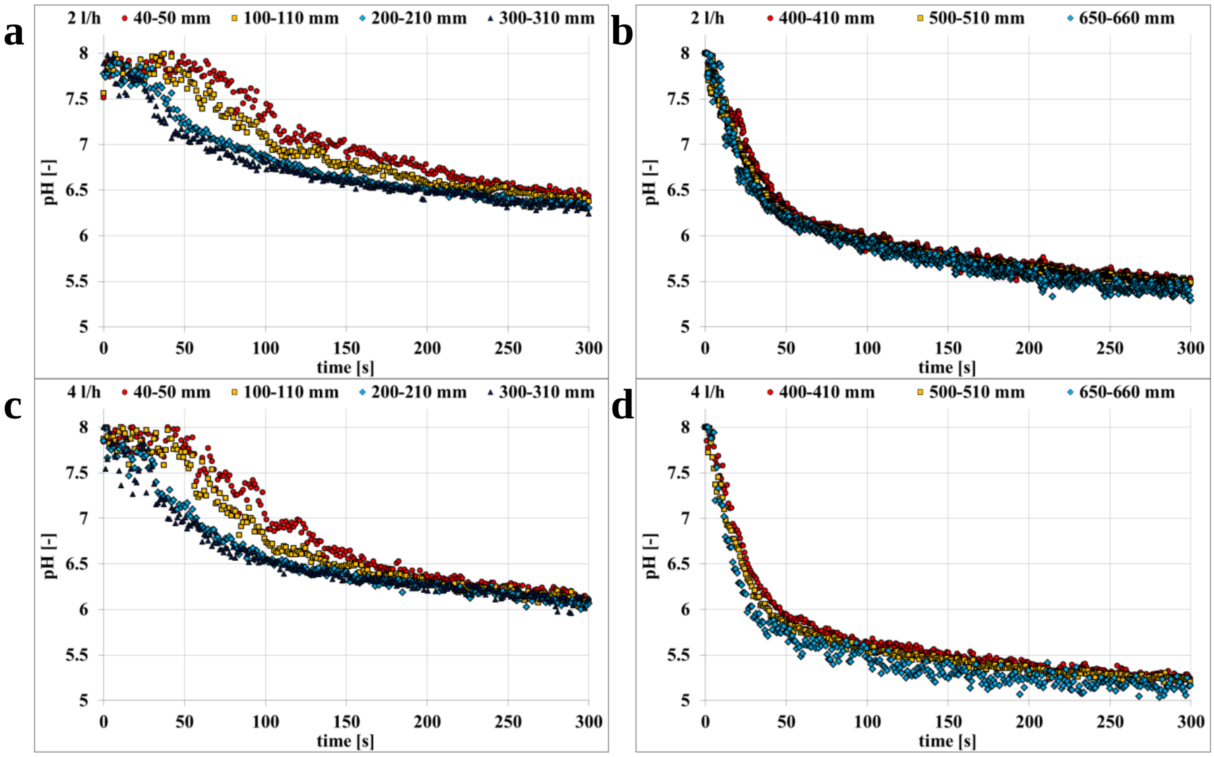

Figure 5.4: pH change at different heights in the bubble column for a CO_2 bubble chain during the first 300 seconds at 2 l/h (a and b) and 4 l/h (c and d) air equivalent CO_2 gas flow rate.

At the bottom of the bubble column, up to 50 seconds, almost no reaction can be observed in both flow rate cases. At the heights 200 mm and 300 mm the pH starts to decrease much faster, from 15-20 seconds on. This different progress can be explained with the bubble and liquid motion. In the first, around 100 mm from the bottom, the bubbles rise almost straight in a very narrow area, therefore the bubble velocities are the highest here and the residence time is the smallest. There, the upward motion of the surrounding liquid is similarly high (Figure 5.3, e). Therefore, the liquid with dissolved gas is quickly transported upwards. Moreover, because of the recirculation zone at the bottom (Figure 5.2, b and e), fresh, not yet reacted liquid is transported from the outer sections to the column centre and this slows down the pH change in the bottom section as well. From 150 mm, bubbles start to spread in a wider area, their upward velocity decreases and thus their residence time increases. Consequently, it leads to a higher dissolved gas concentration in that upper region, which induces a faster pH change (Figure 5.4, b and d).

After around 200 seconds from the start of the bubbles, the pH becomes similar in all of the four investigated bottom cross sections and the progress of pH change slows down. In the first 300 seconds at 2 l/h gas flow rate the pH starting pH=8 decreases to pH=6.5 (Figure 5.4, a), while at 4 l/h gas flow rate, a pH of 6 can be measured at the end (Figure 5.4, c). In the top sections the pH change progress is much faster and almost similar in all three examined heights. Just a small time delay can be noticed between the three investigated sections (Figure

5.4, b and d). After the first bubbles, during the first 50 seconds, the amount of dissolved gas raises significantly, thus the pH decreases steeply too. The reasons of this fast change are the recirculation zones at the top of the column (Figure 5.2, b and e). After the bubbles reach the surface, a high amount of dissolved gas accumulates in the top section since it is trapped in the vortices of the recirculation zone. Moreover, due to the recirculation zone, liquid with higher dissolved gas amount can spread much faster in the whole column width and causes a fast pH change. In few seconds the flow recirculation in the whole column is developed and this concentrated dissolved CO_2 is transported back downwards near the walls. After 50 seconds, the decrease of pH becomes slower. At 2 l/h gas flow rate an end pH value of 5.5 was reached in 300 seconds, while at 4 l/h pH=5.2 was measured.

The difference in the speed of the pH change at different flow rates is also distinguishable on Figure 5.4. 20-40 seconds are needed in the top section for the pH to drop from the initial pH=8 to a value of 6.5 (Figure 5.4, b and d), while at the bottom, 160-260 seconds are needed for the same pH difference (Figure 5.4, a and c). Then, the decrease from pH=6.5 to pH=6 needs just 10-20 seconds at the top at higher gas flow rate, while with 2 l/h gas flow rate this change needs 40-50 seconds. Much larger time differences can be seen in the bottom section (Figure 5.4, a and c). Here, the mixing is not so effective as in the top section (Figure 5.4, b and d). The strong upward liquid and bubble flows in the centre of the column transport the dissolved gas to the top. Just a small amount of liquid with lower pH can flow back near the wall and the pH change considerably slows down in the bottom section: 210-250 seconds are needed here for the pH change from 6.5 to 6. Moreover, the pH value of 5.5 could be reached just in the top sections, the 600 seconds recording time was not enough for that in the bottom section.

5.2.4. Conclusions

In this chapter the liquid velocity and the mass transfer measurements with a CO_2 bubble chain were presented. The aim of these experiments was to characterize the liquid flow and investigate the pH change at two different gas flow rates. To characterize the liquid flow PIV was employed. Using two investigation windows along the column height, a full description of the hydrodynamics in the whole bubble column was obtained, showing much lower liquid velocities compared to the bubble velocities, with a clear recirculation loop near the walls along the whole column and recirculation zones at the top and at the bottom. As it was expected, with higher gas flow rate the liquid velocity is increased as well, but the overall character of the flow in the column remained the same.

Through the LIF experiments, the effect of the gas flow rate was investigated on the mass transfer through a neutralization reaction. These experimental results have shown that higher mass transfer from gas to liquid can be achieved with higher gas flow rate. The time to reach a certain pH in the column is prolonged at lower gas flow rate. It has been found, that the speed of the pH change decreases from the top of the column to the bottom. The reason for that is the recirculation loop at the top, where the liquid with dissolved gas is trapped. From this loop just a small amount of liquid is transported near the wall downward to the column bottom, with a low velocity, therefore a remarkable delay in pH change exists at the bottom.

5.3. Experiments with bubble curtain

This chapter within the CO_2-water system deals with the experiments with a bubble curtain in the model bubble column reactor. In these experiments the bubble curtain was generated with four in-line nozzles. The induced bubbles occupy almost the whole column width and because of the swarm effect and the interaction between the bubbles, the liquid flow becomes fluiddynamically more complex than the liquid flow with a bubble chain. For this reason, the bubble curtain was investigated in more detail. Preliminary experiments were carried out separately with low-speed PIV and LIF measurements in de-ionized water [8]. Then, with a high-speed recording system, purchased in the meantime, time-resolved high-speed PIV measurements were realized again in pure water [23]. These high-speed recordings allowed calculating more precisely the liquid flow velocities near the inlet nozzles. With the experience based on the previous measurements, simultaneous low-speed PIV and 2T-LIF measurements were accomplished in liquids with diverse viscosity and surface tension to investigate those effects on the liquid flow and mass transfer [16]. In these experiments the numbers of investigation windows were reduced. All these results have been published in the International Journal of Multiphase Flow [16], in Heat and Mass Transfer [8] and in Chemical Engineering & Technology [23].

5.3.1. Experimental setups and flow conditions

The bubble curtain of CO_2 was generated in the bubble column with four, in-line placed stainless steel nozzles, with an inner diameter of 0.25 mm. Through these nozzles, bubbles with a diameter of 1.5-6.5 mm are produced. The flow rate of the CO_2 gas was set up through a variable-area flow-meter to 7.5 l/h air equivalent flow rate (6 l/h CO_2 flow rate). To obtain different viscosities, 0, 25, and 50 m% water-glycerol mixtures were used for the simultaneous 2T-LIF and PIV measurements. To vary the surface tension, 1.9 g/l sodium dodecyl sulphate (SDS) was added to the solutions. The physical properties of these mixtures can be found in Chapter 3, Table 3.1.

Unfortunately, the surfactant SDS caused an interaction with pyridine-2 that lead to a very strong image intensity, which was also visible on the uranine images. It also changed with decreasing pH and could not be used as a pH-independent background image. As no chemical explanation could be found for this phenomenon, the pH measurements have only been done without surfactant, thus only varying the viscosity. In the cases where surfactant was added, simple PIV measurements were carried out without fluorescent dyes for the simultaneous determination of pH. The detailed measurement conditions of the experiments can be found in Chapter 2 (Table 2.2, No. 5-8).

5.3.1.1. Experimental setups for liquid velocity measurements with PIV

The PIV measurements in the bubble column were realized with three different technical setups. The detailed technical information about these measurement setups can be found in Chapter 2, Table 2.6, No.5, 6 and 8.

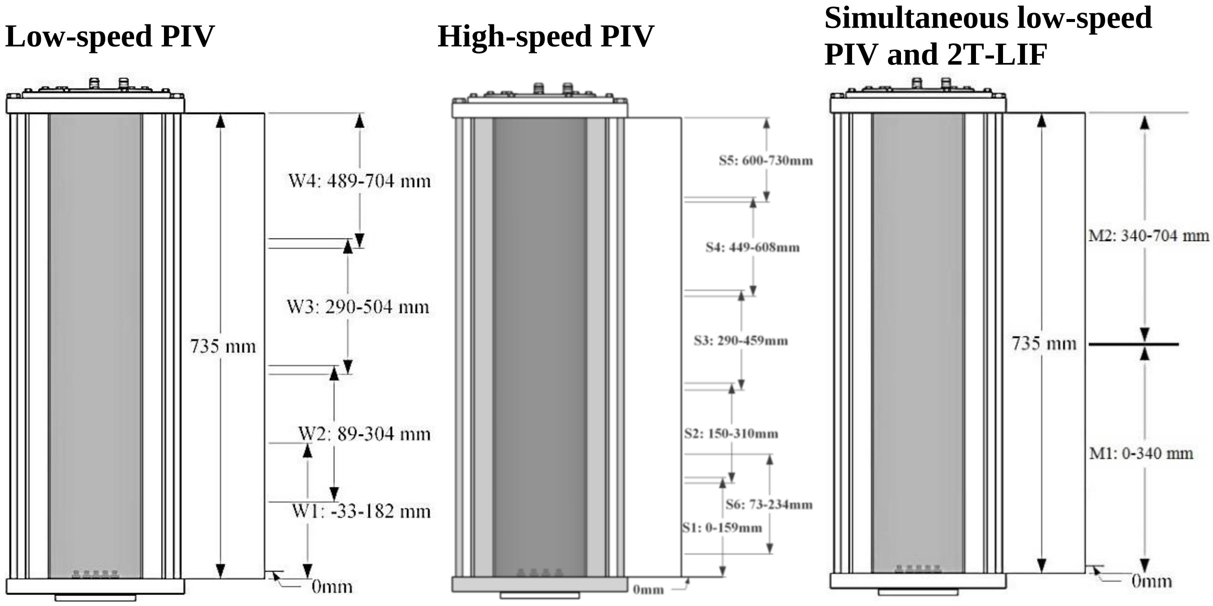

Figure 5.5: Experimental setup for low-speed PIV in a CO_2 bubble curtain and measurement windows.

Since the field of view of one camera with an appropriate spatial resolution covers only a part of the overall bubble column height, the bubble column has been divided into several measurement sections. These sections were monitored one after the other by moving the camera(s) and laser light sheet to the corresponding height. Accordingly, depending on the employed camera lens and the camera resolution, 2-6 measurement sections were chosen to cover the whole column height. The distribution of these sections is presented on Figure 5.5 for each experimental setup.

Because of the applied diverse cameras and different number of investigated sections, the recording speed, the spatial resolution and the final vector resolution differs also. These differences are summarized in Table 5.1.

During the PIV experiments in each investigation window separate image sets were acquired and from these, individual instantaneous velocity fields were calculated with a common PIV cross-correlation algorithm. More details of this processing can be found in subsection 2.4.1 and inTable 2.3, No. 5, 6 and 8. As final step, the individual PIV-images were averaged.

Table 5.1: Recording properties of each PIV system.

	Recording speed	**Number of investigated sections**	**Number of recorded images per section**	**Averaged time**	**Spatial resolution**	**Vector resolution**
Low-speed PIV	3.33 Hz	4	2x1000	600 s	0.15 pixel/mm	0.42 vector/mm
High-speed PIV	1000 Hz	6	20x3140	62.8 s	0.08 pixel/mm	1.54 vector/mm
Simultaneous low-speed PIV and 2T-LIF	3.33 Hz	2	4x1000	1200 s	0.15 pixel/mm	0.83 vector/mm

In the experiments, the laser light sheet comes from the left side of the column and bubble shadows develop on the opposite right side of the bubbles. The flow field reconstruction in these areas is limited, especially in the bottom section, close to the nozzles, where the bubble swarm is still dense and the bubbles are rising in the light sheet. For this reason, the calculated PIV-images contain many masked areas on the shadow side. In the simultaneous PIV and 2T-LIF experiments the signal of the PIV-particles was reduced noticeably on the bubble shadow side due to the light absorption of the tracer dyes, added for LIF. Even with the high number of images acquired here, a reliable mean of the velocity fields could not be achieved for the right half of the column in the simultaneous PIV and 2T-LIF experiments. Therefore, in the following, only the left half of the resulting 4000 vector fields was averaged for each glycerol-water-surfactant mixture. In the other two – high-speed and low-speed – experiments, where only PIV-particles were added to the liquid, the average flow field was obtained over the whole column width.

5.3.1.2. Experimental setups for pH measurements with 2T-LIF

Two measurement campaigns were carried out with 2T-LIF for the measurement of the pH in the bubble column, changing due to the absorption reaction of CO_2. In the first case the pH change was investigated in pure de-ionised water; in the second case the effect of viscosity on the mass transfer was studied and simultaneously the liquid flow was recorded also.

For the 2T-LIF method, a very accurate image overlapping is mandatory. For this reason, the LIF cameras were coupled with a 50%-50% beam splitter (Figure 2.13, 7.), that allows for the observation of the same region of interest with very low perspective distortion. In order to obtain a sufficient geometrical resolution, the full column height was divided into four measurement sections (Figure 5.6, b, W1-W4) in the first, and into 2 sections (Figure 5.6, c, M1 and M2) in the second measurement campaign, which are monitored one after the other by moving the cameras and laser light sheet to the corresponding height. More details of the technical equipment can be found in Table 2.6, No. 7 and 8.

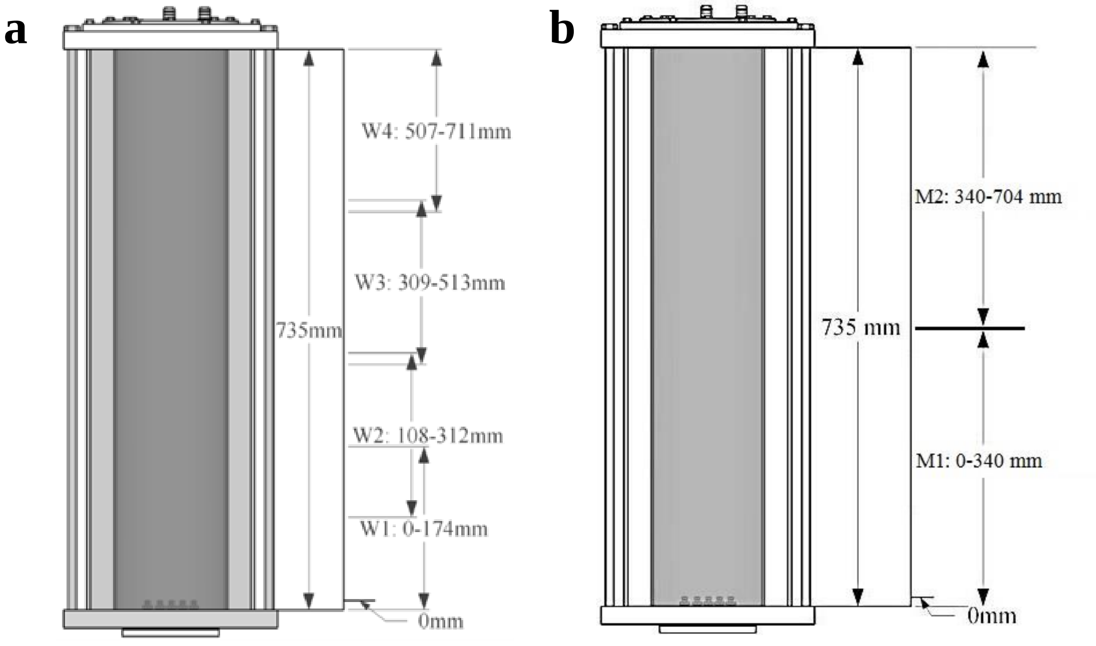

Figure 5.6: Measurement windows for the two 2T-LIF measurement campaigns (a and b).

The pH-change during absorption of CO_2 from the bubbles in the liquid was visualized and quantified with 2T-LIF in the bubble column. In order to transform the measured fluorescence intensities into pH-values, a calibration curve for each water/glycerol/SDS-solution had to be established. To this end, a proper image processing was necessary, which is described in detail in subsection 2.4.2. The processing steps can be also found in Table 2.4., No. 7 and 8.

5.3.2. Flow fields in the bubble column with bubble curtain

After combining the results of all measurement windows (obtained separately) a full view of the liquid flow field within the column can be obtained. Both, the high-speed and low-speed results show nearly the same vertical and horizontal velocity fields. As expected, the averaged images show an almost symmetric vertical velocity field in the bubble column, with a large ascending part around the centre of the column and a thin descending zone near the column walls (Figure 5.7). The small differences in the flow structure come from the different spatial resolution and from the length of the averaged time (see Table 5.1). It appears that, due to the high temporal resolution of the PIV images, the 62800 images already taken at each position during the high-speed experiments are still not fully sufficient to get the mean velocities in the column; velocity changes still occur over a longer time-scale. Still, a very good reconstruction of the hydrodynamic fields is already possible in the whole column, compared to the low-speed result, which was obtained over a ten times longer time range.

Figure 5.7 shows also the measured mean horizontal velocity field. As expected, the recirculating loop at the top of the column can clearly be recognized, having the highest radial component. On this horizontal velocity field, compared to the velocity field obtained with the bubble chain (Figure 5.2), the second recirculation zone at the bottom does not exist. The reason for that are the bubbles from the outer nozzles, that disturb the axi-symetrical flow field at the bottom of the column and do not allow a clear recirculation zone. Over the height of the column, positive and negative fluctuating regions are alternating, showing the outward spreading of the bubbles, entraining the liquid along their zig-zagging path.

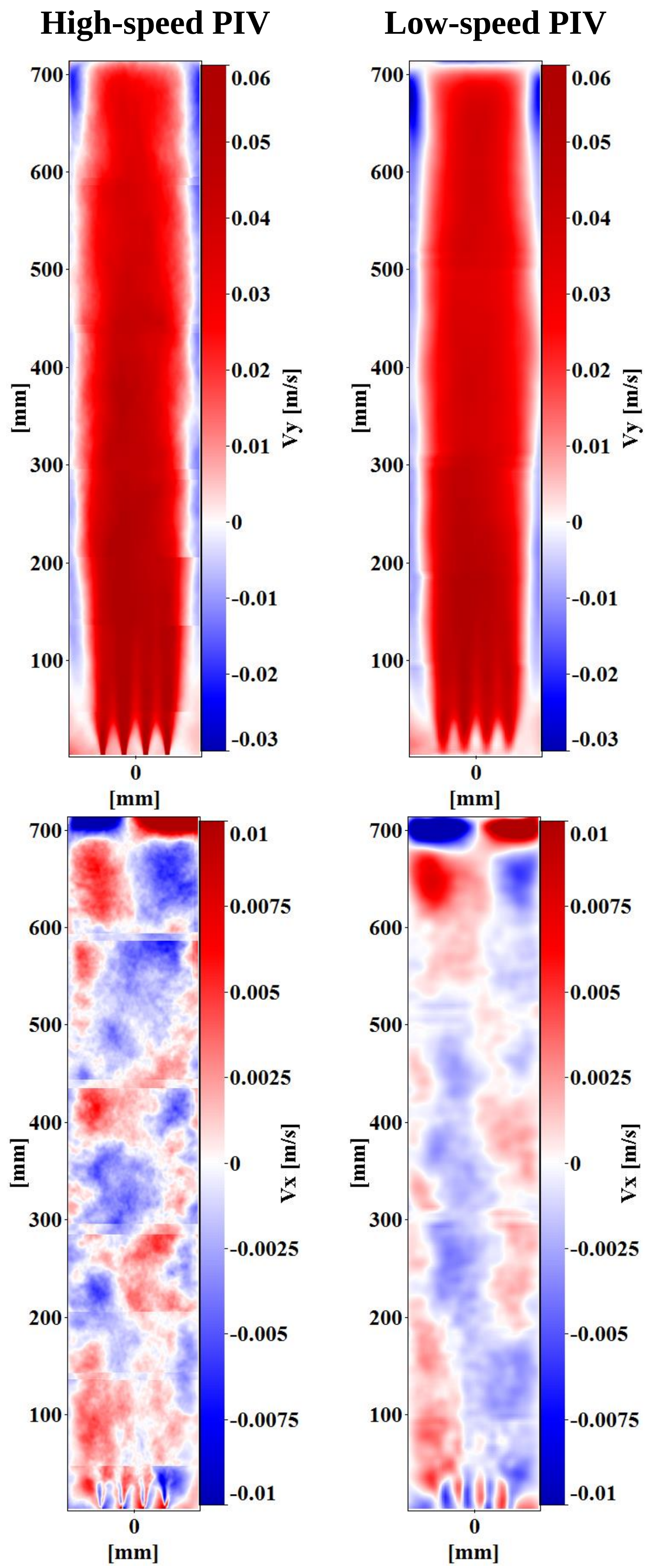

Figure 5.7: Mean vertical and horizontal liquid velocity fields in a CO_2 bubble curtain, obtained from high-speed and low-speed PIV measurements.

The main benefits of the high-speed recordings, the higher spatial and temporal resolution, capture more accurately the flow close to the outlet nozzles and close to the bubbles. For this reason, the high-speed results show a slightly higher vertical liquid velocity especially at the bottom of the column where the jet-like structures, generated by the bubbles, are more distinct (Figure 5.8, b).

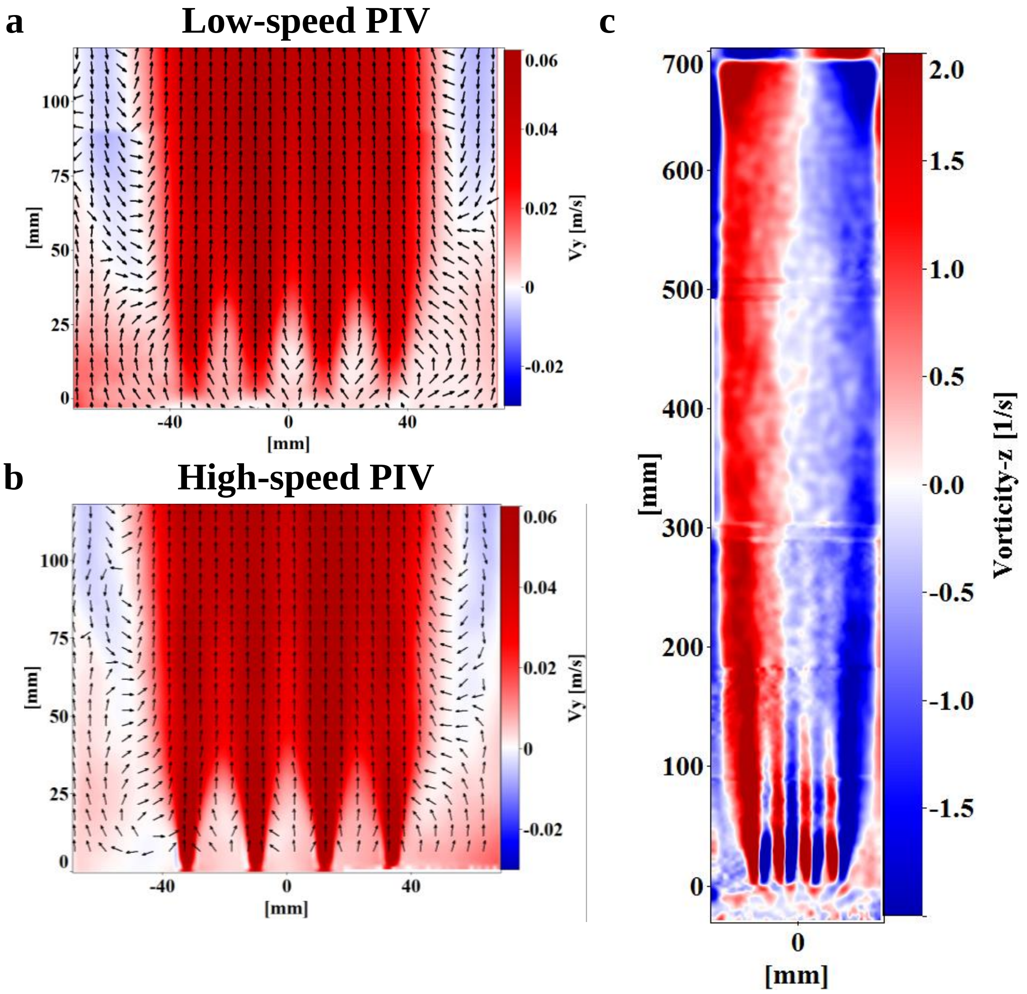

Figure 5.8: : Mean vertical velocity at the bottom of the column obtained from the low-speed (a) and from the high-speed (b) experiments and vorticity distribution in a CO$_2$ bubble curtain (c), obtained from the low-speed experiments.

The vorticity above each nozzle in the curtain shows a similar pattern (Figure 5.8, c) as it was observable above the single nozzle in the bubble chain (Figure 5.2). The vorticity in the centre is the strongest, it diminishes to the outer nozzle. Furthermore, at the top of the column, strong vortex structures, due to the recirculation on the top, can be observed.

Based on the experience gained from the low-speed and high-speed PIV measurements, simultaneous low-speed PIV and 2T-LIF measurements were carried out in liquids with different viscosity and surface tension to investigate those effects on the liquid flow and mass transfer.

To compare the flow fields of the different PIV setups, horizontal velocity profiles were taken at six different heights (Figure 5.9). At a first glance, the vertical velocity profiles are very similar in most cases and for both setups, but the high-speed PIV results show a bit higher vertical velocities at almost all plotted heights. The reason for that was described before; with higher spatial resolution the liquid flow near the bubbles can be captured most accurately, therefore the higher mean velocities.

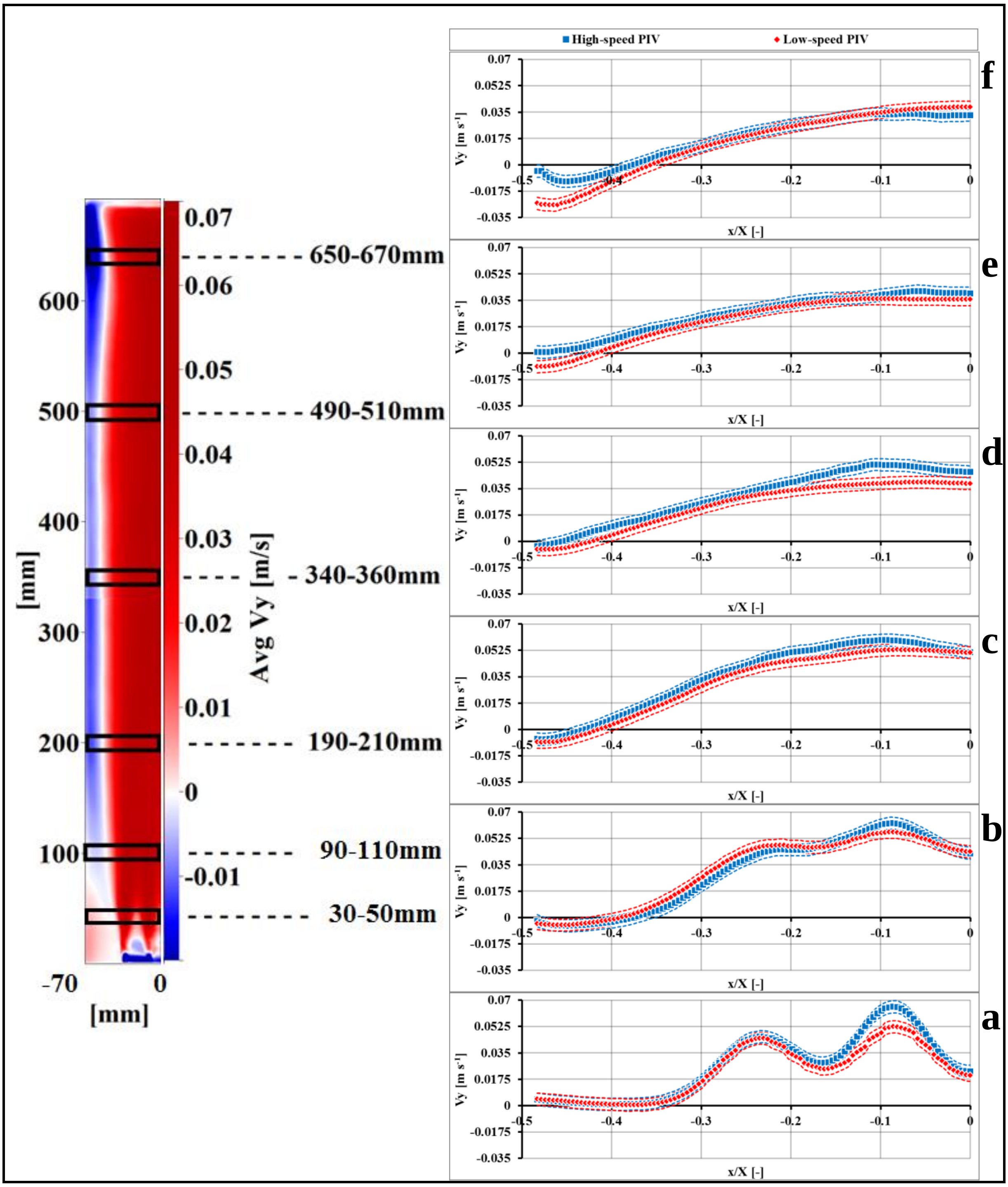

Figure 5.9: Comparison of mean vertical velocity profiles (marks) obtained from the high-speed and low-speed PIV experiments in a CO_2 bubble curtain at 30-50 mm (a), 90-110 mm (b), 190-210 mm (c), 340-360 mm (d), 490-510 mm (e), 650-670 mm (f), together with standard deviation (dashed).

At 30-50 mm, near the bottom of the column, the effect of the four bubble nozzles on the liquid velocity is clearly visible (Figure 5.9, a). The bubbles rise here close to each other and generating small-scale flow structures. Due to the twice higher spatial and 2-3 times higher vector resolution of the high-speed measurements (Table 5.1) the liquid velocity is captured more accurately in this range with that setup. Within the first 0.3 m, as long as the bubble swarm is still concentrated, the mean vertical velocity reaches a maximum value around 6 cm/s (Figure 5.9, b and c). Above 0.3 m, the bubbles start to spread sideways and finally occupy the whole width of the column, the process finishing at a height around 0.5 m. As a consequence of bubble spreading, the overall mean velocity is decreasing slightly (Figure 5.9, d and e). In the top window, a clear and relatively large backflow near the reactor wall exists (Figure 5.9, f), showing the recirculation loop of the liquid after the bubbles leave through the free surface.

This comparison shows that both PIV setups achieved similar velocity fields. Both setups have benefits and drawbacks and therefore it is hard to choose the most accurate one. Generally, the higher the number of investigation windows, the more precise the results, because of a higher spatial resolution. However, calibrating several measurement windows is a more difficult task, inducing probably supplementary errors. The temporal effort to run and process the experiments increases as well enormously. On the other hand, with high-speed time-resolved PIV it is possible to acquire the small-scale velocity fluctuations, but again, it is much more time and storage consuming than a low-speed recording. Therefore, long time-scale velocity fluctuations can probably not be recorded. Therefore, if small-scale structures and fluctuations have to be investigated, a high-speed time-resolved PIV system with high spatial resolution can be a good choice, while when a coarse mean flow field is the aim, a low-speed PIV system with lower spatial resolution could be sufficient.

Taken into account the above mentioned reasons, a low-speed PIV system with two investigation windows was employed in the further experiments with different de-ionised water–glycerol–surfactant mixtures.

For the mean velocity fields presented here, 4000 images were averaged in each section and for each solution. As shown in Figure 5.10, a, the rising bubbles generate an ascending flow in the centre of the column, which reaches the surface and evolves into a thin, descending backflow near the wall. To analyse the flow fields of the 6 different solutions, horizontal velocity profiles were taken at five different heights (Figure 5.10, b-f). At a first glance, the vertical velocity profiles are very similar in most cases and for all the different solutions.

The biggest difference can be recognized for the lowest velocity profiles at 90-110mm, close to the nozzles (Figure 5.10, b). It is clearly visible that in the 50% glycerol-water mixture, the bubble curtain is still concentrated in lines above the outlets, with and without surfactant. Therefore, higher velocity peaks are observable. In the 50% glycerol-water mixture with surfactant, this effect is much stronger because the bubbles are rising in straight lines above the nozzles for much longer (Figure 3.8).

Above 0.2 m, the bubbles begin to occupy the whole column width; thus the vertical velocity profiles become more even. After 0.35 m, the highest vertical liquid velocity can always be measured in the 50% glycerol solution, followed by the 25% glycerol solution and the distilled water. In the solutions with surfactant, these differences are much smaller and the velocity profiles are almost identical. The reason for this behaviour is that in the 0% and 25% glycerol solutions without surfactant, significant bubble shrinkage was observable which affects bubble motion, while in the solutions with surfactant, the average bubble sizes and velocities are very similar, which results in similar liquid motion.

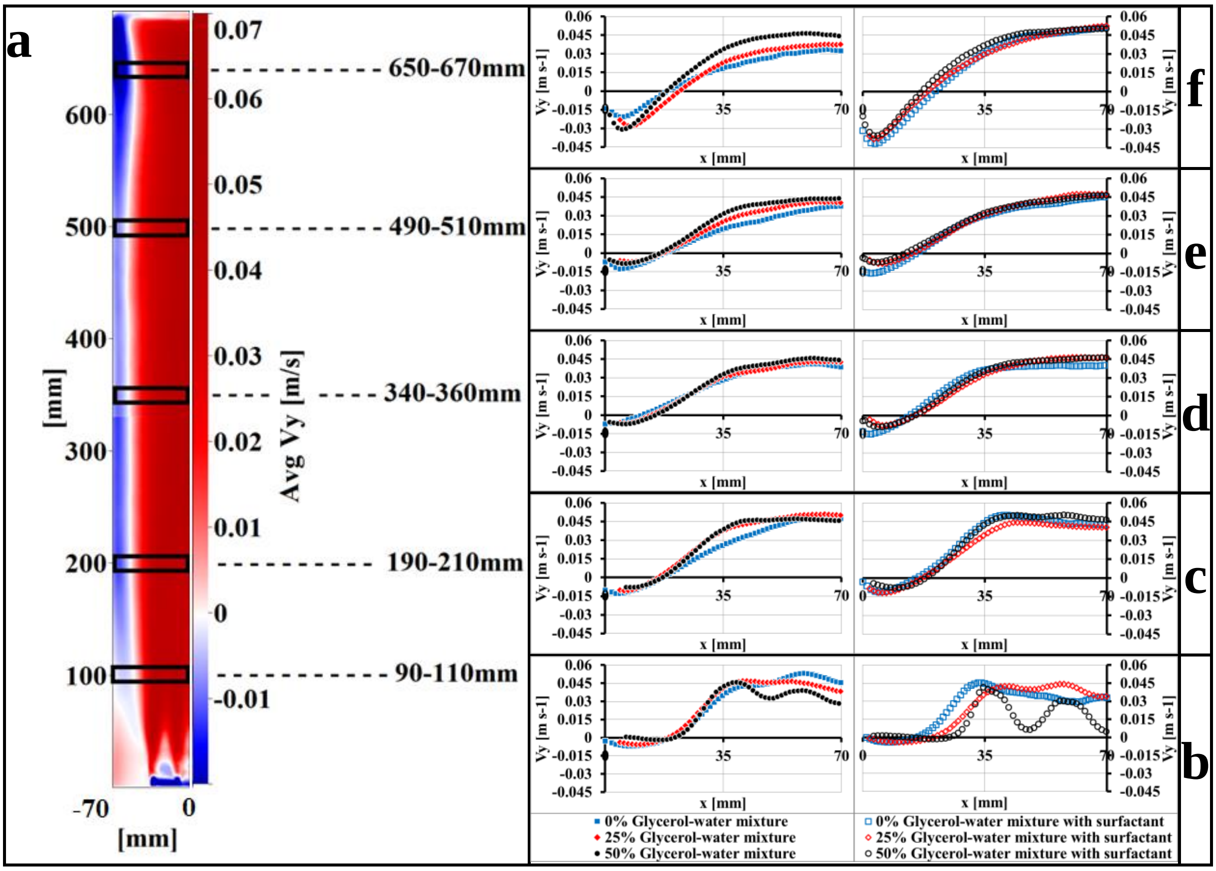

Figure 5.10: Mean vertical liquid velocity in a CO_2 bubble curtain in a 25% Glycerol-water mixture with (a) 1.9 g/l surfactant, (b) mean vertical velocity profiles at 90-110 mm, (c) 190-210 mm, (d) 340-360 mm, (e) 490-510 mm, and (f) 650-670 mm for the mixtures without surfactant and those with 1.9 g/l surfactant. From [16].

5.3.3. Concentration fields (pH) in the bubble column, obtained with 2T-LIF

The exemplary snapshot images (from the first measurement campaign with pure de-ionized water) in Figure 5.11 are taken 40 seconds after starting the CO_2-injection in the centre plane of the column, cutting out the 4 gas inlets at the bottom of image W1. It is clearly visible, that the pH has already decreased considerably from around 8 at the starting time to values smaller than 6 at the top of the column (W4). This shows the differences in mass transfer along the height of the column.

The exemplary snapshots from the second measurement campaign show similar results as well (Figure 5.12). These snapshots were taken at measurement sections M1 and M2, 30 seconds after the start of the measurement (start of bubbles). It can also be recognized here, that at the top of the bubble column (Figure 5.12, b) the liquid already reaches a pH of around 6, but the pH at the bottom is still higher than 7 at that moment (Figure 5.12, a). This decreasing pH from the bottom to the top of the bubble column is also visible along a vertical profile line (Figure 5.12, c) in the centre of the column. With increasing height, the pH values decrease, meaning that the concentration of dissolved CO_2 is increasing.

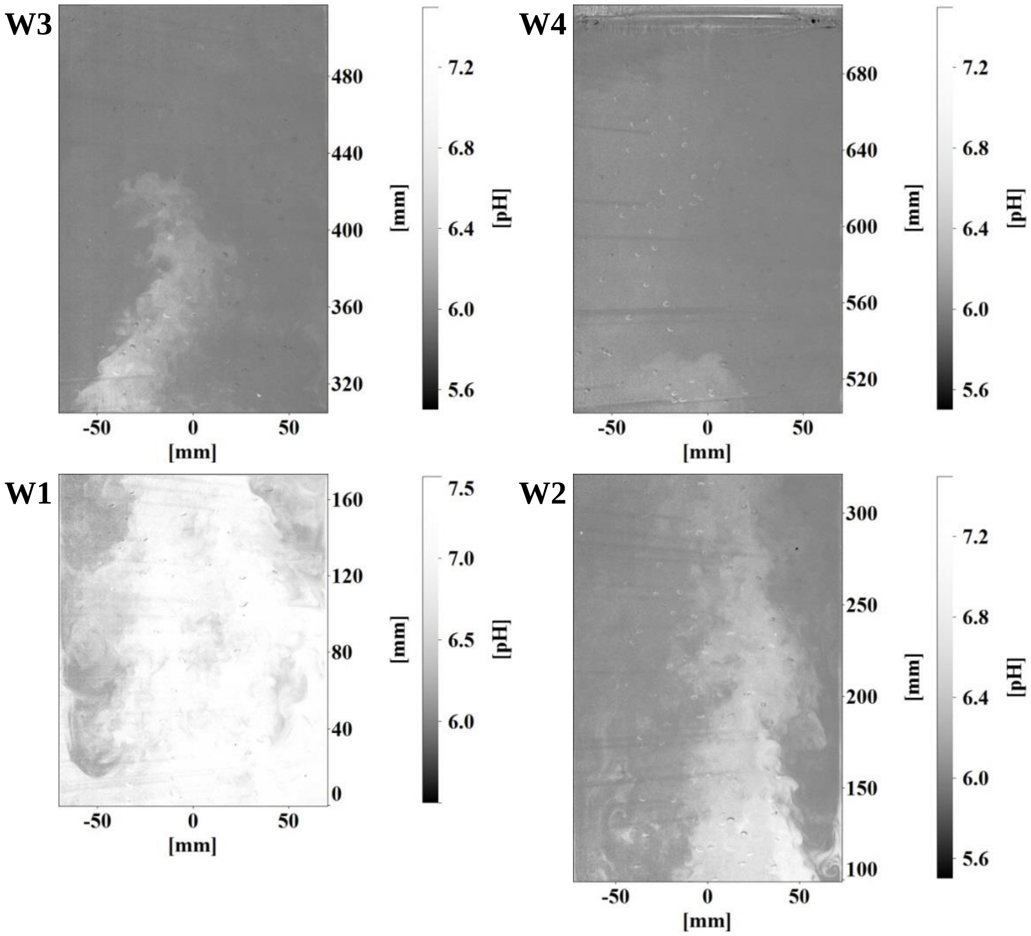

Figure 5.11: Processed snapshot images of pH in the four measurement windows (W1-W4) of the first measurement campaign in a CO_2 bubble curtain, at *t*=40s. From [23].

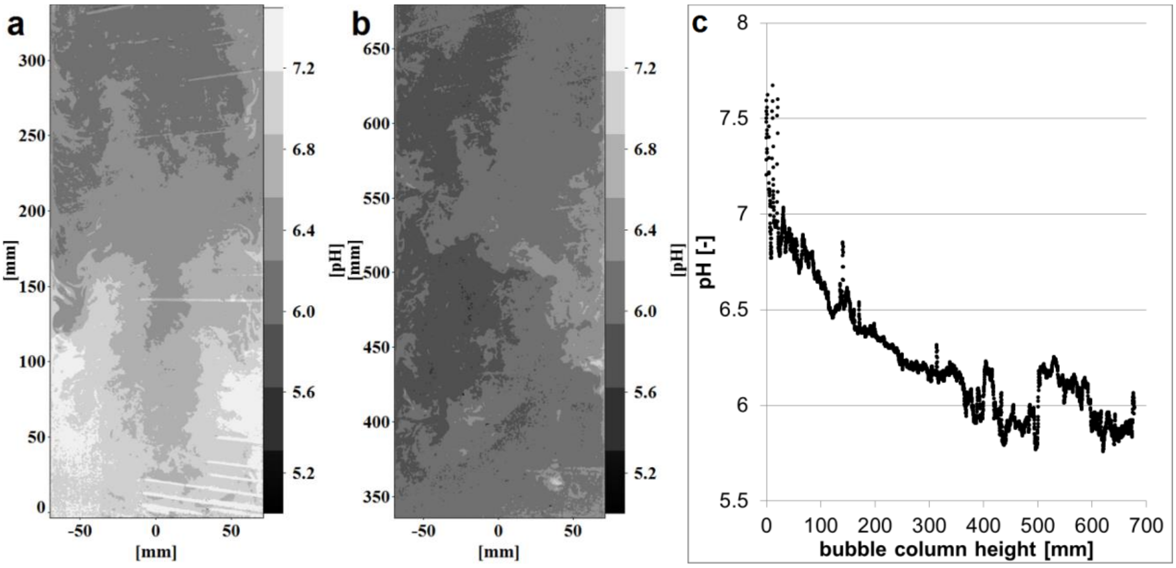

Figure 5.12: Processed images of pH at *t*=30 s at the (a) bottom and (b) top measurement sections, and (c) the corresponding pH values along a vertical profile line in the centre of the column from the second measurement campaign in a CO_2 bubble curtain. From [16].

It is important to recall that pH values have a logarithmic scale. Therefore, a pH change from 8 to 7 means much smaller CO_2-concentration changes, than a pH change from 6 to 5. For example, 1.025 µg/l CO_2 are dissolved in the liquid at pH=7, whereas the dissolved gas concentration at pH 5 is 10.25 mg/l. These images show also the capacity of the 2T-LIF method to minimize the effect of bubble shadows on the measured pH-fields. No such shadows or reflections disturb the pH measurement results.

Figure 5.13 represents the pH change versus time in de-ionized water, obtained from the two measurements. To this end, the pH-results of six horizontal sections of 20 mm thickness (origin of coordinate system is the top of the gas nozzles) were geometrically averaged in function of time. Here it has to be mentioned that reliable pH values can only be obtained from pH≤7.6…8. This means, that the pH value in the first 10-20 seconds does not remain constant as one could interpret the curves on Figure 5.13, but the fluorescent dye was not able to monitor the pH change from 9.5 to about 7.6. For this reason, on Figure 5.13, b, where the measurements were started from pH=8, this delay in pH change is much shorter. In general, the speed of the pH change is almost the same in all of the investigated height, except at the bottom, where the mixing is not so effective; therefore, a delay of around 10 seconds can be observed.

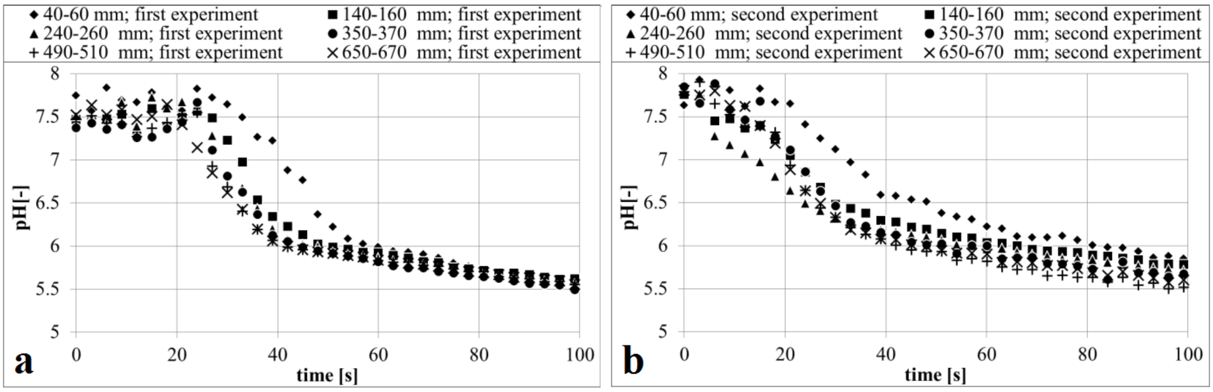

Figure 5.13: pH change in de-ionized water at different heights during the first 100 s in the first (a) and in the second (b) measurement campaign in a CO_2 bubble curtain.

This phenomenon can be explained by the bubble and liquid velocity measurements. In the bottom section the liquid velocity in the centre of the column is twice as high as in the other sections, due to the high bubble velocity. Therefore, dissolved CO_2 is transported quickly to the upper parts of the column. Additionally, high bubble velocity means shorter contact time. At a height of about 300 mm the bubbles are occupying almost the whole column width, and the liquid flow will become slower. Hence, the overall pH change will be faster there due to a longer contact time between the phases. It also can be recognized on these plots, that the pH-change from pH=8 to 6 is much faster, than the change from pH=6 to 5.5. The reason for this is the logarithmic scale of the pH values. Both experiments show the same progress. However, the experiments started from pH=9.5 (Figure 5.13, a) show a faster pH drop from pH=8 to 6, than those started at pH=8 (Figure 5.13, b).

The same horizontal sections were used to compare the pure water results in the first 100 seconds of reaction with three different water-glycerol mixtures (without SDS) (Figure 5.14). In all cases, the slowest pH change can be observed in the lowest section close to the inlet nozzles, where pH change is mainly due to the convective transport of the liquid from the upper regions of the column. In the case of pure water (Figure 5.14, a), the pH drops during the first 40 seconds from around pH=8 to pH=6.5, first in the upper sections and then in the lower ones. From about pH=6.5, this decrease becomes slower at all heights. At the bottom of the column, the pH value stagnates around the starting pH value for up to 20 seconds, while in the upper investigated sections the CO_2-absorption is already in progress. In the 25% water-glycerol mixture (Figure 5.14, b), the results are rather the same: the lowest section shows a delay and the longest pH-change, while in the topmost section it is the fastest. The pH-change in the 50% water-glycerol mixture (Figure 5.14, c) is overall slower and the slope is smaller in all investigated heights. But, in this case, the slope becomes steeper between the lower, developing region and the upper part of the column, where bubbles become more elliptical and change their trajectories (see Figure 3.8). In this part, mass transfer is enhanced through the zig-zagging motion and the resulting longer residence time of the bubbles, compared to the nearly spherical, vertically ascending bubbles in the lower part of the column

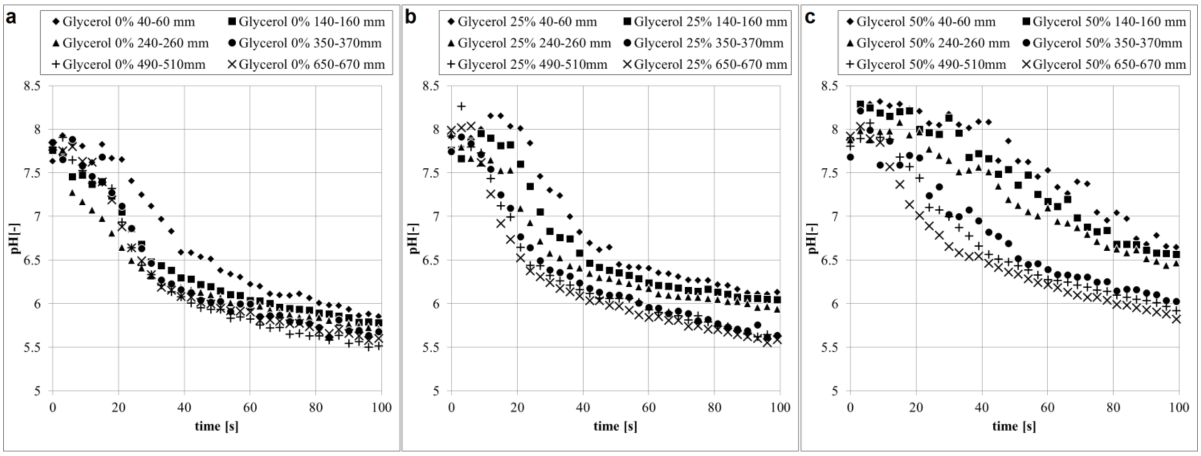

Figure 5.14: pH change in a CO_2 bubble curtain at different heights during the first 100 s: (a) pure water, (b) 25% glycerol, and (c) 50% glycerol. From [16].

The difference in pH change in the different solutions is also distinguishable on a longer timescale (Figure 5.15). 45-80 seconds are needed at the top of the column for the pH to drop from the initial pH=8 to a value of 6. At the bottom, 80-215 seconds are needed for the same pH difference. Then, the decrease from pH=6 to pH=5.5 again needs 50-80 seconds at the top, whereas it lasts 100-150 seconds at the bottom of the bubble column. Thus, the pH change from pH=8 to pH=5.5 is 1.5 times slower at the bottom of the reactor in the 25% water-glycerol mixture and twice slower in the 50% water-glycerol mixture, compared to the change in pure water. These findings support the results of several authors in the literature, who also stated reduced mass transfer for higher viscosities.

In Figure 5.15, at a height of around 300 mm, an increasing time delay can be recognized for each measurements series to attain the respective pH of 6 and 5.5. Whereas for pure water the trend is continuous, at 25% glycerol and even stronger at 50% glycerol, a kink can be seen at this height. This delay of the pH change in the solutions with glycerol is a complex result of the gas and liquid flow in the column and of the resulting mixing and mass transfer. As presented in Figure 5.14, mass transfer decreases globally with increasing glycerol concentration, therefore the pH change is the slowest in the case of the highest glycerol concentration. Due to the differences in bubble form and motion between the 3 viscosity cases examined, CO_2 is more or less dissolved in the upper part of the column. For pure water, bubble sizes and trajectories are more homogeneous over the different heights than for 50% glycerol, where nearly spherical, vertically ascending bubbles exist in the lower part and elliptical, zig-zagging bubbles in the upper. There, mass transfer is enhanced and the lower pH solution is also trapped in the existing top liquid vortices. Just small amounts of liquid descend near the column wall to the bottom and lead to the pH change in the bottom section. Therefore, the rate of pH change will be slower in this section with increasing viscosity and lead to the aforementioned delay.

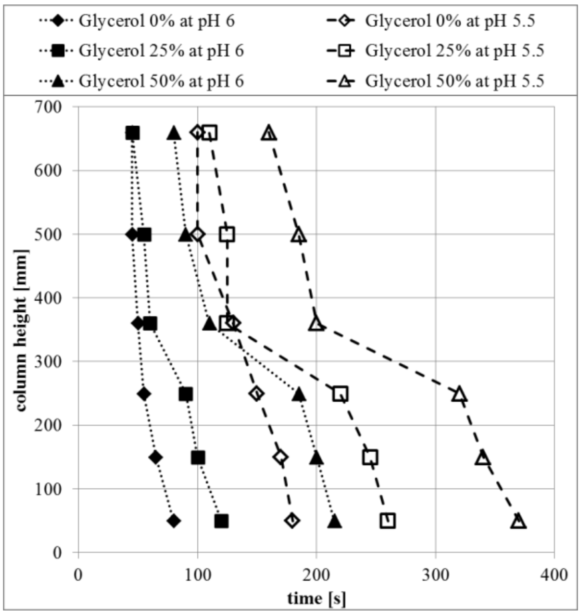

Figure 5.15: Comparison of pH-value development during the reaction in different mixtures at different heights in a CO_2 bubble curtain. From [16].

5.3.4. Conclusions

Through several experiments, the liquid velocity and CO_2-mass transfer from gas to liquid were examined experimentally in the model bubble column for different viscosities and surface tensions.

Using PIV, the flow field in the bubble column reactor with four gas inlets could be investigated in detail. Combining the measurement windows, a full description of the hydrodynamics in the whole column was obtained, showing much lower liquid velocities compared to the bubbles, with a clear recirculation loop near the reactor walls.

The comparison of different PIV techniques and spatial resolutions has shown that with all PIV setups nearly similar velocity results could be achieved. However, as expected, the higher the spatial resolution, the more accurate are the instantaneous velocity result. The drawback of the higher spatial resolution are higher experimental and calibration efforts and post-processing time and, of course, the storage size for the raw data increases as well. Therefore, if small-scale structures and fluctuations have to be investigated, a high-speed time-resolved PIV system with high spatial resolution could be a good choice, while when a coarse mean flow field is the aim, a low-speed PIV system with lower spatial resolution could be enough.

Due to the change in bubble size and velocity, the liquid flow field is evidently not the same for different viscosities and surface tensions. The highest velocities could be found in the high viscosity solutions. With surfactant, the liquid velocity profiles resemble each other for different viscosities, apart from the bottom section of the column where the liquid flow field mirrors the straight ascension line of the bubbles. All these results support the existence of a dual effect of viscosity on bubble column fluid dynamics already found in the literature.

After the hydrodynamic characterization, the neutralization reaction in pure water and the effect of viscosity change was investigated on mass transfer through 2T-LIF. These experimental results have shown, that the highest mass transfer from gas to liquid can be achieved with pure distilled water. The addition of surfactant and glycerol has a large influence on bubble size and velocity, but neither of them has advantageously affected the mass transfer. The time to reach a certain pH in the column is always prolonged in the solutions with glycerol.

The obtained experimental data has already been used for a systematic validation of numerical models describing large-scale bubble columns [184-186], supporting the further development of predictive simulations concerning mass transfer in bubble columns. In the frame of a Priority Program of the DFG (SPP 1740 “Reactive Bubbly Flows”) an Internet-based database has been created to share all relevant data with the scientific community, supporting validation of numerical simulations and comparisons with results from other groups. The complete data sets containing bubble diameters, bubble and liquid velocity fields as well as the pH measurement results are available through this online database, freely accessible with a password under http://141.44.132.124/spp1740/.

Chapter 6

Measurement results of the air–water system

Parts of the results and subsections presented in this chapter have been presented in a peer-reviewed paper and presentation at the 19th International Symposium on the Application of Laser and Imaging Techniques to Fluid Mechanics, 2018, in Lisbon, Portugal [102].

Contents

6.1. INTRODUCTION 110
6.2. EXPERIMENTS WITH AN AIR BUBBLE CHAIN 110
  6.2.1. Experimental setup and flow conditions for the simultaneous LIF–PIV measurements 110
  6.2.2. Liquid velocity in the bubble column with the air bubble chain 111
  6.2.3. O_2 concentration fields in the bubble column with bubble chain 114
6.3. EXPERIMENTS WITH AN AIR BUBBLE CURTAIN 117
  6.3.1. Experimental setup and flow conditions for the simultaneous LIF-PIV measurements 117
  6.3.2. Liquid velocity in the bubble column with an air bubble curtain 118
  6.3.3. O_2 concentration fields in the bubble column with an air bubble curtain 121
6.4. CONCLUSIONS 123

6.1. Introduction

This chapter deals with the optical measurements in the bubble column reactor with the second investigated reaction, the O_2 mass transfer, quantified with the help of the resorufin redox reaction. The aim of these measurements was the quantification of oxygen mass transfer from air bubbles in a model scale bubble column. As explained in Chapter 2, through a simple redox reaction the amount of dissolved O_2 can be calculated from the fluorescence intensity of the resorufin dye. This reaction can be followed by LIF. The liquid flow field in the bubble column was determined with PIV, in the same way as for the neutralization reaction.

In these experiments two different cases were studied:

- Mass transfer and simultaneous liquid velocity measurements in the bubble column with an air bubble chain,
- Mass transfer and liquid velocity measurements in the bubble column with an air bubble curtain.

6.2. Experiments with an air bubble chain

First, experiments with a bubble chain will be presented. Using simultaneous PIV and LIF measurements the velocity field in the bubble column and the mass transfer from air bubbles into the liquid bulk were determined at two different gas flow rates.

6.2.1. Experimental setup and flow conditions for the simultaneous LIF–PIV measurements

To generate a bubble chain in the bubble column reactor, one stainless steel capillary with an inner diameter of 0.25 mm was mounted in the centre of the bottom plate of the reactor. The bubble column was filled with 11.3 l of a solution (Table 2.1), consisting of de-ionized water, glucose, sodium hydroxide, resazurin and PIV-particles. The air bubbles were generated at two different gas flow rates, 2 and 4 l/h. The detailed measurement conditions can be found in Chapter 2 (Table 2.2, No. 12).

The experimental images were recorded in this case with an Imager Intense CCD camera for PIV and on the opposite side with an Imager LX 8M CCD camera for LIF, simultaneously. For a better spatial resolution, the bubble column was divided into two measurement sections (Figure 6.1, F1 and F2). More technical details concerning this setup can be found in Chapter 2 (Table 2.6, No. 12).

Since here the experimental setup and recording procedure was similar to the one for the bubble chain of CO_2 (subsection 5.2), for PIV processing and post-processing the same steps were used. Only the interrogation window sizes had to be enlarged because of a larger particle size. More details of this processing can be found in subsection 2.4.1 and in Table 2.3, No. 12. At last, the calculated instantaneous velocity fields were averaged.

For the O_2 concentration calculation, the measurement and calibration images had to be processed to transform the raw images into concentration fields. The processing steps were the same as the steps for the single bubbles, but they were extended with an additional laser-sheet correction step (see Table 2.4, No. 3.). These image processing steps are described in detail in subsection 2.4.2.

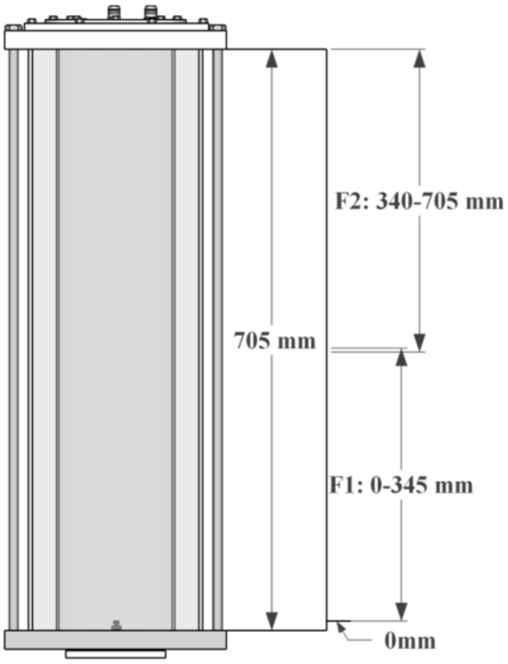

Figure 6.1: Measurement windows for the air bubble chain measurements.

6.2.2. Liquid velocity in the bubble column with the air bubble chain

The structure of the liquid velocity fields at 2 and 4 l/h air flow rate (Figure 6.2) are expectedly very similar with the CO_2 results (Figure 5.2). The rising bubbles occupy just the centre of the column and they are generating a vertical upward flow. On Figure 6.2 it is also clearly visible, that the vertical liquid velocity is decreasing from the bottom to the top, due to the bubble motion. The rising elliptical bubbles follow a continuously widening helical path and their initial vertical velocity decreases. Therefore, the vertical liquid velocity also decreases. In addition, where no bubbles exist, a wide descending zone can be seen near the column walls down to the bottom of the column. The horizontal velocity components are nearly zero, except at the top and bottom of the column, where recirculating zones exist.

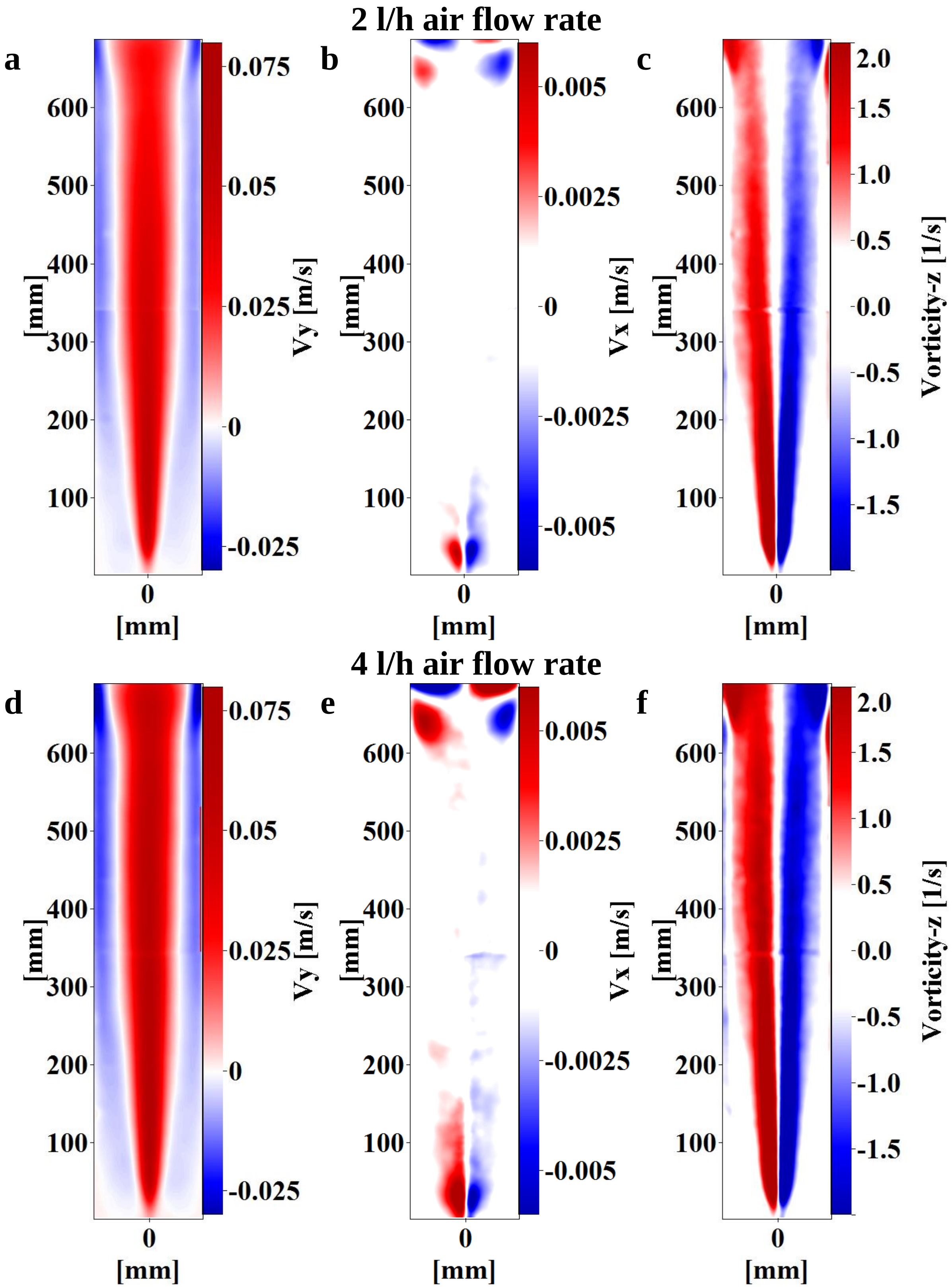

Figure 6.2: Mean vertical and horizontal liquid velocity fields in an air bubble chain for 2 l/h (a and b) and 4 l/h (d and e) air flow rate, and corresponding vorticity for both cases (c and f).

This flow behaviour can also be seen in detail on the horizontal velocity profiles of the horizontal and vertical velocity components (Figure 6.3, a-d). With increasing height, the maximum of the vertical velocity decreases in both cases and the profiles are more flattened (Figure 6.3, a and b). Expectedly, at 4 l/h air flow rate this drop in the maximum is much less, as it was also observed in the experiments with CO_2 bubbles (Figure 5.3).

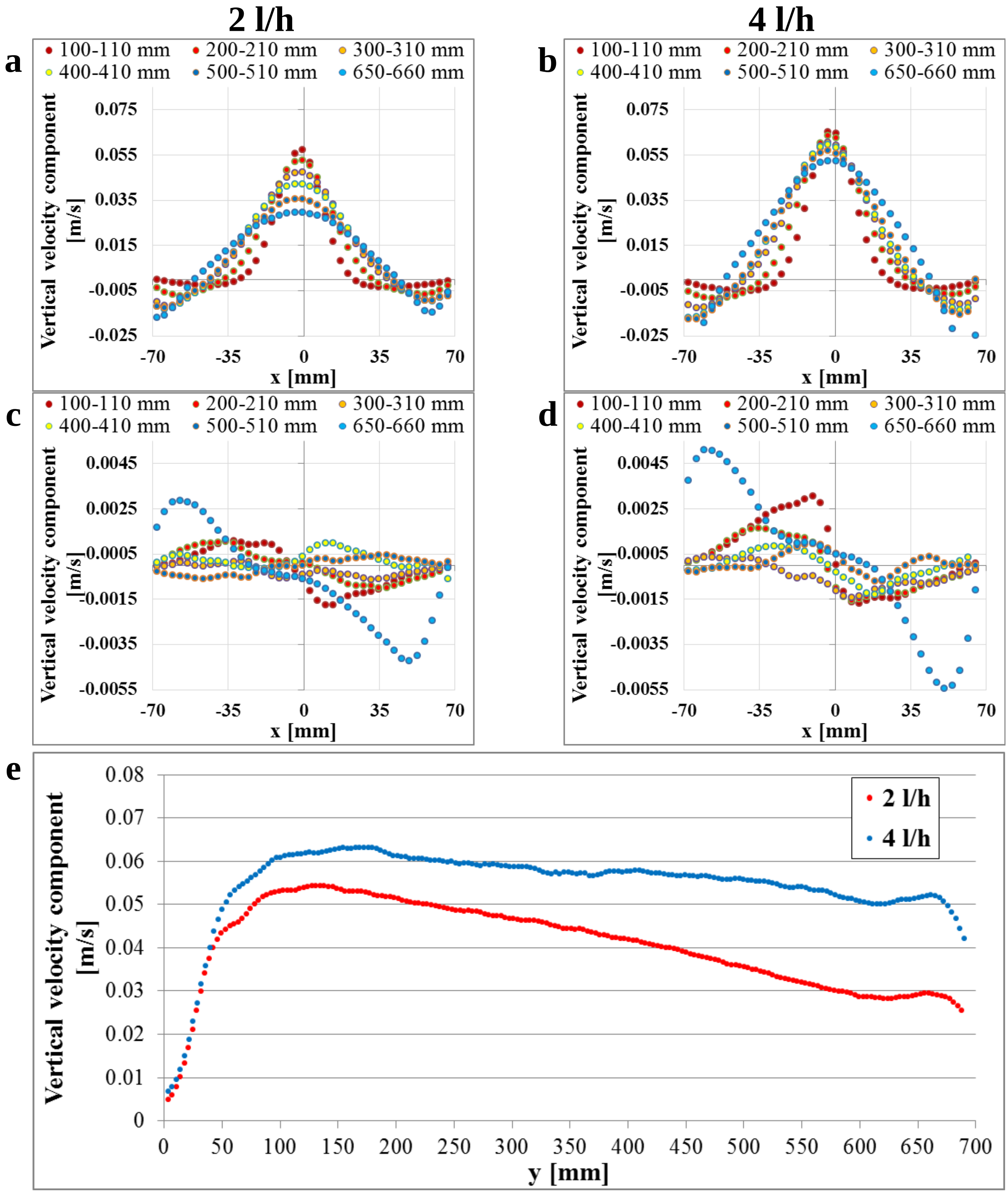

Figure 6.3: Mean velocity profiles in an air bubble chain in different sections: vertical (a, b) and horizontal velocity component (c, d) at different heights; vertical profile of vertical velocity component in the centre of the bubble column (e).

At the same time, the backflow velocity close to the wall is increasing. In the recirculation zones at the bottom and on the top, high horizontal velocities can be found, but heading to the centre of the column, the horizontal velocities drastically decrease (Figure 6.3, c and d). On the vertical profiles of the mean vertical velocities (Figure 6.3, e) a similar systematic shift can be observed as in the measurements with CO_2, that is due to the doubled gas flow rate.

The initially generated CO_2 bubbles were a bit smaller than the air bubbles, therefore their terminal velocity was higher. For this reason they induce higher vertical liquid velocity. Then, with increasing height, the liquid velocity decreases gradually in the case of CO_2, because of the bubble shrinkage; the buoyancy force of the bubbles decreases, smaller bubbles carry less liquid upwards. Preliminary experiments have shown that this bubble size change does not exist in the case of the air bubbles. Therefore, the vertical liquid velocity decreases less over the column height (Figure 6.4).

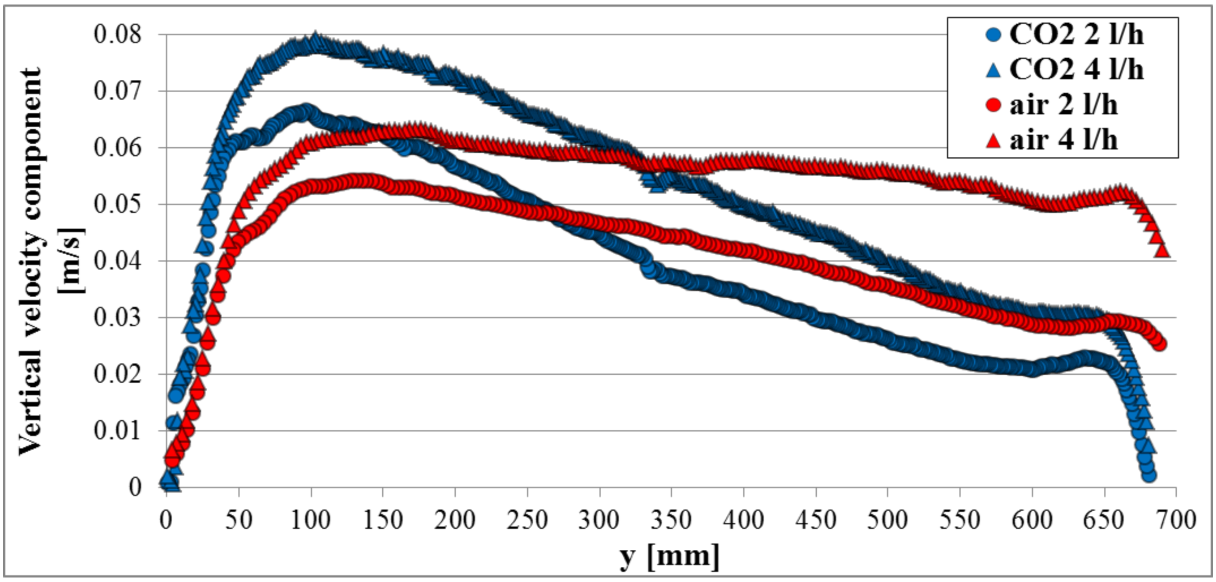

Figure 6.4: Mean vertical liquid velocity profiles in the centre of the bubble column along the whole height for air and CO_2 bubble chains.

6.2.3. O_2 concentration fields in the bubble column with bubble chain

Figure 6.5 shows the O_2 concentration fields with 2 l/h air flow rate during the first 50 seconds. After starting the aeration, the chain of air bubbles rises in the centre of the column and a small amount of oxygen is dissolved in the liquid (*t*=5s). It is remarkable, that at *t*=10 s the dissolved oxygen concentration is higher at a height between 300 and 400 mm than above and below. Then this liquid plume with higher oxygen concentration is moving upwards and around *t*=15 s reaches the surface of the liquid. There, it is deviated and moves downwards near the wall. This backflow is visible at *t*=20 s and *t*=25 s and increases first in the top region and then downwards to the bottom of the column. After 50 s the dye colour is saturated at the top at around 0.025 mg/l equivalent oxygen concentration, but it is still not saturated at the bottom.

The concentration evolution with time can also be seen on the horizontally averaged oxygen concentrations at different heights in Figure 6.6, a. About 5-15 s after aeration start, steep concentration increases are visible on these curves. This corresponds to the spreading of the high concentration plumes in the column and becomes evident, when e.g. comparing the LIF image (Figure 6.5) at 10 s with a high concentration plume at about 400 mm with the 400-410 mm curve in Figure 6.6, a. At around 20 seconds, when this higher concentrated plume reaches the surface (Figure 6.5), the steep increase is visible on the curve at 640 mm in Figure 6.6, which corresponds to the near-surface region of the column. From this moment, the oxygen-containing plume occupies the whole column width, which leads to a higher oxygen concentration in the averaged diameter.

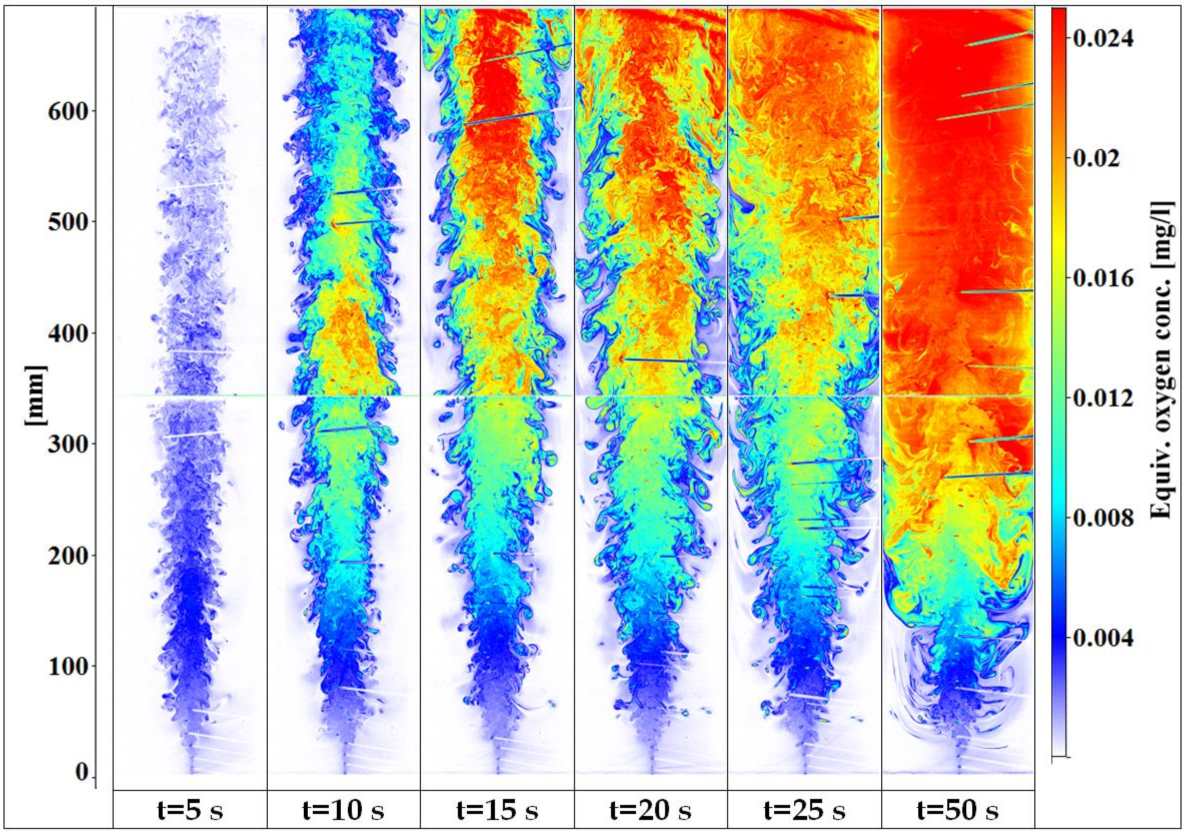

Figure 6.5: Equivalent oxygen concentration in the bubble column for the air bubble chain with 2 l/h air flow rate at different times *t*. From [102].

With the backflow, the liquid with higher oxygen concentration is moving downwards near the wall and increases further the diameter-averaged concentrations in the lower sections. On this plot, the influence of hydrodynamics on the concentration distribution during mass transfer from the gas to the liquid is clearly visible. On the top of the column, saturation is reached the fastest (in 30 seconds). The centre section is slower, it needs at least 50 seconds for saturation and the bottom section will be saturated just after 100-150 seconds, which is not plotted on the diagram for visibility reasons.

Similar mass transfer progress can be found with the higher, 4 l/h air flow rate (Figure 6.6, b), but of course in this case, the process is faster due to the higher gas flow rate. The generated bubbles are larger, therefore the liquid velocity is increasing too (see Figure 6.3, e). Because of the increased liquid velocity, the liquid with dissolved gas is transported faster to the top and from there with the backflow heads faster downwards to the bottom. This effect can be seen clearly on the curves at 100, 200 and 300 mm, where higher concentrations are reached much earlier in the case of 4 l/h.

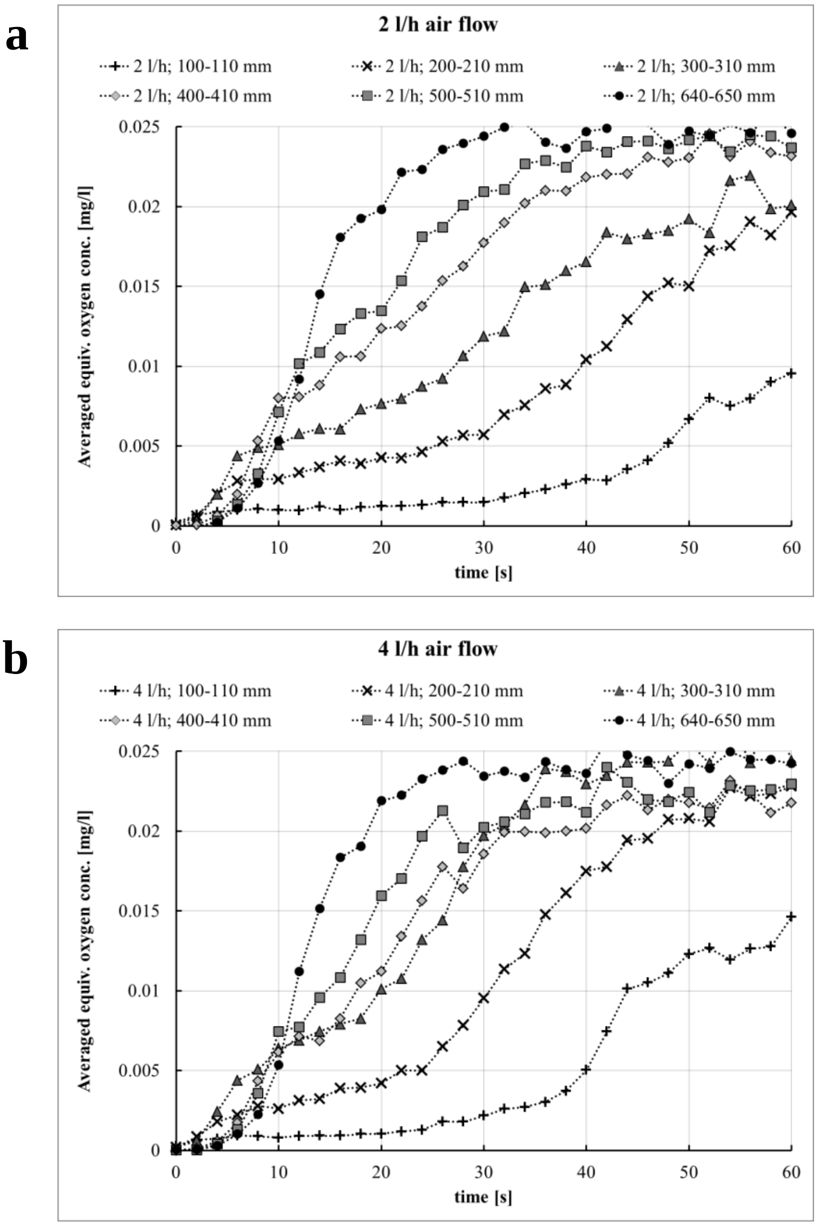

Figure 6.6: Mean equivalent oxygen concentration in the bubble column for the air bubble chain with 2 l/h (a) and 4 l/h (b) air flow rate in different horizontal sections.

6.3. Experiments with an air bubble curtain

With the bubble chain experiments it was proven, that the air-water system with resazurin is suitable to visualize and quantify the mass transfer of oxygen into the liquid bulk via LIF in larger scale applications. To go one step further, the experiments were carried out in the fluiddynamically more complex system with four gas inlet nozzles. Low-speed PIV and LIF measurements were carried out simultaneously to characterize the flow in the bubble column with this reaction system and to measure the mass transfer from the air bubbles.

6.3.1. Experimental setup and flow conditions for the simultaneous LIF-PIV measurements

For these simultaneous LIF and PIV measurements, the measurement method and process was similar to the bubble chain experiments with resazurin (see subsection 6.2.1). The base plate was changed to the one with four nozzles and the air flow rate was set to 6 and 8 l/h. To increase the measurement system sensitivity and the spatial and temporal resolution, the cameras were changed to two Imager sCMOS cameras. A 50%-50% beam splitter enhances the image overlapping accuracy between the two cameras. The reactor was filled with 11.3 l solution (Table 2.1), and the experiments were carried out with two, 0.225 mg/l and 0.45 mg/l resorufin concentrations to investigate also the influence of the dye concentration on the mass-transfer process and saturation speed in the bubble column. The detailed measurement conditions can be found in Chapter 2 (Table 2.2, No. 13).

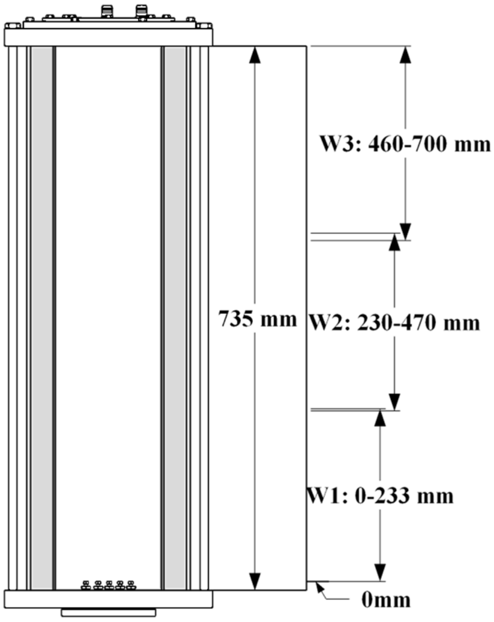

Figure 6.7: Measurement windows for the air bubble curtain measurements.

To gain a higher spatial resolution, the bubble column was divided into three measurement sections (Figure 6.7: W1-W3). More detailed technical information concerning this measurement setup can be found in Chapter 2, Table 2.6, No.13.

In these measurements the velocity fields were calculated in the same way as in the bubble chain experiments, only the final interrogation window size was reduced to 32x32 pixels, because of the higher spatial resolution. More details of this processing can be found in subsection 2.4.1 and in Table 2.3, No. 13. At last, the calculated instantaneous velocity fields were averaged.

From the simultaneously recorded LIF images, the dissolved oxygen concentration was determined. The processing steps were the same, as the steps for the bubble chain (see Table 2.4, No. 13.). These image processing steps are described in detail in subsection 2.4.2.

6.3.2. Liquid velocity in the bubble column with an air bubble curtain

As expected, the obtained flow fields (Figure 6.8), show very similar flow pattern to the CO_2 case (Figure 5.7). As previously observed, a wide upward flow developed in the centre of the bubble column, due to bubble motion. On the top of the column a recirculation zone forms with two counter-rotating vortices. From these vortices the liquid flows back to the bottom of the column, close to the walls, thus establishing the complete liquid circulation in the bubble column.

The highest vertical velocity peaks are around 5.5 cm/s, as it was also observed in the CO_2 experiments. From around 300 mm up to 450 mm the upward flow occupies almost the whole column cross section, therefore the vertical upward velocity becomes dominant and almost no horizontal velocity was measured in this region. A considerable change in the horizontal velocity can be noticed just on the top, in the recirculation zone, and at the bottom, where also a recirculation zone is established, but with much less strength.

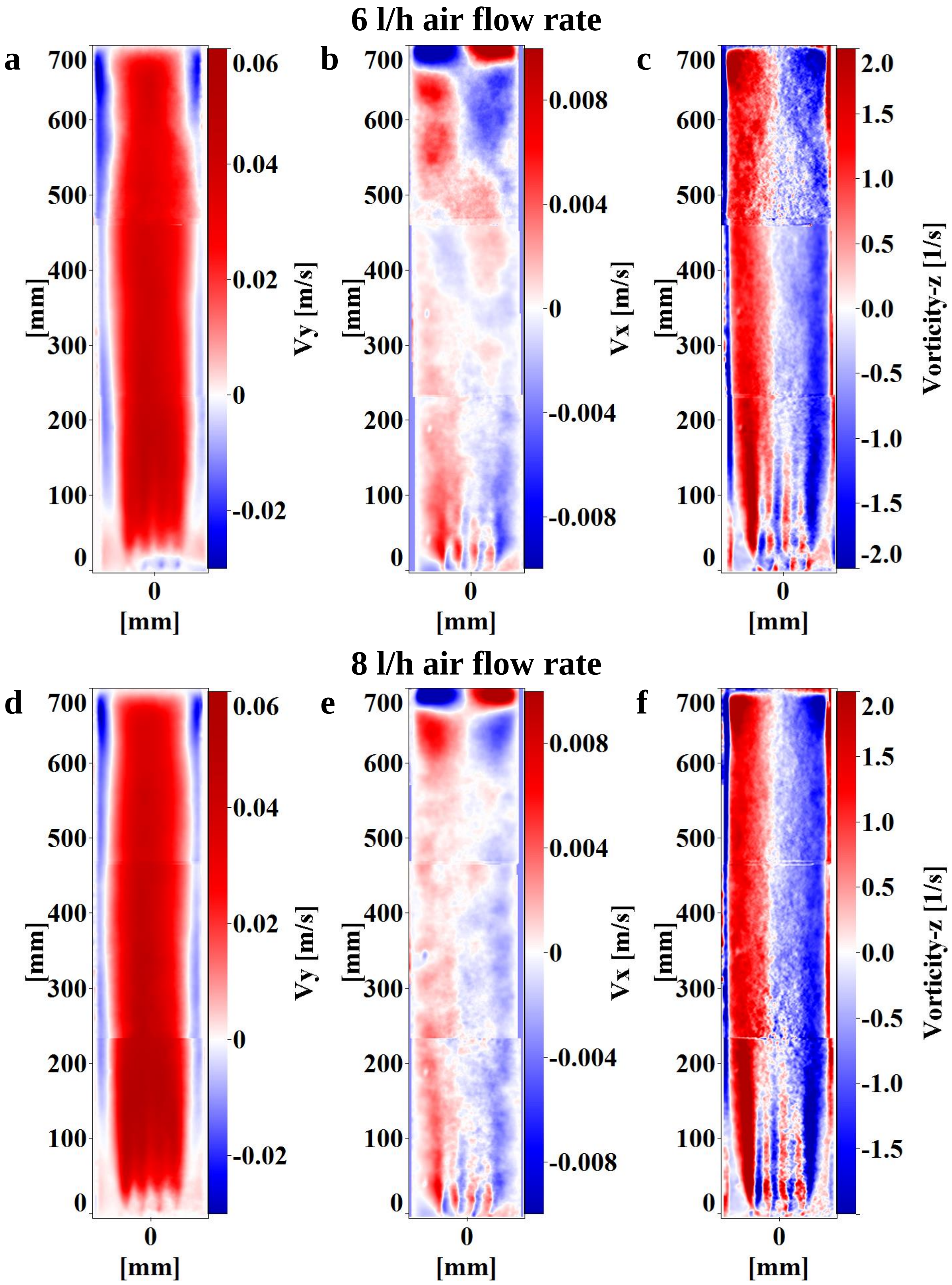

Figure 6.8: Mean vertical and horizontal liquid velocity field in an air bubble curtain for 6 (a and b) and 8 l/h (d and e) air flow rate, and corresponding vorticity for both cases (c and f).

To compare the flow fields calculated for the two different gases – air and CO_2, horizontal velocity profiles were taken at five different heights (Figure 6.9). At a first glance, the vertical liquid velocity profiles are very similar.

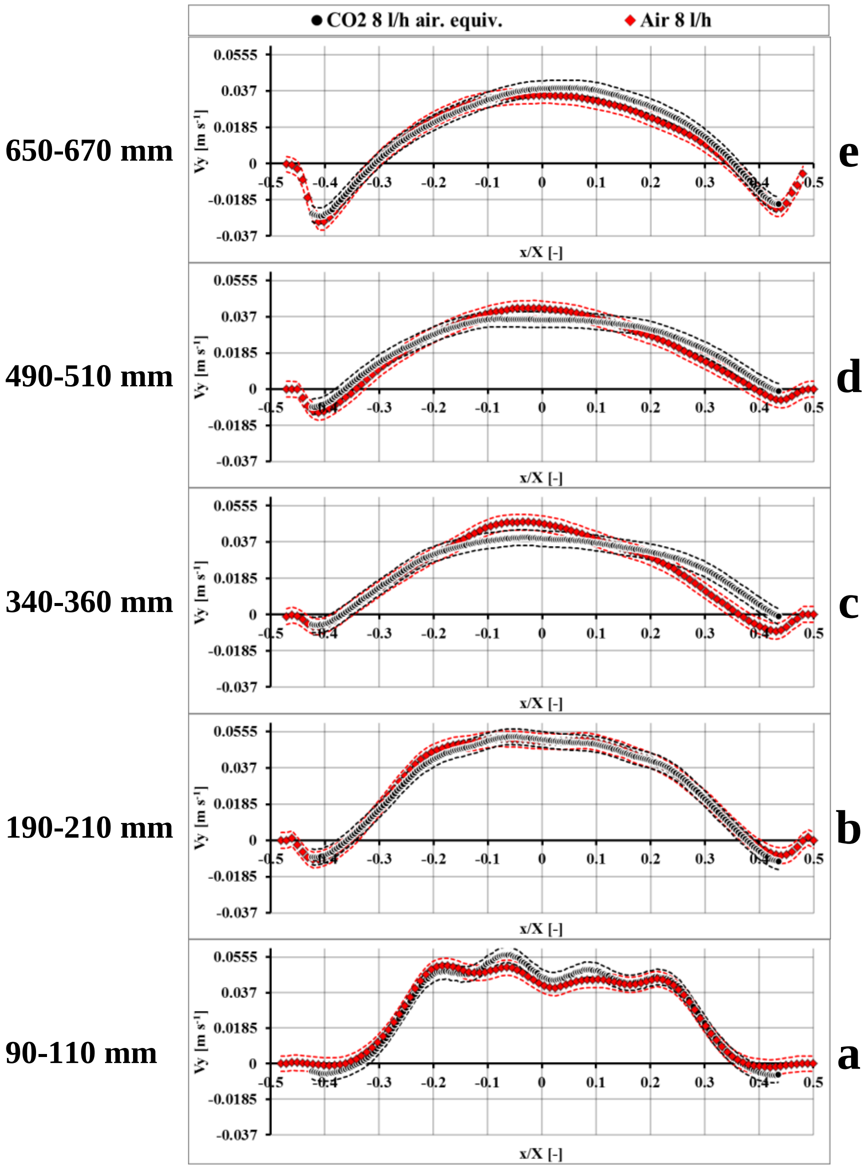

Figure 6.9: Comparison of mean vertical liquid velocity profiles (marks) obtained from the PIV experiments in a bubble curtain with air and CO_2 bubbles at 90-110 mm (a), 190-210 mm (b), 340-360 mm (c), 490-510 mm (d), 650-670 mm (e), together with standard deviation (dashed).

At 90-100 mm, near the bottom of the column and the outlet nozzles, the effect of the four bubble nozzles on the liquid velocity is clearly visible (Figure 6.9, a). With CO_2, the velocity peaks above each nozzle are more pronounced, because of the slightly higher bubble velocities. Within the first 0.3 m, as long as the bubble swarm is still concentrated, the mean vertical liquid velocity reaches a maximum value around 5.5 cm/s in both cases (Figure 6.9, b). Above 0.3 m, the bubbles start to spread sideways and finally occupy the whole width of the column. As a consequence of bubble spreading, the vertical liquid velocity is decreasing (Figure 6.9, c and d). At these heights the vertical liquid velocity measured with CO_2 is lower than the vertical liquid velocity with air. It could be explained by the shrinkage of the CO_2 bubbles, these slightly smaller bubbles generate less upward flow. At the top of the bubble column, the vertical liquid velocities in both cases become again very similar. A clear and relatively large backflow near the reactor walls exists in both cases (Figure 6.9, e), showing the recirculation loop of the liquid after the bubbles leave through the free surface. Considering all results, slight differences in the vertical liquid velocity between the two investigated cases can be found, but the overall hydrodynamics is very similar for both cases.

6.3.3. O_2 concentration fields in the bubble column with an air bubble curtain

Figure 6.10 shows exemplary O_2 concentration field snapshots from the bottom investigation window. Since 2T-LIF could not be used in the redox-reaction system, the shadows of the bubbles are clearly visible on these images. The calibrated images show clearly how sensitive is the utilized resazurin redox reaction. The 0.45 mg/l resazurin solution used here saturates with 0.0229 mg/l dissolved oxygen. 2 seconds after starting the bubbly flow, the measured dissolved equivalent oxygen concentration in the bottom section is just below 0.001 mg/l, but it can be measured reliably. The dissolved oxygen is transported upwards in the centre of the column (*t*=10 s). Then, liquid with higher oxygen concentration flows back close to the walls (*t*=18 s). After 26 seconds from the start, liquid with much higher amounts of dissolved oxygen appears on the bottom of the column, but it is still far from saturation. Please mind, that Figure 6.10 and Figure 6.11 are scaled between 0 and 0.005 mg/l for better visibility. It is worthwhile to mention also, that the lowest part of this section after 26 seconds still contains very low dissolved oxygen concentrations.

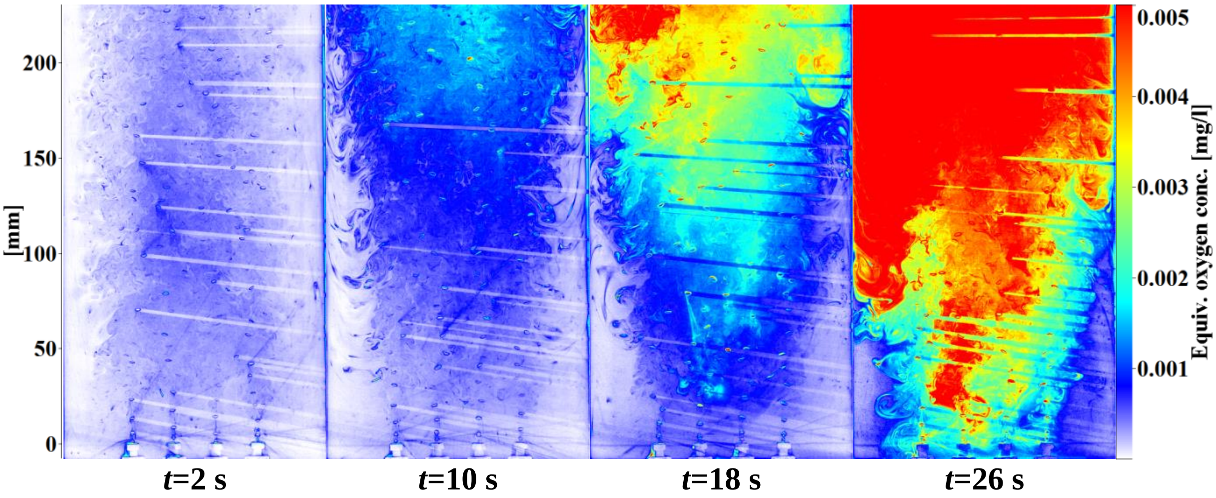

Figure 6.10: Exemplary snapshots from the bottom measurement window (W1) with air bubble curtain at 8 l/h air flow rate and different times, *t*.

Contrary to the bottom section, the mass transfer process is much faster in the other two – W2 and W3 – sections. For example, in the top section W3 (Figure 6.11) around 3 seconds after the measurement start, similar concentrations can be measured, as in the bottom section at *t*=2 s. But then the process becomes much faster, because of the recirculation loop at the column top. During the next 6 seconds (9 seconds after start) this section reaches the concentration of 0.005 mg/l almost everywhere, while this value is just reached at *t*=26 s in the bottom section.

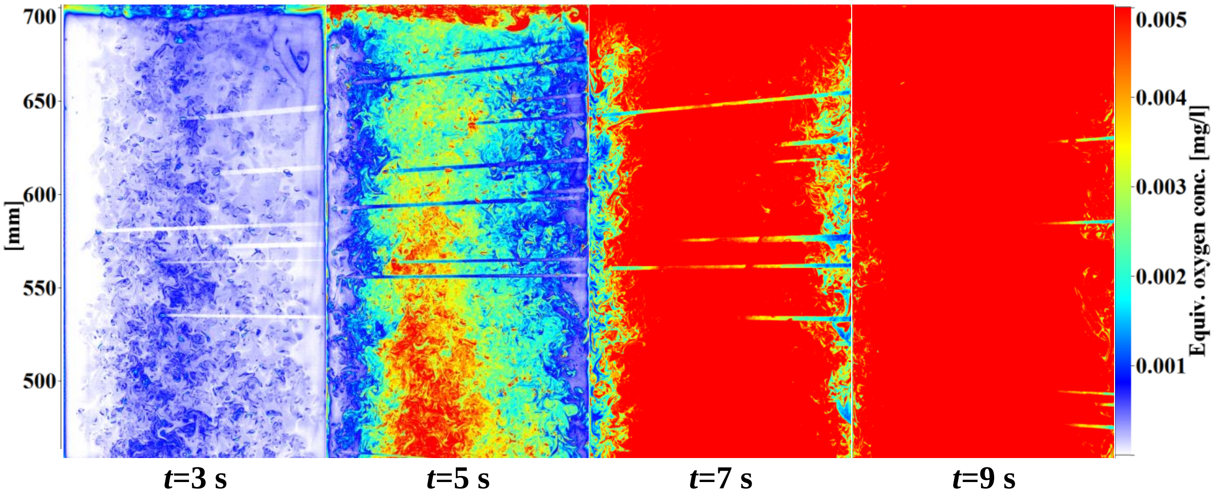

Figure 6.11: Exemplary snapshots from the top measurement window (W3) with air bubble curtain at 8 l/h air flow and different times, *t*.

These different dissolved oxygen concentration evolutions can also be followed quantitatively on the horizontally averaged oxygen concentrations at different heights (Figure 6.12). These results show that the mass transfer process with 6 and 8 l/h gas flow rate behaves similar, but some characteristic differences exist. Compared to the saturation speed with the bubble chain (Figure 6.6), mass transfer with the bubble curtain is evidently faster.

With lower dye content (Figure 6.12, top), the process is noticeably faster in the bottom sections at higher gas flow rate, while with higher dye content (Figure 6.12, bottom) it becomes slower. During these measurements the fluorescent dye consumes the available dissolved oxygen up to its saturation level. Since the liquid with dissolved gas is transported upwards with the bubble flow and the contact time of the bubbles is the highest at the top of the column, it is obvious, that the highest dissolved gas concentration could be measured in the top section of the column. Moreover, in the recirculation zone at the top, this liquid with dissolved gas is trapped, and leads to a higher overall oxygen concentration. It can be assumed that at higher dye concentration the available dissolved oxygen is consumed almost completely by the reaction in the top section. For this reason, no oxygen is transported with the backflow to the bottom. Only after 20 seconds, when the top section is saturated, the lower sections become more concentrated. Accordingly up to 200 mm the O_2 concentration increases more slowly at higher dye concentration, than in the case with lower dye content. In the upper part (300-700 mm), concentrations change almost with the same speed. Just a few seconds after the measurement start, the amount of dissolved oxygen increases rapidly and it reaches the saturation level after around 20 seconds, while for the saturation at the bottom 40-60 seconds are needed.

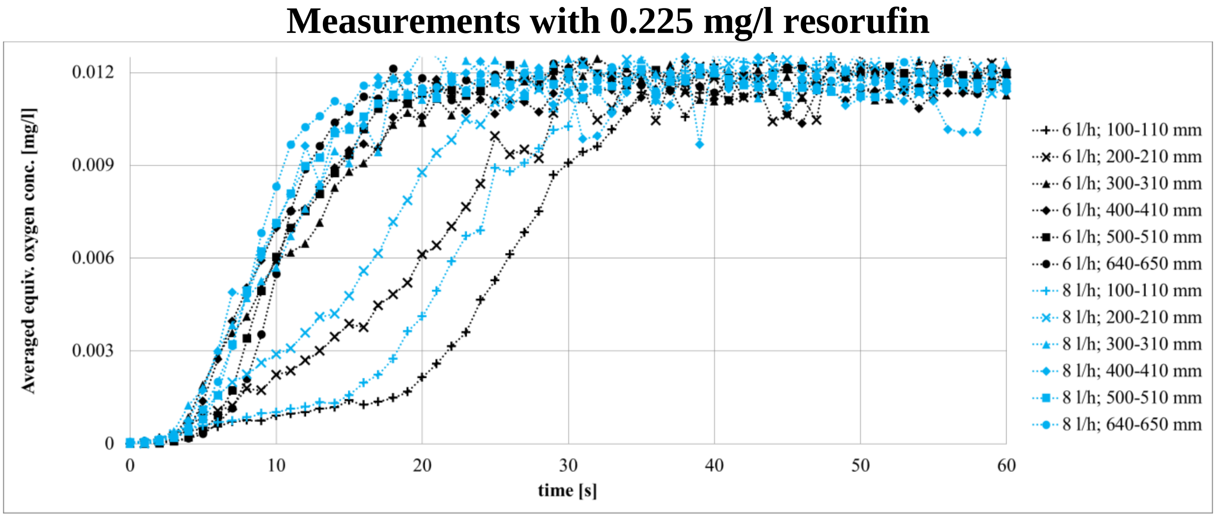

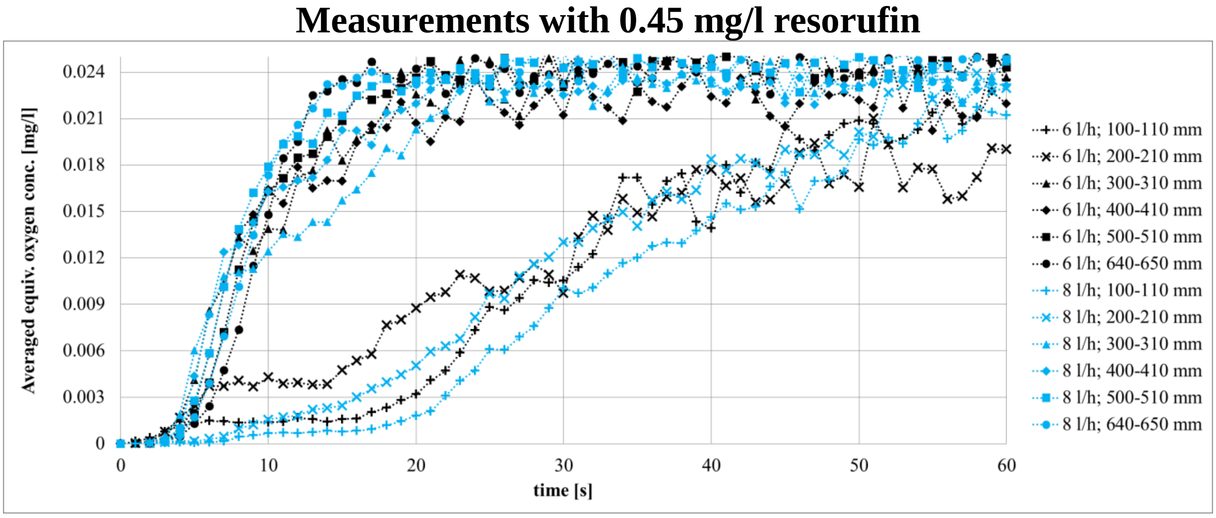

Figure 6.12: Mean equivalent oxygen concentration in the bubble column for the air bubble curtain with 6 l/h and 8 l/h air flow rate in different horizontal sections.

6.4. Conclusions

In this chapter the liquid velocity and mass transfer measurements with air bubbles were presented. The aim of these experiments was to prove the applicability of a new air-water reaction system with resazurin fluorescence for bigger scale installations. To this end, an air bubble chain with 2 and 4 l/h gas flow rate and a bubble curtain with a gas flow rate of 6 and 8 l/h with four inlet nozzles were generated. Moreover, the measurements with bubble curtain were carried out with two different dye concentrations to investigate the effect of the dye concentration on the reaction process in the bubble column.

The velocity field in the bubble column was measured with PIV and in addition, the dissolved equivalent oxygen concentration was measured simultaneously with LIF. A full description of the hydrodynamics in the whole bubble column was obtained in both cases.

The liquid velocity results of the air bubble chain show lower liquid velocities in the bottom part of the column and higher velocities in the upper part compared to the experiments with CO_2. The reasons are the different bubble sizes at the bubble generation and the stronger bubble size change of the CO_2 bubbles over the column height. The overall structure of the liquid flow field is nevertheless the same: clear recirculation loops near the walls along the whole column and recirculation zones at the top and at the bottom. Moreover, as it was expected, with higher gas flow rate the liquid velocity is increased as well, but the overall pattern of the flow in the column remained the same.

Nearly similar liquid velocities were measured with air bubble curtain as obtained with CO_2, with similar flow structure: clear recirculation loops at the top and a thin backflow area near the walls along the whole column. Because of the small difference between the investigated two air flow rates, nearly the same liquid velocity and flow pattern was obtained from the PIV measurements for both cases.

The LIF results have shown that with the air bubble chain faster saturation can be achieved with higher gas flow rate. The time to reach the saturated value of the applied dye in the column is prolonged at lower gas flow rate. It has been also found, that the speed of the saturation process decreases from the top to the bottom of the column. The saturation level is reached considerably faster in the upper half of the bubble column, because of the recirculation loops at the top, where the liquid with dissolved gas is trapped. From this loop just a small amount of liquid is transported near the wall downward to the column bottom, with a low velocity, therefore the remarkable delay in the process at the bottom.

In the case of the bubble curtain it has been found, that the gas flow rate had almost no effect on the mass transfer in the investigated cases, because of the small differences in the applied gas flow rates. The saturation speed decreases from the top to the bottom of the column, similarly to the bubble chain. As long as the fluorescent dye is not saturated in the top section, just a small amount of available dissolved oxygen is transported to the bottom sections. For this reason, a significant time delay exists between the saturation times of the top and bottom sections. It has been found that at higher dye concentration the available dissolved oxygen is consumed almost completely by the reaction in the top section. For this reason, no oxygen is transported with the backflow to the bottom, just after the saturation of the top section. Thus, the time delay is extended at higher dye concentration at the same gas flow rate. This influence of the tracer concentration on the measurement results progress has to be kept in mind, when doing such experiments.

The results have shown that the reaction of resazurin with oxygen is fast enough to visualize and quantify the mass transfer by LIF in a bubble column reactor and its sensitivity at low concentrations is remarkable. It provides reliable and detailed information about the mixing and mass transfer process in the bubble column. Thus it can be used, in combination with PIV, for the determination of mass transfer studies in various experimental situations.

Chapter 7

Uncertainty considerations

Contents

7.1. INTRODUCTION 126
7.2. GENERAL ERROR SOURCES 127
7.3. UNCERTAINTY OF THE SHADOWGRAPHY RESULTS 129
7.4. UNCERTAINTY OF THE VELOCITY FIELD RESULTS 130
7.5. UNCERTAINTY OF THE CONCENTRATION FIELD RESULTS 131
7.6. SUMMARY 132

7.1. Introduction

Every experiment, even the most precise one, which was prepared with the highest care and attention, will involve errors. Therefore, the uncertainty of the results has to be estimated.
The result of a measured variable contains errors, usually denoted with σ, which are the difference between the measured and the true values. These errors can be classified into two classes, namely random and systematic errors. Their addition results in the final error, σ. The random errors r are unpredictable and usually change their values during the measurements, but their mean value can be estimated and reduced by repeated measurements. The systematic errors s are constant errors, which are fixed to their sources and therefore some of them are known and can be corrected. Any error, whose exact value is not known, is a source of uncertainty. The uncertainty is a quantification of the doubt about the measurement result.

To estimate the standard uncertainties, usually two types of evolution are needed according to the origin of the uncertainty. For statistically estimated uncertainties (for example repeated readings in the case of random errors) the standard uncertainty can be calculated as follows:

$$u_a = \frac{S}{\sqrt{N}}, \text{ where} \tag{7.1}$$

$$S = \sqrt{\frac{\sum_{i=1}^{n}(x_i - \bar{x})^2}{(N-1)}} \text{ is the standard deviation for a series of } N \text{ measurements,} \tag{7.2}$$

with x_i the result of the ith measurement and $\bar{x}$ the arithmetic mean of the N results.
In some cases the uncertainty has to be estimated not from statistical information, but from calculations, calibration certificates etc.. In this case it can be assumed, that the measured value can fall in between a measured upper and lower limit. For this reason, the standard uncertainty of these errors is calculated for a rectangular distribution:

$$u_b = \frac{hw}{\sqrt{3}}, \tag{7.3}$$

where *hw* is the half-width between the upper and lower limits.

From the calculated standard uncertainties, the combined standard uncertainty u_C is obtained from the sum of the squares of all influencing uncertainties:

$$u_C = \sqrt{\sum u_{a,i}{}^2 + \sum u_{b,j}{}^2}. \tag{7.4}$$

To define the confidence level of the calculated combined standard uncertainty, it has to be multiplied by a coverage factor k. For most scientific experiments the error distribution can be expected Gaussian. Therefore, the coverage factors of 1, 2 and 3 provide confidence levels of approximately 68%, 95% and 99.7% respectively. Thus the expanded uncertainty of the experiments will be

$$U = k\sqrt{\sum u_{a,i}{}^2 + \sum u_{b,j}{}^2}. \tag{7.5}$$

Most of the error sources for the presented experiments are summarized in Table 7.1 and relevant errors will be discussed in the following subsections for each measurement method.

Table 7.1: Origin and source of the errors in the presented experiments.

Origin	Error source	Measurement method
Flow field	out-of-plane motion, repeatability, initial motion	PIV
Bubbles	out-of-plane motion, orientation, light scattering, shadows	Shadowgraphy, PIV, LIF
Tracer particles	time response, density, particle size distribution	PIV
Optical access	refractive index, optical distortion, scattering, shadows	Shadowgraphy, PIV, LIF
Illumination	light sheet thickness, light absorption, homogeneity	Shadowgraphy, PIV, LIF
Imaging system	camera sensitivity, lenses, filters, geometrical calibration	Shadowgraphy, PIV, LIF
Supply system	flowmeter accuracy, pH and O_2 probe accuracy	Shadowgraphy, PIV, LIF
Environment	temperature, pressure, free surface gas composition	Shadowgraphy, PIV, LIF
Liquid mixtures	mixture composition, concentration of dyes, water quality	Shadowgraphy, PIV, LIF
Mechanical set-up	Construction uncertainties, diameter and orientation of gas needles	Shadowgraphy, PIV, LIF

7.2. General error sources

Some of the error sources are general for all measurement methods, therefore, and to avoid unnecessary repetitions, they will be described in the following.

In all experiments, the gas flow rate was regulated by a variable area flow meter. Therefore, the first, and maybe the most relevant error source is its accuracy. According to the manufacturer's calibration certificate, the applied rotameter has an uncertainty of 2.5-5% for the used measurement range. This uncertainty is given already with a confidence level of 95% (coverage factor 2). Therefore, dividing by 2 gives the standard uncertainty to be 1.25-2.5% (0.1-0.2 l/h). The divisions on the rotameter are spaced almost linear in the measurement range, with around 5 mm spacing, which corresponds to 0.5 l/h. It can be assumed, that the reading to the nearest division gives an error no more than ±1 mm (0.1 l/h). Taking the reading as uniformly distributed uncertainty, the standard uncertainty will be 0.115 l/h, which results in 1.15-2.3% reading error, depending on the adjusted flow rate.

All experiments were carried out in the same bubble column, which was surrounded with a rectangular acrylic tank to decrease the optical distortions. This rectangular tank was always filled with the actually used working fluid, thus optical distortions on the curved walls of the column could always be reduced to a minimum, which is further reduced during geometrical calibration. The effect of the remaining optical distortions therefore will be neglected.

The experiments were performed at nearly the same environmental conditions in the experimental hall. They were carried out at atmospheric pressure, its changes between and during the experiments were minimal. The average atmospheric pressure in our region lies between 1000 and 1030 hPa (www.niederschlagsradar.de). For an exemplary CO_2 bubble with a diameter of 4 mm this atmospheric pressure change results in a 0.037 mm diameter change, and 0.01 mm standard uncertainty, calculated from the bubble volume change. This uncertainty corresponds to a 0.27% diameter error, which can be neglected.
The experiments were carried out at room temperature in the big experimental hall, that varies very slightly around 20°C, and which in summer may rise up to 23°C. This change in the temperature is 15% with a standard uncertainty of 0.866°C. However, these 3 degrees lead to the following changes in the water and in the 50% water-glycerol mixture properties: density: 0.07% / 0.15%; surface tension: 0.6% / 0.27%; viscosity: 6.8% / 11.3 %. Thus, only the eventual changes in viscosity should be kept in mind. Here it is important to mention, that during one measurement campaign the temperature alteration was not higher than ±1°C, therefore the change in viscosity decreases to 2.4% / 4% during one measurement campaign.

For the mixtures, de-ionized water and glycerol originating always from the same source/manufacturer is used, thus their quality should also be as much as possible the same. The composition of the mixtures was performed with the possible highest care and precision therefore the error, originating from the mixture composition (volume and weight errors, mixing errors) was assumed not higher than 1%.

The optical errors caused by the camera, lenses and filters are difficult to estimate. The applied technical equipment was with the highest scientific quality (scientific-grade cameras, high quality glass filters, and Nikon and Tokina lenses). Therefore, the errors, originating from the equipment should not be high. In fact, the errors caused by the optical equipment affect the accuracy of the geometrical calibration in the investigated area. Therefore, these errors are already taken into account during the geometrical calibration.

The measurements were carried out with four different cameras. The error of the geometrical calibration was always calculated during the calibration process as the root-mean-square (RMS) of the fit to the ideal grid of the used calibration plate. This error depends highly on the camera resolution. According to the manual of the software DaVis, used for the geometrical calibrations, a value lower than 0.3 pixel gives an excellent fit for a 2 Megapixel camera, while a larger error is also acceptable at higher camera resolutions. The calculated average geometrical calibration errors of each camera are summarized in Table 7.2. Taking into account all geometrical calibration errors of the experiments, an average geometrical calibration uncertainty of 1.49% was calculated.

Table 7.2: Average RMS and uncertainty values, calculated from the geometrical calibrations for the different camera models used.

	Pixel size [µm]	**Resolution (horizontal x vertical)** [pixels]	**Average RMS** [pixels]	**Uncertainty** [%]
Imager Intense	6.45	1376 x 1040	0.174	1.26
Imager LX 8M	5.5	3312 x 2488	0.219	0.88
Imager pro HS 4M	11	2016 x 2016	0.384	1.91
Imager sCMOS	6.5	2560 x 2160	0.492	1.92

7.3. Uncertainty of the shadowgraphy results

The shadowgraphy measurements were carried out with a background illumination, which has illuminated the back of the measurement areas homogeneously. The remaining illumination errors were removed during image processing (geometrical calibration, background subtraction) and therefore its effect can be neglected.

Due to the linear nozzle setup, the bubbles were situated in the centre of the column. Because of their helical path, the deviation from the centre plane in depth was maximal ±3cm. This change in the bubble–camera distance results in slightly smaller or bigger bubble images. Taking the depth change as uniformly distributed uncertainty, the standard uncertainty of the bubble size change in function of the depth change will be 2%.

For the shadowgraphy experiments with the high-speed cameras (Table 2.5, Imager pro HS 4M), the calibration error was 0.21 pixel, which corresponds to 0.032 mm. Taking into account the whole camera resolution 2016x2016 pixels^2, the calibration uncertainty results in 1.04%.

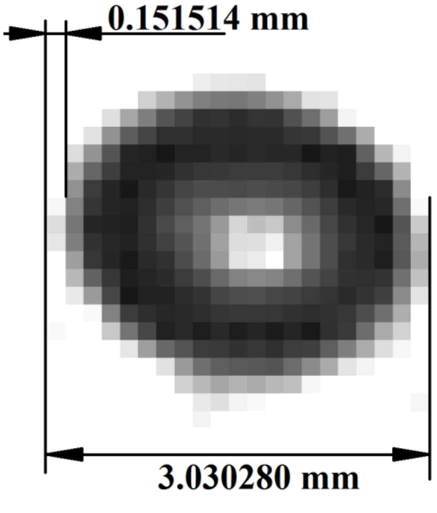

Figure 7.1: Exemplary bubble from the shadowgraphy experiments.

In the shadowgraphy experiments the bottleneck concerning diameter errors is the image resolution. Figure 7.1 shows an exemplary bubble image from the experiments. During the recognition process, the bubble diameters are calculated from the geometrical pixel to mm calibration, and the optical resolution of the system was 0.151514 mm/pixel. Calculating with uniformly distributed uncertainty, the standard uncertainty results in 0.044 mm, approximately. In the case of an average bubble size of 3 mm, this leads to 1.46% uncertainty in the recognition, while this error is 0.73% for the biggest bubbles with 6 mm and 2.19% for the smallest bubbles with 2 mm.

7.4. Uncertainty of the velocity field results

The tracer particle size used for the PIV experiments was in the range of 10-50 μm with a density close to water. Particles with this size appeared 4-9 pixel-sized on the recorded images, therefore the peak-locking error can be neglected [148].

To avoid out-of-plane particle motions and too large or too small particle displacements, the time delay between the two frames was chosen in a way, to get 2-8 pixels particle displacements in average. Moreover, the seeding density was also set to around 0.05 ppp (particle per pixel). Therefore, these error sources can be estimated as very small.

For the experiments scientific grade double pulsed Nd:YAG or Nd:YLF lasers were used and their laser beam was converted with laser sheet optics to a less than 0.5 mm thin laser sheet to illuminate the tracer particles. Because of the thin laser sheet, it was assured, that just the 2D motion of the particles was taken into account in the flow field calculations.

During the PIV evaluations the uncertainty of the PIV results was also calculated with the PIV processing software, DaVis. The built-in operation calculates the uncertainty of each vector component in a single instantaneous PIV field (Figure 7.2, a) with correlation statistic methods, described in Wieneke [187]. The thusly calculated uncertainties result in 0.001-0.005 m/s for the mean liquid velocity, depending on the location of the investigated vector and on the liquid flow field. This corresponds to 4-28% of the mean velocity. If the vector is situated in the vicinity of a bubble or its shadow, the uncertainty value is higher (Figure 7.2, a red areas); in other, undisturbed places, the uncertainty remains lower.

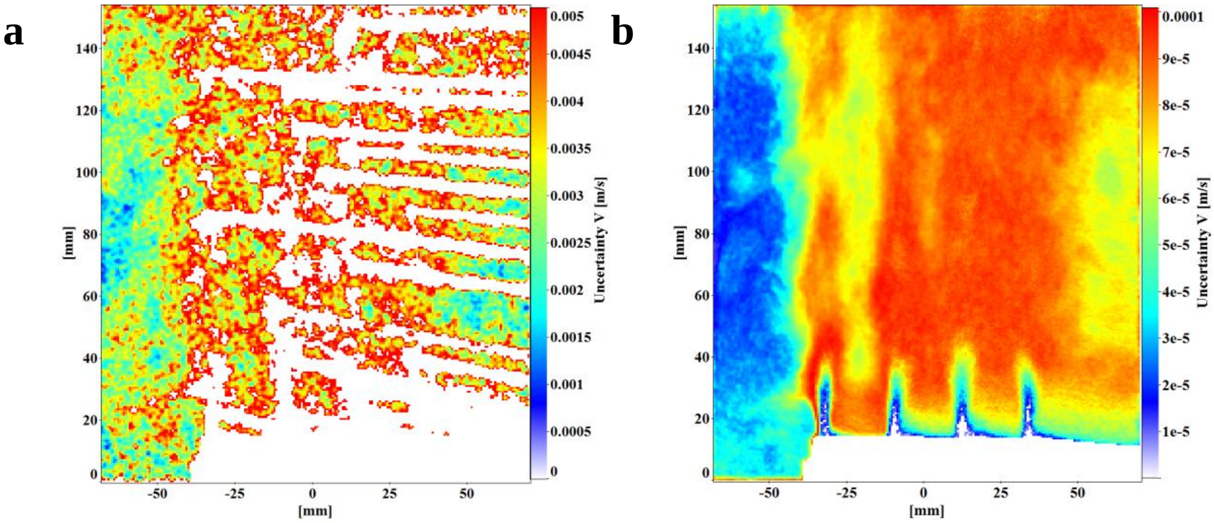

Figure 7.2: Exemplary instantaneous (a) and average (b) PIV uncertainties at the bottom of bubble column in measurement window S1 (high-speed experiment).

Figure 7.3 shows the calculated liquid velocities and their uncertainties in two horizontal line plots at 60 mm and at 120 mm. It is clearly visible, that despite of the high calculated uncertainties over the whole flow field, the local uncertainties, which belong to the specific velocity vectors, remain close to the calculated velocity value. It is also visible, that the uncertainty bands become broader close to the masked areas (e.g. at the right hand side of the profiles).

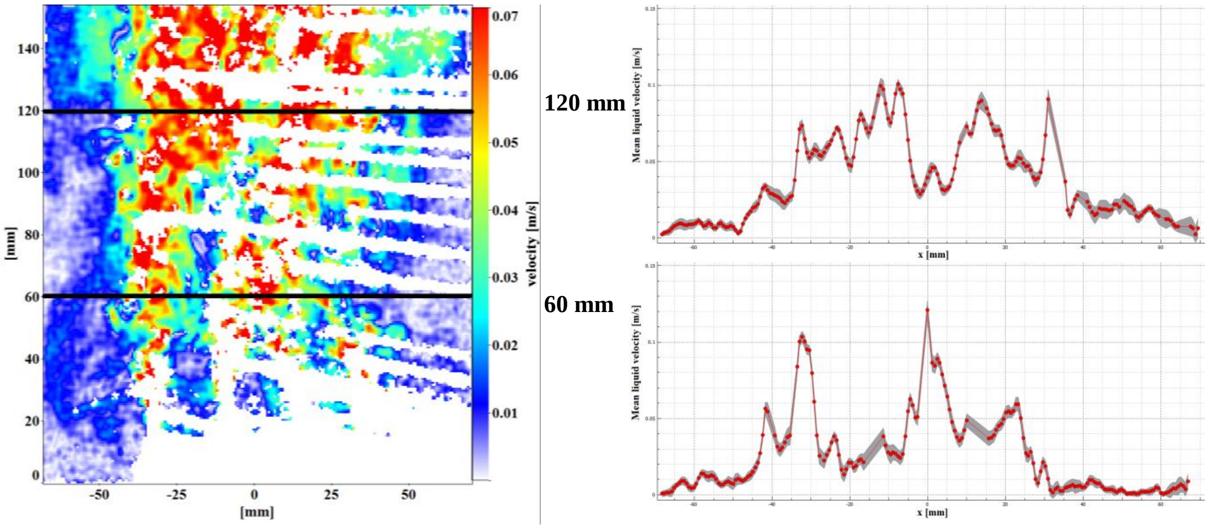

Figure 7.3: Mean liquid velocity and horizontal velocity profiles (red lines) with uncertainty band (grey) at 60 mm and at 120 mm of one exemplary instantaneous liquid velocity field at the bottom of bubble column in measurement window S1 (high-speed experiment).

Using Eq. (7.1), the uncertainty of the averaged flow field can then be calculated, where *S* is the standard deviation of the uncertainties of *N* instantaneous PIV fields (Figure 7.2, b).

It results an average uncertainty of $5 \cdot 10^{-05} – 1 \cdot 10^{-04}$ m/s for the mean liquid velocity of the average flow field. The measure of uncertainty depends highly on the number of averaged instantaneous fields, *N*. Taking into account the averaged mean liquid velocities, the estimated uncertainties of the averaged PIV fields are less than 1%.

7.5. Uncertainty of the concentration field results

In the LIF measurements two different reaction systems were applied, but from a point of view of errors, they are very similar, because nearly the same image acquisition and image processing steps are used.

From the raw intensity images the known errors, originating from the camera and illumination, were reduced with different image processing steps. From all calibration and measurement images the digital noise was removed with background subtraction. The inhomogeneity of the laser light sheet was corrected with a light sheet correction process or with an absorption correction. With these steps the errors connected to the image recording were minimized.

The most fundamental error source is the intensity calibration for the pH and the equivalent oxygen concentration. These calibration curves are based on pre-recorded calibration images, which were recorded and processed in the same way as the experimental images. From these images linear or polynomial regression curves are established with an accuracy over 98%, which leads to a mean error of 2%.

On the other hand, for the pH calibration the accuracy of the pH probe has to be accounted for. A WTW Profiline 3320 Multi pH-meter with a SenTix HWD pH probe was used. The accuracy of this probe is 0.001 pH, which is far below the accuracy of the polynomial calibration curve and it can therefore be neglected.

The main error source of the pH and the equivalent oxygen concentration measurements is the concentration of the applied dye. In the experiments, dyes originating from the same manufacturer and from the same batch are used. Therefore, their quality should be as much as possible the same. These dyes were added to the mixtures always in the same manner, with the highest precision and care. To reduce mixing errors, stock solutions with high dye concentrations were prepared from the powder of the tracer dyes. The required amount of dye was then added to the column from this high concentrated source with the help of appropriately chosen measuring cylinders and syringes.

For instance, for the concentration of 20 mg/l fluorescein, from a previously mixed 1 g/l stock solution, 226 ml was added into the bubble column (11.3 l). It was measured with a 50 ml measuring cylinder, with ml divisions. Reading to the nearest division gives an error no more than ± 0.5ml, therefore the estimated uncertainty from Eq. (7.3) is 0.35 ml, approximately. To measure 226 ml, five readings are necessary; therefore the final combined uncertainty from Eq. (7.4) will be 0.78 ml, approximately. With a coverage factor of 2, it gives 1.56 ml, which results in a final error of 0.7% for the fluorescein concentration in the bubble column. Concentration uncertainties calculated in that way for all setups are below 3%.

7.6. Summary

In Table 7.3 all above estimated uncertainties are summarized for the applied measurement techniques.

Table 7.3: Estimated uncertainties of the performed experiments.

General errors			
	Flow meter uncertainty	1.25-2.5%	(0.1-0.2 l/h)
	Flow meter reading uncertainty	1.15-2.3 %	(0.115 l/h)
	Atmospheric pressure effect on the bubble size	0.27%	(0.005-0.016 mm)
	Temperature effect on the mixture		
	uncertainty of density	0.07-0.15%	
	uncertainty of surface tension	0.27-0.6%	
	uncertainty of viscosity	2.4-4%	
	Mixture composition uncertainty	1%	
	Mean geometrical calibration uncertainty	1.49%	(0.3176 pixel)
Measurement technique specific errors			
Shadowgraphy			
	bubble size uncertainty in depth	2%	(0.03-0.13 mm)
	bubble size determination uncertainty	0.73-2.19%	(0.044 mm)
PIV			
	velocity vector uncertainty	4-28%	(0.001-0.005 m/s)
	time-averaged velocity vector uncertainty	1%	(5e-05 – 1e-04 m/s)
LIF			
	Intensity calibration curve uncertainty	2%	
	Applied dye concentration uncertainty	0.7-2.8%	

Taking into account both considered uncertainties, the complete uncertainty of the adjusted flow rate is 1.7 – 3.4%, depending on the adjusted value.

The bubble size determination depends on two types of bubble size uncertainties and on the accuracy of the geometrical calibration. The combined uncertainty results in 2.37 – 3.14%, depending on the bubble size.

The calculated instantaneous PIV vector fields show a higher uncertainty, especially in the vicinity of bubbles and their shadows, but due to the time-averaging, these errors were reduced. The final combined uncertainty consists of the PIV uncertainty and the calibration uncertainty. Taking the mean geometrical calibration error, it results in 1.8%, approximately.

The results of the pH and equivalent oxygen concentration measurements depend highly on the applied dye concentrations and on the intensity calibration curves. Taking into account these uncertainties, the combined uncertainty of the LIF measurements is 2.1 – 3.5%, depending on the applied dye and its concentration.

The overall effect of the uncertainty of temperature, pressure and mixture composition on the bubble size, bubble generated flow field and mass transfer is complex and cannot be determined from the available data.

Obviously, the here listed and estimated errors are not covering all error sources, but it gives an impression of the uncertainty of the presented results.

Chapter 8

Validation of numerical simulations with the measurement data

Contents

8.1. SCIENTIFIC DATABASE 135
8.2. SIMULATIONS WITH PURE WATER AS THE LIQUID MEDIUM 135
  8.2.1. Validation of simulations with Euler-Euler two-fluid model for gas fraction and liquid velocity 135
  8.2.2. Validation of simulations with Euler-Euler model in water for bubble parameters, liquid velocity and mass transfer 140
8.3. SIMULATIONS IN MIXTURES WITH DIFFERENT VISCOSITIES AND SURFACE TENSIONS 144
  8.3.1. Validation of simulations with Euler-Lagrange model in low to high viscous liquids 145
  8.3.2. Validation of simulations with an Euler-Lagrange model in water and 50% water-glycerol mixture 148
8.4. SUMMARY 150

8.1. Scientific database

A large part of the experiments presented in this thesis were financed and carried out in the framework of the German Research Foundation (DFG) SPP 1740 ‘‘Reactive Bubbly Flows’’ under project No. ZA-527/1-1. According to the project proposal, a scientific database was created to support the other research teams with experimental data for comparison or data validation. In this database the experimental results and the exact geometry of the bubble column reactor can be found and it gives short introductions concerning the different measurement techniques (Figure 8.1).

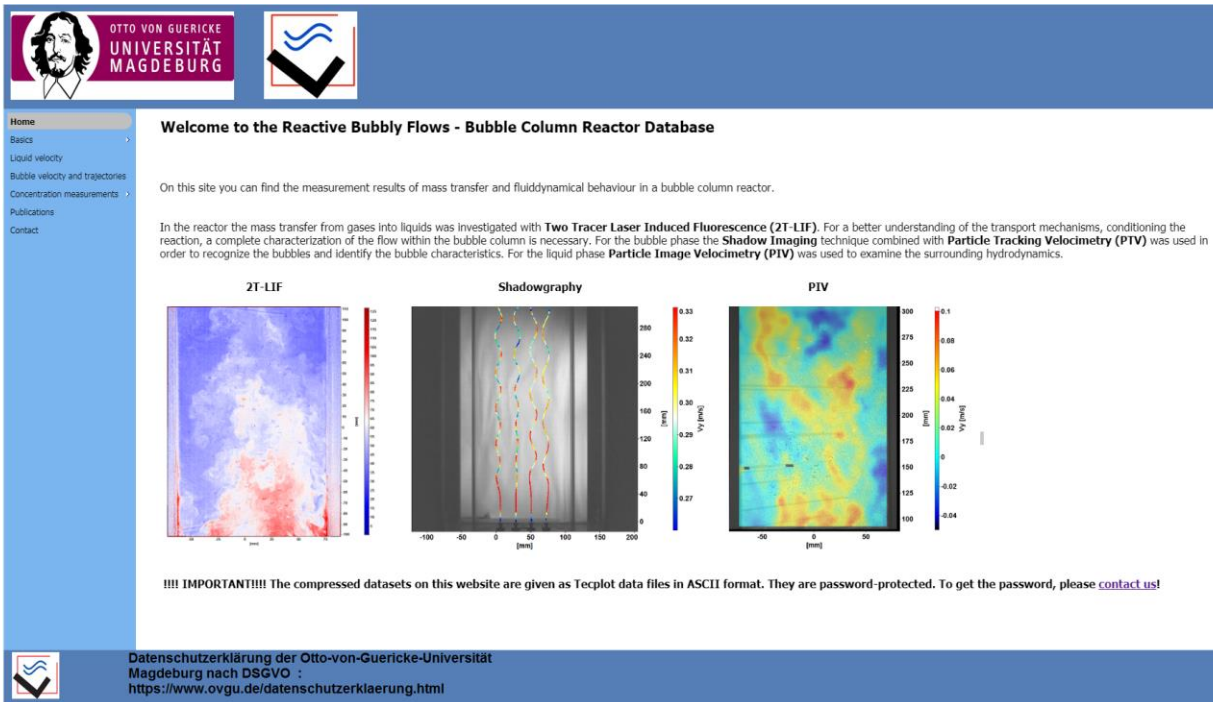

Welcome to the Reactive Bubbly Flows - Bubble Column Reactor Database

On this site you can find the measurement results of mass transfer and fluiddynamical behaviour in a bubble column reactor.

In the reactor the mass transfer from gases into liquids was investigated with **Two Tracer Laser Induced Fluorescence (2T-LIF)**. For a better understanding of the transport mechanisms, conditioning the reaction, a complete characterization of the flow within the bubble column is necessary. For the bubble phase the **Shadow Imaging** technique combined with **Particle Tracking Velocimetry (PTV)** was used in order to recognize the bubbles and identify the bubble characteristics. For the liquid phase **Particle Image Velocimetry (PIV)** was used to examine the surrounding hydrodynamics.

!!!! IMPORTANT!!!! The compressed datasets on this website are given as Tecplot data files in ASCII format. They are password-protected. To get the password, please contact us!

**Datenschutzerklärung der Otto-von-Guericke-Universität Magdeburg nach DSGVO :
https://www.ovgu.de/datenschutzerklaerung.html**

Figure 8.1: Snapshot of the main page of the scientific database.

In the following subsections the comparison of the measured data with the results of different CFD-simulation tools in different working groups within the SPP1740 will be presented. These validations are based on the shared experimental results of the measurements in our bubble column reactor and have been published in several common research papers [184-186] and a book section [188].

8.2. Simulations with pure water as the liquid medium

In the following, validation of simulations will be presented, where pure water has been used as the liquid medium.

8.2.1. Validation of simulations with Euler-Euler two-fluid model for gas fraction and liquid velocity

The aim of these simulations was to provide a broadly applicable predictive model for bubbly flows. To this end, the Euler-Euler two fluid model was applied in the simulations. They were carried out by the group of Dr. Roland Rzehak at the Helmholtz-Zentrum, Dresden-Rossendorf. The detailed description of this simulation can be found in the published article [186], where also parts of the following results are presented. The validations of such models are necessary and important and with the comparison of the numerical and

experimental results, the confidence in the model for predictive applications, such as optimization and scale-up of chemical engineering processes can be enhanced.
For the comparison with the numerical results the PIV (subsection 5.3; Table 2.2 No. 6) and Shadowgraphy (Chapter 3; Table 2.2 No. 9) results obtained with high-speed cameras in the bubble curtain were used.

The following sections are a summary of the joint paper, published in "International Journal of Multiphase Flow": Rzehak, R., Krauß, M., Kováts, P. and Zähringer, K.: Fluid dynamics in a bubble column: New experiments and simulations, International Journal of Multiphase Flow, 89, 2017, pp. 299-312, Doi: 10.1016/j.ijmultiphaseflow.2016.09.024.

All calculations were performed with a customized version of ANSYS-CFX 14.5 (ANSYS, 2012a). The simulations were run in transient mode on the full 3D domain. Results were averaged over a simulated physical time of 10 min which is sufficiently long, to that the resulting average does not change significantly anymore.
A subset of test cases was selected for the comparison from the larger experimental database. Conditions for the selected test cases are summarized in Table 8.1.

Table 8.1: Experimental parameters.

System	Q_G (l/h)	$\langle d_B \rangle$(mm)	Available data
Air / water	7.5	2.9	gas fraction, front and side view
Air / water	10	3.1	gas fraction, front and side view
CO_2 / water	6.4	2.7	gas fraction and velocity, front view only

Considering first the air / water system at a flow rate of $Q_G = 7.5$ l/h, Figure 8.2 shows the two-dimensional distribution of gas fraction in the measurement plane for front (a and c) and side view (b and d) up to a height of ~300 mm, where measurements were carried out. The bubbles are more concentrated near the inlet nozzles, while an almost homogeneous bubble distribution is observed in the upper part. Some fluctuation is still visible in the experimental data but the degree of symmetry with respect to the centreline is high. Comparison of experimental (a and b) and simulation (c and d) results shows a well reproduction of the gas distribution by the simulations. Similar good agreement is found for the air / water system at a flow rate of $Q_G = 10$ l/h.
Results for the gas fraction in the CO_2 / water system at a flow rate of $Q_G = 6.4$ l/h, are depicted in Figure 8.3 and Figure 8.4. The comparison of the two-dimensional experimental (a) and simulation (b) gas distributions shows that the overall pattern of the gas distribution is reproduced quite well by the simulations (Figure 8.3).

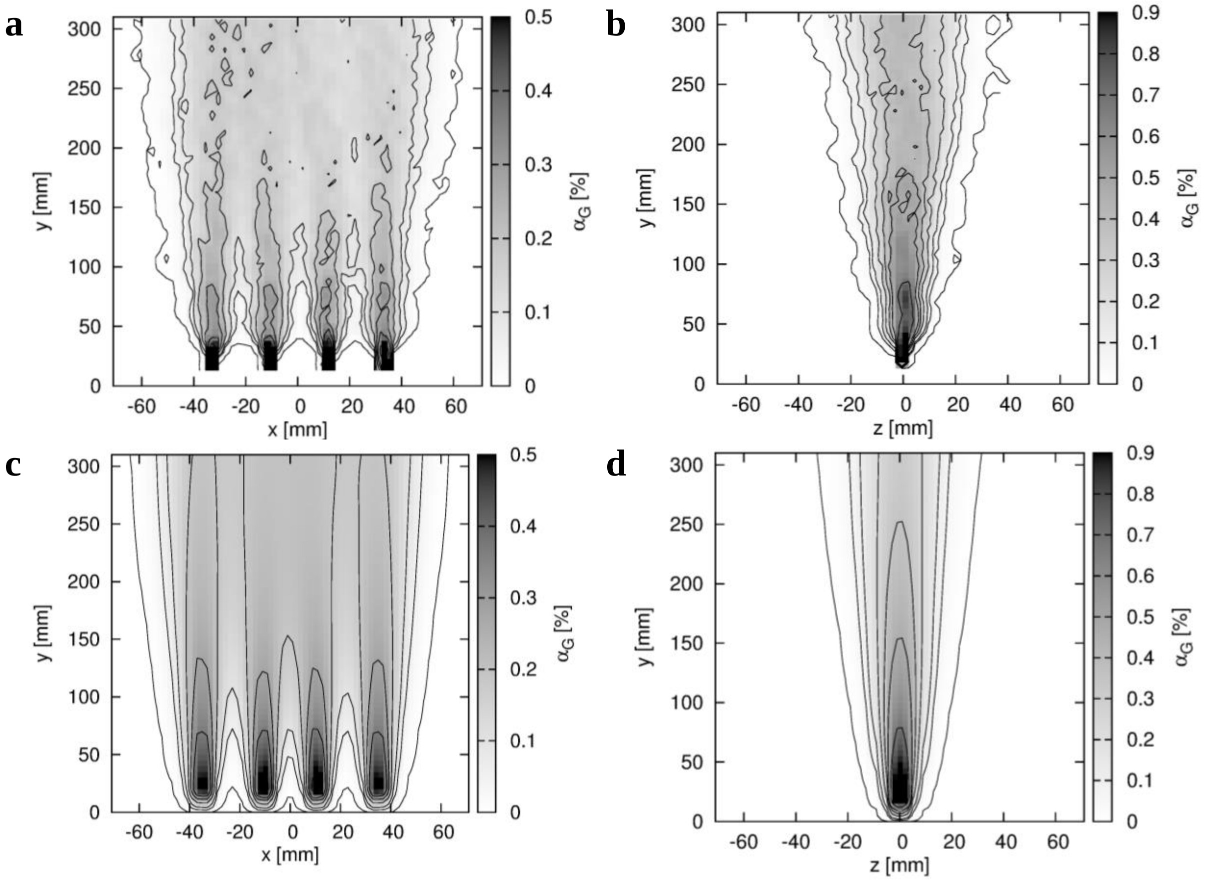

Figure 8.2: Comparison of gas fraction ε_G calculated from the shadowgraphy measurements (a and b) and from the simulation results (c and d) for air bubbles in water at Q_G = 7.5 l/h. a and c: 2D fields in front view; b and d: 2D fields in side view. From [186].

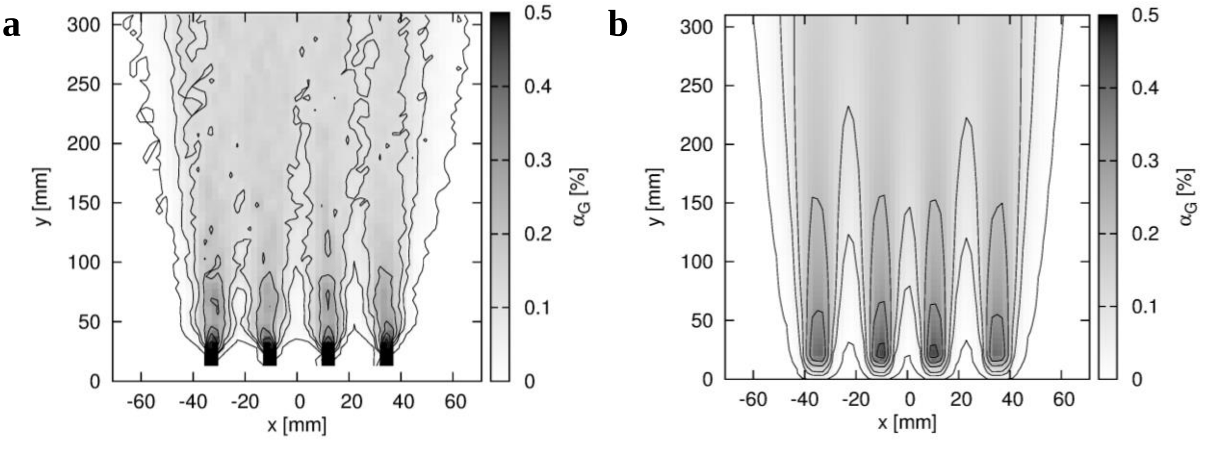

Figure 8.3: Comparison of gas fraction ε_G calculated from the shadowgraphy measurements (a) and from the simulation results (b) for CO_2 bubbles in water at $Q_G \approx$ 6.4 l/h. From [186].

Extracting horizontal profiles from the gas-fraction fields allows a more quantitative comparison. The profiles are taken at three different heights, at 50 mm, 150 mm and 250 mm distance from the bottom (Figure 8.4). It is seen that for this case the quantitative agreement between experiment and simulation is also quite good.

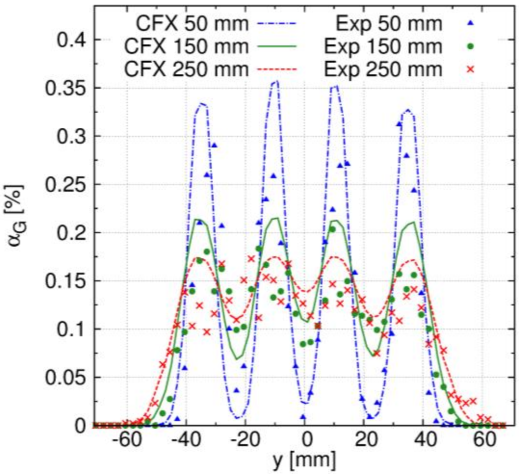

Figure 8.4: Comparison of gas fraction ε_G calculated from the shadowgraphy measurements (symbols) and from the simulation results (lines) for CO_2 bubbles in water at $Q_G \approx 6.4$ l/h. Profiles in front view, taken at different heights as indicated in the legend. From [186].

For the CO_2 / water system at $Q_G = 6.4$ l/h, also the measured vertical and horizontal components of the mean liquid velocity are compared with the simulations, as shown in Figure 8.5.

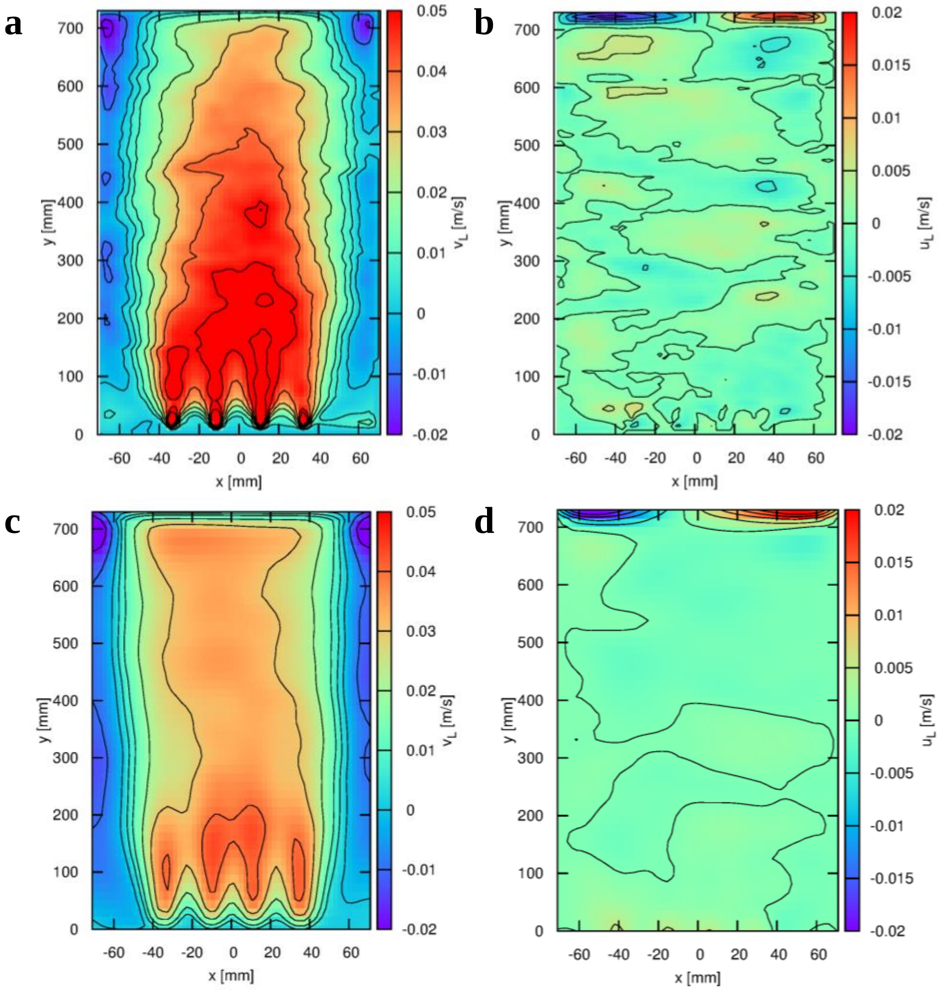

Figure 8.5: Comparison of average liquid velocity components v_L and u_L obtained from the PIV measurements (a and b) and from the simulation results (c and d) for CO_2 bubbles in water at $Q_G \approx 6.4$ l/h. a and c: vertical component; b and d: horizontal component. From [186].

A slight asymmetry is visible in both experimental and simulations results, which comes from the finite averaging time and, in the experimental case, from slight manufacturing differences between the four nozzles. Comparing the mean liquid flow pattern in experiment and simulation there is good agreement, however, as it can be seen on the images, the magnitude of the vertical velocity is underestimated by the simulations.

Horizontal profiles of the vertical velocity component were taken at 50 and 600 mm heights for a quantitative comparison (Figure 8.6). At 50 mm (Figure 8.6, a) in the experiments the bubbles generated by the second nozzle from the right apparently produced a faster liquid flow than the others. The origin of this difference could be explained with slight manufacturing differences between the four nozzles. The remaining effect of higher liquid flow can also be seen at 600 mm (Figure 8.6, b). Comparing experimental and simulation results, it is seen that at 50 mm, the simulations predict a too low liquid velocity especially at the peaks in the profile. At the higher level, the difference between simulation and experiment has become smaller and can partly be attributed to the remaining asymmetry in the latter.

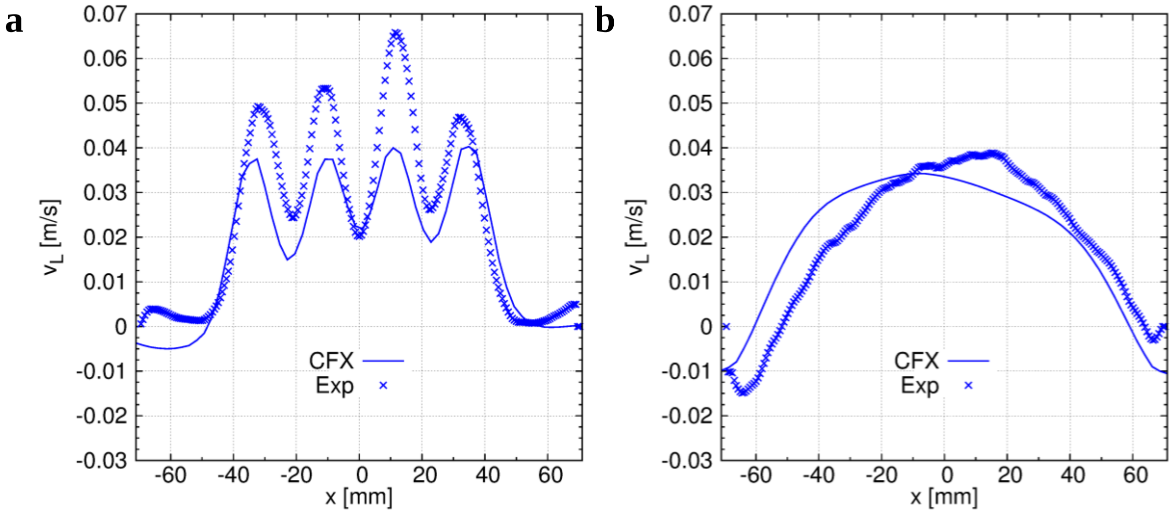

Figure 8.6: Comparison of average vertical liquid velocity component v_L obtained from the PIV measurements (symbols) and from the simulation results (lines) for CO_2 bubbles in water at $Q_G \approx 6.4$ l/h at 50 mm (a) and 600 mm (a) heights. From [186].

The fluctuations of the liquid velocity in vertical and horizontal directions are also compared in Figure 8.7. For the vertical fluctuations (Figure 8.7 a and c), the simulations are in good agreement with the experimental results in the centre of the column. However, the horizontal fluctuations are somewhat overpredicted in the simulations (Figure 8.7 b and d).

Overall the comparison is quite good for the gas fraction. Some deviations occur, but do not follow any clear trend. For the mean vertical liquid velocity, the simulations give systematically ~20% lower values, the deviation being somewhat more pronounced close to the inlet nozzles than in the upper section of the column. The origin of the discrepancy remains unclear at present. Mean horizontal liquid velocity is close to zero except for two recirculation zones near the free surface at the top of the column. These are also captured well by the simulations. Concerning fluctuations of the liquid velocity, there is quite good agreement between simulation and experiment for the vertical direction. Fluctuations in the horizontal direction are overpredicted in the simulations by about 50%.

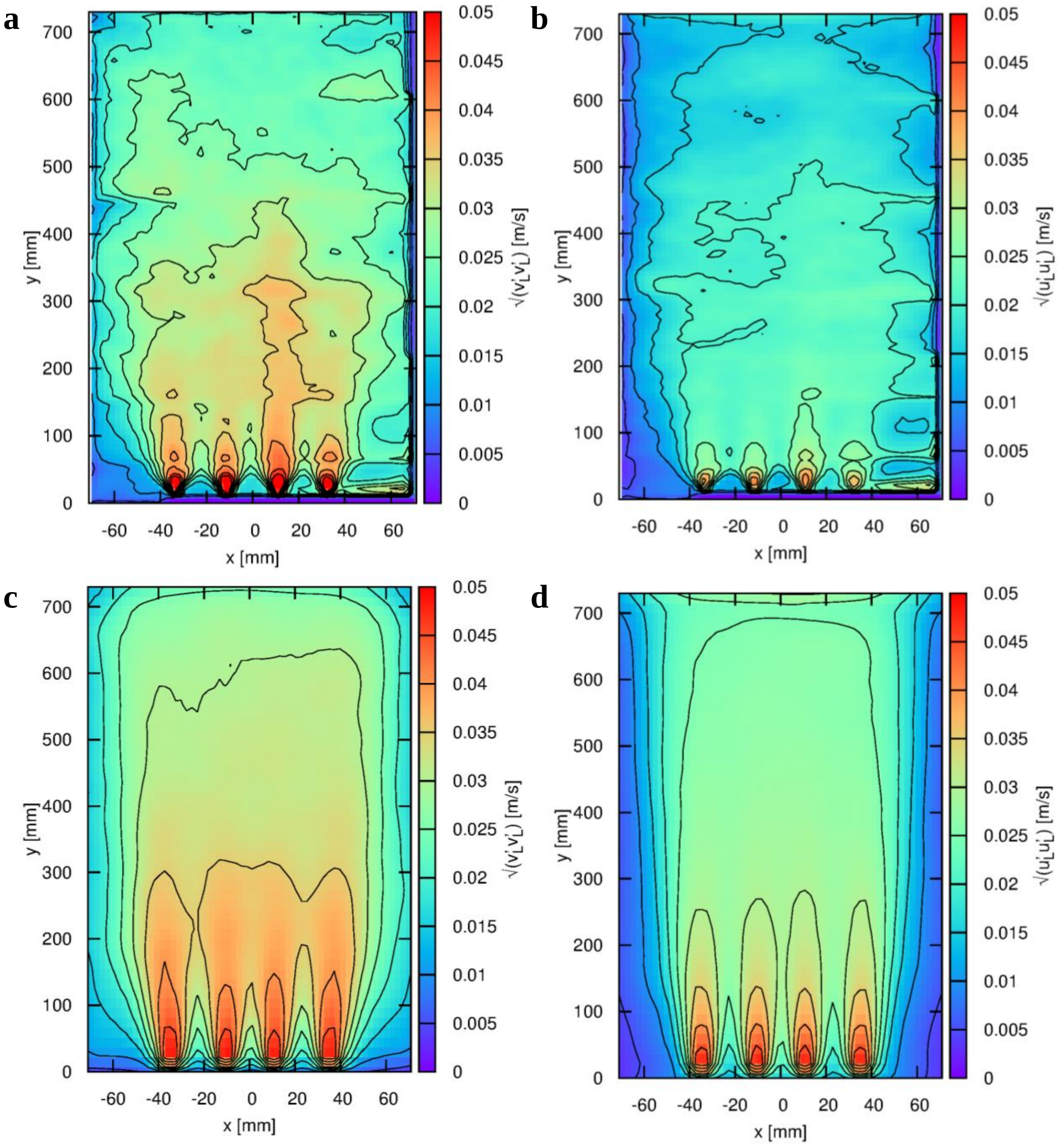

Figure 8.7: Comparison of liquid velocity fluctuations $\sqrt{(v'_L v'_L)}$ (a and c) and $\sqrt{(u'_L u'_L)}$ (b and d) obtained from the PIV measurements (a and b) and from the simulation results (c and d) for CO_2 bubbles in water at $Q_G \approx 6.4$ l/h. From [186].

8.2.2. Validation of simulations with Euler-Euler model in water for bubble parameters, liquid velocity and mass transfer

For this validation the local measurements of hydrodynamics, bubble size and velocity (described in Chapter 3; Table 2.2 No. 9), liquid velocity and concentration (described in subsection 5.3; Table 2.2 No. 6 and 8) in the bubble column reactor with bubble curtain were used. The results were compared to Euler-Euler based computational fluid dynamics simulations that take into account the ongoing reaction. These simulations were carried out by the group of Dr. Mark Hlawitschka at TU Kaiserslautern.

The following sections are a summary of the joint paper, published in "Chemical Engineering Science": Hlawitschka, M. W., Kováts, P., Zähringer, K. and Bart, H. J.: Simulation and experimental validation of reactive bubble column reactors, Chemical Engineering Science, 170, 2017, pp. 306-319, http://dx.doi.org/10.1016/j.ces.2016.12.053.

The simulation setup corresponds to the experimental setup. The geometry is discretized using the meshing "snappyhexmesh" in 31600 cells. In total, 190 seconds were simulated, where the simulation started with the initial gassing in accordance to the experiments. During the simulation, the time step is kept constant at 0.001 sec.

All experimental data were averaged corresponding to the numerical mesh for an area of 7x7 mm². Along the column height, three positions were compared, where the vertical centre of the investigated areas are at 33.5 mm, 183.5 mm and 303.5 mm.

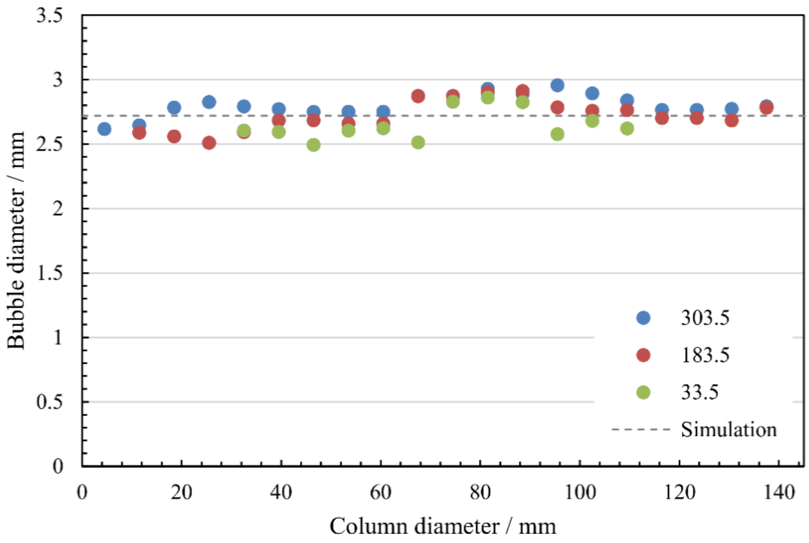

Figure 8.8: Mean bubble diameters at column heights of 33.5 mm, 183.5 mm and 303.5 mm. From [184].

The mean bubble sizes for the investigated test case are shown in Figure 8.8. At 33.5 mm the bubbles are located near the inlet nozzles on the bottom of the column. With increasing height, during their rise, the mean bubble size does not change considerably. The measured average bubble sizes are 2.65 mm, 2.71 and 2.80 mm at 33.5 mm, 183.5 mm and 303.5 mm height respectively. Due to the investigated conditions, there is no bubble coalescence and breakage. As a consequence of the very small change in bubble size, a constant bubble size of 2.72 mm is employed for the simulation in this study.

The comparison of the mean vertical bubble velocity component from experimental data and simulation is depicted in Figure 8.9. The measured average bubble rising velocities are 0.30 m/s, 0.30 m/s and 0.28 m/s at 33.5 mm, 183.5 mm and 303.5 mm column height, respectively. The fluctuations of the measured bubble velocities along the column diameter are from 0.21 m/s up to 0.33 m/s. The bubble velocity in the simulations reaches an average value of 0.30 ms^{-1}. In the lower part of the column (33.5 mm), due to the position of the inlet nozzles, bubbles only exist in the centre of the column, in dense streams over the nozzles.

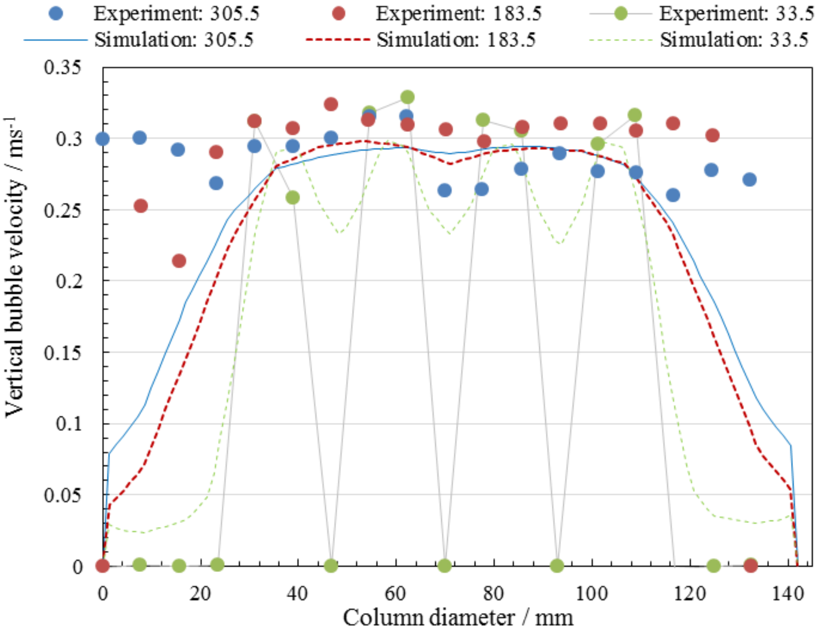

Figure 8.9: Mean vertical bubble velocity profiles at column heights of 33.5 mm, 183.5 mm and 303.5 mm. From [184].

The comparison of the mean vertical liquid velocity component is presented in Figure 8.10 at three heights. At the lowest 33.5 mm position, the liquid velocity is influenced by the dense bubble streams over the nozzles (Figure 8.10, a). At 183.5 mm (Figure 8.10, b) and 303.5 mm (Figure 8.10, c), where the bubbles occupy a larger area, the liquid velocity shows a bell-shaped distribution, with a maximum of 6.3 cm s^{-1} at 183.5 mm. Comparing experimental and simulation results, the simulations predict lower liquid velocities at 33.5 and 183.5 mm heights. At 303.5 mm, the difference between simulation and experiment has become smaller.

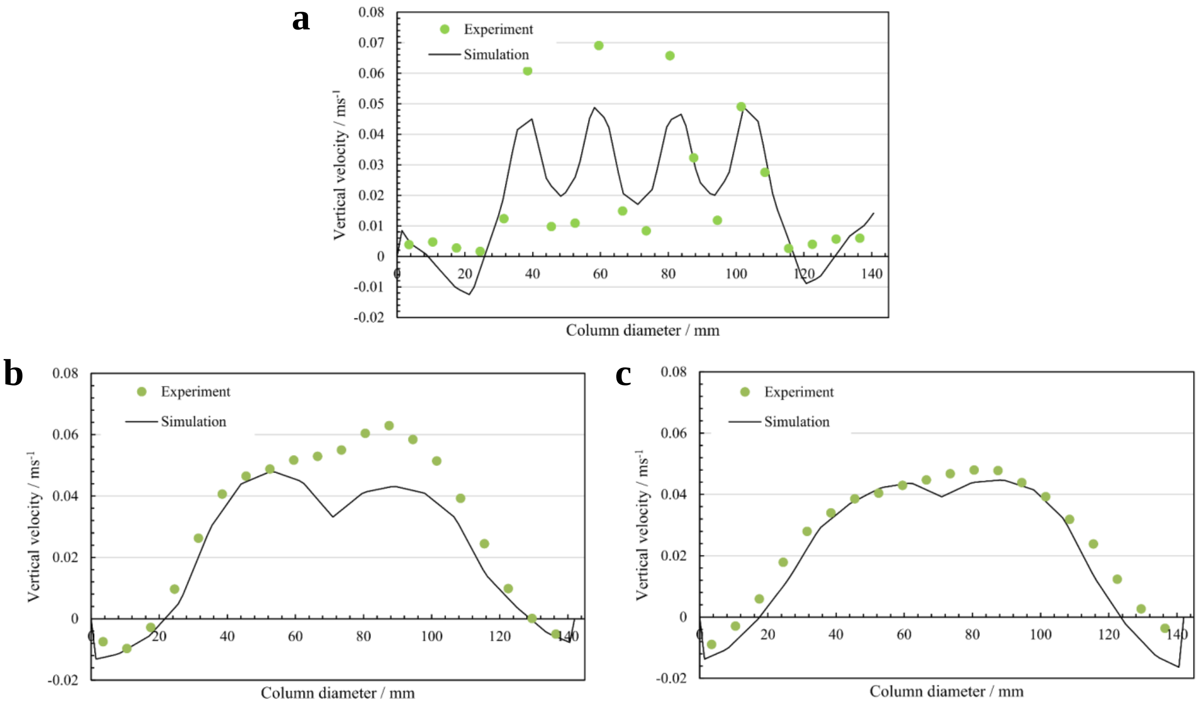

Figure 8.10: Mean vertical liquid velocity profiles at column heights 33.5 mm (a), 183.5 mm (b) and 303.5 mm (c). From [184].

The temporal pH-value evolution of the experiments during 190 seconds is compared to the simulation results in three sections in Figure 8.11. The measured concentrations were averaged for a column height of 100-321 mm, 305-518 mm and 503-716 mm (Figure 8.11, a, b and c). An initial pH-value of 9 is used in both cases, but the applied experimental method can only visualize reliably pH values below 8. All pH-values, which are bigger than 8, appear with the same intensity. For this reason, plots are started in the figures only from about 20-40 s, when the pH becomes smaller than 8 in the measurements. The simulation results were averaged over the same domain for each 10 seconds of simulation. For the lowest two investigated sections (Figure 8.11, a and b), the development of the pH-value predicted by the simulation fits to the experimental values from a simulation time of 40 seconds until the end of the measurement. For the top section (Figure 8.11, c), the pH-value is slightly lower from a simulation time of 60 seconds on than the one obtained from the experiment. In this section, the influence of the free surface in the experiment compared to the boundary conditions used in the simulation maybe the source of the deviation between the experimentally observed pH-value developments.

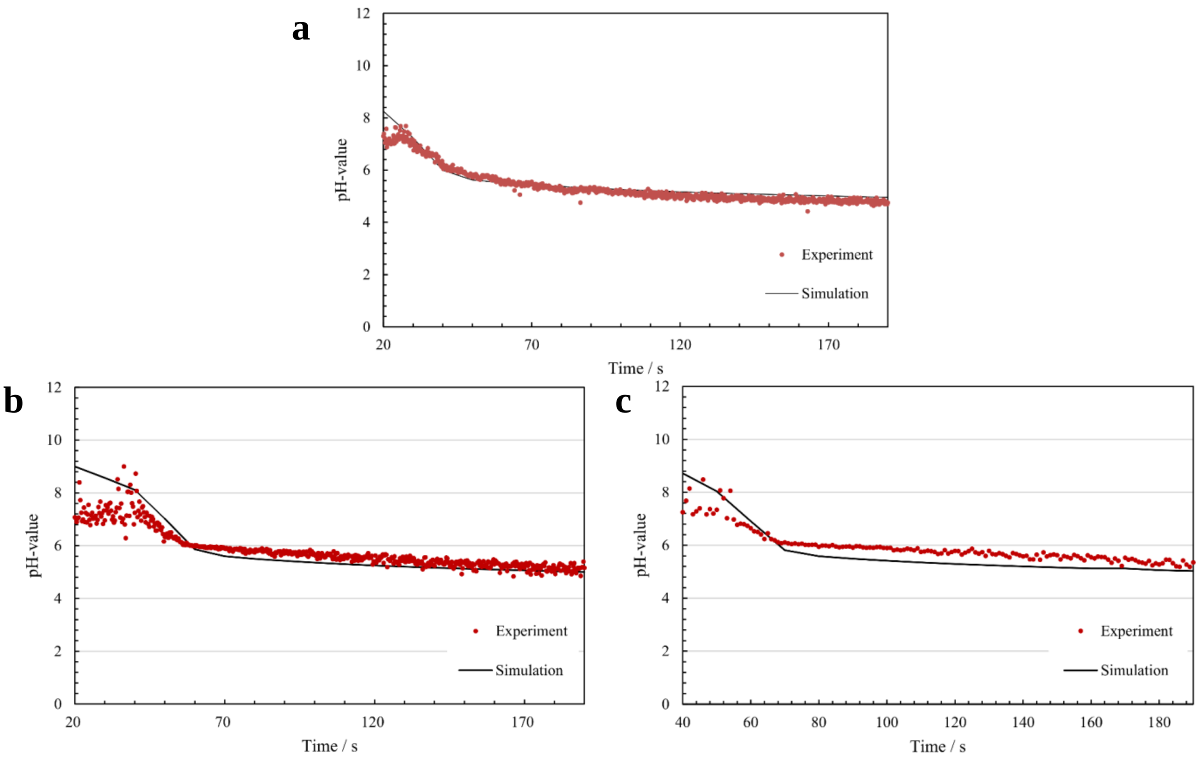

Figure 8.11: Mean temporal pH-value evolution averaged for column sections of 100-321 mm (a), 305-518 mm (b) and 503-716 mm (c). From [184].

Comparing experimental and simulation results, a reasonable agreement could be obtained for the hydrodynamics in the bubble column. Close to the inlet, the bubbles are located in dense streams over the nozzles in the centre of the column, then they distribute across the column, occupying almost the whole width on their way up to the top. The higher liquid velocities over the nozzles and the backflow close to the wall are also captured well by the simulations.

For the pH-value development of the solution, after 40 seconds from the measurement start a good agreement between experiments and simulation has been found.

8.3. Simulations in mixtures with different viscosities and surface tensions

In this subsection, validation of simulations will be presented, where water-glycerol-surfactant mixtures were used as the liquid medium. In addition to the presented bubble characteristics in Chapter 3, the aspect ratio, the direction of motion γ and the inclination of the bubbles were also determined from the obtained bubble data, as explained in [189] (Figure 8.12).

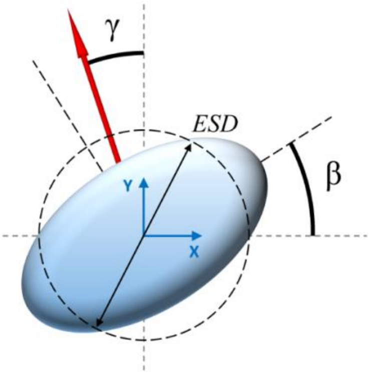

Figure 8.12: Additional bubble properties.

As an example, on Figure 8.13 the development of the equivalent sphere diameter, aspect ratio, bubble inclination and the direction of the bubble motion over the column height is depicted for the 25% water-glycerol mixture without surfactant with 4 l/h CO_2 gas flow rate.

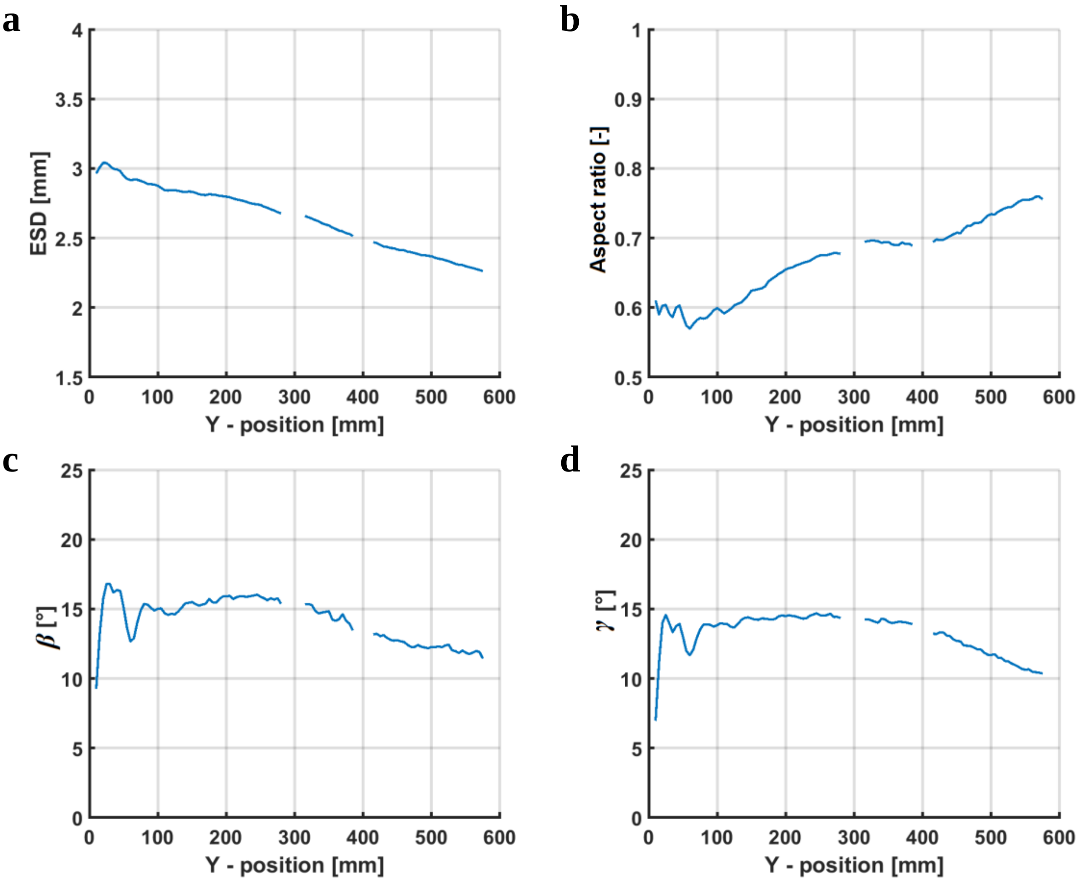

Figure 8.13: Equivalent sphere diameter (a), aspect ratio (b), bubble inclination (c) and the direction of the bubble motion (d) over the column height for 25% water-glycerol mixture without surfactant with CO_2; Q_g=4 l/h.

The figure shows an obvious change in the bubble form and motion over the whole column height. At the bottom of the column the bubbles are elliptical (aspect ratio 0.6), but during their way upwards, the bubble size decreases and the aspect ratio increases up to around 0.76. This increasing aspect ratio shows that the bubbles become more spherical on the way upwards. For this reason, their motion changes as well. After the bubble size gets below 2.5 mm with an aspect ratio over 0.7, the angle of the bubble motion and the bubble inclination decrease. Gaps in the course of the curves on Figure 8.13 are due to the edges of the used paper sheets, which were used to generate a homogenous background illumination. In these areas accurate bubble recognition was not possible, therefore these areas were masked out for the data processing.

These detailed bubble characteristics can then be used for bubble motion models development and a better quantitative comparison with numerical results, where the wobbling of the bubbles is also taken into account.

8.3.1. Validation of simulations with Euler-Lagrange model in low to high viscous liquids

In this numerical work the influence of viscosity on bubble dynamics is studied using an Euler-Lagrange framework with an added oscillation and reaction model. For comparison and validation, experimental data in water-glycerol solutions was used, obtained in the bubble curtain (Table 2.2 No. 10), as already presented in Chapter 3 and in subsection 5.3. Glycerol leads thereby to a change in viscosity and surface tension. Further, the interfacial tension was modified by the addition of a surfactant. These simulations were carried out also by the group of Dr. Mark Hlawitschka in the TU Kaiserslautern.

The following sections are a summary of the joint paper, published in "Experimental and Computational Multiphase Flow": Hlawitschka, M. W., Kováts, P., Dönmez, B., Zähringer, K. and Bart, H. J.: Bubble motion and reaction in different viscous liquids, Experimental and Computational Multiphase Flow, 2020, pp. Doi: 10.1007/s42757-020-0072-4.

In these simulations a rotation equation has been introduced into the Euler-Lagrange (EL) framework – namely in the derived solver from OpenFOAM "sprayFOAM", to calculate more precisely the bubble motion in the bubble column by modelling the shape of the bubbles and the resulting spiralling motion. The solver was further extended to account for reactions in the liquid phase.

The bubbles in the simulation were approximated by an oblate spheroid. The species mass transport in the continuous fluid is accounted by an additional scalar transport equation and the transferred mass is calculated based on the two-film theory, where a homogeneous and constant species mass fraction is considered in the bubbles. The investigated chemical reaction is the chemisorption of carbon dioxide (CO_2) in a sodium hydroxide (NaOH) – water solution.

In the simulation the glycerol concentration was varied in three steps: 0%, 25% and 50% glycerol. In addition, three different surfactant concentrations were also investigated (0 mg/g (T0), 2mg/g (T1) and 6 mg/g (T2)). The liquid properties, measured for these solutions, are listed in Chapter 3, Table 3.1.

The bubble size itself is influenced by the system properties such as viscosity and surface tension. In this study, the boundary conditions for the simulations were set to the experimentally obtained inlet values.

In the case of higher viscosity (50% glycerol), the individual bubbles started to follow a straight path close to the inlet in the experiments and mixed further upwards in the column. This has to be accounted for in the simulation.

The resulting bubble movement from experiment and simulation is compared in Figure 8.14 as an overlay. The figure depicts the lowest 30 cm of the column. The simulated bubbles are depicted as green spheres, while bubbles obtained from the experiment are in black. The simulation predicts slightly higher amplitudes of the oscillations at high glycerol concentrations compared to the experiment, while the transition to helical motion is still described rather correctly. Overall, a reasonably good agreement could be found concerning bubble oscillation. In the case of 0% glycerol and 6 mg/g SDS (Figure 8.14, T2), the transition from straight bubble rise to the helical bubble movement is observed at a height of approximately 0.018 m (Figure 8.14, red line)

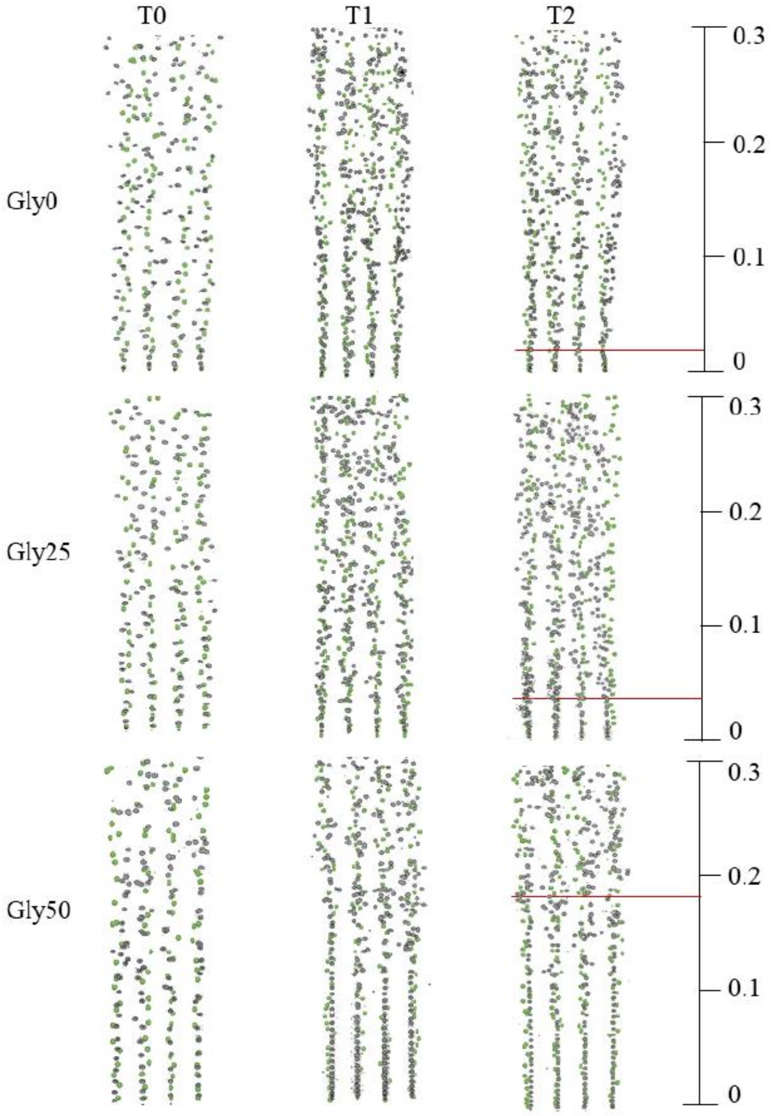

Figure 8.14: Bubble distributions from simulations (green) in comparison to the experiments (black) along the height of the column. Red lines indicate the transition points at an SDS concentration of 6 mg/g. The simulation visualization excludes information about bubble deformation. From [185].

Comparing the experiment and simulation, the time-averaged vertical liquid velocities are depicted in Figure 8.15 for the case of 25% glycerol at a column height of 210 and 410 mm, respectively. At the height of 210 mm, the velocity peaks in the simulation are more pronounced than the velocity profile obtained from the experiments. The experimental vertical liquid velocity reaches a value of 0.56 m/s, while in the simulation an average value of 0.57 m/s was predicted. At 410 mm, experiment and simulation show nearly the same vertical liquid velocity profile.

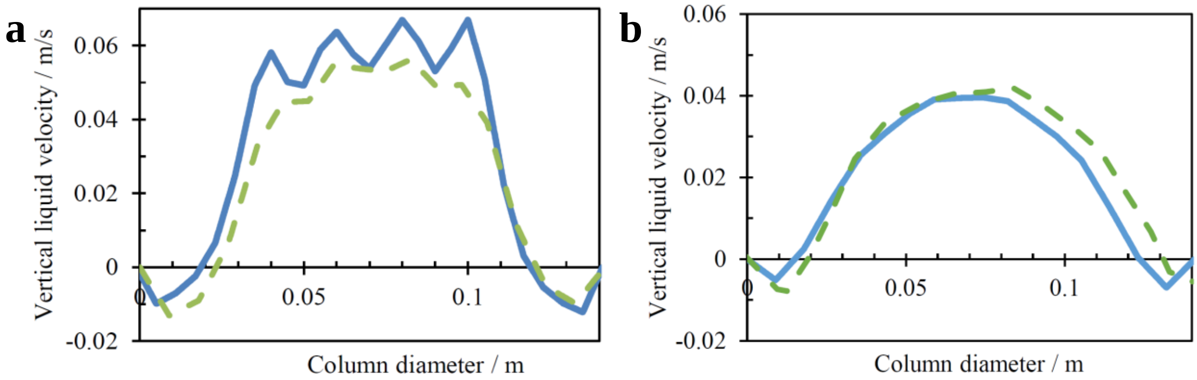

Figure 8.15: Comparison of the liquid vertical velocity from experiment (green, dashed) and simulation (blue) at a glycerol concentration of 25% at a column height of 210 mm (a) and 410 mm (b). From [185].

The influence of the glycerol concentration on the reaction progress is also investigated and is compared to the experimental data at 370 mm (Figure 8.16). It can be seen, that the lowest viscosity (0% glycerol) leads to the fastest decrease of the pH-value. Higher glycerol concentrations lead to slower mass transfer and pH-value decrease. In the case of 0% and 25% glycerol, the change in the pH-value is predicted by the simulation quite well; however, the end concentrations are slightly underpredicted. At the highest glycerol concentration (50%), a deviation between the pH-value development from experiment and simulation can be observed in the first 90 seconds.

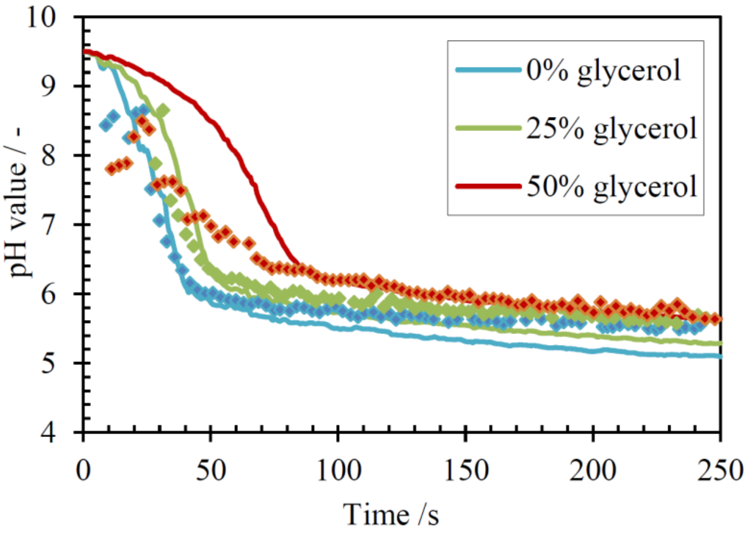

Figure 8.16: pH-value development for the cases of 0% glycerol, 25% glycerol and 50% glycerol at a column height of 370 mm; symbols: experiment, lines: simulation. From [185].

A good agreement could be found concerning bubble oscillations using an Euler-Lagrange framework to describe bubble oscillations in higher viscosity. In addition, the simulations were in good agreement concerning reactive mass transfer investigations at higher viscosity of the liquid which led to a lower mass transfer rate. Overall, the velocity fields and bubble positions can be predicted with good agreement with the simulations for the different viscosity conditions. Also the pH-value development shows a good agreement at lower glycerol concentrations; however with 50% glycerol a much slower pH drop is predicted by the simulation.

8.3.2. Validation of simulations with an Euler-Lagrange model in water and 50% water-glycerol mixture

In this numerical work the influence of viscosity on bubble dynamics and on mass transfer is studied using a LES-Euler/Lagrange point-particle approach, taking into account not just the bubble dynamics, but the bubble eccentricity and bubble motion. The CFD model, developed by the group of Prof. Martin Sommerfeld (OVGU Magdeburg) is implemented in the open source platform OpenFOAM as a custom solver. The developed model for the bubble rise prediction in a continuous liquid phase takes into account the bubble dynamics, bubble motion, mass transfer and chemical reactions. For comparison and validation, experimental data in pure water and 50% water-glycerol solutions was used, obtained in the bubble curtain (Table 2.2, No.10) and already presented in Chapter 3 and in subsection 5.3. The liquid properties, measured for these solutions, are listed in Chapter 3, Table 3.1.

The simulations were carried out by the group of Prof. Martin Sommerfeld from the Otto-von-Guericke-Universität Magdeburg. The detailed description of the simulation setup can be found in Taborda et al. [190].

The following sections are a summary of a common book section, published at "Springer International Publishing": Hampel, U., Kipping, R., Zähringer, K., Kováts, P., Sommerfeld, M., Taborda, M. A., Rzehak, R., Hlawitschka, M., Klüfers, P. and Oßberger, M.: Chemical reactions in bubbly flows, in: Reactive Bubbly Flows, Schlüter, M., Bothe, D., Herres-Pawlis, S. and Nieken, U., Editors. 2021, Springer International Publishing. No of pages 490.

For the comparison of experimental and numerical results, cross-sectional profiles of the bubble mean diameter were taken at two heights, at 100 mm and 350 mm above the bottom of the bubble column (Figure 8.17).

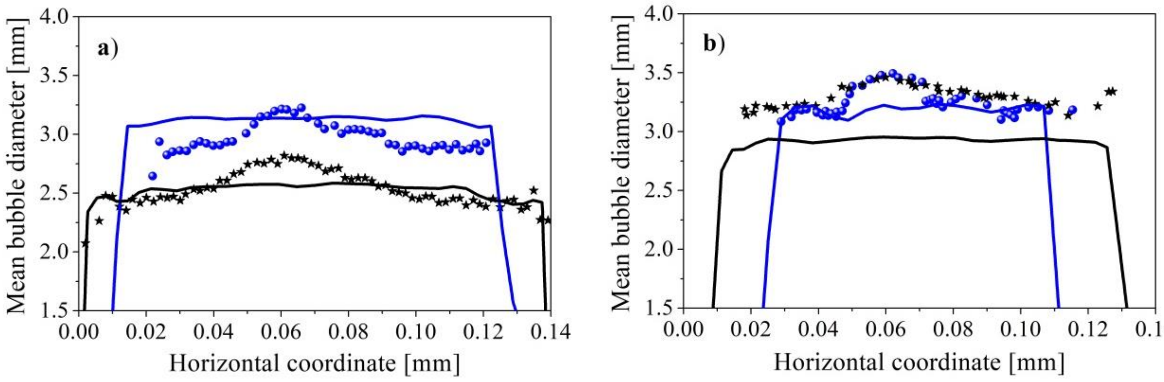

Figure 8.17: Profiles of number mean bubble diameter at two cross-sections within the column (blue color: z = 100 mm and black color: z = 350 mm, symbols: experiments, lines: numerical simulations); a) for a NaOH solution without glycerol; b) for a NaOH solution with 50% glycerol. From [188].

From the simulations, the mean diameter is determined by averaging over an entire computational cycle of 150 s, exactly as done in the experiment. The mean bubble size matches quite well for the case without glycerol (Figure 8.17, a), although the measurements show a small size peak in the core, which could be explained with the manufacturing differences between the inlet nozzles. The profiles also demonstrate the horizontal dispersion development of the bubbles from 100 mm to 350 mm as well as the mean diameter reduction due to mass transfer. With higher liquid viscosity (Figure 8.17, b), the lateral dispersion obtained from the simulation is similar to the experiments and as expected, is lower, compared to the case with pure water. At higher viscosity the numerical results also predict a slight reduction of the mean bubble size, but this size reduction is not observed in the experiments. However, this computed size change along the column is only about 0.2 mm.

For investigating the effect of the novel bubble dynamics model on the hydrodynamics, mean vertical liquid and bubble velocity profiles are extracted at the height of 350 mm (Figure 8.18). The comparison of experimental and simulation data shows very similar profile shapes, with the negative fluid velocities close to the walls, which are also properly captured by the simulations. Bubble velocity magnitudes for both cases show a very good agreement with experimental observations. A higher mean bubble velocity and a wider lateral dispersion of the bubbles over the column cross-section can be investigated for the case with pure water (Figure 8.18, a). At higher viscosity, the bubbles are more concentrated in the centre of the column, since the bubbles tend to rise in more straight paths compared to the case with lower viscosity (Figure 8.18, b).

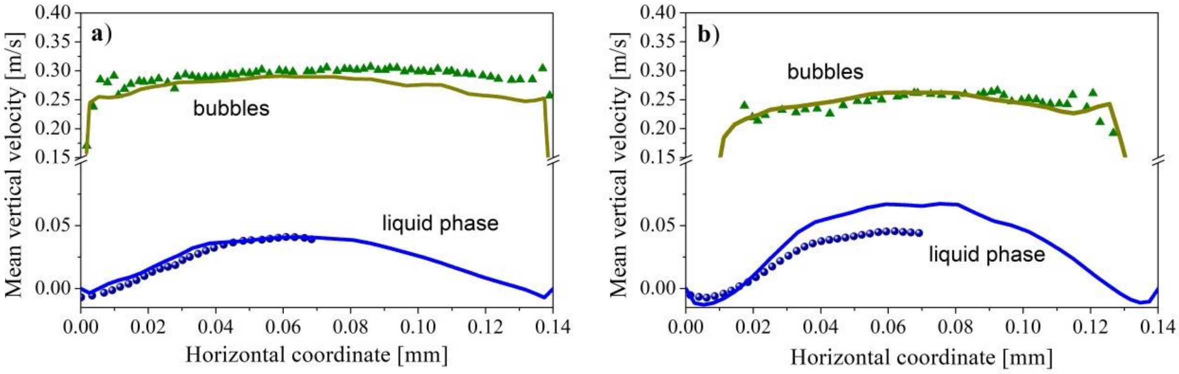

Figure 8.18: Profiles of measured (symbols) and computed (lines) mean vertical velocities (upper lines and symbols correspond to bubble velocity, lower lines and symbols correspond to liquid velocity; only the left half of the experimental liquid velocities is represented due to symmetry and accuracy concerns (see subsection 5.3)); a) measured for the case without glycerol (low viscosity); b) measured for the 50% glycerol NaOH solution (averaging time 150 s). From [188].

This change in the bubble motion can also be seen, if the angle of bubble motion from the experiment is plotted against the column height (Figure 8.19). Thus, as the bubbles are more concentrated in the centre of the column for the 50% glycerol case, the vertical liquid velocity is larger. For the case without glycerol, the better lateral bubble dispersion results in lower vertical liquid velocities.

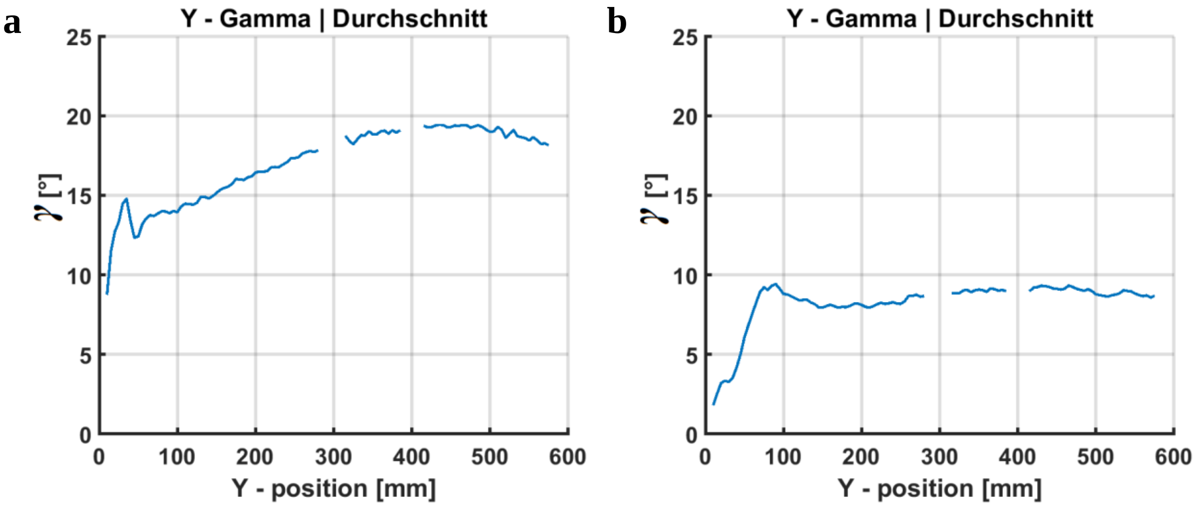

Figure 8.19: Mean bubble motion angle over the column height in pure water (a) and in 50% water-glycerol mixture (b).

The different dynamic behaviour of the bubbles in low and high viscosity liquids will also influence the mass transfer and chemical reaction. The development of pH values for the two cases, without glycerol and with 50% glycerol, is shown in Figure 8.20. The pH value decreases faster in the low-viscosity case (without glycerol), while in the case with 50% glycerol mass transfer and chemical reaction are slower, showing a shallower slope in the pH value. This occurs because the bubbles tend to be more spherical, therefore have straighter rising paths and this leads to less mass transfer. In the case without glycerol, mass transfer should be enhanced due to the effectively larger surface area of the elliptical bubbles. All these tendencies are correctly predicted by the developed dynamics model for bubble motion and the agreement with the measurements is very good for reactive bubbly flows and liquids of different viscosity.

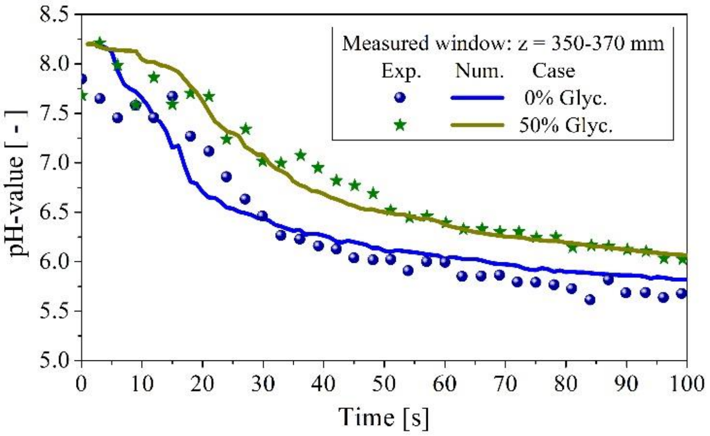

Figure 8.20: Comparison of numerically computed and measured temporal decline of pH values (measurement window 350 – 370 mm above the column bottom) in a reactive bubble column with low and high (50 % glycerol) viscosity NaOH solution. From [188].

8.4. Summary

In this chapter the comparison of our measured data with the results of different CFD-simulations from partner research groups in the SPP 1740 was presented. The validations are based on the shared experimental results of the measurements in the bubble column reactor, presented in Chapter 3 and subsection 5.3.

The validations were performed for two types of CFD simulation models: Euler-Euler and Euler-Lagrange. For the Euler-Euler simulation approach as single input parameter the average bubble size has to be known, and was adapted from the experimental data, while for the Euler-Lagrange simulations with the bubble eccentricity, bubble orientation and motion angle an extended database was used.

The Euler-Euler simulations are in a quite good agreement with the experiments for the gas fractions, bubble sizes and velocities. For the mean liquid velocity, both of them underestimate the measured liquid velocity values by around 20%. However, the typical flow patterns – peaks over the inlet nozzles, backflow near the wall, and recirculation at the top – were captured very well by the simulations. Also the vertical velocity fluctuations show a quite good agreement with the experimental results.

In the second simulation with reaction, also the development of pH values over time was investigated with a good agreement between experiments and simulation.

In the simulations with the Euler-Lagrange approach for different liquid viscosities, not just the average bubble size was taken into account, but also the bubble eccentricity and motion. The presented numerical results for bubble size and velocity are in a good agreement with the measured data. Also the agreement in the vertical liquid velocity is quite satisfactory, showing less difference between the simulation and experiments. Concerning the pH value development, both frameworks can predict quite well the pH change in liquids with different viscosities.

All in all, the presented simulations have shown, how important high quality and detailed experimental data are for the validation of numerical predictions. These results also allow for the further development of such numerical codes.

Chapter 9

Conclusions and outlook

Contents

9.1. CONCLUSIONS 153
9.2. OUTLOOK 156

9.1. Conclusions

In this thesis, different optical measurements techniques have been combined to characterize in detail the fluid dynamics and mass transfer in a laboratory-scale bubble column for different flow conditions, gases and liquids. In the experiments a cylindrical bubble column with an aspect ratio of five, surrounded with a rectangular acrylic tank, to reduce the optical distortions due to the curved column walls, was used. The bubbles were generated through an exchangeable sparger plate from the bottom. According to the type of experiments, two different sparger plates were used: one with a single stainless steel nozzle in the centre of the plate for the single bubble and bubble chain experiments, and one with four in-line nozzles, mounted in the centre plane of the plate, perpendicular to the cameras, for the bubble curtain experiments.

With this technical setup three different flow cases were investigated:

- flow and mass transfer around single, bubbles rising in a stagnant liquid,
- flow and mass transfer with a bubble chain,
- flow and mass transfer with a bubble curtain.

Two different reaction systems were used to quantify mass transfer in these configurations:

- a neutralization reaction system with CO_2 bubbles as gas phase,
- a redox reaction system with air (O_2) bubbles as gas phase.

To characterize the bubble properties shadow imaging technique was applied. The liquid flow field was investigated with the help of PIV. The mass transfer from the bubbles into the liquid bulk was determined with planar LIF.

Through several experiments with Shadowgraphy, bubble size, velocity and aspect ratio were determined experimentally for different water qualities, pH levels, filling heights, viscosities, surface tensions and gas volume flow rates.

It has been found, that only the gas flow rate has a significant influence on bubble size and velocity in pure water. With increased gas flow rate, larger bubbles are generated, and their rising velocities decrease. In the whole bubble column height significant bubble shrinkage, as well as slight bubble velocity change from bottom to the top of the column were observed in the cases with lower viscosity (0 and 25% glycerol) without surfactant. It has also been found, that with increasing viscosity and surface tension the bubble size increases, but the bubble velocity decreases with increasing viscosity and decreasing surface tension. Bubble size and velocity distributions experience not only a shift of the maximum, but also their aspect changes by broadening.

Since bubble shape, size and velocity directly impact mass transfer and mixing, it is clear that the gas flow rate, surface tension, viscosity and bubble eccentricity are essential parameters to determine correctly the liquid side mass transfer coefficient and the volumetric mass transfer coefficient in a bubble column reactor. The addition of glycerol has a large influence on bubble size and velocity, but its effect is not advantageous on mass transfer. The liquid side mass transfer, the specific interfacial area and therefore, the volumetric mass transfer decreases as well with increasing viscosity, due to the larger bubbles generated.

With the addition of surfactant, the bubble size and also the bubble velocity decrease. This results in a higher specific interfacial area and longer contact time in the bubble column. The liquid side mass transfer decreases because of the decreasing Reynolds number, but contrary to this, the volumetric mass transfer increases due to the increasing specific interfacial area. In this work the experimental results have once more shown, that the highest mass transfer from gas to liquid can be achieved in pure de-ionized water without surfactant.

The results obtained from the bubble column experiments have also been used to develop a new correlation for bubble eccentricity, based on the Flow number. This equation was then used to propose a new correlation for the mass transfer coefficient, based on the well-known correlation of Higbie.

Then, the liquid flow and mass transfer around single ascending CO_2 and air bubbles in a stagnant fluid has been examined. Simultaneous PIV and LIF images of single bubbles with straight or zigzagging rising paths were taken. The zigzagging bubbles were investigated before the first inflexion point in their path, where they still have an almost two-dimensional movement. Therefore, it was possible to measure velocity and pH or oxygen concentration in the wake of the bubbles. In the measurements with the neutralization reaction, the dissolved CO_2 is transported to the sides and mainly the bottom of the bubbles, where it lowers the pH of the liquid and forms a long wake behind the bubble. In this wake, the pH is around 0.3 points less than in the bulk liquid. This small pH change can best be followed in the range of pH=6…7, where the applied fluorescent dye (uranine) fluorescence intensity changes the most dynamically.

Based on the experiences gained through the experiments with CO_2 bubbles, combined PIV-LIF experiments were carried out with a redox reaction system with resazurin and air bubbles. Compared to the measurements with CO_2 bubbles, quantifying the amount of dissolved gas was more efficient due to a much higher fluorescence intensity of the applied tracer in this reaction system. The new experiments confirmed the results with CO_2: the liquid with dissolved gas is transported to the sides in the case of ellipsoidal bubbles and forms a double wake, or it is transported to the bottom of the bubbles and forms a stagnant cap, if the bubble is spherical. It was also proved, that the liquid velocity around elliptical bubbles is much higher than around the spherical ones, which leads to a faster liquid renewal on the bubble surface and a higher mass transfer from the bubbles into the liquid bulk.

Further flow fields and concentration fields were presented for a flow setup with a bubble chain and for a more complex setup with a bubble curtain. The velocity fields gained with the help of PIV, showed in all cases much lower liquid velocities compared to the bubble velocities, with a clear recirculation loop at the top of the column and backflow near the walls along the whole column.

In the case of a bubble chain, an additional recirculation zone appears at the bottom of the column, while it significantly weakens in the experiments with the bubble curtain. It has also been found, that the higher gas flow rate induces higher liquid velocities, but the overall flow pattern in the bubble column remains the same.

PIV experiments with three different technical setups were performed with the CO_2 bubble curtain. This comparison of the different PIV techniques and spatial resolutions has shown that with all of the three PIV setups nearly similar velocity fields could be achieved. The

drawback of the higher spatial resolution is a higher experimental, calibration and post-processing time and of course, the storage size for the raw data increases as well. Therefore, if small-scale structures and fluctuations have to be investigated, a high-speed time-resolved PIV system with high spatial resolution could be a good choice, while when a coarse mean flow field is the aim, a low-speed PIV system with lower spatial resolution could be enough.
Due to the change in bubble size, rising path and velocity, the liquid flow field is evidently also not the same for the investigated different viscosities and surface tensions. The highest velocities could be found in the high viscosity solutions. With surfactant, the liquid velocity profiles resemble each other for different viscosities, apart from the bottom section of the column where the liquid flow field mirrors the straight ascension line of the bubbles. All these results support the existence of a dual effect of viscosity on bubble column fluid dynamics already found in the literature. The velocity fields with air bubbles show naturally similar flow structure as the ones with CO_2.

The effect of gas flow rate and the effect of surface tension and viscosity change on the mass transfer were investigated with 2T-LIF in the experiments with a CO_2 bubble curtain through a neutralization reaction. These experimental results have shown that higher mass transfer from gas to liquid can be achieved with higher gas flow rate in pure water. The time to reach a certain pH in the column is prolonged at lower gas flow rates. It has been found, that the progress of the neutralization reaction decreases from the top of the column to the bottom. The reason for that is the recirculation loop at the top, where the liquid with dissolved gas is trapped. From this loop, just a small amount of liquid is transported near the wall downward to the column bottom, with low velocity. Therefore, a remarkable delay exists at the bottom. The addition of surfactant and glycerol has a strong influence on bubble size and velocity, but neither of them has advantageously affected the mass transfer. The time to reach a certain pH in the column is always prolonged in the solutions with glycerol.

The same trend has been found in the experimental results with a bubble chain of air. The time to reach the saturated value of the applied dye in the column is prolonged at lower gas flow rate and this process decreases from the bubble column top to the bottom.
In the new reaction system with resazurin and air bubbles not just the effect of the gas flow rate on mass transfer, but the performance of the applied dye was also investigated through LIF experiments with a bubble curtain of air. These results have shown that the reaction of resazurin with oxygen is fast enough to visualize and quantify the mass transfer in a bubble column reactor by laser induced fluorescence. It provides reliable and detailed information about the mixing and mass transfer process. Moreover, the sensitivity of this system at low concentrations is remarkable.

The obtained experimental data has been used by partner projects inside SPP 1740 for systematic validations of numerical models describing large-scale bubble columns [184-186, 188, 190], thus supporting the further development of predictive simulations concerning mass transfer in bubble columns. In the frame of the Priority Program SPP 1740 “Reactive Bubbly Flows” of the DFG, which financed most of the work presented here, an Internet-based database has been created to share all relevant data within the project and with the scientific community, supporting validation of numerical simulations and comparisons with results from other groups. The complete data sets containing bubble diameters, bubble and liquid velocity fields as well as the pH measurement results are available through this online database, freely accessible with a password under 141.44.132.124/spp1740/.

9.2. Outlook

During this work, a large amount of information and data was analysed from various points of view, mainly concentrating on a full hydrodynamical characterization and the description of mass transfer for the whole bubble column. However, the available data and its temporal and spatial resolution allows for further analysis from various approaches. For example, from the results of shadow imaging, not just the bubble sizes and velocities can be obtained, but it provides information about the bubble path, rising angle, inclination, eccentricity etc. These data can be extracted for different heights or just for one bubble from the bubble swarm. Beginnings of such evaluations have been undertaken (see Chapter 3), but much deeper analysis of this data is possible. With the help of such data analysis a more detailed database could be assembled to help and support model development and the validation of CFD simulations.

The simultaneously recorded PIV and LIF images could be processed also in a way, to get instantaneous mass transfer fields and investigate the mixing and mass transfer enhancement effect of the bubble motion inside the bubble swarm. This kind of evaluations has also been started on the basis of a Bachelor's Thesis [191], that developed a Matlab-Script for the calculation of locally resolved mass transfer. Of course to this end, it is necessary to know the kinetics of the reaction, which is still missing for the resazurin reaction system.
If the kinetics of the resazurin reaction will be known, it is conceivable to perform new single bubble experiments with a 3D tomographic measurement technique. With that technique the flow and concentration field could be reconstructed around one freely rising bubble, which results could support model development for mass transfer around bubbles and validations of detailed numerical simulations with single bubbles.

The experimental setup could be extended with various additional features to gain more industry-relevant conditions for the experiments. One of these features would be the capability for co- and counter-current flow measurements. To this end a new rectangular bubble column was manufactured with a height of 2 m and a cross section of 100x100 mm. This setup allows performing measurements with a counter-current flow up to 50 l/min. The gas is supplied in that column through 7 nozzles, which are controlled separately. In this bubble column new Shadowgraphy measurements will be carried out at diverse flow conditions with three different nozzle diameters to generate bubbles in a wider size range. Moreover these experiments are planned with air and CO_2 bubbles also. With the new results the bubble database will be extended, which can support even better future numerical validations.

References

[1] Lee SY, Tsui YP (1999), Succeed at gas/liquid contacting. *Chem Eng Prog* 95:23-49

[2] Majumder SK (2016) 1 - Introduction. In: Majumder SK (ed) Hydrodynamics and Transport Processes of Inverse Bubbly Flow. Elsevier, Amsterdam, pp. 1-24

[3] Luo H (1993), Coalescence, breakup and liquid circulation in bubble column reactors, Ph.D. Thesis, University of Trondheim.

[4] Kantarci N, Borak F, Ulgen KO (2005), Bubble column reactors. *Process Biochem* 40:2263-2283

[5] Ong B (2003), Experimental investigation of bubble column hydrodynamics: Effect of elevated pressure and superficial gas velocity, Ph.D. Thesis, Washington University in St Louis.

[6] Gemello L, Plais C, Augier F, Cloupet A, Marchisio DL (2018), Hydrodynamics and bubble size in bubble columns: Effects of contaminants and spargers. *Chem Eng Sci* 184:93-102

[7] Besagni G, Gallazzini L, Inzoli F (2018), Effect of gas sparger design on bubble column hydrodynamics using pure and binary liquid phases. *Chem Eng Sci* 176:116-126

[8] Kováts P, Thévenin D, Zähringer K (2018), Characterizing fluid dynamics in a bubble column aimed for the determination of reactive mass transfer. *Heat Mass Transfer* 54:453-461

[9] Bryn T (1933), Steiggeschwindigkeit von Luftblasen in Flüssigkeiten. *Forschung auf dem Gebiet des Ingenieurwesens A* 4:27-30

[10] Haberman WL, R.K. M (1953) An experimental investigation of the drag and shape of air bubbles rising in various liquids. Washington D.C.,

[11] Clift R, Grace JR, Weber ME (1978) Bubbles, drops, and particles. Academic Press, New York

[12] Tomiyama A, Kataoka I, Zun I, Sakaguchi T (1998), Drag Coefficients of Single Bubbles under Normal and Micro Gravity Conditions. *JSME International Journal Series B* 41:472-479

[13] Ishii MZ, N. (1979), Drag coefficient and relative velocity in bubbly, droplet or particulate flows. *AlChE J* 25:843-855

[14] Grace JR (1973), Shapes and velocities of bubbles rising in infinite liquids. *Transactions of the Institution of Chemical Engineers* 51:116-120

[15] Tripathi MK, Sahu KC, Govindarajan R (2015), Dynamics of an initially spherical bubble rising in quiescent liquid. *Nature Communications* 6:6268

[16] Kováts P, Thévenin D, Zähringer K (2020), Influence of viscosity and surface tension on bubble dynamics and mass transfer in a model bubble column. *Int J Multiphase Flow* 123:103174

[17] Joshi JB, Nandakumar K, Evans GM, et al. (2017), Bubble generated turbulence and direct numerical simulations. *Chem Eng Sci* 157:26-75

[18] Bozzano G, Dente M (2001), Shape and terminal velocity of single bubble motion: a novel approach. *Comput Chem Eng* 25:571-576

[19] Wegener M, Paul N, Kraume M (2014), Fluid dynamics and mass transfer at single droplets in liquid/liquid systems. *Int J Heat Mass Transfer* 71:475-495

[20] Rollbusch P, Bothe M, Becker M, et al. (2015), Bubble columns operated under industrially relevant conditions - Current understanding of design parameters. *Chem Eng Sci* 126:660-678

[21] Saito T, Toriu M (2015), Effects of a bubble and the surrounding liquid motions on the instantaneous mass transfer across the gas-liquid interface. *Chem Eng J* 265:164-175

[22] Nagami Y, Saito T (2013), Measurement of modulation induced by interaction between bubble motion and liquid-phase motion in the decaying turbulence formed by an oscillating-grid. *Particuology* 11:158-169

[23] Kováts P, Thévenin D, Zähringer K (2017), Investigation of Mass Transfer and Hydrodynamics in a Model Bubble Column. *Chem Eng Technol* 40:1434-1444

[24] Valiorgue P, Souzy N, Hajem ME, Hadid HB, Simoëns S (2013), Concentration measurement in the wake of a free rising bubble using planar laser-induced fluorescence (PLIF) with a calibration taking into account fluorescence extinction variations. *Exp Fluids* 54:1501

[25] Hanyu K, Saito T (2010), Dynamical mass-transfer process of a CO2 bubble measured by using LIF/HPTS visualisation and photoelectric probing. *Can J Chem Eng* 88:551-560

[26] Nagami Y, Saito T (2014), An Experimental Study of the Modulation of the Bubble Motion by Gas–Liquid-Phase Interaction in Oscillating-Grid Decaying Turbulence. *Flow, Turbulence and Combustion* 92:147-174

[27] Kong G, Buist KA, Peters EAJF, Kuipers JAM (2018), Dual emission LIF technique for pH and concentration field measurement around a rising bubble. *Exp Therm Fluid Sci* 93:186-194

[28] Kück UD, Schlüter M, Räbiger N (2012), Local Measurement of Mass Transfer Rate of a Single Bubble with and without a Chemical Reaction. *J Chem Eng Jpn* 45:708-712

[29] Kück UD, Schlüter M, Räbiger N (2009), Analyse des grenzschichtnahen Stofftransports an frei aufsteigenden Gasblasen. *Chem Ing Tech* 81:1599-1606

[30] Dani A, Guiraud P, Cockx A (2007), Local measurement of oxygen transfer around a single bubble by planar laser-induced fluorescence. *Chem Eng Sci* 62:7245-7252

[31] Francois J, Dietrich N, Guiraud P, Cockx A (2011), Direct measurement of mass transfer around a single bubble by micro-PLIFI. *Chem Eng Sci* 66:3328-3338

[32] Jimenez M, Dietrich N, Hébrard G (2013), Mass transfer in the wake of non-spherical air bubbles quantified by quenching of fluorescence. *Chem Eng Sci* 100:160-171

[33] Butler C, Lalanne B, Sandmann K, Cid E, Billet AM (2018), Mass transfer in Taylor flow: Transfer rate modelling from measurements at the slug and film scale. *Int J Multiphase Flow* 105:185-201

[34] Weiner A, Timmermann J, Pesci C, et al. (2019), Experimental and numerical investigation of reactive species transport around a small rising bubble. *Chemical Engineering Science: X* 1:100007

[35] Paul M, Strassl F, Hoffmann A, Hoffmann M, Schlüter M, Herres-Pawlis S (2018), Reaction Systems for Bubbly Flows. *Eur J Inorg Chem* 2018:2101-2124

[36] Jimenez M, Dietrich N, Grace JR, Hébrard G (2014), Oxygen mass transfer and hydrodynamic behaviour in wastewater: Determination of local impact of surfactants by visualization techniques. *Water Res* 58:111-121

[37] Dietrich N, Francois J, Jimenez M, Cockx A, Guiraud P, Hébrard G (2015), Fast Measurements of the Gas-Liquid Diffusion Coefficient in the Gaussian Wake of a Spherical Bubble. *Chemical Engineering & Technology* 38:941-946

[38] Bork O, Schlüter M, Scheid S, Räbiger N, Analysis of the effect of local hydrodynamics on mass transfer from bubbles using laser induced fluorescence. (2003).

[39] Kück UD, Kröger M, Bothe D, Räbiger N, Schlüter M, Warnecke H-J (2011), Skalenübergreifende Beschreibung der Transportprozesse bei Gas/Flüssig-Reaktionen. *Chem Ing Tech* 83:1084-1095

[40] Kastens S, Hosoda S, Schlüter M, Tomiyama A (2015), Mass Transfer from Single Taylor Bubbles in Minichannels. *Chemical Engineering & Technology* 38:1925-1932

[41] Yamada M, Saito T (2012), A newly developed photoelectric optical fiber probe for simultaneous measurements of a CO2 bubble chord length, velocity, and void fraction and the local CO2 concentration in the surrounding liquid. *Flow Measurement and Instrumentation* 27:8-19

[42] Huang J, Saito T (2017), Influences of gas-liquid interface contamination on bubble motions, bubble wakes, and instantaneous mass transfer. *Chem Eng Sci* 157:182-199

[43] Komasawa I, Otake T, Kamojima M (1980), Wake behavior and its effect on interaction between spherical-cap bubbles. *J Chem Eng Jpn* 13:103-109

[44] Fujiwara A, Tokuhiro A, Hishida K, Application of PIV/LIF and Shadow-Image to a Bubble Rising in a Linear Shear Flow Field. In: *10th International Syposium on Applications of Laser Technique to Fluid Mechanics*, Lisbon, Portugal, (2000).

[45] Tokuhiro A, Fujiwara A, Hishida K, Maeda M (1999), Measurement in the Wake Region of Two Bubbles in Close Proximity by Combined Shadow-Image and PIV Techniques. *J Fluids Eng* 121:191-197

[46] Tokuhiro A, Maekawa M, Iizuka K, Hishida K, Maeda M (1998), Turbulent flow past a bubble and an ellipsoid using shadow-image and PIV techniques. *Int J Multiphase Flow* 24:1383-1406

[47] Brücker C (1999), Structure and dynamics of the wake of bubbles and its relevance for bubble interaction. *Phys Fluids* 11:1781-1796

[48] Hassan YA, Ortiz-Villafuerte J, Schmidl WD (2001), Three-dimensional measurements of single bubble dynamics in a small diameter pipe using stereoscopic particle image velocimetry. *Int J Multiphase Flow* 27:817-842

[49] Ortiz-Villafuerte J, Schmidl WD, Hassan YA (2000), Three-dimensional PTV study of the surrounding flow and wake of a bubble rising in a stagnant liquid. *Exp Fluids* 29:202-210

[50] Fujiwara A, Danmoto Y, Hishida K, Maeda M (2004), Bubble deformation and flow structure measured by double shadow images and PIV/LIF. *Exp Fluids* 36:157-165

[51] Liu Z, Zheng Y, Jia L, Zhang Q (2005), Study of bubble induced flow structure using PIV. *Chem Eng Sci* 60:3537-3552

[52] Liu Z, Zheng Y (2006), PIV study of bubble rising behavior. *Powder Technol* 168:10-20

[53] Funfschilling D, Li HZ (2006), Effects of the Injection Period on the Rise Velocity and Shape of a Bubble in a Non-Newtonian Fluid. *Chem Eng Res Des* 84:875-883

[54] Funfschilling D, Li HZ (2001), Flow of non-Newtonian fluids around bubbles: PIV measurements and birefringence visualisation. *Chem Eng Sci* 56:1137-1141

[55] Kemiha M, Frank X, Poncin S, Li HZ (2006), Origin of the negative wake behind a bubble rising in non-Newtonian fluids. *Chem Eng Sci* 61:4041-4047

[56] Sakakibara K, Yamada M, Miyamoto Y, Saito T (2007), Measurement of the surrounding liquid motion of a single rising bubble using a Dual-Camera PIV system. *Flow Measurement and Instrumentation* 18:211-215

[57] Yamamoto M, Saito T, A study on dynamical mass transfer mechanism between a zigzagging CO2 bubble and its surrounding liquid via PIV/LIF. In: *Turbulence Heat and Mass Transfer 6 Proceedings of the Sixth International Symposium On Turbulence Heat and Mass Transfer*, Rome, Italy, (2009).

[58] Saito T, Sakakibara K, Miyamoto Y, Yamada M (2010), A study of surfactant effects on the liquid-phase motion around a zigzagging-ascent bubble using a recursive cross-correlation PIV. *Chem Eng J* 158:39-50

[59] Sone D, Sakakibara K, Yamada M, Sanada T, Saito T (2008), Bubble Motion and its Surrounding Liquid Motion through the Collision of a pair of Bubbles. *Journal of Power and Energy Systems* 2:306-317

[60] Yoshimoto K, Saito T, 3-dimensional liquid motion around a zigzagging ascent bubble measured using tomographic Stereo PIV. In: *15th International Syposium on Applications of Laser Technique to Fluid Mechanics*, Lisbon, Portugal, (2010).

[61] Nagami Y, Saito T (2014), An Experimental Study of the Modulation of the Bubble Motion by Gas-Liquid-Phase Interaction in Oscillating-Grid Decaying Turbulence. *Flow Turbulence and Combustion* 92:147-174

[62] Fan W, Ma Y, Li X, Li H (2009), Study on the Flow Field around Two Parallel Moving Bubbles and Interaction Between Bubbles Rising in CMC Solutions by PIV. *Chin J Chem Eng* 17:904-913

[63] Zenit R, Magnaudet J (2009), Measurements of the streamwise vorticity in the wake of an oscillating bubble. *Int J Multiphase Flow* 35:195-203

[64] Böhm L, Kurita T, Kimura K, Kraume M (2014), Rising behaviour of single bubbles in narrow rectangular channels in Newtonian and non-Newtonian liquids. *Int J Multiphase Flow* 65:11-23

[65] Böhm L, Brehmer M, Kraume M (2016), Comparison of the Single Bubble Ascent in a Newtonian and a Non-Newtonian Liquid: A Phenomenological PIV Study. *Chem Ing Tech* 88:93-106

[66] Filella A, Ern P, Roig V (2015), Oscillatory motion and wake of a bubble rising in a thin-gap cell. *J Fluid Mech* 778:60-88

[67] Lewandowski B, Fertig M, Ulbricht M, Krekel G (2019), Relationship between bubble characteristics and hydrodynamic parameters for single bubbles in presence of surface active agents. *Chem Eng Sci* 199:179-198

[68] Chaouki J, Larachi F, Duduković MP (1997), Noninvasive Tomographic and Velocimetric Monitoring of Multiphase Flows. *Industrial & Engineering Chemistry Research* 36:4476-4503

[69] Adetunji O, Rawatlal R (2017), Estimation of bubble column hydrodynamics: Image-based measurement method. *Flow Measurement and Instrumentation* 53:4-17

[70] Möller F, Seiler T, Lau YM, et al. (2017), Performance comparison between different sparger plate orifice patterns: Hydrodynamic investigation using ultrafast X-ray tomography. *Chem Eng J* 316:857-871

[71] Chen J, Li F, Degaleesan S, et al. (1999), Fluid dynamic parameters in bubble columns with internals. *Chem Eng Sci* 54:2187-2197

[72] Azizi S, Yadav A, Lau YM, Hampel U, Roy S, Schubert M (2017), On the experimental investigation of gas-liquid flow in bubble columns using ultrafast X-ray tomography and radioactive particle tracking. *Chem Eng Sci* 170:320-331

[73] Barthel F, Bieberle M, Hoppe D, Banowski M, Hampel U (2015), Velocity measurement for two-phase flows based on ultrafast X-ray tomography. *Flow Measurement and Instrumentation* 46:196-203

[74] Kipping R, Kryk H, Schleicher E, Gustke M, Hampel U (2017), Application of a Wire-Mesh Sensor for the Study of Chemical Species Conversion in a Bubble Column. *Chem Eng Technol* 40:1425-1433

[75] Möller F, Kipping R, Lavetty C, Hampel U, Schubert M (2019), Two-Bubble Class Approach Based on Measured Bubble Size Distribution for Bubble Columns with and without Internals. *Industrial & Engineering Chemistry Research* 58:2759-2769

[76] Barkai A, Hajem M, Lacassagne T, Champagne J-Y (2019), Experimental Study of a Gas–Liquid Flow in Vacuum Air-Lift Column Using an Optical Bi-Probe. *Fluids* 4:80

[77] Manjrekar ON, Sun Y, He L, Tang YJ, Dudukovic MP (2017), Hydrodynamics and mass transfer coefficients in a bubble column photo-bioreactor. *Chem Eng Sci* 168:55-66

[78] Esmaeili A, Guy C, Chaouki J (2015), The effects of liquid phase rheology on the hydrodynamics of a gas–liquid bubble column reactor. *Chem Eng Sci* 129:193-207

[79] Wu Q, Wang X, Wang T, Han M, Sha Z, Wang J (2013), Effect of liquid viscosity on hydrodynamics and bubble behaviour of an external-loop airlift reactor. *The Canadian Journal of Chemical Engineering* 91:1957-1963

[80] Parisien V, Farrell A, Pjontek D, McKnight CA, Wiens J, Macchi A (2017), Bubble swarm characteristics in a bubble column under high gas holdup conditions. *Chem Eng Sci* 157:88-98

[81] McClure DD, Kavanagh JM, Fletcher DF, Barton GW (2015), Oxygen transfer in bubble columns at industrially relevant superficial velocities: Experimental work and CFD modelling. *Chem Eng J* 280:138-146

[82] Shah YT, Joseph S, Smith DN, Ruether JA (1985), On the behavior of the gas phase in a bubble column with ethanol-water mixtures. *Industrial & Engineering Chemistry Process Design and Development* 24:1140-1148

[83] Deng Z, Wang T, Zhang N, Wang Z (2010), Gas holdup, bubble behavior and mass transfer in a 5m high internal-loop airlift reactor with non-Newtonian fluid. *Chem Eng J* 160:729-737

[84] Prakash B, Parmar H, Shah MT, Pareek VK, Anthony L, Utikar RP (2019), Simultaneous measurements of two phases using an optical probe. *Exp Comput Multiph Flow* 1:233-241

[85] Chaumat H, Billet AM, Delmas H (2007), Hydrodynamics and mass transfer in bubble column: Influence of liquid phase surface tension. *Chem Eng Sci* 62:7378-7390

[86] Zaruba A, Krepper E, Prasser HM, Reddy Vanga BN (2005), Experimental study on bubble motion in a rectangular bubble column using high-speed video observations. *Flow Measurement and Instrumentation* 16:277-287

[87] Maceiras R, Álvarez E, Cancela MA (2010), Experimental interfacial area measurements in a bubble column. *Chem Eng J* 163:331-336

[88] Colombet D, Legendre D, Cockx A, et al. (2011), Experimental study of mass transfer in a dense bubble swarm. *Chem Eng Sci* 66:3432-3440

[89] Ferreira A, Cardoso P, Teixeira JA, Rocha F (2013), pH influence on oxygen mass transfer coefficient in a bubble column. Individual characterization of kL and a. *Chem Eng Sci* 100:145-152

[90] Sheikhi A, Sotudeh-Gharebagh R, Zarghami R, Mostoufi N, Alfi M (2013), Understanding bubble hydrodynamics in bubble columns. *Exp Therm Fluid Sci* 45:63-74

[91] Besagni G, Inzoli F (2016), Bubble size distributions and shapes in annular gap bubble column. *Exp Therm Fluid Sci* 74:27-48

[92] Besagni G, Brazzale P, Fiocca A, Inzoli F (2016), Estimation of bubble size distributions and shapes in two-phase bubble column using image analysis and optical probes. *Flow Measurement and Instrumentation* 52:190-207

[93] Ziegenhein T, Lucas D (2017), Observations on bubble shapes in bubble columns under different flow conditions. *Exp Therm Fluid Sci* 85:248-256

[94] Cheng L, Li T, Keener TC, Lee JY (2013), A mass transfer model of absorption of carbon dioxide in a bubble column reactor by using magnesium hydroxide slurry. *International Journal of Greenhouse Gas Control* 17:240-249

[95] Böhm L, Kraume M (2015), Fluid dynamics of bubble swarms rising in Newtonian and non-Newtonian liquids in flat sheet membrane systems. *J Membr Sci* 475:533-544

[96] Higuchi M, Saito T (2010), Quantitative characterizations of long-period fluctuations in a large-diameter bubble column based on point-wise void fraction measurements. *Chem Eng J* 160:284-292

[97] Xue T, Qu L, Cao Z, Zhang T (2012), Three-dimensional feature parameters measurement of bubbles in gas–liquid two-phase flow based on virtual stereo vision. *Flow Measurement and Instrumentation* 27:29-36

[98] Shao S, Li C, Hong J (2019), A hybrid image processing method for measuring 3D bubble distribution using digital inline holography. *Chem Eng Sci* 207:929-941

[99] Kiambi SL, Kiriamiti HK, Kumar A (2011), Characterization of two phase flows in chemical engineering reactors. *Flow Measurement and Instrumentation* 22:265-271

[100] Becker S, De Bie H, Sweeney J (1999), Dynamic flow behaviour in bubble columns. *Chem Eng Sci* 54:4929-4935

[101] Pfleger D, Becker S (2001), Modelling and simulation of the dynamic flow behaviour in a bubble column. *Chem Eng Sci* 56:1737-1747

[102] Kováts P, Zähringer K, Detailed measurement of oxygen mass transfer in a bubble column – application of a new fluorescent dye. In: *19th International Symposium on Applications of Laser Techniques to Fluid Mechanics*, Lisbon, Portugal, (2018).

[103] Lu X, Long B, Ding Y, Deng F (2018), Experimental Study and CFD-PBM Simulation of the Unsteady Gas-Liquid Flow in an Airlift External Loop Reactor. *Flow, Turbulence and Combustion* 102:1053-1073

[104] Thet MK, Wang C-H, Tan RBH (2008), Experimental Studies of Hydrodynamics and Regime Transition in Bubble Columns. *The Canadian Journal of Chemical Engineering* 84:63-72

[105] Delnoij E, Westerweel J, Deen NG, Kuipers JAM, van Swaaij WPM (1999), Ensemble correlation PIV applied to bubble plumes rising in a bubble column. *Chem Eng Sci* 54:5159-5171

[106] Deen NG, Hjertager BH, Solberg T, Comparison of PIV and LDA Measurement Methods Applied to the Gasliquid Flow in Bubble Column. In: *10th Int Symp on Application of Laser Techniques to Fluid Mechanics*, Lisbon, Portugal, (2000).

[107] Lindken R, Merzkirch W (2002), A novel PIV technique for measurements in multiphase flows and its application to two-phase bubbly flows. *Exp Fluids* 33:814-825

[108] Bröder D, Sommerfeld M (2002), An advanced LIF-PLV system for analysing the hydrodynamics in a laboratory bubble column at higher void fractions. *Exp Fluids* 33:826-837

[109] Sathe MJ, Thaker IH, Strand TE, Joshi JB (2010), Advanced PIV/LIF and shadowgraphy system to visualize flow structure in two-phase bubbly flows. *Chem Eng Sci* 65:2431-2442

[110] Ghatage SV, Sathe MJ, Doroodchi E, Joshi JB, Evans GM (2013), Effect of turbulence on particle and bubble slip velocity. *Chem Eng Sci* 100:120-136

[111] Zhou X, Doup B, Sun X (2013), Measurements of liquid-phase turbulence in gas–liquid two-phase flows using particle image velocimetry. *Meas Sci Technol* 24:125303

[112] Silva MK, Mochi VT, Mori M, d'Ávila MA (2014), Experimental and 3D Computational Fluid Dynamics Simulation of a Cylindrical Bubble Column in the Heterogeneous Regime. *Industrial & Engineering Chemistry Research* 53:3353-3362

[113] Murgan I, Bunea F, Ciocan GD (2017), Experimental PIV and LIF characterization of a bubble column flow. *Flow Measurement and Instrumentation* 54:224-235

[114] Cerqueira RFL, Paladino EE, Ynumaru BK, Maliska CR (2018), Image processing techniques for the measurement of two-phase bubbly pipe flows using particle image and tracking velocimetry (PIV/PTV). *Chem Eng Sci* 189:1-23

[115] Bouche E, Cazin S, Roig V, Risso F (2013), Mixing in a swarm of bubbles rising in a confined cell measured by mean of PLIF with two different dyes. *Exp Fluids* 54,

[116] Alméras E, Cazin S, Roig V, Risso F, Augier F, Plais C (2016), Time-resolved measurement of concentration fluctuations in a confined bubbly flow by LIF. *Int J Multiphase Flow* 83:153-161

[117] Busciglio A, Grisafi F, Scargiali F, Brucato A (2013), On the measurement of local gas hold-up, interfacial area and bubble size distribution in gas–liquid contactors via light sheet and image analysis: Imaging technique and experimental results. *Chem Eng Sci* 102:551-566

[118] Koynov A, Tryggvason G, Schlüter M, Khinast JG (2006), Mass transfer and chemical reactions in reactive deformable bubble swarms. *Appl Phys Lett* 88:134102

[119] Sathe M, Joshi J, Evans G (2013), Characterization of turbulence in rectangular bubble column. *Chem Eng Sci* 100:52-68

[120] Besbes S, El Hajem M, Ben Aissia H, Champagne JY, Jay J (2015), PIV measurements and Eulerian–Lagrangian simulations of the unsteady gas–liquid flow in a needle sparger rectangular bubble column. *Chem Eng Sci* 126:560-572

[121] Liu L, Yan H, Ziegenhein T, Hessenkemper H, Li Q, Lucas D (2019), A systematic experimental study and dimensionless analysis of bubble plume oscillations in rectangular bubble columns. *Chem Eng J* 372:352-362

[122] Ahmed FS, Sensenich BA, Gheni SA, Znerdstrovic D, Al Dahhan MH (2014), Bubble Dynamics in 2d Bubble Column: Comparison between High-Speed Camera Imaging Analysis and 4-Point Optical Probe. *Chem Eng Commun* 202:85-95

[123] Thiruvalluvan Sujatha K, Jain D, Kamath S, Kuipers JAM, Deen NG (2017), Experimental and numerical investigation of a micro-structured bubble column with chemisorption. *Chem Eng Sci* 169:225-234

[124] Thobie C, Gadoin E, Blel W, Pruvost J, Gentric C (2017), Global characterization of hydrodynamics and gas-liquid mass transfer in a thin-gap bubble column intended for microalgae cultivation. *Chemical Engineering and Processing: Process Intensification* 122:76-89

[125] Zhou X, Sun X, Liu Y (2016), Liquid-phase turbulence measurements in air-water two-phase flows over a wide range of void fractions. *Nucl Eng Des* 310:534-543

[126] Besbes S, Gorrab I, ElHajem M, Ben Aissia H, Champagne JY (2019), Effect of bubble plume on liquid phase flow structures using PIV. *Particulate Science and Technology*:1-10

[127] Ferreira A, Pereira G, Teixeira JA, Rocha F (2012), Statistical tool combined with image analysis to characterize hydrodynamics and mass transfer in a bubble column. *Chem Eng J* 180:216-228

[128] Guan X, Yang N (2017), Bubble properties measurement in bubble columns: From homogeneous to heterogeneous regime. *Chem Eng Res Des* 127:103-112

[129] Besagni G, Inzoli F, Zieghenein T, Lucas D (2019), Experimental study of liquid velocity profiles in large-scale bubble columns with particle tracking velocimetry. *Journal of Physics: Conference Series* 1224:012036

[130] Besagni G, Inzoli F, Ziegenhein T (2018), Two-Phase Bubble Columns: A Comprehensive Review. *ChemEngineering* 2:13

[131] Legendre D, Zevenhoven R (2019), Image analysis assessment of the effect on mixing on aqueous dissolution of CO2 and air bubble swarms in a bubble column. *Chem Eng Res Des* 146:379-390

[132] Kalaga DV, Ansari M, Turney DE, et al. (2020), Scale-up of a downflow bubble column: Experimental investigations. *Chem Eng J* 386,

[133] Zhang L, Yang C, Mao Z-S (2008), Unsteady motion of a single bubble in highly viscous liquid and empirical correlation of drag coefficient. *Chem Eng Sci* 63:2099-2106

[134] Olivieri G, Elena Russo M, Simeone M, Marzocchella A, Salatino P (2011), Effects of viscosity and relaxation time on the hydrodynamics of gas–liquid systems. *Chem Eng Sci* 66:3392-3399

[135] Besagni G, Guédon GR, Inzoli F (2015), Annular Gap Bubble Column: Experimental Investigation and Computational Fluid Dynamics Modeling. *J Fluids Eng* 138:011302-011302-011315

[136] Besagni G, Inzoli F (2017), The effect of liquid phase properties on bubble column fluid dynamics: Gas holdup, flow regime transition, bubble size distributions and shapes, interfacial areas and foaming phenomena. *Chem Eng Sci* 170:270-296

[137] Besagni G, Inzoli F, De Guido G, Pellegrini LA (2017), The dual effect of viscosity on bubble column hydrodynamics. *Chem Eng Sci* 158:509-538

[138] Laupsien D, Cockx A, Line A (2017), Bubble Plume Oscillations in Viscous Fluids. *Chem Eng Technol* 40:1484-1493

[139] Buchholz H, Buchholz R, Niebeschütz H, Schügerl K (1978), Absorption of oxygen in highly viscous newtonian and non-Newtonian fermentation model media in bubble column bioreactors. *European Journal of Applied Microbiology and Biotechnology* 6:115-126

[140] Bajón Fernández Y, Cartmell E, Soares A, et al. (2015), Gas to liquid mass transfer in rheologically complex fluids. *Chem Eng J* 273:656-667

[141] Huang J, Saito T (2015), Influence of Bubble-Surface Contamination on Instantaneous Mass Transfer. *Chem Eng Technol* 38:1947-1954

[142] Takagi S, Matsumoto Y (2011), Surfactant Effects on Bubble Motion and Bubbly Flows. *Annual Review of Fluid Mechanics* 43:615-636

[143] Asgharpour M, Mehrnia MR, Mostoufi N (2010), Effect of surface contaminants on oxygen transfer in bubble column reactors. *Biochem Eng J* 49:351-360

[144] Sardeing R, Painmanakul P, Hébrard G (2006), Effect of surfactants on liquid-side mass transfer coefficients in gas–liquid systems: A first step to modeling. *Chem Eng Sci* 61:6249-6260

[145] Bischof F, Sommerfeld M, Durst F (1993), Stoffaustausch von Gasblasen unter Einwirkung oberflächenaktiver Substanzen. *Chem Ing Tech* 65:1365-1367

[146] Bischof F, Sommerfeld M (1992), Einfluß von Tensiden auf Blasenbildung, Blasenaufstieg und Stoffaustausch. *Chem Ing Tech* 64:187-188

[147] Mouza AA (2018), Design of bubble columns equipped with porous sparger. *Materials Today: Proceedings* 5:27572-27581

[148] Raffel M, Willert CE, Scarano F, Kähler CJ, Wereley ST, Kompenhans J (2018) Particle image velocimetry: a practical guide. Springer,

[149] Adrian RJ (1991), Particle-Imaging Techniques for Experimental Fluid Mechanics. *Annual Review of Fluid Mechanics* 23:261-304

[150] Atkins MD (2016), Velocity Field Measurement Using Particle Image Velocimetry (PIV). *Application of Thermo-Fluidic Measurement Techniques: An Introduction*:125-166

[151] Spectra Viewer, FPbase. https://www.fpbase.org/spectra/

[152] Bordas R, Roloff C, Thevenin D, Shaw RA (2013), Experimental determination of droplet collision rates in turbulence. *New J Phys* 15:1-31

[153] Darmana D (2006), On the multiscale modelling of hydrodynamics, mass transfer and chemical reactions in bubble columns, Ph.D. Thesis, University of Twente.

[154] Lehwald A, Thévenin D, Zähringer K (2009), Quantifying macro-mixing and micro-mixing in a static mixer using two-tracer laser-induced fluorescence. *Exp Fluids* 48:823-836

[155] Lehwald A, Janiga G, Thévenin D, Zähringer K (2012), Simultaneous investigation of macro- and micro-mixing in a static mixer. *Chem Eng Sci* 79:8-18

[156] Dietrich N, Loubière K, Jimenez M, Hébrard G, Gourdon C (2013), A new direct technique for visualizing and measuring gas–liquid mass transfer around bubbles moving in a straight millimetric square channel. *Chem Eng Sci* 100:172-182

[157] Yang L, Loubière K, Dietrich N, Le Men C, Gourdon C, Hébrard G (2017), Local investigations on the gas-liquid mass transfer around Taylor bubbles flowing in a meandering millimetric square channel. *Chem Eng Sci* 165:192-203

[158] Yang L, Dietrich N, Hébrard G, Loubière K, Gourdon C (2016), Optical methods to investigate the enhancement factor of an oxygen‐sensitive colorimetric reaction using microreactors. *AlChE J* 63:2272-2284

[159] Yang L, Dietrich N, Loubière K, Gourdon C, Hébrard G (2016), Visualization and characterization of gas–liquid mass transfer around a Taylor bubble right after the formation stage in microreactors. *Chem Eng Sci* 143:364-368

[160] Maxworthy T, Gnann C, Kurten M, Durst F (1996), Experiments on the rise of air bubbles in clean viscous liquids. *J Fluid Mech* 321:421-441

[161] Abou-El-Hassan ME (1983), A Generalized Bubble Rise Velocity Correlation. *Chem Eng Commun* 22:243-250

[162] Rodrigue D (2001), Generalized correlation for bubble motion. *AlChE J* 47:39-44

[163] Wellek RM, Agrawal AK, Skelland AHP (1966), Shape of liquid drops moving in liquid media. *AlChE J* 12:854-862

[164] Rastello M, Marié J-L, Lance M (2011), Drag and lift forces on clean spherical and ellipsoidal bubbles in a solid-body rotating flow. *J Fluid Mech* 682:434-459

[165] Tadaki T, Maeda S (1961), On the Shape and Velocity of Single Air Bubbles Rising in Various Liquids. *Chem Eng* 25:254-264

[166] Liu L, Zhang H, Yan H, et al. (2021), Experimental studies on bubble aspect ratio and corresponding correlations under bubble swarm condition. *Chem Eng Sci* 236:116551

[167] Liu L, Yan H, Zhao G (2015), Experimental studies on the shape and motion of air bubbles in viscous liquids. *Exp Therm Fluid Sci* 62:109-121

[168] Besagni G, Deen NG (2020), Aspect ratio of bubbles in different liquid media: A novel correlation. *Chem Eng Sci* 215:115383

[169] Higbie R (1935), The rate of absorption of a pure gas into a still liquid during short periods of exposure. *AlChE J* 31:365-389

[170] Frössling N (1938), On the evaporation of falling drops. *Gerland Beiträge zur Geophysik* 52:170-216

[171] Calderbank PH, Moo-Young MB (1961), The continuous phase heat and mass-transfer properties of dispersions. *Chem Eng Sci* 16:39-54

[172] Brauer H (1981), Particle/fluid transport processes. *Chem Eng* 19:81-11

[173] Akita K, Yoshida F (1974), Bubble Size, Interfacial Area, and Liquid-Phase Mass Transfer Coefficient in Bubble Columns. *Industrial & Engineering Chemistry Process Design and Development* 13:84-91

[174] Nedeltchev S, Jordan U, Schumpe A (2010), Semi-theoretical prediction of volumetric mass transfer coefficients in bubble columns with organic liquids at ambient and elevated temperatures. *The Canadian Journal of Chemical Engineering* 88:523-532

[175] Versteeg GF, Van Swaaij WPM (2002), Solubility and diffusivity of acid gases (carbon dioxide, nitrous oxide) in aqueous alkanolamine solutions. *Journal of Chemical & Engineering Data* 33:29-34

[176] Calderbank PHM-Y, M.D. (1961), The Power Characteristics of Agitators for the Mixing of Newtonian and Non-Newtonian Fluids. *Trans Inst Chem Eng* 39:337-347

[177] Brignole EA, Echarte R (1981), Mass transfer in laminar liquid jets. *Chem Eng Sci* 36:705-711

[178] Song D, Seibert AF, Rochelle GT (2014), Effect of liquid viscosity on the liquid phase mass transfer coefficient of packing. *12th International Conference on Greenhouse Gas Control Technologies, Ghgt-12* 63:1268-1286

[179] Farajzadeh R, Barati A, Delil HA, Bruining J, Zitha PLJ (2007), Mass Transfer of CO2 Into Water and Surfactant Solutions. *Pet Sci Technol* 25:1493-1511

[180] Kulkarni AA, Joshi JB (2005), Bubble Formation and Bubble Rise Velocity in Gas−Liquid Systems: A Review. *Industrial & Engineering Chemistry Research* 44:5873-5931

[181] Kováts P, Zähringer K, Simultaneous 2-Tracer-LIF and PIV for the study of mass transfer around single CO2-bubbles. In: *18th International Symposium on Applications of Laser Techniques to Fluid Mechanics*, Lisbon, Portugal, (2016).

[182] Bothe D, Kröger M, Alke A, Warnecke H-J (2009), VOF-based simulation of conjugate mass transfer from freely moving fluid particles. *Computational Methods in Multiphase Flow V*:157-168

[183] Aboulhasanzadeh B, Thomas S, Taeibi-Rahni M, Tryggvason G (2012), Multiscale computations of mass transfer from buoyant bubbles. *Chem Eng Sci* 75:456-467

[184] Hlawitschka MW, Kováts P, Zähringer K, Bart HJ (2017), Simulation and experimental validation of reactive bubble column reactors. *Chem Eng Sci* 170:306-319

[185] Hlawitschka MW, Kováts P, Dönmez B, Zähringer K, Bart HJ (2020), Bubble motion and reaction in different viscous liquids. *Exp Comput Multiph Flow*

[186] Rzehak R, Krauss M, Kovats P, Zahringer K (2017), Fluid dynamics in a bubble column: New experiments and simulations. *Int J Multiphase Flow* 89:299-312

[187] Wieneke B (2015), PIV uncertainty quantification from correlation statistics. *Meas Sci Technol* 26:074002

[188] Hampel U, Kipping R, Zähringer K, et al. (2021) Reactive Bubbly Flows Fluid Mechanics and Its Applications. 1 edn. Springer International Publishing, pp. 490

[189] Dreher A (2020), Datenanalyse zum Stoffübergang von CO_2 und O_2 in einer Blasensäule, Bachelor Thesis, Otto-von-Guericke-Universität Magdeburg.

[190] Taborda MA, Sommerfeld M, Muniz M (2021), LES-Euler/Lagrange modelling of bubble columns considering mass transfer, chemical reactions and effects of bubble dynamics. *Chem Eng Sci* 229:116121

[191] Pfister E (2018), Rechnerische Auswertung von Stofftransferkoeffizienten aus gemessenen Blasengrößenverteilungen, Geschwindigkeits- und Konzentrationsfeldern zur Analyse von Gasübergangsvorgängen in Zweiphasenströmungen, Bachelor Thesis, Otto-von-Guericke-Universität Magdeburg.

Own publications

Journal publications

1. Kováts, P., D. Thévenin, and K. Zähringer, Influence of viscosity and surface tension on bubble dynamics and mass transfer in a model bubble column. *Int J Multiphase Flow*. 123, (2020) p. 103174.
2. Hlawitschka, M.W., P. Kováts, B. Dönmez, K. Zähringer, and H.J. Bart, Bubble motion and reaction in different viscous liquids. *Exp Comput Multiph Flow*. (2020).
3. Kováts, P., F.J.W.A. Martins, M. Mansour, D. Thévenin, and K. Zähringer, Tomographic PIV measurements and RANS simulations of secondary flows inside a horizontally positioned helically coiled tube. *Exp Fluids*. 61(5), (2020).
4. Kováts, P., C. Velten, M. Mansour, D. Thévenin, and K. Zähringer, Mixing characterization in different helically coiled configurations by laser-induced fluorescence. *Exp Fluids*. 61(9), (2020).
5. Mansour, M., P. Khot, P. Kováts, D. Thévenin, K. Zähringer, and G. Janiga, Impact of computational domain discretization and gradient limiters on CFD results concerning liquid mixing in a helical pipe. *Chem Eng J*. 383, (2020) p. 123121.
6. Jokiel, M., N.M. Kaiser, P. Kováts, M. Mansour, K. Zähringer, K.D.P. Nigam, and K. Sundmacher, Helically coiled segmented flow tubular reactor for the hydroformylation of long-chain olefins in a thermomorphic multiphase system. *Chem Eng J*. 377, (2019) p. 120060.
7. Sarker, D., W. Ding, R. Franz, O. Varlamova, P. Kovats, K. Zähringer, and U. Hampel, Investigations on the effects of heater surface characteristics on the bubble waiting period during nucleate boiling at low subcooling. *Exp Therm Fluid Sci*. 101, (2019) p. 76-86.
8. Kováts, P., D. Thévenin, and K. Zähringer, Characterizing fluid dynamics in a bubble column aimed for the determination of reactive mass transfer. *Heat Mass Transfer*. 54(2), (2018) p. 453-461.
9. Kováts, P., D. Pohl, D. Thévenin, and K. Zähringer, Optical determination of oxygen mass transfer in a helically-coiled pipe compared to a straight horizontal tube. *Chem Eng Sci*. 190, (2018) p. 273-285.
10. Mansour, M., P. Kováts, B. Wunderlich, and D. Thévenin, Experimental investigations of a two-phase gas/liquid flow in a diverging horizontal channel. *Exp Therm Fluid Sci*. 93, (2018) p. 210-217.
11. Kováts, P., D. Thévenin, and K. Zähringer, Investigation of Mass Transfer and Hydrodynamics in a Model Bubble Column. *Chemical Engineering & Technology*. 40(8), (2017) p. 1434-1444.
12. Hlawitschka, M.W., P. Kováts, K. Zähringer, and H.J. Bart, Simulation and experimental validation of reactive bubble column reactors. *Chem Eng Sci*. 170, (2017) p. 306-319.
13. Rzehak, R., M. Krauss, P. Kováts, and K. Zähringer, Fluid dynamics in a bubble column: New experiments and simulations. *Int J Multiphase Flow*. 89, (2017) p. 299-312.

Book chapters

1. Hampel, U., Kipping, R., Zähringer, K., Kováts, P., Sommerfeld, M., Taborda, M. A., Rzehak, R., Hlawitschka, M., Klüfers, P. and Oßberger, M.: Chemical reactions in bubbly flows, in: *Reactive Bubbly Flows*, Schlüter, M., Bothe, D., Herres-Pawlis, S. and Nieken, U., Editors. 2021, Springer International Publishing. pp. 490.
2. Zähringer, K. and Kováts, P.: Experimental characterization of gas-liquid mass transfer in a reaction bubble column using a neutralization reaction, in: *Reactive Bubbly Flows*, Schlüter, M., Bothe, D., Herres-Pawlis, S. and Nieken, U., Editors. 2021, Springer International Publishing. pp. 490.

Conference proceedings

1. Hlawitschka, M.W.K., P.; Dönmez, B.; Zähringer, K.; Bart, H.-J., Bubble oscillation in low to higher viscous liquids. In: *International Conference on Multiphase Flow (ICMF) 2019*, Rio de Janeiro, (2019).
2. Martins, F.J.W.A., P. Kováts, D. Thévenin, and K. Zähringer, Tomo-PIV measurements inside a helically coiled tube. In: *13th International Symposium on Particle Image Velocimetry ISPIV 2019*, Munich, Germany, (2019).
3. Kováts, P., M. Mansour, C. Velten, D. Thévenin, and K. Zähringer, Mischungscharakterisierung in Helixreaktoren mittels laser-induzierter Fluoreszenz. In: *27 Fachtagung Experimentelle Strömungsmechanik (GALA)*, Erlangen, Germany, (2019).
4. Kováts, P. and K. Zähringer, Detailed measurement of oxygen mass transfer in a bubble column – application of a new fluorescent dye. In: *19th International Symposium on Applications of Laser Techniques to Fluid Mechanics*, Lisbon, Portugal, (2018).
5. Kováts, P., D. Pohl, and K. Zähringer, Colorimetric study of oxygen mass transfer in a helically coiled pipe. In: *19th International Symposium on Applications of Laser Techniques to Fluid Mechanics*, Lisbon, Portugal, (2018).
6. Kováts, P., F.J.W.A. Martins, D. Thévenin, and K. Zähringer, Tomographic PIV measurements in a helically coiled reactor. In: *Conference on Modelling Fluid Flow (the 17th International Conference on Fluid Flow Technologies)*, Budapest, Hungary, (2018).
7. Kováts, P., D. Thévenin, and K. Zähringer, Optical measurement of oxygen mass transfer in a coiled reactor. In: *Jahrestreffen der ProcessNet-Fachgruppe Mehrphasenströmungen*, Dresden, Germany, (2017).
8. Kováts, P. and K. Zähringer, Simultaneous 2-Tracer-LIF and PIV for the study of mass transfer around single CO2-bubbles. In: *18th International Symposium on Applications of Laser Techniques to Fluid Mechanics*, Lisbon, Portugal, (2016).
9. Kováts, P., D. Thévenin, and K. Zähringer, Fluiddynamical characterization of a bubble column for investigation of mass-transfer. In: *Conference on Modelling Fluid Flow (the 16th International Conference on Fluid Flow Technologies)*, Budapest, Hungary, (2015).
10. Zähringer, K., L.-M. Wagner, P. Kováts, and D. Thévenin, Experimental characterization of the mass transfer from gas to liquids in a two-phase bubble column. In: *7th International Berlin Workshop (IBW7) on Transport Phenomena with Moving Boundaries and More*, Berlin, Germany, (2015).
11. Kováts, P., D. Thévenin, and K. Zähringer, Experimentelle Untersuchung von Strömungsfeldern in den Zwischenräumen grober Schüttungen. In: *23 Fachtagung Lasermethoden in der Strömungsmesstechnik*, Dresden, Germany: GALA, (2015).